Implantable Electrodes for Upper Limb Prosthetic Control

Henry Thomas Lancashire

A dissertation submitted in partial fulfillment

of the requirements for the degree of

Doctor of Engineering

of the

University College London.

Department of Chemistry

University College London

10th September 2015

I think you'll find it's a bit more complicated than that ...

Dr. Ben Goldacre (badscience.net)

I, Henry Thomas Lancashire, confirm that the work presented in this thesis is my own. Where information has been derived from other sources, I confirm that this has been indicated in the thesis.

_____ *Name*

_____ *Date*

Abstract

This thesis describes a study investigating implantable interfaces with muscles and peripheral nerves. Current prostheses for upper limb amputees do not provide intuitive control over hand, wrist and elbow motion. By implanting electrodes for recording and stimulating onto muscles and into nerves in the amputation stump a greater number of control signals may be made available, signals which will be used to control dextrous hand movements.

An implantable epimysial interface was developed using a bone-anchored device to hard-wire signals across the skin barrier. In a single ovine model pilot study the bone-anchor was implanted transtibially and the epimysial electrode was place superficially to *m. peroneus teritus*. Physiological signals were obtained over 12 weeks during treadmill walking. The external connector on the bone-anchor failed at 12 weeks, correlating with a drop in signal quality in an otherwise robust interface integrated with bone and skin tissue. The ovine bone-anchor model was repeated in 6 sheep for 19 weeks, with epimysial recordings made regularly. Increasing signal quality was seen during the study and was significantly greater from implanted electrodes compared with skin surface electrodes at 19 weeks ($p = 0.016$). Some complications with skin-implant integration were observed in proximally located implants. Crosstalk between muscles was assessed using pre-terminal nerve stimulation, and was found to be dependent upon muscle location and innervation. The ovine *m. peroneus teritus* model was used to assess recovery following targeted muscle reinnervation. Muscle signal recovery was observed approximately one month after surgery correlating with the start of functional recovery (assessed by force plate analysis). These studies indicate that a suitably modified bone-anchored device may be suitable for signal transmission in human patients, providing a stable, long-term solution to both prosthesis attachment and control.

The potential of nerve interfaces for prosthetic control was investigated. The microchannel neural interface (MNI) was chosen because it overcomes limitations with other neural microarray designs: signal strength; cross-talk, and the locations of Nodes of Ranvier. MNIs confine regenerating nerves to small, ~ 100 μm diameter, insulating tubes, this increases the length within which nerve signals can be recorded and amplifies the recorded signals. However, *in vivo* MNIs can become occluded by fibrosis that reduces or prevents axon regeneration. Two *in vitro* studies of neurocompatibility were carried out to investigate strategies for improving axon regeneration within microchannels.

The first *in vitro* study compared the effect of different adsorbed endoneurial basement membrane

proteins on PC-12 cell neurite extension on silicone substrates. The optimal protein coating concentrations for poly-D-lysine, collagen-IV and laminin-2,(-4) were determined. The optimal concentrations were compared with mixtures of basement membrane proteins, the effect of mixture coating order and constitution were investigated. It was found that endoneurial BM proteins significantly enhance neurite outgrowth compared with controls. Two coatings were suggested as most suited for improving neural regeneration within microchannels: a single layer coating of 10 μg/cm^2 collagen-IV; and a mixed coating of 10 μg/cm^2 collagen-IV, 1 μg/cm^2 laminin-2,(-4), and 0.175 μg/cm^2 nidogen-1.

The second *in vitro* study investigated the effect of grooved, roughened and multi-scale silicone surfaces on on PC-12 cell neurite extension. Deeper, narrower grooves were shown to increase the extent of neurite alignment, while resulting in fewer, longer, neurites. Roughening surfaces was shown to increase the amount of protein (collagen-IV) which adsorbed from solution and increase the number of neurites each cell extended. Surfaces with multiscale topographies synergistically increased the number and length of neurites and guided neurite growth along the groove direction.

MNIs were manufactured for *in vivo* testing. These MNIs were used to determine the effect of adsorbed endoneurial basement membrane proteins on nerve regeneration *in vivo*, but the multiscale topographies were not applied during manufacturing. Four alternative manufacturing methods were investigated and iterative improvements were made to create a stacked interface with multiple microchannel layers. Microchannel layers were created by laser patterning silicone and metal foil components, followed by plasma bonding to create a 3-dimensional structure with 150 μm deep, 200 μm wide microchannels. Electrode impedances of 27.2 ± 19.8 kΩ at 1kHz were achieved by DC etching. The method overcomes some current limitations on electrode connectivity and microchannel sealing, and may improve recording capabilities over single layer designs by increasing the ratio of electrodes to microchannels.

Manufactured MNIs were tested in a rat sciatic nerve transection model. Following implantation nerves were allowed to regenerate for one and two months. First, suture and fibrin glue were compared as MNI fixation methods for one month, the nerve regenerated within the fibrin glue, outside the interface lumen, therefore sutures were chosen as a long term fixation method. The influence of endoneurial basement membrane protein coatings, identified previously, on nerve regeneration with MNIs was investigated. Nerves regenerated through the MNIs over two months and began to reinnervate the distal limb. Improvements in the sciatic function index were observed over two months, with no significant differences between protein coated and control interfaces. Some weak histological evidence for the use of protein coatings was found, with axon diameters increased distal to protein coated MNIs. Electromyographic and electroneurographic recordings demonstrated similar signal amplitudes to previous studies.

In order to bring the research described in this thesis to clinical practice further engineering im-

provements to the design and manufacture of electrodes, which utilise materials or coatings to enhance neurocompatibility, is required. Avenues for further research are discussed and additional experiments and investigations are described. By combining developments in implantable muscle and nerve interfaces with surgical techniques and improvements in neurocompatibility the promise of upper limb prosthetic control may be realised.

Acknowledgements

I would like to thank everyone who helped and supported me throughout my studies at UCL. First and foremost my supervisors: Gordon Blunn and Catherine Pendegrass. Dr. Yazan al Ajam for his surgical expertise and work on muscles. Nick Donaldson and James Fawcett for pointing me in the right direction. The staff and students at the IOMS including Rob Dowling, Victoria Jenkins, Mark Harrison, Steve Taylor, Elena Garcia, Jay Meswania, Rebecca Porter, Melanie Coathrup, Keith Rayner, Shiying Hao, Anita Sanghani, Dara McCreary, Sara Ajami, Claire Walsh, Dara McCreary, Shirin Shahbazi, and Umber Cheema. The staff and students of the UCL Medical Physics IDG including Nick Donaldson, Anne Vanhoestenberghe, Nathaniel Dahan, Tim Perkins, Sandy Mosse, Elliot Magee, and Joe Evans. The staff at the RVC, including Gillian Hughes, Fran, and Roberta Ferro de Godoy. The M^3S group at UCL Chemistry including Nora de Leeuw, Zhimei Du and Ricardo Grau-Crespo. Everyone else who has made this thesis happen: Alejandro Carnicer, Norbert Kang, and many others. The EPSRC, M^3S and Professor Blunn for funding this research. Ro and Steve for putting up with me in September 2011. My parents and grandparents for supporting me. And last but not least, Heather, for putting up with me all the way through.

Publications

Work presented in this thesis has been published, presented or submitted as follows:

Trent International Prosthetics Symposium, Loughborough, UK, 2012.

"The use of skeletal muscle to amplify action potentials in transacted peripheral nerves."

Presenting Author: Yazan Al-Ajam

57th Annual Meeting of the Plastic Surgery Research Council, Ann Arbor, MI, USA, 2012.

"The Use of Skeletal Muscle to Amplify Action Potentials in Transected Peripheral Nerves." [1]

Presenting Author: Yazan Al-Ajam

8th International Workshop for Musculoskeletal & Neuronal Interactions, Ipswich, UK, 2012.

"Evaluation of a hard-wired epimysial electrode construct for multi-channel, high bandwidth prosthetic control."

Presenting Author: Henry T Lancashire

British Orthopaedic Research Society Annual Meeting, London, UK, 2012.

"Bone-Anchored Devices For Neuromuscular Prosthetic Control."

Poster Presentation

Presenting Author: Henry T Lancashire

IEEE Transactions on Biomedical Engineering, 2013.

"The Use of a Bone-Anchored Device as a Hard-Wired Conduit for Transmitting EMG Signals from Implanted Muscle Electrodes." [2]

Authors: Yazan Al-Ajam, Henry T Lancashire, Catherine Pendegrass, Norbert Kang, Robert P. Dowling, and Gordon Blunn.

UK Society for Biomaterials 13th Annual Conference, Birmingham, UK, 2013.

"*In Vitro* Neurite Outgrowth on Endoneurial Basement Membrane Proteins."

Presenting Author: Henry T Lancashire.

Runner Up: Oral Presentation Prize.

European Society for Biomaterials Annual Meeting, Madrid, Spain, 2013.

"Basement Membrane Protein Coatings for *In Vitro* Neural Regeneration for Nerve Electrodes."

Presenting Author: Henry T Lancashire.

American Association for Hand Surgery Annual Meeting, Hawaii, USA, 2014.

"Myoelectric Signal Transmission from Implanted Epimysial Electrodes Using a Bone-Anchor as a Conduit."

Presenting Author: Yazan Al-Ajam.

European Plastic Surgery Research Council Meeting, Hamburg, Germany, August 2013.

"Use of bone-anchored devices for intuitive muscular prosthetic control."

Presenting Author: Yazan Al-Ajam

1st International Conference on Repair, Regeneration and Reconstruction, London, UK, 2014.

"Using bone-anchor as a hard-wired engineered conduit for myoelectric signal transmission from implanted muscle electrodes."

Short Oral Presentation.

Presenting Author: Yazan Al-Ajam.

Winner: Best Short Oral Presentation.

Contents

1 Introduction **24**

1.1 Aims and Overview . . . 24

1.2 Upper-Limb Amputation . . . 25

1.2.1 Restoring Function without Prostheses . . . 26

1.3 Requirements for Upper-Limb Prostheses . . . 26

1.4 Upper-Limb Prosthesis Designs . . . 27

1.4.1 Cosmetic Prostheses . . . 27

1.4.2 Body-Powered Prostheses . . . 27

1.4.3 Myoelectric Prostheses . . . 28

1.4.4 Neuroelectric Prostheses . . . 29

1.4.5 Hybrid Prostheses . . . 29

1.5 Biology and Electrophysiology for Recordings . . . 29

1.5.1 Peripheral Nerve Physiology . . . 29

1.5.2 Muscle Physiology . . . 31

1.5.3 Bioelectricity . . . 32

1.5.4 Extracellular Electrophysiology . . . 35

1.5.5 Peripheral Nerve Injury and Regeneration . . . 37

1.6 Recording Interface Designs . . . 38

1.6.1 Muscle Interfaces . . . 39

1.6.2 Nerve Interfaces . . . 41

1.6.3 Other Considerations for Electrophysiology . . . 48

1.7 The Host Response to Implanted Devices . . . 49

1.7.1 Biocompatibility . . . 49

1.7.2 Myocompatibility . . . 50

1.7.3 Neurocompatibility . . . 50

1.8 Surgical Approaches to Control . . . 54

1.8.1 Targeted Reinnervation . . . 54

1.9 Implantable Interfaces and the Skin Barrier . . . 55
1.9.1 Telemetry . . . 55
1.9.2 Hard-Wired Connections . . . 55
1.10 Summary . . . 59

2 *In Vivo* Electromyography **60**
2.1 Introduction . . . 60
2.1.1 Implantable EMG Electrodes . . . 61
2.1.2 Targeted Muscle Reinnervation . . . 62
2.1.3 Transcutaneous Signal Transmission . . . 63
2.1.4 Aims and Hypotheses . . . 64
2.2 Methodology . . . 65
2.2.1 Implantable Myoelectrodes 1 . . . 65
2.2.2 Implantable Myoelectrodes 2 . . . 70
2.2.3 Targeted Muscle Reinnervation 1 . . . 71
2.2.4 Data Analysis . . . 72
2.3 Results . . . 72
2.3.1 Implantable Myoelectrodes 1 . . . 72
2.3.2 Implantable Myoelectrodes 2 . . . 74
2.3.3 Targeted Muscle Reinnervation 1 . . . 77
2.4 Discussion . . . 81
2.4.1 Implantable Myoelectrodes 1 . . . 81
2.4.2 Implantable Myoelectrodes 2 . . . 82
2.4.3 Targeted Muscle Reinnervation . . . 84
2.4.4 Conclusions . . . 86

3 *In Vitro* Neuron Adhesion Studies: Basement Membrane Proteins **88**
3.1 Introduction . . . 88
3.1.1 Endoneurial Basement Membrane . . . 89
3.1.2 Aims and Hypotheses . . . 90
3.2 Methodology . . . 91
3.2.1 Preparation of Silicone Surfaces for *In Vitro* Assays . . . 91
3.2.2 Protein Coating of Silicone Surfaces . . . 94
3.2.3 Analysis of Coating by Raman Microscopy . . . 96
3.2.4 Analysis of Coating by BCA Assay . . . 96
3.2.5 Cell Line . . . 97

3.2.6 Cell Seeding . . . 97
3.2.7 Neurite Outgrowth Assay . . . 97
3.2.8 Data Analysis . . . 99
3.3 Results . . . 99
3.3.1 Raman Microscopy . . . 99
3.3.2 BCA Assay . . . 99
3.3.3 Protein Concentration Optimisation . . . 100
3.3.4 Laminin-2,(-4) and Laminin-1 . . . 106
3.3.5 Comparison of Optimal Concentrations . . . 106
3.3.6 Comparison of Multi-Protein Coatings: Experiment 1 . . . 107
3.3.7 Comparison of Multi-Protein Coatings: Experiment 2 . . . 108
3.3.8 Cell Morphology . . . 109
3.4 Discussion . . . 113
3.4.1 Analysis of Coatings by Raman Microscopy and BCA Assay . . . 113
3.4.2 Protein Concentration Optimisation . . . 114
3.4.3 Laminin-2,(-4) and Laminin-1 . . . 115
3.4.4 Comparison of Optimal Concentrations . . . 115
3.4.5 Comparison of Multi-Protein Coatings . . . 115
3.4.6 General Discussion . . . 117

4 *In Vitro* Neuron Adhesion Studies: Topography 119

4.1 Introduction and Hypotheses . . . 119
4.1.1 Contact Guidance and Groove Dimensions . . . 120
4.1.2 Roughened Surfaces and the Neural Extracellular Matrix . . . 121
4.1.3 Multiscale Topographies . . . 121
4.1.4 Aims and Hypotheses . . . 121
4.2 Methodology . . . 122
4.2.1 Fabrication of Patterned Templates . . . 122
4.2.2 Fabrication of Patterned Silicone Substrates . . . 123
4.2.3 Vertical Scanning Interferometry . . . 124
4.2.4 Water Contact Angles . . . 124
4.2.5 Surface Functionalisation . . . 124
4.2.6 Analysis of Coating by Bicinchoninic Acid (BCA) Assay . . . 125
4.2.7 Cell Line . . . 125
4.2.8 Cell Seeding . . . 126

4.2.9 Scanning Electron Microscopy . . . 126
4.2.10 Immunoflourescence Microscopy . . . 127
4.2.11 Image Analysis . . . 127
4.2.12 Data Analysis . . . 128
4.3 Results . . . 128
4.3.1 Surface Roughness by Vertical Scanning Interferometry . . . 129
4.3.2 Surface Topography by Vertical Scanning Interferometry . . . 129
4.3.3 Water Contact Angles . . . 129
4.3.4 BCA Assay . . . 132
4.3.5 Intraclass correlation . . . 132
4.3.6 HF Etched Surfaces . . . 132
4.3.7 Grooved Surfaces . . . 134
4.3.8 Multiscale Surfaces: Experiment 1 . . . 134
4.3.9 Multiscale Surfaces: Experiment 2 . . . 136
4.3.10 Protein Mixes on Multiscale Surfaces . . . 138
4.3.11 Cell Morphology . . . 140
4.4 Discussion . . . 145
4.4.1 Water Contact Angles . . . 145
4.4.2 BCA Assay . . . 145
4.4.3 HF Etched Surfaces . . . 145
4.4.4 Grooved Surfaces . . . 146
4.4.5 Multiscale Surfaces: Experiment 1 . . . 147
4.4.6 Multiscale Surfaces: Experiment 2 . . . 148
4.4.7 Protein mixes on Multiscale Surfaces . . . 148
4.4.8 Conclusions . . . 149

5 The Manufacture of Microchannel Neural Interfaces 151

5.1 Introduction and Hypotheses . . . 151
5.1.1 Microfabrication Techniques for Neural Interfaces . . . 151
5.1.2 Conductive Polymers . . . 153
5.1.3 Thin film electrode arrays . . . 153
5.1.4 Electrode surface roughening . . . 157
5.1.5 Microchannel Neural Interfaces . . . 158
5.1.6 Challenges . . . 159
5.1.7 Aims and Hypotheses . . . 159

5.2 Methodology . . . 160
5.2.1 Microchannel Neural Interface Design . . . 160
5.2.2 Connecting to Microchannel Neural Interfaces . . . 166
5.2.3 Impedance Reduction by Electroetching . . . 166
5.3 Results . . . 168
5.3.1 3D template method . . . 168
5.3.2 Metal negative method . . . 168
5.3.3 Plasma bonding method . . . 170
5.3.4 Stacking Method . . . 173
5.3.5 Impedance Reduction by Electroetching . . . 173
5.4 Discussion . . . 176
5.4.1 Microchannel Neural Interface Design . . . 176
5.4.2 Materials choice . . . 177
5.4.3 Impedance Reduction by Electroetching . . . 178
5.4.4 Conclusions . . . 178

6 *In Vivo* testing of Microchannel Neural Interfaces 179

6.1 Introduction and Hypotheses . . . 179
6.1.1 Neural Interfaces *In Vivo* . . . 179
6.1.2 Assessing Neural Regeneration *In Vivo* . . . 183
6.1.3 Fibrin Glue . . . 185
6.1.4 Neural Extracellular Matrix . . . 185
6.1.5 Aims and Hypotheses . . . 186
6.2 Methodology . . . 186
6.2.1 Cadaveric implantation of a regenerative neural electrode . . . 186
6.2.2 An *In Vivo* Comparison of Tissue Glue and Suture for Microchannel Neural Interface Implantation . . . 187
6.2.3 An *In Vivo* Comparison of Internal Surface Coatings for Microchannel Neural Interface Implantation . . . 188
6.2.4 Electroneurography using Microchannel Electrodes . . . 190
6.2.5 Histological Procedures . . . 191
6.2.6 Gait Analysis by the Sciatic Functional Index . . . 192
6.2.7 Data Analysis . . . 195
6.3 Results . . . 195
6.3.1 Cadaveric Implantation of a Microchannel Neural Interface . . . 195

6.3.2 An *In Vivo* Comparison of Tissue Glue and Suture for Microchannel Neural Interface Implantation . . . 195
6.3.3 An *In Vivo* Comparison of Internal Surface Coatings for Microchannel Neural Interface Implantation . . . 196
6.4 Discussion . . . 212
6.4.1 Cadaveric implantation of a regenerative neural electrode . . . 212
6.4.2 An *In Vivo* Comparison of Tissue Glue and Suture for Microchannel Neural Interface Implantation . . . 212
6.4.3 An *In Vivo* Comparison of Internal Surface Coatings for Microchannel Neural Interface Implantation . . . 213
6.4.4 General Discussion . . . 215

7 General Discussion, Contribution to Scientific Research and Proposals for Future Work 217
7.1 Conclusions . . . 223
7.2 Future Work . . . 224

Appendices 227

Bibliography 258

List of Figures

1.1 Prosthesis users' comments. 26
1.2 Commercially available myoelectric hands. 28
1.3 Structure of a typical peripheral nerve trunk. 30
1.4 Anatomy of a typical peripheral nerve trunk. 31
1.5 Structure of a typical skeletal muscle. 32
1.6 Structure of a typical skeletal muscle fibre. 33
1.7 Sunderland's five degrees of nerve injury. 37
1.8 The invasivity/selectivity for implantable electrodes. 39
1.9 A comparison of different peripheral nerve interface designs. 41
1.10 Differential amplification for bipolar, tripolar and quasi-tripolar amplification. 49
1.11 A key issue in neurocompatibility. 50
1.12 Targeted muscle reinnervation. 55
1.13 The intraosseous transcutaneous amputation prosthesis (ITAP) in position. 56
1.14 The intraosseous transcutaneous amputation prosthesis (ITAP) in a transhumeral amputee after 2 years. 57
1.15 The intraosseous transcutaneous amputation prosthesis (ITAP) in veterinary cases. 57

2.1 2D CAD design of the implant device. 66
2.2 The finished bone-anchored device with epimysial electrode. 66
2.3 Intraoperative images demonstrating implantation of the bone-anchored device and epimysial electrode. 68
2.4 Bone-anchored device post-operative plain radiographs. 68
2.5 Implant skin interface after 12 weeks. 72
2.6 A representative epimysial EMG recording. 73
2.7 Log-log plot of electrode impedance. 73
2.8 Skin-Implant and Bone-Implant interfaces of bone-anchored device. 74
2.9 Soft tissues responses to bone-anchored device and epimysial electrode. 74
2.10 Change in mean EMG SNR with time following surgery, n = 6. 76

2.11 Change in individual mean EMG SNRs with time following surgery, n = 6. 76
2.12 Comparison between implanted and skin surface EMG electrodes, n = 5. 77
2.13 Representative epimysial and skin surface EMG recordings. 78
2.14 Peak EMG signal during selective muscle stimulation. 79
2.15 Peak stimulus artefact during selective muscle stimulation. 79
2.16 1kHz impedance of epimysial electrodes following 19 weeks implantation. 80
2.17 EMG recordings following TMR. 80
2.18 Force plate analysis following TMR. 81

3.1 Structure of a Basement Membrane. 90
3.2 Raman Spectra of protein coated and uncoated PDMS surfaces. 100
3.3 Protein concentration by BCA assay. 101
3.4 PC-12 cell neurite outgrowth on Poly-D-Lysine coated samples. 102
3.5 PC-12 cell neurite outgrowth on Collagen-IV coated samples. 103
3.6 PC-12 cell neurite outgrowth on Collagen-IV coated samples. 104
3.7 PC-12 cell neurite outgrowth on Laminin-2,-4 coated samples. 105
3.8 PC-12 cell neurite outgrowth on Laminin-2,-4 coated samples. 105
3.9 PC-12 cell neurite outgrowth on Laminin-2,-4 and Laminin-1 coated samples. 106
3.10 PC-12 cell neurite outgrowth on samples coated with optimal protein concentration. . . . 107
3.11 PC-12 cell neurite outgrowth on samples coated with multi-protein coatings. 108
3.12 PC-12 cell neurite outgrowth on samples coated with multi-protein coatings. 109
3.13 Scanning Electron Micrographs of PC-12 cells on protein coated surfaces. 111
3.14 Scanning Electron Micrographs of PC-12 cells on protein coated surfaces. 112

4.1 A diagram of water contact angle measurement. 124
4.2 Change in Ra with HF etching time. 129
4.3 VSI of a control surface. 130
4.4 VSI of a roughened surface. 130
4.5 VSI of a roughened surface. 130
4.6 VSI of a grooved surface. 130
4.7 VSI of a grooved surface. 131
4.8 VSI of a grooved surface. 131
4.9 VSI of a multiscale surface. 131
4.10 VSI of a multiscale surface. 131
4.11 Water contact angles on modified surfaces. 132
4.12 Protein concentration on roughened surfaces. 133

4.13 PC-12 cell neurite outgrowth on HF etched samples. 133
4.14 PC-12 cell neurite outgrowth on grooved samples. 135
4.15 PC-12 cell neurite angles on grooved samples. 135
4.16 PC-12 cell neurite outgrowth on grooved and etched samples. 136
4.17 PC-12 cell neurite angles on grooved and etched samples. 137
4.18 PC-12 cell neurite outgrowth on grooved and etched samples. 138
4.19 PC-12 cell neurite angles on grooved and etched samples. 139
4.20 PC-12 cell neurite outgrowth on protein coated grooved and etched samples. 140
4.21 PC-12 cell neurite angles on protein coated grooved and etched samples. 141
4.22 Scanning Electron Micrographs of PC-12 cells on grooved and roughened surfaces. . . . 142
4.23 Vinculin stained PC-12 cells on modified topographies. 143
4.24 Actin stained PC-12 cells on modified topographies. 144

5.1 Schematic representation of a thin-film electrode array. 156
5.2 Microchannel neural interface diagram. 160
5.3 Overview of microchannel neural interface manufacture by the metal negative method. . 163
5.4 Overview of microchannel neural interface manufacture by plasma bonding. 164
5.5 Overview of microchannel neural interface manufacture by stacking. 167
5.6 3D templating method method processing steps and results. 169
5.7 Metal negative method microchannel interface. 170
5.8 Laser groove sizes. 171
5.9 Microchannel neural interface profiles. 172
5.10 Plasma bonded microchannel neural interface. 172
5.11 Stacking method processing steps. 174
5.12 A stacked microchannel neural interface. 175

6.1 Cadaveric assessment of neural interface implantation. 187
6.2 Rat footpad traces. 194
6.3 Passive microchannel neural interfaces *in situ*. 196
6.4 Sequential transverse histology of tissue glue implanted interface. 197
6.5 Transverse histology of suture implanted interface. 198
6.6 Sciatic Function Index following regeneration through glued and sutured conduits. . . . 198
6.7 Stacked microchannel neural interface in situ after 60 days. 199
6.8 Light micrographs of microchannel neural interface dissection. 199
6.9 Scanning Electron Micrographs of microchannels. 200
6.10 Light micrograph of a split microchannel neural interface. 200

6.11 Muscle mass changes following microchannel neural interface implantation. 201
6.12 Transverse histology of regenerated nerves after 4 weeks. 203
6.13 Transverse histology of regenerated nerves after 8 weeks. 204
6.14 Transverse and oblique histology of microfasciles after 8 weeks. 205
6.15 Histograms of axon diameter following microchannel neural interface implantation. . . . 206
6.16 Axon diameter and axon density following microchannel neural interface implantation. . 206
6.17 Sciatic Function Index following neural interface implantation. 208
6.18 Rate of Sciatic Function Index following neural interface implantation. 208
6.19 Nerve signals recorded from microchannel neural interfaces. 209
6.20 Stimulated muscle signals recorded from tibialis anterior. 209
6.21 Signal-to-noise ratios for stimulation and recording with microchannel neural interfaces. 210
6.22 Change in impedance following implantation. 211

List of Tables

1.1 Typical equilibrium potentials for mammalian neurons. 34

1.2 Overview of muscle and nerve interfaces. 45

2.1 Serial dehydration procedure for soft tissue samples: epimysial electrode. 70

3.1 Protein sources, solvents and incubation conditions. 93

3.2 Protein coating concentrations used for each experiment or group of experiments. 95

3.3 Alcohol series used for dehydration of cell monolayers on silicone sample. 98

4.1 Groove geometries achieved in silicone. 123

4.2 Alcohol series used for dehydration of cell monolayers on silicone sample. 126

4.3 Angles of neurite alignment on grooved surfaces. 134

4.4 Angles of neurite alignment on grooved and multiscale surfaces. 138

5.1 Young's Modulus values for neural interface materials. 154

5.2 Laser parameters for metal negative method. 162

5.3 Groove designs for metal negative method. 164

6.1 Axon densities following microchannel neural interface implantation. 205

6.2 Sciatic Function Index data for 8 weeks following surgery. 207

6.3 Correlation details for change in Sciatic Function Index by days following surgery. . . . 207

List of Abbreviations

All-in-one Collagen-IV + Nidogen-1 + Laminin-2,-4 mixed coating

ASIC Application Specific Integrated Circuit

BCA Bicinchoninic Acid Assay

BIONs Bionic Neurons

BM Basement Membrane

C-IV Collagen-IV

CL Collagen-IV + Laminin-2,-4 layer-by-layer coating

CL All-in-one Collagen-IV + Laminin-2,-4 mixed coating

CNL Collagen-IV + Nidogen-1 + Laminin-2,-4 layer-by-layer coating

CNS Central Nervous System

DC Direct Current

DoF Degrees of Freedom

ECM Extracellular Matrix

EMG Electromyogram / Electromyography

ENG Electroneurogram / Electroneurography

FCS Foetal Calf Serum

FES Functional Electrical Stimulation

FINE Flat Interface Nerve Electrode

Fn Fibronectin

HF Hydrofluoric Acid

HTCC High-Temperature Cofired Ceramics

IMES Implantable MyoElectric Sensor

IMS Industrial Methylated Spirits

ITAP Intraosseous Transcutaneous Amputation Prosthesis

LIFE Longitudinal Intra-Fascicular Electrode

LC Laminin-2,-4 + Collagen-IV layer-by-layer coating

Ln Laminin (-1,-2,-4...)

LNC Laminin-2,-4 + Nidogen-1 + Collagen-IV layer-by-layer coating

MEA Microelectrode Array

MNI Microchannel Neural Interface

MUAP Motor Unit Action Potential

NCP Normalised Cumulative Periodogram

NEO Nonlinear Energy Operator

NGC Nerve Guidance Conduit

Nid Nidogen (-1,-2)

NMJ Neuromuscular Junction

PBS Phosphate Buffered Saline

PC-12 Neuron-like rat adrenal gland pheochromocytoma cell line

PDL Poly-D-Lysine

PDMS Polydimethysiloxane (a silicone)

PEDOT Poly(3,4 ethylenedioxythiophene)

PLO Poly-L-Orthinine

PNS Peripheral Nervous System

PPy Poly(pyrrole)

PSS Poly(4-styrenesulfonic acid)

PTFE Polytetrafluoroethylene

RPNI Regenerative Peripheral Nerve Interface

sECM See All-in-one

SEM Scanning Electron Microscope / Microscopy

sEMG Surface Electromyogram / Surface Electromyography

SFI Sciatic Function Index

SNR Signal-to-Noise Ratio

TIME Transverse Intra-Fascicular Multichannel Electrode

TMR Targeted Muscle Reinnervation

TSR Targeted Sensory Reinnervation

USP Class-VI United States Pharmacopeia Class-VI toxicity and implant testing

Chapter 1

Introduction

1.1 Aims and Overview

This thesis investigates the control of upper limb prostheses using implanted devices for amputees. The research covers *in vitro* and *in vivo* studies of neural interfaces and *in vivo* studies of muscle interfaces. **The overall aim of the thesis is to improve implanted devices for reliable and long lasting prosthetic control.**

This thesis comprises 7 individual chapters:

Chapter 1 presents an introduction to the challenges experienced by upper limb amputees. Current systems for upper limb control are presented and the need for improvement is demonstrated. This chapter briefly describes the electrophysiology of muscle and nerve and how this relates to prosthesis control. An overview of implantable muscle and nerve interfaces is given and key points are noted including biocompatibility and the need for communication across the skin barrier.

Chapter 2 investigates the use of a bone-anchored device for electromyography (EMG) from implanted electrodes. Signal quality and cross-talk from implanted electrodes are considered in long term *in vivo* tests. In addition, a model of targeted muscle reinnervation is presented. The aim of this chapter is to record muscle signals from implanted electrodes in cognisant, moving animals and transfer these signals using a bone-anchored device. It is hypothesised that: signal quality will be better with implanted epimysial electrodes compared with skin surface EMG electrodes; and that cross-talk from adjacent muscles will be minimal compared with the target muscle when using epimysial electrodes. It is also hypothesised that neural regeneration and muscle activity will be observed following targeted muscle reinnervation in a sheep hind limb model.

Chapter 3 is an *in vitro* study of biological augmentation to improve neurocompatibility of neural interface surfaces. Experiments assess the use of single-protein and multi-protein coatings to improve neurite outgrowth. Coatings are optimised and compared against commercial standard coatings. The aim of this chapter is to develop and test a coating that could be applied within a microchannel neural interface (MNI) to improve peripheral nerve regeneration within microchannels. It is hypothesised that:

endoneurial basement membrane protein coatings increase neurite outgrowth on silicone surfaces compared with control coatings; and that a mix of basement membrane proteins improves neurite outgrowth to the same extent as a commercial ECM gel coating.

Chapter 4 presents an *in vitro* study of topographical augmentation to improve neurocompatibility of neural interface surfaces. Experiments assess the use of surface roughening and grooving to improve neurite outgrowth. Combined roughened and grooved surfaces are investigated, and use of multiscale surface topographies is discussed. The aim of this chapter is to develop and test a surface topography that could be applied within a microchannel to improve neural regeneration. It is hypothesised that: a combination of grooves and nanoscale roughening will increase neurite outgrowth compared with grooved samples and increase neurite alignment compared with roughened samples; and that PC-12 cells will exhibit contact guidance and alignment on multiscale surface topographies. It is also hypothesised that combining multiscale topography and mixed endoneurial basement membrane protein coatings will increase neurite outgrowth compared with multiscale topography and single-protein coatings.

Chapter 5 discusses manufacturing techniques for neural implants with a particular focus on microchannel neural interfaces. The chapter describes materials selection and fabrication methods. Four designs are covered and the advantages and disadvantages of each discussed. The chosen design was fabricated and this is described in detail with improvements to electrode performance using DC etching presented. The aim of this chapter is to investigate manufacturing processes for microchannel neural interfaces and to assess the resulting interface designs. It is hypothesised that direct current etching will significantly reduce electrode impedance.

Chapter 6 is an *in vivo* study of microchannel neural interfaces. Building upon chapters 3 and 5 biological augmentation of the microchannel surface using multi-protein coatings is investigated through function, electrophysiology and histology. The aim of this chapter is to test multi-protein coatings *in vivo* as a modification for MNIs. It is hypothesised that: multi-protein coatings improve functional, histological and electrophysiological outcomes following MNI implantation in a rat sciatic nerve model.

Chapter 7 presents the general conclusions and proposes key future work.

1.2 Upper-Limb Amputation

In the UK 215 people underwent an upper limb amputation in 2006/07. Over 85% of these new referrals were aged under 65 years, reflecting the etiology of the condition (primarily trauma, 58%) [3]. Approximately 0.11 major upper limb amputations per 100,000 person-years take place in Maryland (USA) and Sweden [4]. In the USA over 70% of trauma related amputees are aged under 65 years, and over 90% of upper limb amputations are trauma related (over 70% of trauma related amputations are upper limb); there are approximately 541,000 people living with an upper limb amputation in the USA, of whom 41,000 have major limb loss (2005 estimates) [5]. Younger, more active, individuals are most likely to

suffer traumatic amputation and will be most affected by the loss of an upper limb and the resulting loss of function [4].

Central to improving quality of life for upper limb amputees is restoring full, intuitive hand, wrist and elbow motion.

1.2.1 Restoring Function without Prostheses

Surgical procedures have aimed to prevent the need for amputation. Microsurgery allows the repair of fine structures within the limb, recreating the vasculature and neural pathways needed for correct limb function, although success can be limited. These techniques can now save limbs which would previously have been amputated [6].

Where a limb is completely severed, but the extent of soft tissue injury is minimal, microsurgical techniques have made re-implantation and transplantation possible [6]. Survival rates in modern procedures are approximately 90%, however, functional outcome is typically poor, with patients regaining only weak hand function and some sensory perception [7–9]. In addition, transplantation requires a suitable donor and immunosuppression of the patient to prevent rejection [7].

Where surgical repair is contraindicated, for example in cases of severe injury, crush injury or otherwise untreatable osteosarcoma, amputation may be required. For amputees wishing to regain some upper limb and hand function artificial limbs or prostheses are the most common solution.

1.3 Requirements for Upper-Limb Prostheses

Patients' requirements for upper limb prostheses are diverse. Users often try a number of designs before settling on one or more which are suitable for daily use [10,11]. Amputees value the comfort and function of their prostheses highly, however, regular activities such as housework, exercising, cooking and driving are regularly described as challenging [10, 12]. Patients almost universally want better prostheses and some are dissatisfied with the current options (see fig. 1.1). Dudkiewicz *et. al.* found that at least 50% of powered prosthesis users swap to cosmetic prostheses; complaints included limited hand movement and difficultly using the prosthesis [11]. Commercially available powered prostheses are reliable, but typically have limited degrees-of-freedom (DoF), range of motion and intuitiveness and cannot achieve the capabilities of the natural human hand [13] .

"...in the 30+ years since my amputation I haven't seen great improvements in arms..."
Respondent 509.

"I would like it to be connected to my brain, where it moves when I think about it moving."
Respondent 112.

Figure 1.1: Prosthesis users' comments to Biddiss *et. al.*, 2007 [10].

Advancements in prosthesis design and control systems have been made recently, however few of

these are in widespread clinical use. Farina *et. al.* [14] state that:

> None of the systems so far proposed in the literature fulfills [*sic*] all the important criteria needed for widespread acceptance by the patients, i.e. intuitive, closed-loop, adaptive, and robust real-time ... control, minimal number of recording electrodes with low sensitivity to repositioning, minimal training, limited complexity and low [power] consumption.

In a human hand there are 22 degress of freedom (DoF) controlled by 38 muscles [15]. To fully mirror hand motion upper limb prostheses require 38 actuators, each with a separate activating signal from the user [1]. A key limitation of current solutions is the number of control channels. Therefore in order to improve hand control, an increase in the number of control channels is required.

This thesis will focus on solutions to improve prosthetic control. In particular implantable devices and surgical approaches will be considered.

Other factors are key to prosthetic control, including signal acquisition, control algorithms and external prosthesis design. These will be considered and discussed briefly in this introduction, however, these are beyond the main scope of this thesis.

1.4 Upper-Limb Prosthesis Designs

Prosthesis designs have different advantages and disadvantages which lead users to choose a particular design. Broad prosthesis types are discussed below, however other designs are available, for example specialist sports prostheses [4, 12, 17].

1.4.1 Cosmetic Prostheses

Cosmetic prostheses aim to reproduce lifelike appearance at the expense of any active movement. Also referred to as aesthetic prostheses, they are typically lighter, placing less stress on the amputation stump than other prosthetic designs.

1.4.2 Body-Powered Prostheses

Body-powered prostheses use a cable system to transmit a body movement into the movement of the prosthesis [18]. Body-powered prostheses are typically low cost and light, also providing some direct haptic feedback to the user via the cable. However, they are often designed with function rather than appearance in mind and are not life-like.

Cable systems often require complex strap systems which are difficult to apply. For amputees with high level trans-humeral amputation or shoulder-disarticulation this can involve a vest, a common source of users' complaints.

[1] Underactuated prostheses can achieve more degrees of freedom than they have actuators, allowing for life-like motion with lighter prostheses [16].

1.4.3 Myoelectric Prostheses

Many current prostheses are controlled using muscle signals captured using skin-surface electrodes, typically two, placed on antagonist muscles. These signals can be used: to drive a single degree of freedom (DoF) following rectification and, often, continuous time-averaging; or to control a finite-state map, where modes (grasp patterns or individual DoFs) are selected by a rarely used signal, commonly co-contraction or double-contraction [13, 19].

Myoelectric hands do not appear life-life, however many manufacturers make cosmetic socks or sleeves to mimic normal appearance (see fig. 1.2). Some users decide they prefer the "cyborg" look of the normal prosthesis and choose not to use a cosmetic covering [personal correspondence with manufacturers].

The inherent disadvantage of this system is that it is unintuitive, and because the prosthesis is controlled in a non-physiological way, actions can only be performed in series, interposed by mode switching to change the DoF. Unintuitive control strategies are associated with a steep learning curve for patients, requiring many visits to an outpatient centre or prosthetist.

Figure 1.2: Commercially available myoelectric prostheses. (a) Ottobock DMC Plus. (b) Touchbionics iLimb. (c) Ottobock Michaelangelo hand. (d) RSL Steeper Bebionic. (a) Is a typical hand widely used in clinical practice providing proportional control over a single degree of freedom (wrist rotation can be added separately). (b–d) Are the most advanced hand prostheses clinically available to date (Jan 2014) allowing patients to control a range of grasp patterns. Reproduced from [13] permission received, with kind permission from Springer Science and Business Media. REDACT IN ONLINE COPY.

1.4.4 Neuroelectric Prostheses

Neuroelectric prostheses are typically modified myoelectric prosthesis, and function in the same manner. The key difference is that control signals are obtained from patients' nerves. Interfaces with nerves also enable sensory feedback to be provided to the patient, therefore neuroelectric protheses can be fitted with pressure sensitive finger-pads or other sensors.

1.4.5 Hybrid Prostheses

Hybrid prostheses combine two alternative control strategies into one design. Commonly a myoelectric hand is coupled to a body powered elbow introducing more DoF without vastly complicating the prosthesis design [18].

1.5 Biology and Electrophysiology for Recordings

1.5.1 Peripheral Nerve Physiology

The peripheral nervous system (PNS) is defined by John Hubbard as:

> "the cranial nerves, spinal nerves and peripheral ganglia which lie outside the brain and spinal cord." [20]

It is these nerves that will be considered for implantation of neural interfaces.

Peripheral nerves (figs. 1.3 and 1.4, page 30) are formed of bundled axons (nerve fibres or neurons) surrounded by connective tissue, the epineurium [21]. The epineurium mainly consists of collagen and adipose tissue. It also contains blood and lymphatic vessels. Collagens (predominantly Type I) and elastic fibres (eg. elastin) of the epineurium are longitudinally aligned. Slight undulations in alignment give nerves flex and stretch [22]. The epineurim also has small populations of macrophages, fibroblasts and mast cells.

Each fascicle (nerve bundle) is surrounded by inner epineurium, in turn surrounded by outer epineurium. Between the epineurium and the nerve bundles is the perineurium, a sheath, which controls the substances transported into the fascicle, forming a blood-nerve barrier [23]. The perineurium is formed of cell layers and type IV collagen fibrils with a basement membrane of collagen, fibronectin, laminin and glycosaminoglycans [22]. Basement membranes (BMs) are thin extracellular matrix layers which are present basolateral to cell monolayers, the composition of BM is tissue specific [24]. Perineurial cells are hypothesised to originate from a fibroblast lineage *in vivo* [25]. Fascicles are arranged spatially within the nerve according to their target organ, discrete fascicles branch from the nerve trunk to innervate a distal target organ or group [26].

Axons within the perineurium are surrounded by endoneurium, formed primarily from connective tissue, but also containing fibroblasts, macrophages, blood vessels and mast cells. Type I and III collagen

are present in the endoneurium. The endoneurium also helps maintain the blood-nerve barrier, creating an environment appropriate for nerve fibres.

Peripheral nerve axons are subdivided into two types: myelinated and unmyelinated. Myelinated axons are surrounded by an insulating myelin sheath, formed by Schwann cells. At regularly spaced intervals Nodes of Ranvier are present, separating individual Schwann cells. The nodes of Ranvier dramatically increase the conduction velocity of myelinated axons (up to 80 m/s). The axons themselves are typically large, α axons are 5 - 12 μm in diameter, with smaller β, γ and δ axons typically larger than 1 μm diameter. Human myelinated axon density is between 7,000 - 15,000 mm^{-2} [22]. Not all axons are myelinated; up to 20 unmyelinated axons can be associated with a single Schawann cell in an arrangement called a Remak bundle. These small axons (0.4 - 1.2 μm diameter) have lower conduction velocities (0.5 - 2 m/s) than unmyelinated axons. Human unmyelinated axon density is approximately 30,000 mm^{-2} [22]. Schwann cells are surrounded by their own basement membranes composed mainly of type IV collagen and laminin. The structure within this basement membrane is described by Zochodne as the axon-SC-BM complex [22].

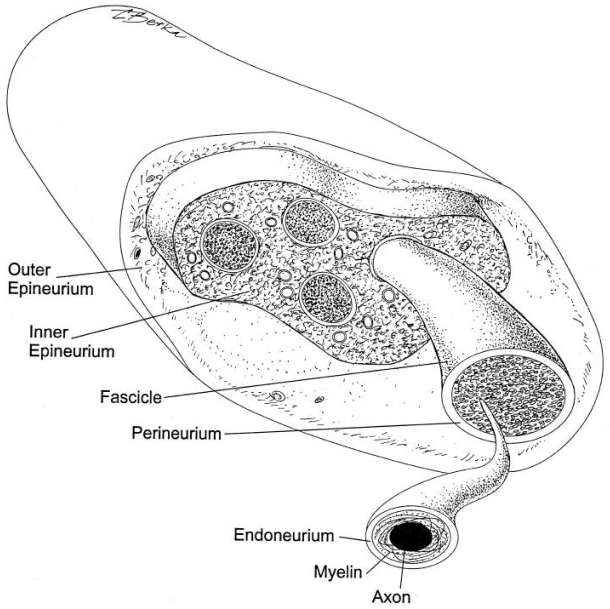

Figure 1.3: Structure of a typical peripheral nerve trunk. The structure of particular nerves can vary greatly from the structure shown in terms of the number of fascicles and the organisation of inner and outer epineurium. PNS nerves can be >1mm thick [23, 27], reproduced from [23] with kind permission from John Wiley and Sons. ©2000 Anatomical Society of Great Britain and Ireland.

1.5.1.1 Neurons

In the nervous system signals are carried by neurons. A typical neuron has 3 parts: a cell body, many dendrites and one axon. For peripheral nervous system neurons cell nuclei are located within the spinal cord or within ganglia. The cell body contains the nucleus and most of the cells' organelles. Dendrites and axons are processes, which transfer neural signals. The dendrites interface with other neurons or

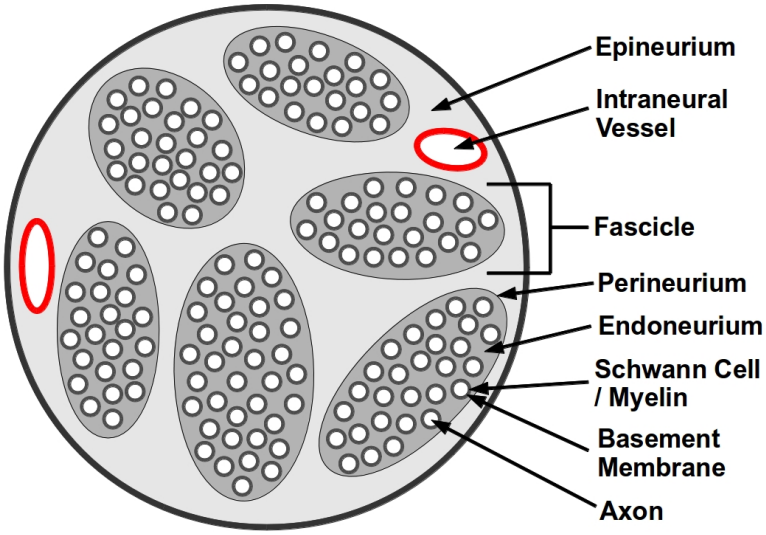

Figure 1.4: Anatomy of a typical peripheral nerve trunk. The structure of particular nerves can vary greatly from the structure shown in terms of the number of fascicles and the organisation of inner and outer epineurium.

with sensory cells, receiving signals. The signals are then transferred to the axon, which conducts the signal to another neuron or an end organ. Axons can divide, having multiple terminals each forming a synapse, where communication with the next cell or dendrite takes place [28].

1.5.1.2 *In Vitro* Neural Models

The nervous system and neural cells may be modelled *in vitro* using *ex vivo* cell cultures, as primary cultures or tissue slice cultures, and cell lines [29, 30]. The most widely used cell line is the PC-12 pheochromocytoma [31]. This line, derived from rat adrenomedullary tumour, is sensitive to nerve growth factor (NGF); exhibiting a change in phenotype to neuron-like [22, 32].

1.5.2 Muscle Physiology

Muscles are the body's motors. There are three types of muscle in the human body: cardiac, smooth, and skeletal muscle [28, 33]. This thesis will consider skeletal muscle (see fig. 1.5).

Skeletal muscle is controlled voluntarily and is responsible for movement and posture. Skeletal muscles are composed of bundles of muscle fibres, myocytes, which form from multiple fused cells (see fig. 1.6). Muscle fibres are elongated structures with a sarcolemma, or plasma membrane, surrounding a cell with multiple nuclei, organelles, channels (transverse tubules and sarcoplasmic reticulum) and myofibrils. Myofibrils, within muscle fibres generate muscle contractions by the sliding-filament mechanism.

Individual muscle fibres are surrounded by a basement membrane and a sheath of connective tissue called the endomysium. The endomysium and other connective tissues are mainly composed of collagen which transmits force from the muscle to the bone through tendons. Bundles of tens to hundreds

of muscle fibres (fasciculi or fascicles) are surrounded by a connective layer called perimysium. The fascicles are arranged into an entire muscle, which is covered in the epimysium.

Where a motor neuron axon meets a muscle fibre a neuromuscular junction (NMJ) forms. The NMJ is a synapse between the nerve and muscle, this allows the transmission of a nerve action potential to the muscle by the neurotransmitter acetylcholine. A muscle fibre is innervated by only one motor neuron, however a single motor neuron can innervate multiple muscle fibres. The group of muscle fibres stimulated by a single motor neuron is a motor unit.

Figure 1.5: Structure of a skeletal muscle. The muscle is surrounded by epimysium. With the muscle, fibre bundles, called fasciculi are surrounded by perimysium. Each fibre is surrounded by endomysium. The structure of particular muscles can vary from the generic structure shown. Reproduced from [33,34] permission received. REDACT IN ONLINE COPY.

1.5.3 Bioelectricity

Nerves and muscles are electrically active tissues. The importance of electricity in the control of movement has been known since 1781 when Galvani first experimented on the muscles of dissected frogs [35, 36]. In a series of experiments up to his death in 1798 Galvani showed that electrical stimulation from both lightning and a static generator elicited responses when applied to the sciatic nerve trunk of a frog, and that nerves were the conductors of this "animal electricity" [37, 38]. [2]

[2]Others credited with discovering the link between electricity and movement include: Dutch scientists in the South Americas; Benjamin Franklin; and Peter Abildgaard, a Danish veterinarian [39, 40]. There is evidence that electrical stimulation has been used medically since 2500BCE, when the Ancient Egyptians used Nile catfish to deliver 400V shocks for the relief of haemorrhoid

Figure 1.6: Structure of a skeletal muscle fibre. The muscle fibre is has a plasma membrane, or sarcolemma. Within the membrane are special organelles called myofibrils. Myofibrils are arranged in sarcomeres, a banded, longitudinal structure of actin and myosin between z-lines. Organelles including mitochondria and the sarcoplasmic reticulum support myofibril function by providing ATP and calcium ions respectively. Reproduced from [33, 34] permission received. REDACT IN ONLINE COPY.

Later, in the 19th Century, Emil Heinrich Du Bois-Reymond showed that nerve impulses are accompanied by a change in voltage, the action potential [44]. It is this action potential, or the summation of action potentials from a number of neurons, which can be measured by neural electrodes.

1.5.3.1 Nerve Electrophysiology

Neurons at rest actively maintain a negative membrane potential, with a positive charge externally and a negative charge internally (varying between –40 mV and –75 mV depending upon neuron type and behaviour). The resting potential is achieved by actively maintaining concentration gradients of Na^+, K^+, Ca^{2+} and Cl^- across the cell membrane. This resting potential is generated both actively and passively. Active potential generation is by ionic pumps, such as the Na^+-K^+ pump (Na^+, K^+-ATPase). In the presence of intracellular Na^+ the Na^+-K^+ pump hydrolyses ATP and extrudes $3Na^+$ in exchange for $2K^+$, generating a membrane potential. Additional ionic pumps: extrude Ca^{2+} and Cl^-; and regulate the intracellular pH.

Passive maintenance of the resting potential is by ionic diffusion along concentration gradients. As K^+ is concentrated within the cell it will tend to diffuse across the membrane. Diffusion of K^+ across the membrane creates a voltage difference, attracting K^+ to diffuse into the cell. At the equilibrium potential (E_{ion}) these two factors are balanced. Typical mammalian neuron equilibrium potentials are shown in table 1.1.

Ion	Equilibrium Potential (mV)
K^+	–102
Na^+	+56
Ca^{2+}	+125
Cl^-	-76

Table 1.1: Typical equilibrium potentials for mammalian neurons.

Action potentials are mediated by the opening of selective ion channels in the cell membrane. Opening these ion channels rapidly increases the membrane permeability to their specific ions. The action potential begins with ligand gated ion channels, which open upon neurotransmitter binding, allowing ions such as Na^+ and Ca^{2+} to diffuse into the cell, this depolarises the membrane. Depolarisation to the action potential threshold (typically –55 mV) opens voltage gated Na^+ channels, further depolarising the membrane, and opening more voltage gated Na^+ channels in a positive feedback loop. The membrane potential further depolarises reaching a positive potential (typically +40 mV, a change of about +100 mV). K^+ channels are activated during depolarisation which act to repolarise the cell, after which the channels deactivate (close) and the resting potential is generated by ion pumps. The action

pain [41,42]. A concise discussion of the scientific discovery of the nervous system is available from "In Our Time - The Nervous System" (BBC Radio 4, 10th February 2011) [43].

potential travels along the axon due to these local membrane depolarisations, lasting for approximately 1 ms [45–48].

1.5.3.2 Muscle Electrophysiology

Muscle fibres exhibit "action potentials" similarly to neurons. At the neuro-muscular junction the release of acetycholine neurotransmitter from the motor axon causes the activation of ligand gated ion channels permeable to Ca^{2+}. This in turn leads to the opening of calcium-induced Ca^{2+} channels in the sarcoplasmic reticulum throughout the muscle fibres in a positive feedback loop. Intracellular Ca^{2+} causes the activation of ATP-ase activity, changing the binding of myosin and actin in the myofibrils, and contracting the sarcomere in a process known as the sliding filament mechanism. In the muscle the action potential propagation occurs within one motor unit and can last between 2 ms and 5 ms [48, 49].

1.5.4 Extracellular Electrophysiology

The magnitude of the action potential can only truly be captured by intracellular recordings: by comparing the potential across the cell membrane [50]. Intracellular action potentials in myofibrils and neurons are approximately 100 mV. Intracellular recordings damage cells, and are unsuitable for recording across many neurons or a whole muscle.

To record from many cells extracellular recordings are used, this is known as electroneurography (ENG) and electromyography (EMG). Extracellularly the action potentials can be observed in the local changes in charge distribution. These charge distributions are the result of ion flow across the membrane during depolarisation and repolarisation varying extracellular ionic concentration. This creates an electric potential or voltage, which can be measured using electrodes. These voltages are typically small, in the range of: 1 mV for muscle potentials and <100 μV for neural potentials [51].

In addition to signal amplitude, frequency is a consideration for electrophysiology. The maximum frequency of an active cell is dependent upon the time taken for re-polarisation of the membrane, the kilohertz range is typical, with many action potentials every second. The signals from individual neurons or myofibrils can be recorded with small electrodes (<4000 μm^2) placed close to the cell of interest [52]. Typically even a very small electrode will record signals from multiple neurons or myofibrils [53]. In muscles large electrodes can be used to record the EMG signal across an entire muscle. When multiple myofibrils fire at once (in a muscle contraction) the separate extracellular action potentials sum forming a motor unit action potential (MUAP). Individual MUAPs can be identified from a complex signal by sorting based upon the MUAP amplitude and shape [54]. The recorded EMG can be used to determine whether a muscle is active, an estimate of contraction force, and the extent of muscle fatigue [55].

For nerves similar action potentials (spikes) form from the sum of multiple extracellular action potentials. Neurons, which fire separately or simultaneously, create recordable spikes that sum to form the recorded ENG signal. As with MUAPs spikes can be identified by sorting, allowing small, functionally

similar, groups of neurons to be identified [54]. By mapping the ENG activity to particular actions or stimuli, spikes responsible for particular motor or sensory signals can be determined.

1.5.4.1 Signal-to-Noise Ratios in Electrophysiology

To record small signals, in the μV scale of ENG, the signal must be distinguishable above the noise level. The signal-to-noise ratio (SNR), the ratio of the signal amplitude to the noise amplitude, describes the signal quality [56]. In order to distinguish the signals, the SNR should be at least 5:1 [52, 57].

Noise is defined as the components of the recording which are not part of the signal of interest. This can include: biological noise from adjacent electrically active tissues; electrical noise from outside sources (e.g. 50 Hz power lines); movement artefacts; and thermal noise [52, 56, 58].

Thermal noise (Johnson-Nyquist noise) can be reduced by keeping electrode impedance low. Impedance is a measure of resistance to alternating current flow. The relationship between thermal noise (root mean squared voltage, v_n) and impedance is described by eq. (1.1), a function of temperature (T, Kelvin), impedance (Z, Ohms) and bandwidth (Δf, Hz), where k_B is Boltzmann's Constant (joules per Kelvin). For a typical electrode impedance of 1 MΩ at body temperature with a recording bandwidth of 10kHz the thermal noise is around 13.1 μV rms, or 40 μV peak-peak. This is in the order of a typical recorded AP (action potential) [59].

EMG electrodes are larger, with lower impedances ($<$10 kΩ) and the bandwidth of interest is smaller ($\sim$1kHz). Coupled with a greater signal amplitude (1 mV) this means that thermal noise is less likely to cause problems when recording muscle signals.

$$v_n = \sqrt{4k_B T Z \Delta f} \tag{1.1}$$

The electrode/tissue interface plays a key role in the SNR. The signal amplitude is dependent upon the electrode/source distance, which is determined by the electrode/tissue interface. To minimise this distance a neural interface design that supports intimate electrode/tissue contact over long implantation periods (years to decades) should be chosen [26, 53, 60–62]. Alternatively, or additionally, interface designs can aim to 'bring the nerves to the electrode' [26]. Neural biocompatibility will determine whether an interfaces supports intimate electrode/tissue contact. 'Surface [neural] biocompatibility' is discussed below, and is a major theme of this thesis [63].

Signal amplitude decreases rapidly with distance from the axon membrane and from the Nodes of Ranvier (voltage is approximately inversely proportional to distance from the current source, see eq. (1.2)[3]). Nodes of Ranvier are small, 1μm long, unmyleinated sections 100's of micrometers apart. Small, penetrating electrodes are unlikely to be positioned in proximity to the nodes of most adjacent axons. FitzGerald *et. al.* showed that increasing the length of nerve from which signals are collected

[3]The potential (voltage, ϕ) at distance (r) from a point source in a homogenous volume conductor Where: I_0 is the total applied current at source; and σ is the conductivity of the volume conductor [63].

will increase the signal amplitude irrespective of Node position and reduce problems such as cross-talk and electrode — nerve distance [59].

$$\phi = \frac{I_0}{4\pi\sigma r} \tag{1.2}$$

1.5.5 Peripheral Nerve Injury and Regeneration

The implantation of any nerve electrode will cause a degree of nerve injury. Sunderland defined five degrees of nerve injury, from least to most severe these are listed in fig. 1.7 [64, 65]. Routine electrode procedures, such as nerve conduction studies, may cause nerve damage, although to 2003 no reported cases are known [66]. Temorary parethesia, a tingling sensation, is occasionally encountered during or following needle electrode procedures, indicating low severity nerve injury [personal correspondence]. Other needle procedures have been reported to cause severe nerve injuries of type 3 and above, causing functional impairment [67, 68]. Implantation of microchannel neural interfaces (MNIs) requires complete nerve transection, a type 5 nerve injury. To acquire signals using a MNI, regeneration must take place. MNI design is discussed further below.

First Degree Injury A temporary block to conduction in the axon.

Second Degree Injury Axonal damage, causing degeneration below the lesion to axon(s) only. Endoneurial tube remains intact.

Third Degree Injury Endoneurial damage, where the fascicles remain in continuity. Structures within the fascicles become damaged.

Fourth Degree Injury Fascicular damage, where only the outer epineurium remains in continuity. All the structures within the nerve trunk are damaged.

Fifth Degree Injury Part or full transection of the nerve, where no structures are left in continuity and surgical repair is required.

Figure 1.7: The five degrees of nerve injury described by Sunderland. From least severe (First Degree) to most severe (Fifth Degree) [64, 65]. Sixth Degree, or mixed nerve injury, has also been described.

The processes following nerve injury were first described in 1850 by Waller [69]. Wallerian degeneration is the breakdown of axons following a transecting peripheral nerve injury. Distal to the injury site axons degenerate completely, although the distal axons remain intact and electrically active for several days following injury [70]. Proximal axons also sometimes degenerate, as far as the closest proximal Node of Ranvier. Proximal neurons can exhibit cell body atrophy, and, in severe cases, complete neurite degeneration [71].

Following injury Schwann cells down-regulate myelin synthesis, proliferate, and, along with macrophages, phagocytose the myelin sheath [71]. 3 to 4 weeks following injury most of the myelin has been removed, leaving nerve stump endoneurial tubes filled with Schwann cells [70, 72]. If a gap is present in the severed nerve Schwann cells proliferate and form bands of Bunger (cords of nucleated cells) to

bridge the gap [71]. Where a microchannel interface or a nerve guidance conduit is interposed in the nerve gap, bands of Bunger can be expected to form within the lumen(s) of the device. The lumen is the opening along the guidance conduit through which the nerve can regenerate.

Neural regeneration begins with axons sprouting from the intact proximal nerve, 1 to 3 days after the nerve injury [71]. In the absence of structural cues from a distal nerve sheath or an end organ (common in amputation) a neuroma forms, and may persist. Neuromas are deposits of connective scar tissue around the regenerating axon sprouts [73]. Successful regeneration occurs if axon sprouts enter the proximal end of the distal nerve section. Axon regeneration is then guided by Schwann cells and endoneurial sheaths, regenerating at approximately 1 mm/day in humans [74]. Following reinnervation of an end organ Schwann cells begin the process of myelination, forming nodes of Ranvier; however, full functionality does not return immediately following myelination [71]. Nerve structure matures over time following reinnervation. 'Mini-fascicles' can form in advance of consolidation into classical nerve fascicle structure [22]. Changes in axon organisation, cross sectional area, and fascicular arrangement, following regeneration cause the pattern of innervation to be altered.

If the nerve is not severed, for example in crush injuries, regenerating axons demonstrate substrate mediated responses, where Wallarian degeneration occurs but the myelin sheath remains in continuity (2° Sunderland Injury, [65]). In this case regeneration is directed within the original endoneurial tube and the pattern of innervation is similar to before injury [64].

4° and 5° injury typically require surgical intervention [64]. Nerve repair by end-to-end coaptation is limited to cases where the nerve gap is smaller than 5 mm [75,76]. For repair of gaps longer than 5 mm (the scale of a MNI) the current clinical gold standard is autograft [71,76,77]. Nerve guidance conduits aim to replace autograft in clinical practice; however, functional recovery is often poor compared with the gold standard [78].

1.6 Recording Interface Designs

This thesis aims to improve upon implanted devices for prosthetic control. Interfaces designed for EMG and ENG recording will be considered separately, because, although there is some cross-over in designs, the approaches are usually different.

Interfaces can be grouped by their level of invasiveness [55,79] (see fig. 1.8). Increasingly invasive designs are typically more selective, able to record from a smaller volume of tissue, and therefore from fewer nerve or muscle fibres. However, more invasive surgical procedures are more likely to cause severe tissue reactions [80]. Designs will be considered from the least to most invasive (see table 1.2).

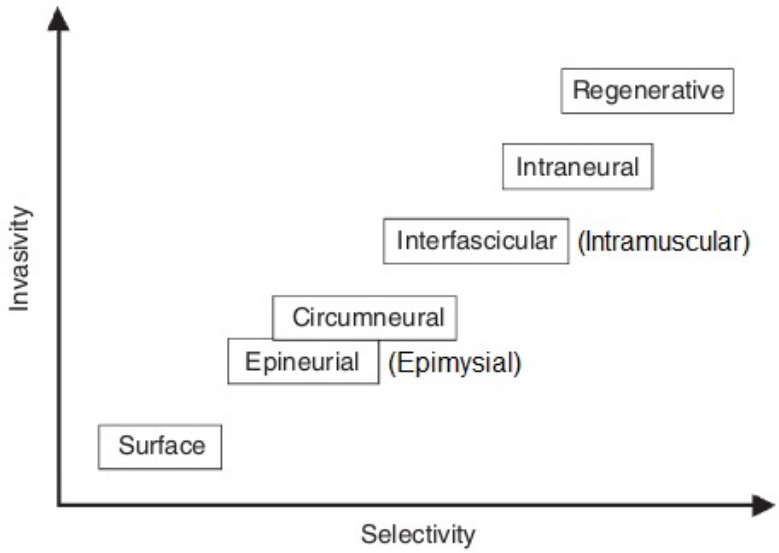

Figure 1.8: A comparison of different peripheral nerve electrode (and muscle electrode) designs. In practice these factors are also influenced by patient anatomy, implantation method and the foreign body response. Adapted from [55], with kind permission from John Wiley and Sons. ©2005 Peripheral Nerve Society.

1.6.1 Muscle Interfaces

1.6.1.1 Surface Myoelectrodes

The majority of EMG recording is not accomplished with implantable electrodes, but with electrodes placed on the skin surface or with acute invasive needle procedures.

Surface electrodes are typically large, with conductive gel pads for acute recordings or metal pads for long-term surface electromyography (sEMG) [58]. These record global data from the tissues underlying the electrode. Surface electrodes are limited by a number of reliability issues: difficulty placing the electrodes in repeatable locations; electrode lift-off; impedance variations due to atmospheric moisture and perspiration; changes in muscle location relative to the skin; crosstalk from deep or adjacent muscles [15, 81]. Recording from deep residual muscles using sEMG is a particular challenge, low pass filtering by connective tissue and signals from superficial muscles can mask the signal [15, 82].

Crosstalk is a key consideration for sEMG. When several muscles are active at the same time, electrodes, which record from a large area will observe interference from local muscles. When using one muscle to control one action this reduces the number of independent control channels available [13]. To avoid this problem alternative control strategies such as pattern recognition and regression analysis have been used. Alternatively selectivity could be increased by directly placing the recording site closer to the muscle: within the body [83].

1.6.1.2 Needle Myoelectrodes

Needle myoelectrodes, or fine wire electrodes, are used for short term clinical tests of muscle and nervous function. Although they have been used in laboratory conditions to test control strategies and experimental hypotheses [15, 84], they are not suitable for long-term use by patients [79].

1.6.1.3 Implantable Myoelectrodes

Placement of the electrodes directly on or in the muscles of interest is one solution for the problems associated with skin surface electrodes. This allows individual muscles (both superficial and deep) responsible for specific actions to be targeted, increasing selectivity and reducing cross-talk [4, 81, 84].

Electrodes implanted on muscles are epimysial electrodes, while electrodes implanted within muscles are intramuscular electrodes (see fig. 1.8). Epimysial electrodes are mounted in a backing, which is sutured onto the epimysium. Following implantation a fibrous capsule forms around these electrodes, holding them in place [85].

Epimysial electrodes have been used for functional electrical stimulation (FES) for over 20 years [86–88]. FES uses electrical currents to activate the motor nerves of otherwise paralysed muscles in patients following spinal cord injury, stroke, and other conditions. These interfaces often use large single (monopolar) electrodes, these can be used for recording, however small bipolar or tripolar designs are more common [89]. The electrodes are mounted in a backing which is sutured onto the epimysium. Following implantation a fibrous capsule forms around these electrodes, holding them in place [85].

Intramuscular electrodes can be used percutaneously, as needle electrodes, or implanted permanently. Helically wound wire with an uninsulated tip is commonly used, inserted into the belly of the muscle, with a barbed anchor to hold the electrode in place. However, this design can damage muscle fibres. Intramuscular electrodes have been used for functional electrical stimulation (FES), although in fewer cases than epimysial electrodes [86].

Wireless intramuscular electrodes have been developed. The Implantable Myoelectric Sensor (IMES) enables signal capture from up to 32 bipolar electrode implants, although first in human trials have used only four implants [81, 90–92]. Other wireless systems have been designed, with connections for up to four bipolar electrodes [93, 94].

Alternative myoelectrode designs have been developed. These aim to provide more recording sites, for increased selectivity or recording over a larger area. [83, 95, 96]. Intramuscular wires with multiple sites along the interface have been used in acute experiments and multi-electrode epimysial sheets have been used for months in animal models.

Fibrosis surrounding implanted myoelectrodes may be advantageous. A fibrous capsule will hold the electrode in place, maintain a constant environment, and counter-intuitively increase signal strength [81, 97]. Signal strength is partially dependent upon tissue resistivity according to Ohm's law: restricting

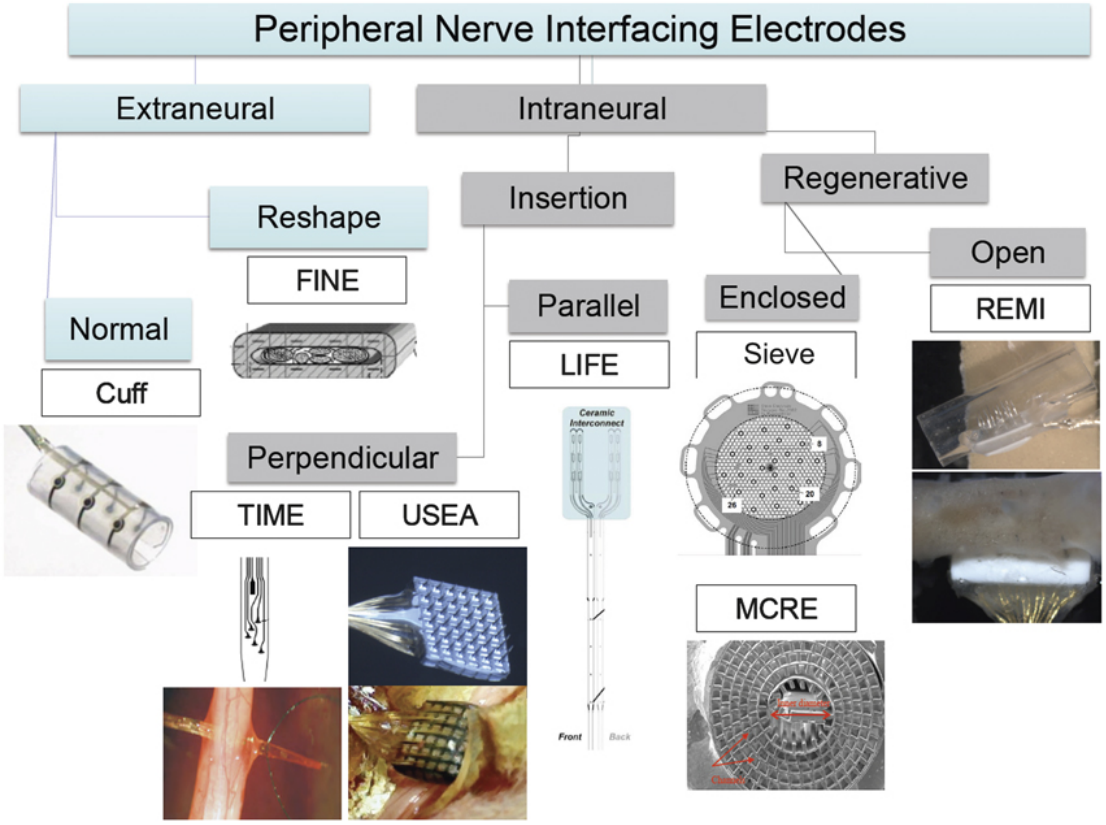

Figure 1.9: A comparison of different peripheral nerve interface designs. Extraneural (epineural) electrodes are cuffs or flat interface nerve electrodes (FINE) [104]. Intraneural electrodes can penetrate the nerve Utah slant electrode array (USEA) [105, 106], longitudinal intra-fascicular electrodes (LIFEs) [107, 108], and transverse intra-fascicular multichannel electrodes (TIMEs) [109, 110]. Regenerative electrodes can have electrodes enclosed in holes (sieve) [111, 112], microchannels (microchannel roll electrode, MCRE) [51, 113], or open on a flat surface (regenerative multielectrode interface, REMI) [114, 115]. Reproduced from [103], with kind permission from Cambridge University Press.

current flow, at the interface of the low resistivity muscle and the high resistivity fibrous capsule [98, 99], proportionally increases potential difference.

1.6.2 Nerve Interfaces

Interfacing directly with the peripheral nervous system could enable upper limb amputees to control multichannel prosthetic limbs intuitively [100]. However, developing neural interfaces for chronic implantation remains a challenge [101]. Microchannel peripheral nerve interfaces, which are a focus of this thesis, overcome some of the difficulties encountered with extracellular neural recordings from peripheral nerves [59].

Neural interfaces have been widely reviewed in the literature [4, 26, 52, 53, 55, 58, 79, 83, 102, 103], and the main designs and their advantages and limitations will be discussed (see fig. 1.9, table 1.2). Implantation within or onto a nerve is a delicate, invasive process, which can damage nerves. Regeneration of the nerve and the biocompatibility of the neural interface is critical for stable chronic applications [80]. The trade-off between invasivity and selectivity is a major challenge in neural recordings (see fig. 1.8).

1.6.2.1 Epineural Interfaces

Epineural interfaces follow the same design principles as epimysial electrodes. An insulating backing holds two or more electrodes, which is then sutured onto the epineurium [55]. Damage to the nerve trunk is avoided, however the selectivity is low, because signals from the entire nerve are recorded. Epineural electrodes have been used for functional electrical stimulation, enabling selectivity over muscle activation not achieved using surface electrodes [87].

1.6.2.2 Cuff Neural Interfaces

Cuff interfaces are commonly used for implanted functional electrical stimulation [88], however the same design can monitor neural activity within the whole nerve. Cuffs encircle the nerve with an insulating backing containing electrodes designed as complete rings or single points. Both cuff and epineurial designs are less invasive, and less selective than intrafasciular designs [55], and are easily replaced in the event of failure [79]. By insulating the nerve from its surroundings, cuff electrodes can shield the electrodes from local EMG signals [26]. To increase the selectivity of cuff designs flat interface nerve electrodes (FINEs) have been developed which flatten nerves, increasing separation between fascicles. FINEs have been shown to damage nerves flattened to high degree [104, 116]; however, FINEs are now in use in patient trials [117].

1.6.2.3 Interfascicular Interfaces

Interface designs which introduce electrodes between fascicles are interfascicular interfaces. The slowly penetrating interfascicular nerve electrode (SPINE) separates fascicles using blunt silicone tabs with exposed electrodes [118]. Over 24 hours the tabs rearrange fascicles allowing greater functional selectivity than epineural designs, however longer term testing is required to test their stability [55, 118].

1.6.2.4 Intrafascicular Interfaces

Intrafascicular interfaces are inserted within the peripheral nerve. The simplest intrafascicular electrode is a microwire, such as the stainless steel wires used by Strumwasser for cortical recording in the 1950's [102, 119]. Gold, platinum alloys, tungsten and other metals are also used to form $<$100 μm diameter wires which penetrate the nerve [42, 57]. By stacking microwires, in 2D and 3D, arrays of exposed tips can be formed to record from throughout a nerve [120–122].

Modern microwire designs such as the multi-electrode longitudinally implanted intra-fascicular electrodes (LIFEs) have improved the selectivity and stability recordings [107, 108]. LIFEs are not metal wires, but are polymeric thin films with patterned metal electrodes and tracks [108], they can be arrayed to access many fascicles within a single nerve [123]. LIFEs and their further development transverse intra-fascicular multichannel electrodes (TIMEs) have achieved multi-electrode capacity with diameters of $<$100 μm and insertable lengths of up to 5 mm [109, 110]. Recently TIME implants have been used to control a prosthesis and provide sensory feedback in real-time over 30 days for an upper-limb amputee

[124], *in vivo* experiments indicate that longer implantation will be possible in the near future (ethical approval permitting) [125]. Thin-film processes have been used to create soft, compliant microelectrode arrays which are promising for *in vivo* spinal cord stimulation and recording [126]. Microwires formed from carbon fibres <10 μm diameter have been promising for cortical applications, and may be suitable for peripheral nerve recordings in future [127, 128].

1.6.2.5 Microelectrode Arrays

Arrays of electrodes known as "Microelectrode Arrays" (MEAs) are a common approach to selective interfaces with the central and peripheral nervous systems. They are typically designed to penetrate the neural tissue, acting as intrafascicular interfaces.

The 'Utah Array', an array of 100 silicon needle electrodes, is the "workhorse for [most] cortical interfaces" [129], and has been applied to the PNS [102, 105]. The electrodes often have platinum coated tips and are isolated from neighbouring spikes with a silicon nitride coating. Design variations include slanted arrays for the measurement and stimulation of fibres at different depths within a nerve, and high density arrays for interfacing with small structures [130]. This MEA has been successfully tested in the PNS of a human subject (Dr. K. Warwick). However, 80% of the electrodes failed over 96 days, due to fatigue of percutaneous wires, and signal quality had declined [131, 132]. Cortically, the Utah Array has been used to provide control over prosthetic hands for tetraplegic patients, with usable control signal after 1000 days implantation [133, 134]. The Utah Array has been used chronically for 1 year in cat and 2 months in rat peripheral nerves [135–137]. The interface causes persistent inflammation and fibrosis, with some nerve regeneration and reduced fibre diameter observed. In both these cases axons were present within the expected recording volumes. The Utah array has been commercially marketed by Braingate™Co. as the Bionic Array [62, 138]. Prior to the start of the research described in this thesis Utah array designs were considered for investigation, however they are currently prohibitively expensive for research [personal communication].

Other MEA designs include the "Michigan Electrode", after designs by Wise et. al. in the 1970's, which is a thin-film MEA with penetrating silicon needles. The design allows a high density of electrode sites with minimal tissue displacement by patterning several electrodes onto each shank of an electrode [42, 102, 139]. This design enables a true 3-dimensional array of electrodes to be introduced into the tissue.

The profusion of MEA designs presents researchers and clinicians a problem when trying to choose an implant. A comparison of 5 MEAs, including the Utah and Michigan interfaces, has shown that design does affect the implant suitability [140]. Following cortical implantation in rats immune response was observed surrounding all the tested designs, and impedance and mean SNR were highly variable, both within and between electrode designs. Although MEA design does impact upon implantation response,

the authors suggested that implant application should be the most significant factor in interface choice [140].

1.6.2.6 Regenerative Interfaces

Regenerative interfaces, or sieves, are the most invasive group of peripheral nerve interfaces. Their design requires complete nerve transection (type 5 nerve injury) and regeneration of axons though holes or slits in the interfaces. Electrodes are sited at the holes are used to record from the axon or axons which have regenerated [53].

For regenerative interfaces to work axons must regenerate through the holes in the device and remain functional for the lifetime of the patient [55]. The theoretical selectivity limit for regenerative interfaces is to have one axon per hole. This would require holes of 2 μm to 10 μm diameter, which has not been feasible in practice. Axons do not regenerate through small diameter holes, or become damaged by any small movement of the implant [55, 141]. Early interfaces were manufactured using stiff silicon or ceramic substrates, however soft polyimide sieve designs have been used more recently, demonstrating improvements in regeneration in the short term with a functional decline during chronic implantation [55, 111, 112].

Regenerative interfaces have been introduced into nerve guidance channels. The "regenerative scaffold electrode" is a flat epoxy sheet with longitudinal electrodes inserted within the lumen of a guidance channel, which is then sutured within a transected nerve [114, 142]. Axons regenerate well in the open channel structures, however the flat interface limits the selectivity of this design.

To date regenerative interfaces have not been tested in human subjects. Limits on implantation time for first-in-human trials mean that there is often insufficient time for axons to regenerate and recover from the nerve transection at surgery. A key issue for the use of regenerative electrodes with long-term amputees is whether the nerve will regenerate following transection. Delayed nerve repair causes a dramatic reduction in the number of axons which regenerate (up to 67% in animal models) [143]. This applies in the case of amputees, where the nerves have been left without an end organ since the amputation.

Flat sieve designs are typically only 10 μm thick, therefore it is unlikely that nodes of Ranvier will be close to an electrode. Neural signal strength is greatest closest to the nodes of Ranvier [63]; however, the nodes can be 100's of μm apart, and are approximately 1 μm in length, therefore the likelihood of positioning a small recording electrode in proximity to a node is low. This limits the selectivity of basic regenerative interfaces.

1.6.2.7 Microchannel Neural Interfaces

The neural interface type considered in this work are the microchannel neural interfaces, a subset of regenerative electrodes. Microchannel neural interface manufacture is discussed in detail in chapter 5

and *in vivo* testing is discussed in chapter 6. This thesis will mainly consider the previous work by a collaboration between the University of Cambridge, University of Birmingham and EPFL, Switzerland, although alternative, similar designs have been proposed.

Microchannel interfaces are designed to overcome key issues with many neural electrode designs, signal strength and the role of nodes of Ranvier. The microchannel encloses a group of regenerated axons within a long insulating tube approximately 100 μm diameter and up to 5 mm in length [51, 59, 113]. Confining the nerve and electrodes within a small diameter electrically insulating channel increases the length of axon from which signals can be recorded. In addition, microchannels increase signal amplitude and reduce cross-talk, a phenomenon first described in the 1960's, which has since been demonstrated both *in vitro* and *in vivo* [59, 144]. Microchannel interfaces can record meaningful signals even if the electrode (metal) surface is not immediately proximal to a node of Ranvier, because the signal is confined within the insulating tube. The most impressive results to date have recorded *in vitro* signals as large as 4.5 mV from cortical neural tissue using 10 μm diameter, 400 μm long, channels. This is a gain over recordings in open culture of approximately 20 times and an SNR up to 450 [145].

A range of microchannel interface designs have been developed. Removable formers have been used to create circular cross-section microchannels in silicone [113, 146–148]. Thin-film processes have been used to create ridged structures with metal electrodes at the base of U-shaped troughs, by rolling the structures or capping the trough with a second thin film enclosed microchannels can be formed [146, 149–154]. Other microchannel devices also propose to use thin-film manufacturing techniques: the Georgia Tech Regenerative Electrode (GT-RE) [114, 115, 155, 156]; and the regenerative microchannel based electrode interface (ReME) [157, 158].

The greatest signal gain is achieved by using long, narrow microchannels [146]. However, nerve regeneration through microchannels is impeded, with myelinated axon regeneration greatest in shorter, larger microchannels [113]. *In vivo* small diameter channels of 50 μm become blocked with fibrous, connective tissue [51, 113]. In addition, the trauma of implantation and resulting foreign body reaction cause fibrosis, which can either completely occlude microchannels, or reduce the space for axonal regeneration [51, 113]. Microchannel neural interfaces should be designed such that neural regeneration is encouraged and fibrosis is discouraged.

Table 1.2: An overview of muscle and nerve interfaces suitable for use in upper-limb prosthetic control. References to key examples are cited in the table, additional detail is provided in the main text of this thesis and the following reviews [4, 26, 52, 53, 55, 58, 79, 83, 102, 103].

Interface	Design	Advantages	Disadvantages
Muscle Interfaces			

Interface	Design	Advantages	Disadvantages
Surface Myoelectrodes	Large pads placed on the skin surface	Simple to use, non-invasive	Non-intuitive, low number of control channels, variable signals
Needle Myoelectrodes	Stiff needles or microwires which are implanted transcutaneously	High selectivity at motor unit level	Only suitable for acute laboratory experiments
Epimysial Electrodes	Insulating backing placed on epimysium with one of more point electrodes	Increased number of control channels compared with surface myoelectrodes, reduced cross-talk	Non-intuitive, invasive
Intramuscular Electrodes	Helically wound wire with an exposed tip implanted into the muscle belly	High selectivity over individual muscles, reduced cross-talk	Cause muscle damage, can migrate following fibrosis and muscle movement
IMES [81, 91, 92]	Hermetically sealed capsule(s) with bipolar electrodes	Increased number of control channels compared with surface myoelectrodes, reduced cross-talk	Cause muscle damage, limited by wireless link
Epimysial Arrays [95, 96]	Non-targeted array of electrodes placed on the epimysium of one or more muscles	Detailed information suitable for pattern recognition	Large implants required
Nerve Interfaces			
Epineural Interface	Insulating backing placed on epineurium with one of more point electrodes	Minimise nerve damage, easily removed if damaged	Low selectivity
Cuff Interface	Insulating backing surrounds nerve with circumferential or point electrodes	Minimise nerve damage, easily removed if damaged, shield nerve from local EMG	Low selectivity, can cause nerve damage if compression or micro-movement occur
Flat Interface Nerve Electrode (FINE) [104]	Cuffs designed to flatten nerves and separate fascicles	Increased selectivity over cuff interfaces	Cause nerve damage if the compression is too great

Interface	Design	Advantages	Disadvantages
Microwires	Fine metal wires with exposed recording tip	Easily manufactured, high selectivity in acute experiments	Commonly used percutaneously, not designed for chronic implantation
Longitudinally Implanted Intra-Fascicular Electrodes (LIFEs) [107, 108]	Microwires or thin-films with multiple electrodes implanted parallel along a single nerve or fascicle	Fascicle and subfascicle selectivity, high flexibility reduces nerve damage	Implanted within fascicles causing moderate, fibre level, nerve damage, requires multiple implants to interface with a large volume within a single nerve
Transverse Intra-Fascicular Multichannel Electrodes (TIMEs) [109, 110]	Microwires or thin-films with multiple electrodes implanted across a nerve through multiple fascicles	Fascicle and subfascicle selectivity, high flexibility reduces nerve damage	Implanted within fascicles causing moderate, fibre level, nerve damage
Utah Slant Electrode Array (USEA) [105, 106]	Array of silicon spikes with electrodes at the tips	High density electrode sites in 3 dimensions, high selectivity	Stiff silicon causes persistent tissue response
Sieve (regenerative) Interface [111, 112]	An array of holes through a planar substrate with electrode sited at the holes	High selectivity	Require complete nerve transection, regeneration through small holes is poor, micromotion can cause nerve damage in chronic implantation
Regenerative Multielectrode Interface (ReMI) [114, 115]	Flat sheet of electrodes mounted in a nerve guidance channel	Create intimate contact between nerves and the interface surface	Require complete nerve transection, limited selectivity over a small subset of neurons
Microchannel Neural Interface (MNI) [51, 113, 148]	An array of insulating tubes containing point electrodes for nerve regeneration	Increased signal amplitude, signals recorded irrespective of Node of Ranvier position, shield nerve from local EMG, high selectivity	Require complete nerve transection or nerve root surgery, regeneration through long and small microchannels is poor

1.6.3 Other Considerations for Electrophysiology

1.6.3.1 Amplification of EMG and ENG signals

ENG and EMG signals must be amplified prior to data analysis, recording or decoding. This is usually achieved using differential amplification, which amplifies the difference between two inputs (typically two electrodes placed along the length of the muscle or nerve) while rejecting signals common to the two inputs [56]. The common signal includes noise from distant muscles (increasing selectivity) and 50 Hz power lines, this quality is described as “common mode rejection”.

Amplification can reduce the role of thermal noise. Cables have inherent impedance, increasing approximately proportionally with length. Amplifying the signal close to the electrodes reduces the role of cable impedance before amplification. This pre-amplification will lift the signal over the thermal noise level for the remaining cable length.

Increased EMG and ENG selectivity can be achieved by using different recording electrode arrangements. Monopolar electrodes record differences with respect to a remote reference electrode, gathering information around the electrode with signals inversely proportional to distance from the electrode. Bipolar electrodes, ’single differentials‘, also record from a volume of tissue around the electrodes. The ’double-differential‘ electrode design, or the mathematically equivalent branched electrode (a.k.a. quasi-tripole), reduces crosstalk and the tissue volume within which signals are recorded (see fig. 1.10, pg. 49) [159–162]. Further modifications, such as the revised quasi-tripole configuration, can improve the signal quality yet further [163]. Quasi-tripolar electrode arrangements have been chosen for MNIs in order to reduce noise and to allow directional stimulation for feedback applications [51, 59, 113].

1.6.3.2 Active Implantable Interfaces

In order to amplify signals close to implanted interfaces, pre-amplification can be included within the interface. This is a common approach for implantable myoelectrodes, for examples the IMES [81, 90–92]. Amplifier systems have been designed to connect to with cortical interfaces such as the Utah Array [164] and to include wireless systems for data and power transfer [165–167].

A key consideration for implanting electronics is preventing short-circuits forming between otherwise separate conductive tracks, and preventing corrosion of conductive track. A major issue therefore is water ingress. To prevent water or moisture getting to electronics over long-term implantation a hermetic, sealed, package should be used [165, 168, 169]. Implantable active electronics are not considered in this thesis, however these concepts could be applied to the devices discussed in this thesis.

1.6.3.3 Spike Sorting and Information Decoding

Once recorded, neural signals must be sorted to identify spikes from different neurons and the information contained must be decoded. This will enable the control signals for a prosthesis to be determined

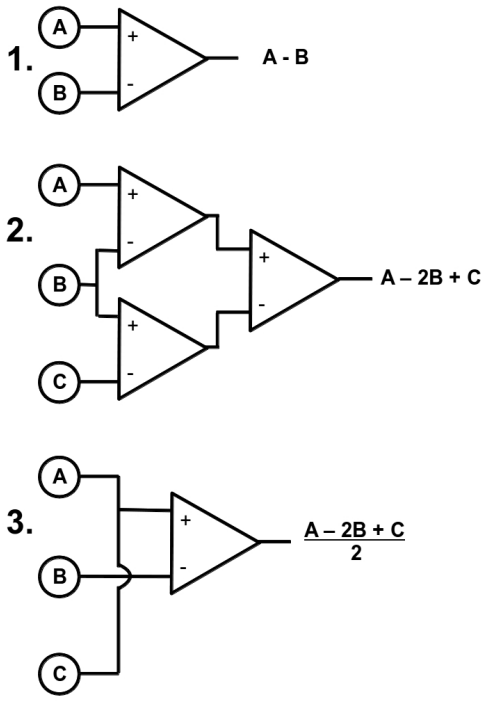

Figure 1.10: Electrode set-ups to obtain: 1. Single Differential, ($\mathrm{Output} = \mathrm{A} - \mathrm{B}$); 2. Double-Differential or True-Tripole, ($\mathrm{Output} = (\mathrm{A} - \mathrm{B}) - (\mathrm{B} - \mathrm{C}) = \mathrm{A} - 2\mathrm{B} + \mathrm{C}$); 3. Branched Electrode or Quasi-Tripole, ($\mathrm{Output} = \frac{\mathrm{A}+\mathrm{C}}{2} - \mathrm{B} = \frac{\mathrm{A}-2\mathrm{B}+\mathrm{C}}{2}$). Adapted from [159, 160].

from the noisy neural signal. This is not a focus of this thesis but, the following references are suggested for more information [54, 170, 171].

A key disadvantage with current processes is the selectivity of spike sorting algorithms, which cannot differentiate between more than 8 to 10 spike types within the same spike train [172]. This further reinforces the need to spatially isolate neurons within microchannels, therefore reducing the number of spikes observed per electrode. However, improving electrode minaturisation and recording spike trains with more than one electrode may allow increased differentiation as spatial and temporal components of the signal could be considered.

1.7 The Host Response to Implanted Devices

1.7.1 Biocompatibility

This thesis aims to develop interfaces for nerve and muscle, which can be implanted chronically. Therefore the interfaces must be biocompatible [79]. Biocompatibility is:

> "the ability of [a] device to perform its intended function, with the desired degree of incorporation in the host, without eliciting any undesirable local or systemic effects in that host." [173]

"The lack of understanding of the biological response to implanted constructs and the inability to monitor the sites and match the mechanical properties of the probe to the neural tissue properties continue to be an unsolved problem."

Figure 1.11: A key issue in neurocompatibility identified by Durand *et. al.* following the International Neuromodulation Society's 11th World Congress and the 6th International Neural Engineering Conference [129].

Dependent upon function, a biocompatible device may be: inert, bioactive or bioresorbable. For the chosen application, implantable recording devices for long-term use, the bulk of the device must be protected, therefore an inert encapsulating layer is required. Improving the interface with soft tissue, however, requires a bioactive or bioresorbable layer.

1.7.2 Myocompatibility

The biocompatibility of implantable muscle electrodes is rarely considered beyond the need for an inert encapsulant. Myocompatibility, the extent to which a device is biocompatible with muscle, must be considered for long-term implants.

Fibrosis around myoelectrodes is currently considered positive, preventing movement of the implant away from the muscle [81, 97]. However, a persistent foreign body reaction may cause complications. Tissue engineering presents possible solutions, where the encapsulant could be designed to form a scaffold for muscle tissue growth, improving integration and reducing fibrosis [174, 175]. Myoelectrodes must withstand the forces exerted by the muscle they are placed within or on. To date research has primarily used designs with long working histories in clinical use. That these devices are approved for long-term implantation and their function is good means there is less imperative to develop advanced biocompatible approaches when compared with neural interfaces.

1.7.3 Neurocompatibility

Neurocompatibility is the extent to which a device is biocompatible with the nervous system. Neural tissue is soft and easily damaged during implantation surgery or subsequently during the interface lifetime. In peripheral nerves the fibrotic or glial scar responses can increase the distance between an interface and the target axons. Over a few months *in vivo* the biological response to most neural interfaces causes signals to fade and disappear [98, 129]. Understanding and overcoming this limitation of neural interfaces is a key issue, see fig. 1.11.

To improve the regeneration through MNIs the channel surfaces or bulk properties can be modified. Current implant materials, silicone and polyimide, are suited for implantation as inert materials; however, channels can become blocked with fibrous tissue [51, 113]. Increasing the neurocompatibility of MNIs will reduce fibrosis which currently limits minimum channel diameter, and may improve neural regeneration, allowing smaller channels to be used, increasing selectivity.

A range of strategies have been used to improve neurocompatibility and neural regeneration within Nerve guidance conduits [71, 76, 78, 103, 176–180]. The main materials modifications explored in the literature will be discussed below.

1.7.3.1 Bulk Neurocompatibility

It has been hypothesised, and demonstrated, that a mismatch between the mechanical properties of the interface and the nerve can easily damage soft nerve tissues, and that better mechanical matching between the soft neural tissue and the interface will reduce the foreign body response [4, 83, 98, 126, 181–183]. Mechanical properties also alter response on a cellular scale *in vitro*, encouraging neurite outgrowth at optimal substrate stiffnesses [184–186]. Therefore the bulk properties of the materials chosen must be considered. This study primarily considers silicone (polydimethylsiloxane, PDMS [4]) interfaces. Silicones can be made with a range of properties, but are typically compliant and elastic, but with poor resistance to tear. Soft, medical grade silicones have been used since the 1940's as medical materials for cosmetic implants, the encapsulation of implantable electronics, and as a substrate for neural interfaces [187–189]. Medical grade silicones are known for their biocompatibility and biodurability, remaining stable for over 30 years implantation [189]. However, increasing flexibility of LIFE interfaces has not statistically reduced glial scarring [83]. Therefore additional factors must be considered in order to improve neurocompatibility. Chapter 5 of this thesis discusses the problem of mechanical mismatch and the properties of materials used for neural interfaces.

1.7.3.2 Surface Topography

Cells respond to substrate shape, the topography of the surface. A typical example of this effect is 'contact guidance', where a cell elongates or grows in a preferential direction in response to surface structure [190, 191]. Neuronal cell types exhibit impressive contact guidance on the right surface, with axons, dendrites or neurites growing in alignment with a grooved structure [192–196]. Other surface cues, such as roughness and porosity have shown promise for improving neurite outgrowth and cell adhesion. Several studies have shown that neurite outgrowth can be increased on nanoscale structures [197–199]. Chapter 4 in this thesis investigates the effect of surfaces topographies on neurite outgrowth *in vitro* and the effect of surface topography on neurites will be discussed further in the introduction to this chapter.

1.7.3.3 Chemical Modification

Improvements in neurocompatibility can also be achieved by modifying the interface surface chemistry. This may require directly modifying the surface layer of the bulk material or by adsorbing a layer with different chemical properties. Ion implantation, using hydroxyl-ions and metal ions, has been used to improve neurocompatibility [200, 201]. Creating positively charged materials may improve neurite

[4] Not all silicones are polydimethylsiloxanes. The silicone used in this study, Sylgard 184, is a PDMS elastomer.

outgrowth [180], and –COO^- groups have been proposed (although not used successfully) [202].

1.7.3.4 Conductive Coatings

The conductive polymers poly(pyrrole) (PPy) and poly(3,4 ethylenedioxythiophene) (PEDOT) are commonly used in research as electrode coatings or [42, 98]. These polymers create a compliant surface layer with improved mechanical matching compared with a bare metal electrode. Conductive polymers also lower electrode impedance and increase the area for cell attachment, creating a roughened profile. Conductive polymers can themselves be chemically modified. Peptide sequences have been bonded to PEDOTs and demonstrated improved neurocompatibility *in vitro* [202–204]. Despite their promise, conductive polymers are usually unstable, and rapid failure can occur *in vivo* [60, 205]. Carbon nanotubes have also been proposed as surface coatings for neural implants. Currently these are approached with caution due to their potential toxicity [42].

1.7.3.5 Proteins and Fillers

Peripheral nerve repair *in vivo* follows the path of the degenerated nerve, guided, in part, by the extracellular matrix (ECM) remaining following Wallarian degeneration [206]. Proteins, in particular the basement membrane found basolaterally to peripheral nerve axons [207, 208], provide a "pavement or handhold[s] for [axonal movement]" [22]. The primary components of ECM and basement membrane are: collagens; laminins; nidogens; and proteoglycans. Other components include fibronectin and tenascin [209–211]. These components polymerise either with themselves (e.g. laminin) or by bridging other proteins (e.g. nidogens) [212].

Bellamkonda highlights laminin-1 ($\alpha 1\beta 1\gamma 1$, see [213]) and laminin-derived peptides (e.g. IKVAV) as the most commonly used ECM proteins for peripheral nerve repair [177]. Laminin-1 is abundant in many tissues, while alternative laminin types (e.g. $\alpha 2\beta 1\gamma 1$) may be more applicable to peripheral nerve repair [179, 209, 214]. Proteins can be introduced into guidance conduits as surface coatings or within a gel like scaffold. Where a scaffold is included within the nerve guide this provides and opportunity for guidance in 3-dimensions [177, 180]. Aligned fibres can create a structure with longitudinal cues similar to the native nerve [215]. Directional cues can also be introduced using protein gradients, encouraging neurite growth up a concentration gradient [177]. Chapter 3 in this thesis investigates the use of basement membrane proteins for neural regeneration in an *in vitro* system.

1.7.3.6 Neurotrophic Factors

Neurotrophins are growth factors, which encourage neuron differentiation, regeneration or survival dependent upon the cell and tissue type. In normal neural repair and autografts neurotrophic factors are secreted by support cells and distal organs. The neurotrophic factors proposed to enhance neural regeneration are: nerve growth factor (NGF); brain derived neurotrophic factor; glial cell line-derived neurotrophic factor; neurotrophin-3; neurotrophin-4/5; and neurotrophin-6 [179, 206]. The molecules

can be immobilised to the implant surface, or released in a controlled way to create a chemoattractive gradient [76, 98, 176, 177, 179, 180]. To determine a suitable strategy with neurotrophic factors release kinetics, concentration and co-delivery must be considered [76]. For controlled release within a MNI a carrier must be introduced to the microchannels or to the distal lumen of the device, the use of viscous ECM or synthetic materials would make filling microchannels a challenge. Neurotrophic factors may be a suitable approach for encouraging neural regeneration within microchannels in future; however, current applications can cause undesired side-effects, such as transient neurite sprouting which then degrades rapidly [76].

1.7.3.7 Cell Therapies

Autografts for neural repair contain support cells to encourage axon growth [78]. Schwann cells have been used to align and guide axons *in vivo* [206, 215]. The cells can be seeded around the lumen of a construct, or within a filler gel. These therapies are promising for very large defects [78], however sourcing the cells is a challenge. Schwann cells are slow growing and harvesting autologous cells would cause the donor site morbidity which guidance conduits aim to solve. This may be overcome with stem cell therapies, however these are still in pre-clinical research and are likely to have a long lead-time to clinical practice [76, 176]. The application of cellular therapy for MNIs would require the seeding, and culture, of cells within microchannels *in vitro* prior to implant insertion, maintaining and confirming culture viability within a long microchannel is a challenge. If the challenges with Schwann cell culture and their use in MNIs are overcome this may lead to a new "gold standard" in nerve repair [76].

1.7.3.8 Testing Neurocompatibility

In order to determine whether a surface is neurocompatible prior to *in vivo* tests an *in vitro* assay or assays must be carried out. Typically biocompatibility assays follow ISO10993-5, using fibroblast cell lines and examining cytotoxicity. However, for known non-cytotoxic materials (e.g. implant grade silicones), application specific tests should be used. Chapters 3 and 4 of this thesis describe such *in vitro* neurocompatibility assays. Chapter 6 discusses *in vivo* tests of neurocompatibility.

The outgrowth of neuron processes, neurites, axons or dendrites can be observed *in vitro* [216]. Cell lines and primary cells have been used for this purpose [5]. Primary cells are acquired directly from the tissue of interest, while cell lines are the result of subculture of primary cells *in vitro* [217]. Typical primary cells used for neurocompatibility include: primary neurons from the cerebellum, the hippocampus, and the striatum; dorsal root ganglion cells; [218, 219]. Typical cell lines include: rat pheochromocytoma (PC-12) cells; mouse neuroblastoma N1E-115 cells; and human neuroblastoma SH-SY5Y cells [216].

This thesis uses the PC-12 cell line. PC-12 cells are an immortalised rat adrenal gland pheochromo-

[5] *Ex vivo* slice cultures have also been used, but these are less common.

cytoma cell line, developed in the 1970's, which exhibit a neuronal phenotype on exposure to nerve growth factor [220, 221]. The PC-12 cell neuronal phenotype has made the line popular for neural biocompatibility assays [31, 198, 199, 222–225], and with results comparable to primary neural (spiral ganglion) cells [226]. Cell lines have guaranteed purity and uniformity across the cell population; however, they are a less accurate model of the *in vivo* environment than primary cell cultures. Alternatively, primary neural cultures are heterogeneous, for example DRG neuron cultures also contain glial cells, and have a labour intensive preparation and limited lifespan. A cell line was chosen for this work to minimise variation across and between experiments.

1.8 Surgical Approaches to Control

1.8.1 Targeted Reinnervation

For patients with amputation above the level of the shoulder standard myoelectric control techniques cannot provide intuitive prosthetic control. Below the elbow, pattern recognition, using residual muscles, can be accomplished, because muscles controlling the hand (e.g. extensor digitorm) reside in the limb.

In trans-humeral and, in particular, shoulder-disarticulation amputations the muscles controlling the hand are not present; however, the nerves supplying them are. These can be rerouted to residual muscles or muscle flaps in the amputation stump or torso, a procedure known as targeted muscle reinnervation (TMR, see fig. 1.12) [227, 228]. This surgical technique has the advantage, compared with peripheral nerve electrodes, that muscles act as biological signal amplifiers, and therefore signals can be recorded using either surface electrodes or less invasive implantable myoelectrodes. Following nerve regeneration, actions natural for hand control cause contraction of amputation stump and torso muscles. The signals can then be recorded using standard EMG electrodes, and the muscle areas responsible for specific hand actions can be "mapped-out". Control of prostheses with up to 10 degrees of freedom has been demonstrated, compared with the 1 to 3 DoF available with hybrid or body-powered shoulder-disarticulation prostheses.

Typically TMR uses residual muscles or muscles available in the torso. To increase the number of channels available free muscle flaps could be used [229]. The Regenerative Peripheral Nerve Interface (RPNI) develops further on this principle, by implanting myoelectrodes within the muscle flaps during reinnervation surgery [230, 231].

TMR has an additional advantage. Hand sensation has been observed in the skin overlying TMR patient's reinnervated muscles. Touch, temperature, pain, and vibration could be felt by the patients. This finding has been exploited to directly use targeted sensory reinnervation of cutaneous nerves using sensory fascicles of the median and ulnar nerves, in a single patient case study this has been shown to create a sensory map of the hand at the innervated skin site [232].

Chapter 2 in this thesis presents preliminary investigation of a model to allow better understanding

Figure 1.12: The targeted muscle reinnervation (TMR) procedure. Reproduced from [13] permission received. REDACT IN ONLINE COPY.

of TMR and the biology and electrophysiology of reinnervation.

1.9 Implantable Interfaces and the Skin Barrier

Implantable interfaces are only a realistic clinical intervention if the data can be used outside the body, to control an amputation prosthesis [233]. The challenge is to create a stable data connection across the "skin barrier" without introducing a route for infection.

1.9.1 Telemetry

Wireless transmission has been accomplished using implanted systems [91, 93, 94, 165–167]. These designs are highly complex, and have a limit on the amount of data which can be transferred. For example the IMES system transmits a maximum of 32 channels approximately 470 samples/s, with a low-pass corner of <235 Hz; sufficient only for gross muscle movements [81, 91]. Other designs, including one developed by the author in collaboration with other UCL researchers (not reported in this thesis), have enabled neural data transmission [166, 167]. These designs limit the number of data channels which can be transmitted, or require spike sorting and data reduction within the implant [234].

1.9.2 Hard-Wired Connections

An alternative, requiring simpler implanted devices, is the use of hard-wired connections. At their most simple these are cables, which cross the skin through a cannula-like device. This approach provides a route for infection and is a route of failure as wires break where they cross the skin [131,235]. Hochberg et. al. successfully demonstrated the control of a prosthetic limb by tetraplegic patients using a cortical

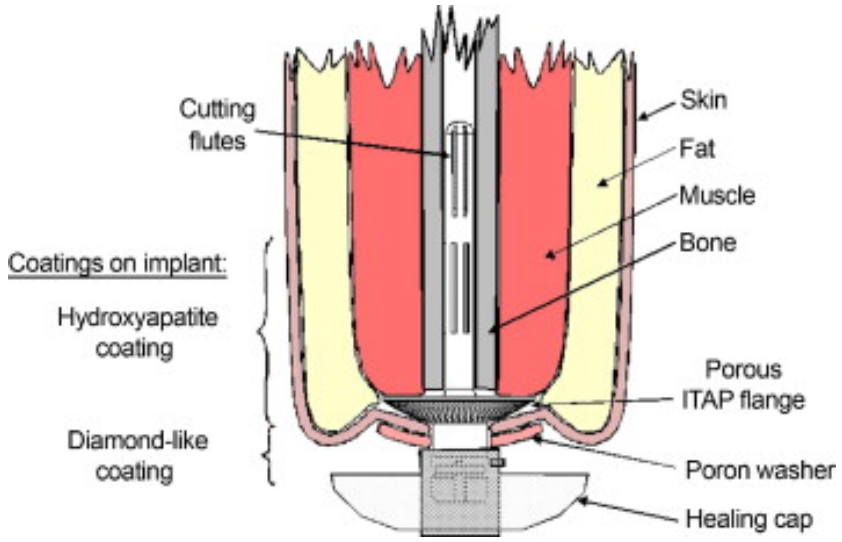

Figure 1.13: The intraosseous transcutaneous amputation prosthesis (ITAP) in position. Cutting flutes prevent rotation. The flange is perforated with 0.7 mm diameter holes, to allow soft tissue in-growth and create a stable skin interface. Healing cap (Stanmore Implants Worldwide) and Poron washer (Algeo Ltd., Liverpool, UK) hold the skin against the flange to allow the soft tissue to adhere to the solid implant. Reproduced from [237], with kind permission from Elsevier. ©2010 ASSH.

MEA; however, connection to the interface was carried out under aseptic conditions, and the design was not suitable for regular use outside a clinical setting [133].

Stable connections across the skin barrier have been developed for prosthesis attachment. Typically patients attach prostheses to their amputation stumps using suction cups, sleeves, sockets or harnesses. This results in discomfort, sweating, chaffing, numbness, heterotopic ossification and potentially serious skin infections (e.g. contact dermatitis). These common complaints by patients have led to research into alternative solutions for attachment [11, 236, 237].

Osseointegration of a transcutaneous implant directly to the residual bone within the stump can provide a solution to problems associated with prosthesis attachment. Work on implants for direct skeletal attachment of external prostheses has been ongoing since the 1970's [236, 238]. Early designs failed quickly due to infection and this remains a challenge the many current designs aim to solve [238].

The intraosseous transcutaneous amputation prosthesis (ITAP) was developed at UCL and RNOHT, Stanmore, in an attempt to overcome the problems with infection (see fig. 1.13). The device has been used successfully in a transhumeral amputee [237] (see figs. 1.14a and 1.14b), in veterinary cases [239] (see figs. 1.15a and 1.15b), and is undergoing clinical trials for use in transfemoral amputees. By including a porous flange intended to mimic a natural transcutaneous structure (antlers) the ITAP creates a stable interface with the soft tissues, intended to seal the skin and prevent infection [240]. The ITAP device has shown promise for improving range of motion [237] and restoring weight bearing [239].

Combining an osseointegrated prostheses with a hard-wired connection will create a robust transcutaneous data connection without the channel limitations associated with signal telemetry. Combining

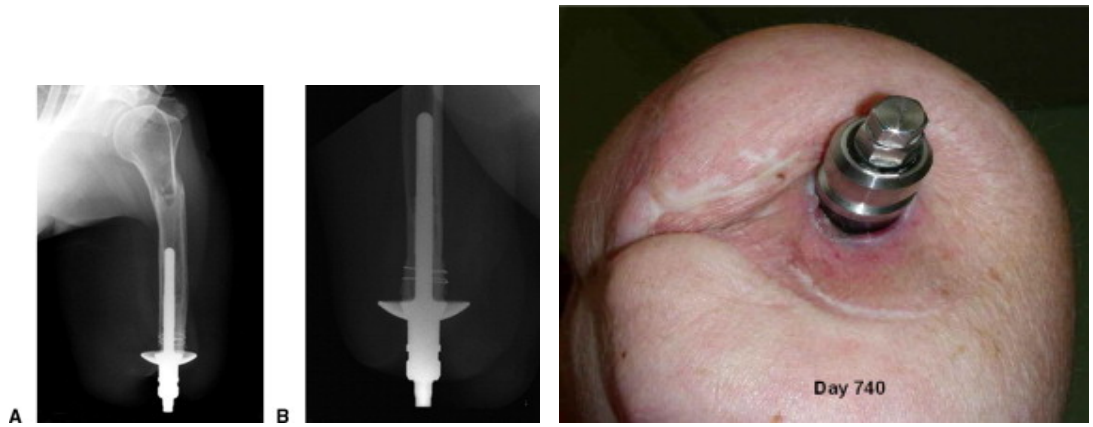

(a) Plain radiographs of the ITAP in position. A. Ventrolateral aspect. B. Dorsal aspect.

(b) Stable skin interface demonstrating skin attachment to the flange (not visible).

Figure 1.14: The intraosseous transcutaneous amputation prosthesis (ITAP) in a transhumeral amputee 2 years following implantation. Reproduced from [237], with kind permission from Elsevier. ©2010 ASSH.

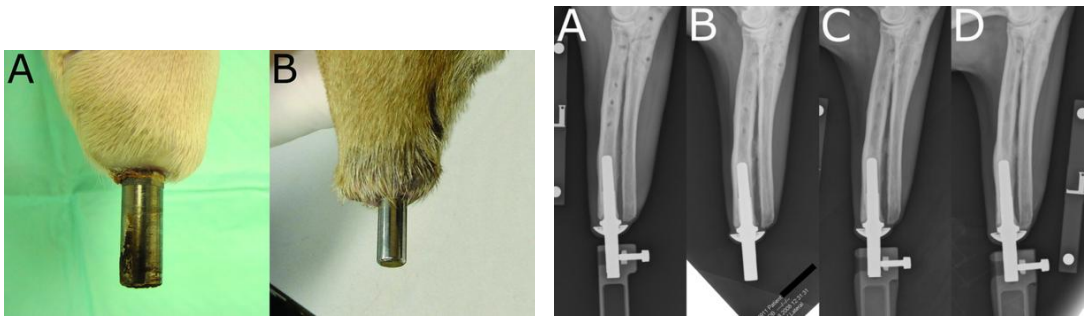

(a) Stable skin interfaces of two dogs, 28 weeks and 14 weeks postoperatively.

(b) Plain radiographs of the ITAP in the radius after A) 6 weeks ;B) 3 months;C) 5 months;and D) 7 months.

Figure 1.15: The intraosseous transcutaneous amputation prosthesis (ITAP) in veterinary cases (two dogs). Reproduced from [239], with kind permission from John Wiley and Sons. ©2011 by The American College of Veterinary Surgeons.

electrophysiological recording and direct skeletal attachment was first reported by Pitkin *et. al.* [241] and has since been demonstrated in human subjects by Ortiz-Catalan *et. al.* [233]. Chapter 2 in this thesis presents work which is both clinically and temporally intermediate to the research described in [241] and [233]. In these studies the wire was routed through a hole in the centre of the transcutaneous implant, and exited the implant within the medullary canal of the bone, holes were drilled through the bone cortex to allow the wire to pass through into the soft tissues of the limb. Pitkin *et. al.* [241] carried this out during the surgery to implant the bone-anchor in a single stage procedure. Ortiz-Catalan *et. al.* [233] used a two stage procedure, first the osseointegrated shaft was implanted into the bone and allowed to heal. The second stage required connecting the transcutaneous part of the implant, passing the wire through the osseointegrated shaft into the medulla and drilling a hole in the bone cortex to route the wires into the soft tissue. The need to route the wire through the bone could be avoided if the connection

exited the transcutaneous implant within the skin-crossing region.

1.10 Summary

This introductory chapter has demonstrated that there is an unmet clinical need for intuitive upper-limb prostheses with the same capabilities as the natural human hand. The current clinically available control systems are unsuitable and users are left with a tradeoff between basic, reliable systems and complex systems with lower reliability but more potential for intuitive control. A particular research focus is on surgical interventions, with implantable muscle and neural interfaces, targeted muscle reinnervation, and osseointegrated connections. These have yet to provide widespread clinical solutions and this thesis aims to improve upon current designs and move these closer to patients.

Chapter 2

In Vivo Electromyography

2.1 Introduction

Current powered upper limb prostheses are typically controlled by body power or surface electromyography (sEMG). Body power is easy to use and responds immediately to patients' actions, however it requires a cumbersome harness and patients must re-learn how to control their limb. sEMG is slower, but allows more degrees of freedom (DoF) to be controlled by implementing mode-switching between the control signals and the motion.

EMG measures electrical events in muscles. These electrical events are the coordinated movement of ions across the membrane of a muscle fibre during muscle movement, creating a current flux and voltage change around the muscle. It is this voltage change which is measured by EMG [56].

Advanced sEMG controlled limbs in clinical use include the "i-Limb Ultra" which allows sequential control of a series of pre-programmed, patient selected, grips and movements [242]. Mode switching is obtained by one or more events, such as twitching, co-contraction of opposing muscles and button-presses [19, 243].

As an electrical signal EMG is susceptible to interference. Firstly, general electrical noise can obscure the signal, the extent to which this occurs is measured by the signal-to-noise ratio (SNR). Second, the signal can be distorted by tissue filtering and other factors [244]. For EMG control, signal distortion should be avoided and the SNR should be large, SNR $\geq$5 has been suggested for neural recordings [52].

Techniques to improve myoelectric control include multichannel proportional control, pattern recognition and targeted muscle reinnervation (TMR) [244–248].

EMG is commonly recorded using skin surface electrodes. Skin surface electrodes are cheap and easy to connect to prostheses, however they have many limitations. Signals from deep muscles are obscured by tissue filtering and by stronger EMG from superficial muscles [15]. In addition, skin movement and subcutaneous fat can make recording from single muscles difficult and increase crosstalk. Surface signals can be unreliable due to other factors: skin impedance changes with humidity; electrode liftoff; and difficulty placing electrodes in a repeatable position [81]. In addition, in a patient with an upper arm

amputation it is very difficult to record many independent signals from the residual arm because there are few remaining muscles.

2.1.1 Implantable EMG Electrodes

Implantable electrodes are typically of two types: intramuscular electrodes, and epimysial electrodes. Epimysial electrodes are placed on the muscle surface, secured with sutures, while intramuscular electrodes are inserted into the muscle belly and hold in place with barbs [86].

Electrodes implanted on muscles have been in use for functional electrical stimulation (FES) for over 20 years, with some implanted systems working for over 15 years [86]. Per-electrode survival rates of 90% at 4 years for lower limb FES electrodes [249] and 98.7% at 16 years for upper limb FES electrodes have been reported [86]. The majority of failures are found within 2 years of implantation, with a plateau in survival after this point. In most cases failure is mechanical with electrode discs becoming detached from the lead wire, or the lead wire fracturing proximal to the electrode [86, 249]. Mechanical failure was found to be more common in high load areas, for example the posterior muscles of the lower limb and in hands following blunt trauma [86, 249]. In addition, there is an infection risk with any implant, one patient (out of 27) experience peri-implant infection in one study, the infection was associated with a suture rather than an electrode and cleared after revision surgery which removed the electrode and lead proximal to the infection site [86].

In an *in vivo* study of 40 electrodes no functional electrode failures were observed. Tissue response to epimysial electrodes typically resulted in a 179 ± 299 μm fibrous capsule with few active fibroblasts and very few or no macrophages present [85]. Intramuscular electrodes have been observed to migrate outside their target muscle and tissue response is typically more severe forming 535 ± 401 μm fibrous capsules with many active fibroblasts and macrophages present [85].

Electrodes designed for FES are typically large and monopolar. Recording guidelines suggest the use of biopolar electrodes with small interelectrode distances of around 20 mm or less [89]. New designs of recording electrode allow multi-channel and multi-polar recording in a smaller area. For example, an intramuscular polyimide wire electrode with 8, 40 μm diameter recording sites [95], and epimysial polyimide paddle electrodes with 5, 800 μm diameter recording sites [96]. Larger numbers of smaller electrodes allow detailed spacial information about the muscle activation to be obtained. This enables more detailed control of prostheses; however, the thin flexible electrodes required may move within the muscle belly altering the recorded signal [95].

The fibrous capsule surrounding implantable myoelectrodes can be of benefit to signal recording [81]. The capsule prevents electrode movement relative to the muscle(s) of interest. In addition, the capsule creates an environment of consistent impedance improving signal reliability [81, 250].

2.1.1.1 Implantable Myoelectric Sensors

Implantable myoelectric sensors (IMES) are a wireless implantable EMG system. Developed from BIONS (bionic neurons), an FES system, IMES are hermetically sealed cylinders 15 mm length, 2 mm diameter, with electrodes at either end [81, 90–92].

The IMES system can operate with up to 32 implants over a wireless power-data link with a coil fitted over the stump (a practical limitation due to coil size and limits on electrode placement) [81, 91]. However, at 32 implants sampling is limited to approximately 500 samples/second (S/s). To satisfy Nyquist's sampling theorem the sample rate should be no less than double the signal bandwidth, or no less than double the highest frequency of interest [251]. Conventionally for EMG the highest frequency components are 500 Hz, therefore sampling at 1 kHz or even 1.5 kHz is recommended [82, 252]. Undersampled signals (such as those recorded by IMES at 500 S/s) will loose information about the EMG signal; however, they may still be useful for prosthetic control as smoothing or averaging may be used in control algorithms [252]. To record the full signal with IMES the number of implants would be reduced to 16 (954 S/s) or 8 (1.8 kS/s) [81], fewer than the required DoF for the full control of a prosthetic hand.

As implantable electrodes IMES benefit from fibrosis holding it in place relative to the muscle. Also, as implantable electrodes IMES avoid complications with subcutaneous fat reducing the radius of the effective recording area from over 10 mm in patients with a thick subcutaneous fat layer [162] to less than 5 mm if implanted [97]. Recording of independent muscle signals in the forearm has been reported with IMES [253] and an acute first in human trial has occurred [92].

Alternative, similar, systems are also in development. For example the MyoPlant (Otto Bock), which can connect to four paddle electrodes and transmit data at up to 4.8 kHz has been demonstrated in vivo [93]. Another implantable system by Ripple LLC connects to four bipolar epimysial electrodes and operates between 20 Hz and 300 Hz bandwidth [94].

2.1.2 Targeted Muscle Reinnervation

For patients with transradial (below elbow) amputations the muscles previously controlling the hand (e.g. extensor digitorm) are often still present. These patients can benefit from pattern recognition techniques to enable more intuitive prosthetic control.

For transhumeral (above elbow) amputees, in particular those with shoulder-disarticulation, the muscles that previously controlled the hand are not present. Patients have to learn new control strategies using surrogate antagonistic muscles for movements. However, nerves previously controlling these patients' limbs are present. By re-routeing these nerves to residual, denervated muscles or muscle flaps in the amputation stump or chest, a technique known as targeted muscle reinnervation (TMR), signals from these nerves are amplified and can be picked up as EMG signals [227, 228]. When the patient attempts an action with the amputated limb the newly reinnervated muscle is activated. Over 40 patients have

undergone TMR to date with favourable clinical outcomes [254]. Further developments to TMR have led to targeted sensory reinnervation (TSR), sensory mapping of the hand in the amputation stump [232], in early patients this occurred through natural competitive skin reinnervation, however this has now been surgically guided by coaption of sensory fascicles from the median and ulnar nerves to cutaneous nerves.

The availability of suitable muscle flaps in the upper arm or chest is limited. To further enhance TMR free muscle flaps can be used to provide a greater number of independent channels where they are not present in the stump [229]. An alternative to TMR is the RPNI (Regenerative Peripheral Nerve Interface) where the addition of electrodes to the flaps during muscle transfer enables EMG recordings [230, 231]. In this case rat muscles are used *m. extensor digitorum longus* was freely transfered to the right thigh and coapted to the peroneal nerve, the muscle is approximately 20 mm long and 5 mm wide, indicating that in a human forearm many RPNIs could be formed. However high levels of cross-talk have been observed [personal correspondence], possibly due to the use of small muscles, and strategies including wrapping muscle flaps in xenogenic matrix are being employed to better isolate the recording sites [231]. Alternatively changes in electrode design, for example using smaller inter-electrode distances, or double-differential (tripolar) electrodes, can increase selectivity and allow the use of smaller muscle flaps for RPNI and TMR [162].

2.1.3 Transcutaneous Signal Transmission

Transcutaneous signal transmission is a significant challenge for implantable electrodes. Two main approaches are used: hard-wired connections, and wireless signal transmission. A study of a peripheral nerve interface in a human volunteer found a $>85\%$ failure rate from 20 channels due to mechanical fatigue of transcutaneous wires [131].

Hard-wired connections can carry a high risk of chronic infection. Head connectors are commonly used hard-wired connections. These have been used successfully in human trials and are used in animal studies [96, 133]. In this case wires are run subcutaneously to the site of interest, these long subcutaneous wires can increase noise levels and short shielded cables are better [56]. Aseptic conditions, impractical outside a clinical or laboratory setting, are required for connecting to head connectors [133]. In laboratory conditions regular antibiotics and topical antiseptic are often required to reduce infection risk [255, 256]. Head connectors, with bone screws or bone cement fixation are an example of bone-anchoring, this provides stability to the connection site reducing fatigue and providing a secure platform for head-stage amplifiers.

Wireless systems have been developed for both muscle and neural signal recording, the IMES discussed above is one example [81, 93, 167, 257]. Transmitting many channels of data at sufficient resolution and bandwidth to reconstruct the recorded signal is a challenge. For neural information data reduction methods must be used, otherwise the required data-rate limits the number of channels [167, 257].

In addition the power requirements for data transmission over a day (8 to 12 hours) is expected to be a major challenge. If the power link is inefficient, the battery would need to be significantly larger and heavier, which is not a suitable solution to this design challenge [258].

2.1.3.1 Amputation Prostheses

Current prostheses attach to the amputation stump using suction cups, sleeves, sockets, harnesses or a combination of these suspension devices. Complications include discomfort, sweating, chaffing, numbness, heterotopic ossification and potentially serious skin infections (e.g. contact dermatitis). Patients complain that "long use means sores the following day" [10]. When considered with unintuitive control systems this leads to low patient satisfaction and high rates of prosthesis disuse [11].

Transcutaneous implants which osseointegrate directly to the residual bone within the stump can avoid complications associated with prosthesis attachment. In addition osseointegrated prostheses can withstand greater stresses than standard stump-socket interfaces, and provide a route for hard-wired data transmission. These prostheses are in clinical use and are proving revolutionary [237].

Skeletal fixation of prostheses provides some unexpected benefits, for example osseoperception, a restoration of tactile sensation, transmitted through the artificial limb and the osseointegrated implants, for example to determine surface hardness [259, 260]. Range of motion also improves with osseointegrated prostheses compared with stump-socket interfaces, making prostheses more intuitive for patients before any control systems are added [261].

Infection is a risk for osseointegrated prostheses. In a study of 39 patients [262], after 2 years there were 6 implant infections (15%) and 11 cases of soft tissue infection (28%). Of all patients surviving to follow up only 2 had normal levels of bacterial growth at the implant site. 3 patients (8%) underwent implant removal before or during the study. Of the 6 patients with implant related infections, 1 recovered following a 6 month course of ciprofoxacin and 5 were undergoing treatment at the end of the study. Failure rates of 20% and infection rates of 38% have been reported for transhumeral patients [263].

Combining bone-anchored prostheses with a hard-wired connection will reduce the fragility of transcutaneous hard-wired connections and avoid most channel limitations associated with signal telemetry. This combination of bio-signal recording and direct skeletal attachment was reported by Pitkin et. al. [241]. In a sedated rabbit amputation model it was shown that EMG signals from intramuscular electrodes could be transmitted through a bone-anchored pylon and then recorded. An intraosseous transcutanous amputation prosthesis (ITAP) could be used to create a permanent transcutaneous conduit. In addition to providing a stable anchor, ITAP integrates with soft tissue around the implant reducing the risk of infection [237].

2.1.4 Aims and Hypotheses

The aims of this chapter are as follows:

- To record epimysial EMG signals in cognisant, moving animals and transfer these signals using a bone-anchored device.
- To investigate targeted muscle reinnervation in a sheep hind limb model using epimysial EMG such that the resulting signals could be transmitted through ITAP.

The hypotheses of this chapter are as follows:

- EMG signal quality will be better from epimysial electrodes compared with skin surface electrodes.
- Cross-talk from adjacent muscles will be minimal compared with the target muscle when using epimysial electrodes.
- Neural regeneration and muscle activity will be observed following targeted muscle reinnervation in a sheep hind limb model.

2.2 Methodology

All *in vivo* procedures described were carried out in accordance with The Animals (Scientific Procedures) Act UK, 1986 (revised 2013) and local guidance.

2.2.1 Implantable Myoelectrodes 1

The following experiment is described in Al-Ajam et. al., 2013, IEEE Trans. Biomed. Eng. [2].

2.2.1.1 Construction of the Electrode / Bone-Anchored Device

A Ti-6Al-4V osseointegrated transcutaneous implanted device was constructed using laser sintering (see fig. 2.1). A tapered stem allowed press fit of the device into bone. The device had a porous flange with a strut size of 300 μm and a pore size of 700 μm, with struts arranged in an open-faced, cubic structure. The device was shot-blasted and hydroxyapatite (HA) coated to improve soft tissue and bone adhesion. During shot-blasting and coating, the external portion of the device was masked to maintain a smooth finish.

A straight 2 mm hole was drilled from the uppermost surface of the device, exiting immediately below the flange. This area was presumed to be within the soft tissues and above the region of the implant associated with osseointegration, this eliminated the need for an additional hole in the tibial cortex. A press fit sleeve was added to the external part of the device to house the electrical connections.

A bipolar epmysial electrode (Ardiem Medical) with Pt10Ir electrodes, interelectrode distance 10 mm, was passed through the implant. The leads were crimped to a 2-pin connector (LEMO UK Ltd, Worthing, U.K) on the external portion of the implant. The lead was 316 stainless steel, 2-core coiled cable with fluoropolymer insulation encapsulated in silicone. The socket was secured using epoxy resin.

The cable was secured in the 2 mm hole using medical grade silicone elastomer (NuSil Med3-4013, NuSil Technology LLC, CA, USA), in addition this was considered to reduce potential flexion of the cable at the internal exit. The silicone was degassed, injected using a syringe, and cured for at least 24 hours at 50°C. The HA coated flange and stem were masked to prevent contact with uncured silicone. The implant was sterilized using ethylene oxide gas.

The implant design is shown in fig. 2.1 and the finished implant is shown in fig. 2.2.

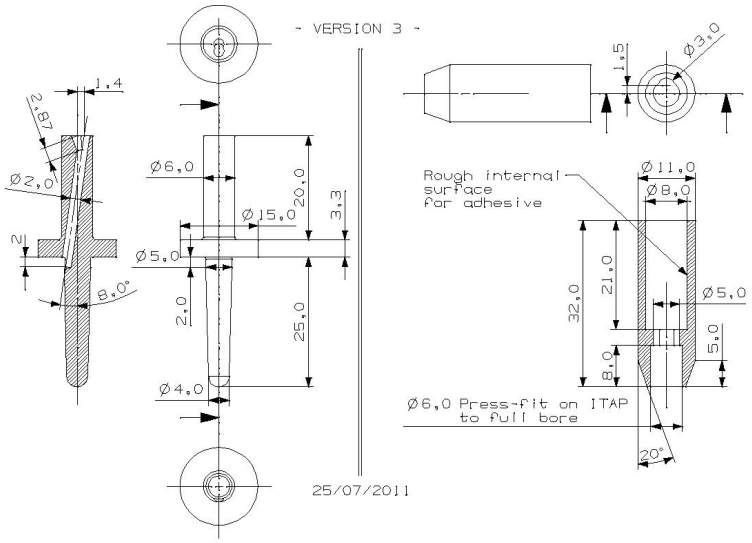

Figure 2.1: 2D CAD design of the implant device showing: tapered stem; 15 mm diameter porous flange; 2 mm diameter hole for electrode cable; press fit sleeve. Image courtesy of Jay Meswania.

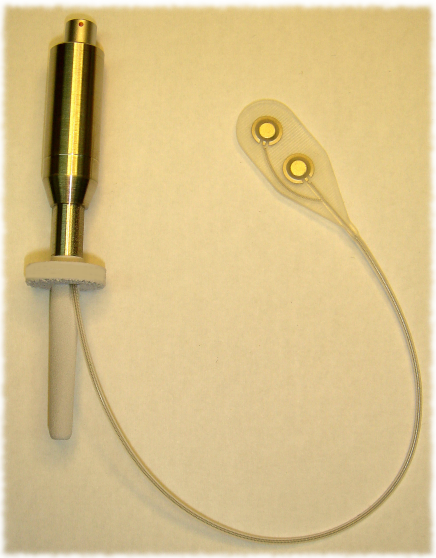

Figure 2.2: The finished bone-anchored device with epimysial electrode. Images from Al-Ajam et. al., IEEE TBME, ©2013 IEEE, with permission [2].

2.2.1.2 Surgical Technique

One female sheep (Mule) was chosen for this study. All animal procedures were carried out in accordance with the United Kingdom Home Office Animals (Scientific Procedures) Act 1986. General anesthesia was administered using isoflurane (Isoflo) in oxygen. A 5 cm incision was made over the left tibia, 10cm inferior to the knee joint on the medial aspect. The tibia was exposed by dissection. Both cortices of the tibia were drilled using a 4.6 mm diameter drill bit. The hole in the medial cortex was enlarged using a 4.8 mm diameter drill bit. Both cortices were reamed, using a custom tapered reamer, and the implant press fitted into the hole. 2 mm was allowed between the flange and the tibia to accommodate the electrode cable and soft tissue growth. This procedure is described as trans-tibial insertion, to differentiate from the amputation model used by Pitkin et. al. [241].

A 10 cm incision was made over the lateral compartment muscles of the left leg. *M. peronius tertius* was identified [264]. A subcutaneous tunnel was made between the 2 incisions through which the epimysial electrode was passed. The electrode was secured to the epimysium at 6 points using 4-0 Prolene (non-absorbable) suture. The incisions were washed with physiological saline solution and closed, tension-free, in 2 subcutaneous and 1 cutaneous layers using Vicryl (absorbable) suture (Ethicon Inc., NJ, USA). Post-operative dressings were applied: Mepitel (Mölnlycke Health Care Limited, Bedfordshire, UK); sterile gauze; and a bandage. Correct positioning of the implant was confirmed by radiographs (fig. 2.4). Antibiotics were given for 3 days post-operatively and fentanyl (analgesic) patches for one week. The animal was individually housed and the first EMG signals were obtained 24 hours post-operatively.

2.2.1.3 EMG Recording

Treadmill walking at 2 km/h was carried out weekly for 12 weeks. EMG signals were recorded using BIOPAC Equipment (MP150 and EMG100, AcqKnowledge software, BIOPAC Systems, Inc., CA, USA). Recording parameters were: 1000 samples per second (sps); 100 Hz to 500 Hz band-pass; 500x amplification. In addition to connecting the 2 pin LEMO connector for recording, a stainless steel needle ground electrode was used, inserted subcutaneously over the left-leg hock joint.

At 2 weeks following surgery skin surface EMG signals were recorded for comparison. *M. peroneus tertius* was identified by palpation. Following shaving and cleaning, self-adhesive surface electrodes (Vermed Inc., VT, USA) were applied with an inter-electrode distance of 20 mm. The needle ground electrode was placed over the hock joint as described above.

Signals were analysed using Acqknowledge software (V4.2, BIOPAC). The signals were rectified. Mean power was calculated for 0.25 second epochs in a selected 4-second period (3 or 4 gait cycles). Epochs with greater than mean average power were considered signal, all other epochs were considered noise. SNR was calculated as the ratio between the mean average rectified signal EMG and the mean

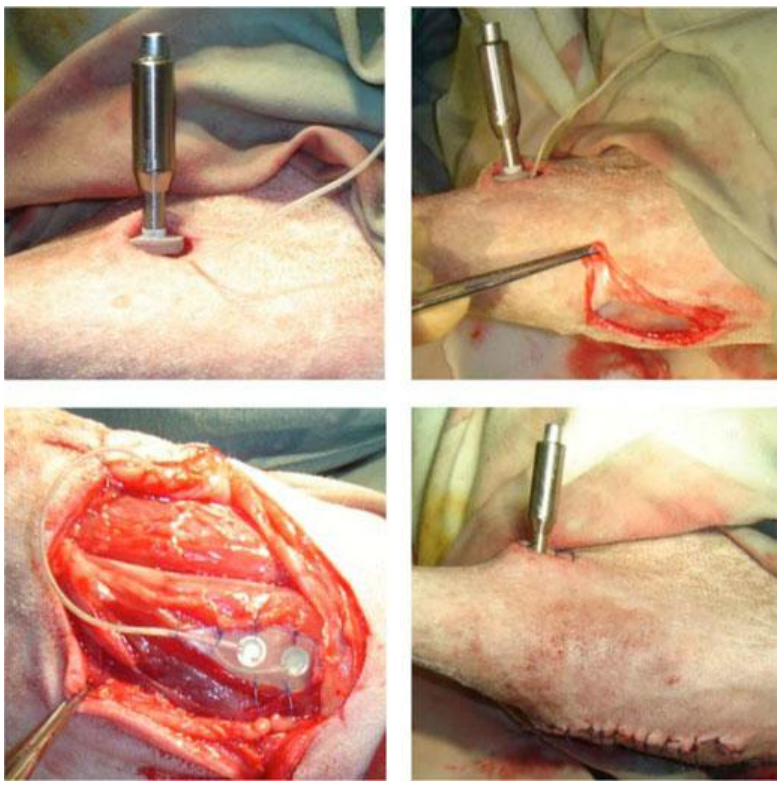

Figure 2.3: The bone-anchored device *in situ*. Intraoperative images demonstrating implantation of the bone-anchored device and epimysial electrode in the ovine tibia. (Top left) Bone-anchored device inserted transtibially. (Top right) Incision made over *m. peroneus tertius*. (Bottom left) Electrode sutured epimysially. (Bottom right) Incision closed. Images from Al-Ajam et. al., IEEE TBME, ©2013 IEEE, with permission [2].

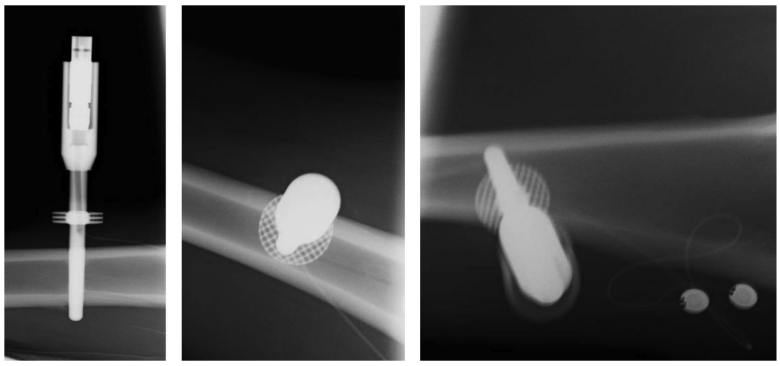

Figure 2.4: Post-operative plain radiographs of the bone-anchored device showing trans-tibial insertion. Left: lateral view; middle: anterior-posterior view; right: oblique view showing bipolar epimysial electrode and electrode wire. Images from Al-Ajam et. al., IEEE TBME, ©2013 IEEE, with permission [2].

average rectified noise EMG.

The process is described in eqs. (2.1) to (2.5).

$$SNR = \frac{|Signal|}{|Noise|} \tag{2.1}$$

$$\text{if } P_t > \bar{P} \text{ then } \text{EMG}_t = Signal_t \tag{2.2}$$

$$\text{if } P_t < \bar{P} \text{ then } \text{EMG}_t = Noise_t \tag{2.3}$$

$$\bar{P} = \frac{\sum P}{n}, \text{ ie. average of all P over samples} \tag{2.4}$$

$$P_t = \frac{\sum_{t>0}^{0.25s} \frac{V_t^2}{f_t}}{n}, \text{ n = number of samples } (0 < \text{t} \leq 0.25\text{s}) \tag{2.5}$$

Mean power is an averaged form of the nonlinear energy operator (NEO), which is large only when the signal is high in power (proportional to V^2) and high frequency [171]. An index which preferentially detects high frequency signals will avoid reporting slow wave changes (e.g. movement artefact) as signal. In addition averaging the NEO reduces the likelihood of false positives resulting from short-lived voltage transients. Averaging is only suitable for the detection of muscle signals composed of many multiple data points, for the detection of single motor unit action potentials averaging should not be used. The use of the overall mean average as a detection threshold created an adaptive method and should reduce experimenter bias and error.

2.2.1.4 Impedance Spectroscopy

In vitro impedance measurements were made using the EVAL-AD5934EBZ impedance monitor (Analog Devices, MA, USA) by the potentiostatic method [265]. The frequency range for the impedance monitor was 10^3 Hz to 10^5 Hz and the impedance range is 500 Ω <Z <1 MΩ, values measured outside this range were considered unreliable. The impedance monitor was calibrated using a 100 kΩ (1%) resistor. Pre-implanted and explanted epimysial electrode impedance was measured in 0.9% saline (physiological saline) at 1 kHz to 77 kHz, 0.4 Vp-p, δ = 150 Hz. Following explantation the electrode impedance was measured with 3 mm of surrounding tissue in 0.9% saline.

2.2.1.5 Post-explant Histology

After 12 weeks the animal was sacrificed by an intravenous injection of 20% pentobarbital solution. The implant was removed: the electrode with a cuff of underlying muscle; and the bone-anchored device

Solution	Time	Repeats	Notes
Neutral Buffered Formal Saline	7 days		Starts immediately following explantation
50% IMS	3 days	1	
75% IMS	3 days	1	
85% IMS	3 days	1	
95% IMS	3 days	1	
100% IMS	3 days	2	
Chloroform	3 days	2	Fat removal
100% IMS	3 days	2	

Table 2.1: Serial dehydration procedure for soft tissue samples: epimysial electrode.

with approximately 5 cm length of tibia and overlying tissue. The specimen was fixed in 10% formalin : 90% buffered saline solution.

The explanted electrode was dehydrated (Industrial Methylated Spirits, IMS) and defatted (Chloroform) for histology as shown in table 2.1.

The specimens were embedded in LR White Resin (London Resin Company Limited, London, UK). Briefly: specimens were transferred to 50% resin / 50% IMS for 5 days, during which the specimens were kept in a darkroom either under vacuum or on a tilted rotating plate. The 50% resin / 50% IMS step was repeated. The specimens were transferred to 100% resin and kept in a darkroom either under vacuum or on a tilted rotating plate for 5 days. The 100% resin step was repeated. Specimens were transferred to plastic containers and cast by immersion in resin:accelerator (10ml:1 drop, London Resin Company Limited, London, UK). The specimens were placed at -20°C to cure for at least 24 hours.

The specimens were sectioned, placed on a clear perspex backing, ground and polished until 100 μm thick. Sections taken through the implant and surrounding tissue was stained with toluidine blue for 20 minutes followed by Paragon stain for 20 minutes. The electrode samples were stained with toluidine blue. Tissue integration of the transcutaneous portion was assessed using an Olympus BH2 microscope (Olympus Optical Company Ltd, Tokyo, Japan) with Zeiss KS300 3.0 image-analysis software (Imaging Associates, Thame, UK). Sections were ground, polished, sputter coated with Au/Pd and osseointegration of the stem portion was assessed using backscatter scanning electron microscopy (JSM-5000, JEOL, Tokyo, Japan).

2.2.2 Implantable Myoelectrodes 2

Bone-anchored devices were created and implanted as described in section 2.2.1. N = 6 skeletally mature sheep (Mules) were used. To protect the external socket connectors silicone masking caps (Greentree Shercon, Tewkesbury, UK) were used. EMG recording was carried out and analysed as described in section 2.2.1. Recordings were made at the following time points: 1, 2, 3, 4, 6, 8, 14 and 19 weeks

following implantation. At 19 weeks surface EMG recording were made for comparison. The animals were sacrificed after 19 weeks. Impedance readings were made as described in section 2.2.1. In addition, *in vivo* impedance readings were made using the same parameters immediately following terminal anaesthesia. Histology was carried out as described in section 2.2.1.

2.2.2.1 Pre-terminal stimulation of adjacent muscles

Pre-terminal muscle stimulation was used to assess crosstalk from adjacent muscles. General anaesthesia was administered as described in section 2.2.1. The leg was shaved and the following muscles were exposed by dissection: peroneus tertius; tibialis anterior; peroneus longus; gastrocnemius. The motor nerve branch to each muscle was identified and exposed. Motor nerves were stimulated using a Medtronic Vari-Stim III Surgical Nerve Stimulator (Medtronic Inc., MN, USA) set to a 1 mA pulse. 6 readings per muscle were elicited over a 60 second period and were recorded using the BIOPAC acquisition system as described above (section 2.2.1). Stimulus peak (V) and muscle signal peak (V) were from adjacent muscles were compared with the targeted muscle, peroneus tertius.

2.2.3 Targeted Muscle Reinnervation 1

A bone-anchored device was created and implanted into one sheep (Mule) as described in section 2.2.1.

2.2.3.1 Surgical Technique

Following implantation of the bone-anchored device as described in section 2.2.1 targeted muscle reinnervation (TMR) was carried out. *M. peroneus tertius* was exposed by a 15 cm incision and the muscle was retracted laterally to expose the peroneal nerve. The nerve branches to *m. tibialis anterior* and the lateral comparment were identified. Three insertion points in *m. tibialis anterior* were identified and one branch was transected close to the muscle. The nerve was freed from surrounding tissue distally to proximally until the branch joined the peroneal nerve. The motor nerve branch to *m. peroneus tertius* was identified and sectioned approximately 1 cm proximal to the insertion point. The distal portion of *n. peroneus tertius* was coapted to the freed proximal portion of *n. tibialis anterior* using 3, 8-0 nylon monofilament sutures (non-absorbable, S&T, Switzerland). Sutures were placed at 120° intervals around the circumference of the epineurium. The epimysial electrode was sutured onto the epimysium of *m. peroneus tertius* as previously described. The incision was closed in layers

2.2.3.2 EMG Recording

EMG recording was carried out and analysed as described in section 2.2.1. Recordings were made weekly.

2.2.3.3 Force Plate Analysis

At weekly intervals before or after EMG recording force plate measurements were carried out. Force plate measurements were first made 4 days before surgery. The force plate (left and right) was calibrated

using a 50kg weight. The sheep was weighed before measurements were taken. The sheep walked across the force plate and at least 6 recordings for each hind limb (left and right) were taken each week. The force measurements were normalised for weight and reported as F_{max}/weight.

2.2.4 Data Analysis

Unless otherwise stated data were analysed using SPSS version 21.0 (Windows and Linux versions). The data were not assumed to be normally distributed, and the conditions for parametric testing were not met, therefore non-parametric tests were used.

2.3 Results

2.3.1 Implantable Myoelectrodes 1

2.3.1.1 Gross morphology

Visual inspection of the skin-implant interface at 12 weeks indicated a stable interface. Slight reddening of the skin was observed (see fig. 2.5), but the wound was dry and no exudate was present. A fibrous capsule had formed around the electrode and cable, however the surrounding muscle appeared healthy. The external socket connector accumulated debris during use. This appeared to be external environmental debris.

Figure 2.5: The bone-anchored device implant skin interface after 12 weeks demonstrating slight reddening. Image from Al-Ajam et. al., IEEE TBME, ©2013 IEEE, with permission [2].

2.3.1.2 EMG Signals

SNR followed an increasing trend for the first 11 weeks of testing, from 4.4 in week 1 to a maximum of 6.5 in week 8. A representative EMG recording is presented in fig. 2.6. From week 5 to week 10 SNR was greater than 5. The SNR at week 2 was greater for epimysial compared with surface electrodes (5.1 and 1.6 respectively). Signal quality deteriorated rapidly after 11 weeks due to the debris accumulation discussed above.

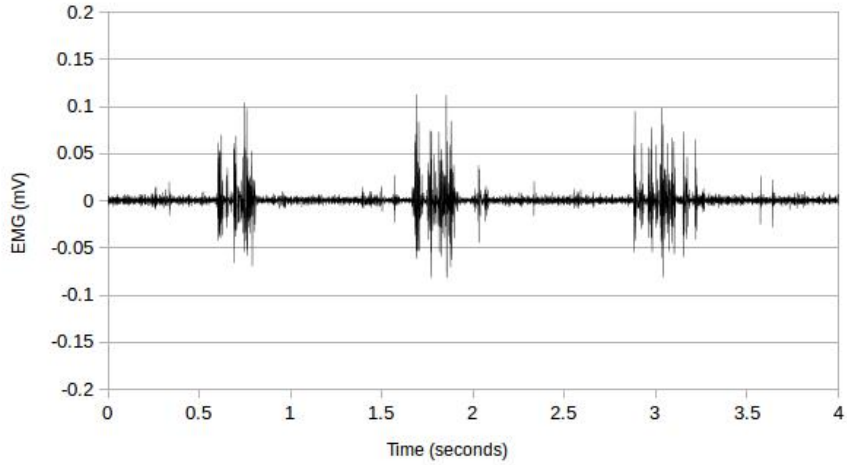

Figure 2.6: A representative epimysial EMG recording taken during treadmill walking. 3 distinct muscle activations can be seen, indicating 3 gait cycles. Adapted from Al-Ajam et. al., IEEE TBME, ©2013 IEEE, with permission [2].

2.3.1.3 Impedance Spectroscopy

The electrode impedance at 1 kHz increased from 1.6 kΩ pre-implantation to 2.3 kΩ post-explantation. A log-log plot of absolute impedance pre-implantation and post-explantation is given in fig. 2.7.

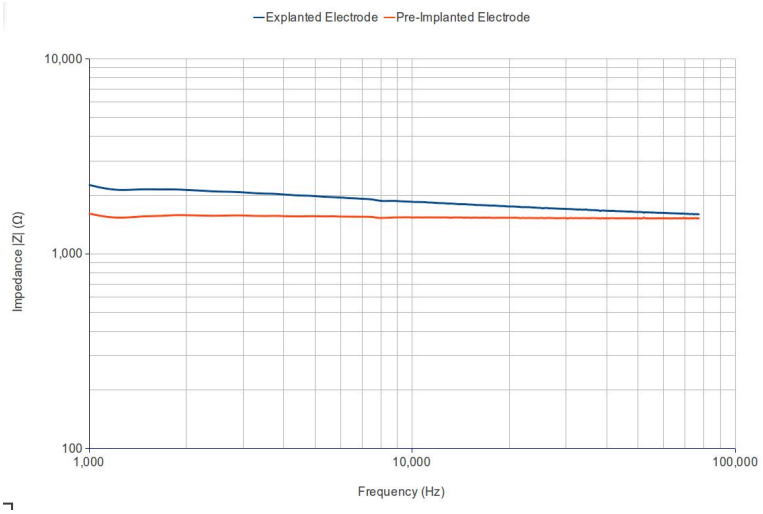

Figure 2.7: Log-log plot of electrode impedance pre-implantation and post-explantation, measured in 0.9% saline.

2.3.1.4 Histology

A fibrous capsule of between 70 μm and 250 μm formed around the electrode, see fig. 2.9b. The capsule consisted of parallel collagen fibres interspersed with similarly aligned fibroblast nuclei. A layer of fibroblasts was present at the electrode–tissue interface. During histological processing the electrode was lost due to failure of the silicone to integrate with the resin, in subsequent histological processing the electrode was removed from the capsule before processing to avoid tissue loss and resin fracture.

Osseointegration of the HA coated stem was observed with bone growth up to the edge of the stem, see fig. 2.8. The dermis anchored to the porous flange and a healthy epidermis was observed above the electrode and early stage bony bridging was observed, see fig. 2.9a. The gap between the flange and the bone was approximately 6 mm, larger than the intended size of 2 mm to 3 mm.

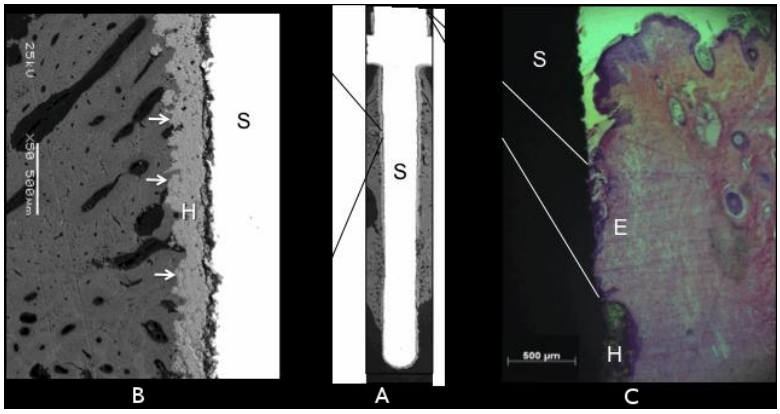

Figure 2.8: A - Backscatter scanning electron micrograph of the bone-anchored device. B - Arrows show 'osseointegration' with the HA coating (H) plasma sprayed onto the stem (S). C - Section through the skin-implant interface showing the keratinized epithelium (E) integrating with the stem (S) and adjacent HA coating (H). Image from Al-Ajam et. al., IEEE TBME, ©2013 IEEE, with permission [2].

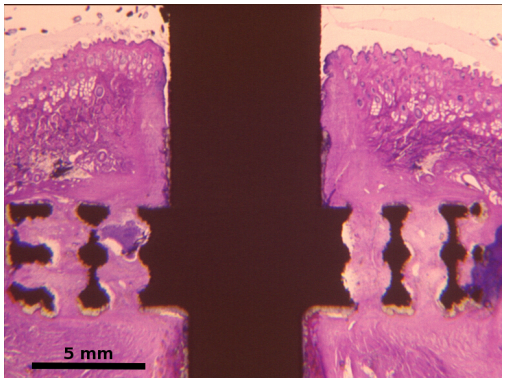

(a) Skin-implant interfaces of bone-anchored device porous flange. The dermis is integrated with the porous section and a healthy epidermis has formed. Some epithelial downgrowth was observed.

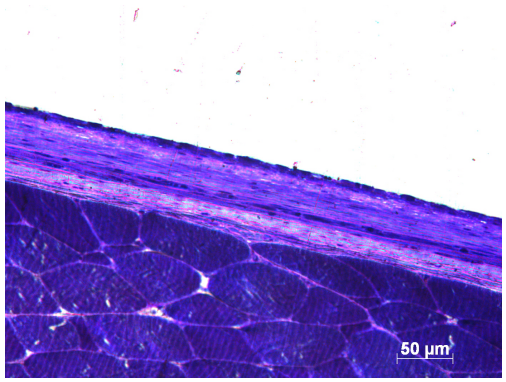

(b) Electrode-tissue interface of the epimysial electrode. A thin fibrous capsule has formed. Muscle fasciculi are present below the fibrous tissue.

Figure 2.9: Soft tissues responses to the bone-anchored device and the epimysial electrode.

2.3.2 Implantable Myoelectrodes 2

A single animal (6036) was diagnosed with osteomylitis following chronic infection of a surgical site involved in a concurrent study, betadine and intramuscular antibiotics were administered, following no recovery at week 5 the animal was sacrificed and a single further animal added to the study. A single animal (6027) exhibited Johne's disease (paratuberculosis), a para-natally acquired infection of ruminants not associated with this study [266], this animal was sacrificed at 12 weeks. A total of 5 animals were sacrificed after 19 weeks.

2.3.2.1 Gross Morphology

In implants placed proximally with large amounts of skin movement sieving was observed. Sieving is the exposure of the flange as the skin moves downward, forming an epidermal layer within or below the flange, rather than above the flange. This complication was first observed at week 4 with thinning and nerosis of the skin overlying the flange. In a single animal this progressed and the flange became visible at 8 weeks with dry necrosis of the skin. Abnormal skin reddening around the flange was not observed in this case and no exudate or other evidence of infection was observed. Fibrous capsules had formed around the electrodes and cable in every animal overlying healthy muscle.

2.3.2.2 EMG Signals

The socket connection was broken on a single animal (6027) and recordings could not be made at week 19.

Non-parametric correlation between signal-to-noise ratio and implantation time was calculated using Spearman's rho. The correlation was significant and positive, with a coefficient of 0.389 (p = 0.006). Using single mean values for each subject at each time point a linear best fit gives R^2 = 0.151 (see fig. 2.10). Of the 6 animals sacrificed after 19 weeks, 5 showed an increasing linear trend in SNR and 1 showed a decreasing linear trend (see fig. 2.11). SNR for implanted electrodes (6.82$\pm$3.59) was significantly greater than for skin surface electrodes (1.46$\pm$0.37) at 19 weeks (p = 0.016). A comparison of signal to noise ratios is shown in fig. 2.12. Representative EMG recordings for implanted and skin surface electrodes are shown in figs. 2.13a and 2.13b. In the skin surface recording, in addition to the muscle activations observed using the epimysial electrode, activity is observed at the level of the muscle of interest where only small or no activations are observed in the epimysial recordings. This indicates contamination with other muscle signals, where the signal is mostly removed in the epimysial recording, but causes crosstalk in the skin surface recording.

2.3.2.3 Pre-terminal stimulation of adjacent muscles

There was a significant reduction in peak stimulus voltage with motor nerve distance from the electrode. Peak stimulus voltage is the magnitude of the stimulus artefact from the nerve stimulator, peak EMG is the magnitude of the muscle response to stimulus. All adjacent muscles exhibited significantly lower peak EMG and stimulus voltages compared with the targeted peroneus tertius ($p < 0.004$, $p_{cut} > 0.008\dot{3}$). Peak EMG fell significantly with muscle distance from the recording site, peak stimulus artefact fell significantly with increasing change in nerve supply between the stimulation site and the recording site.

The muscles with greatest EMG signal are the peroneal nerve muscles: peroneus tertius (0.0259$\pm$0.0040 V), peroneus longus (0.0188$\pm$0.0026 V), and tibialis anterior (0.0084$\pm$0.0025 V). The most distant muscle, the gastrocnemius, has the lowest peak EMG voltage (0.0048$\pm$0.0012 V). Peak EMG signals are plotted in fig. 2.14.

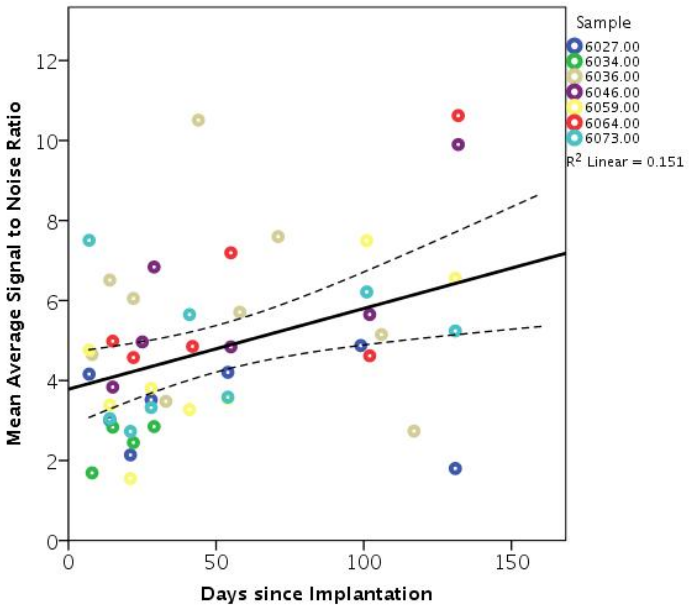

Figure 2.10: Change in mean EMG SNR with time following surgery, n = 6. One animal, 6034, was sacrificed after 30 days. Linear line of best fit with 95% confidence intervals of the mean. The trend is significant $R^2 = 0.151$, $\rho = 0.389$, p = 0.006.

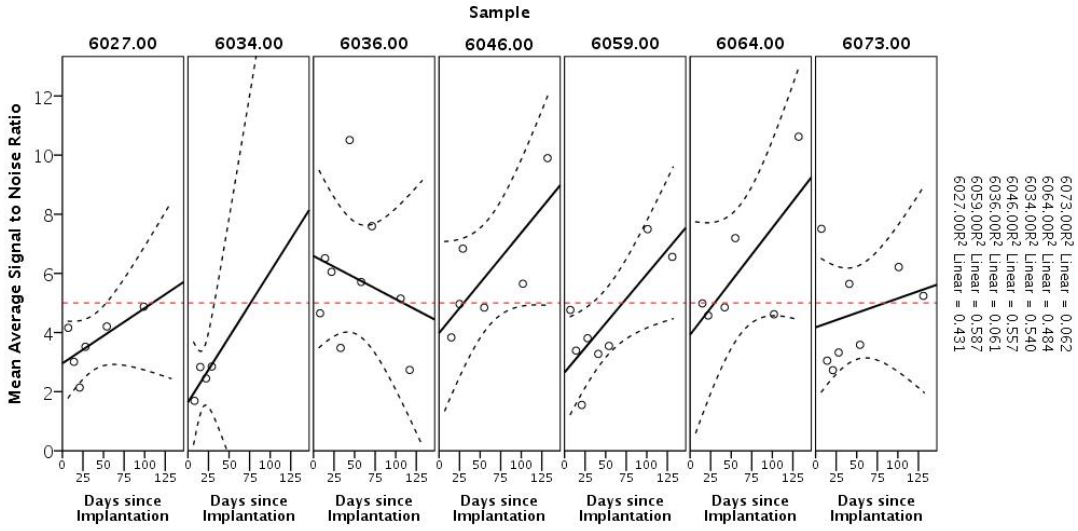

Figure 2.11: Change in individual mean EMG SNRs with time following surgery, n = 6. One animal, 6034, was sacrificed after 30 days. Linear lines of best fit with 95% confidence intervals of the mean.

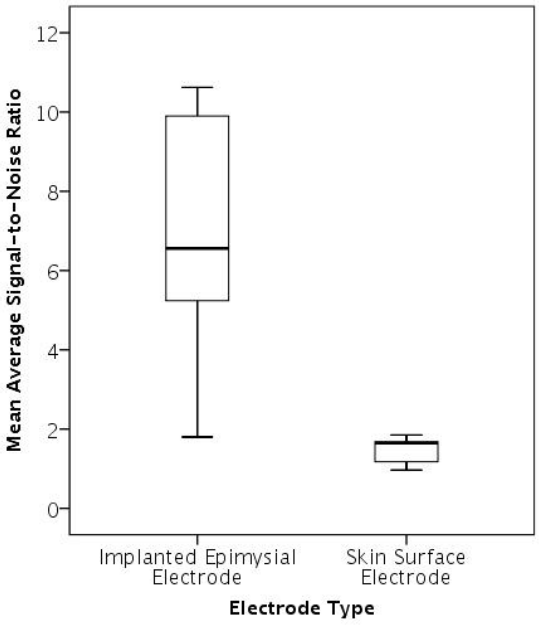

Figure 2.12: Difference in mean EMG SNR between implanted and skin surface electrodes 19 weeks after surgery, n = 5. Due to the broken socket connector animal 6027 was left out of the comparison. The difference is significant p = 0.016.

The greatest stimulus artefact voltage was observed on the deep peroneal nerve muscles: peroneus tertius (0.246±0.031 V) and tibialis anterior (0.134±0.041 V). The muscle on the superficial peroneal nerve, peroneus longus (0.060±0.011 V), when stimulated exhibited the next largest artefact. The gastrocnemius (0.025±0.015 V) is on a different motor branch, the tibial nerve, and had the smallest stimulus artefact. Peak stimulation artefacts are plotted in fig. 2.15.

2.3.2.4 Impedance Spectroscopy

Impedance values are shown in fig. 2.16. Pre-implantation mean impedance was 1.3 kΩ (1338 ± 18 Ω), this increased to 2.2 kΩ (2153 ± 244 Ω) after 19 weeks *in vivo*, and 3.1 kΩ (3093 ± 1296 Ω) following explant. There was a significant difference in impedance between: pre-implant and *in vivo* impedance ($p \leq 0.003$); and pre-implant and explanted impedance ($p \leq 0.008$). There was no significant difference between *in vivo* and explanted impedances ($p \geq 0.245$).

2.3.3 Targeted Muscle Reinnervation 1

2.3.3.1 Gross Morphology

To reduce skin movement the implant was placed in a more distal position than in the n = 6 study. The interface appeared stable. A fibrous capsule formed around the electrode and cable with some muscle atrophy observed on the *m. tibialis anterior* and *m. peroneus tertius*. The coapted nerve was in continuity, however fibrosis had formed along the surgical approach obstructing the view of the coaption site.

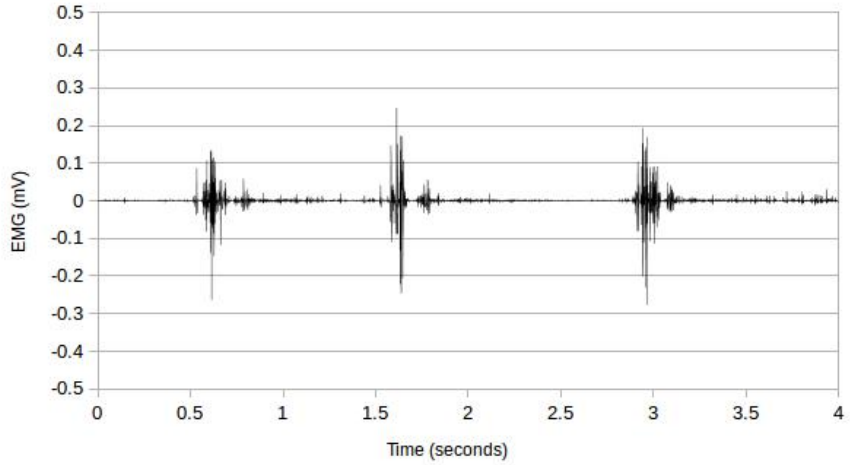

(a) Epimysial EMG.

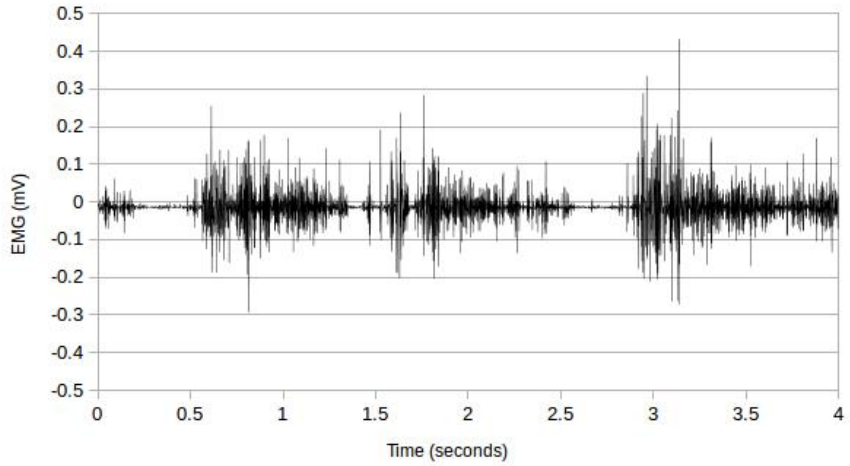

(b) Surface EMG.

Figure 2.13: Representative implanted epimysial and skin surface EMG recordings taken at the same time from the same muscle during treadmill walking. 3 distinct muscle activations can be seen in the epimysial signal, indicating 3 gait cycles.

2.3.3.2 EMG Signals

Muscle activations were first noticed after approximately 1 month with an increase in SNR from 1.86, 22 days post-operatively to 3.20, 29 days post-operatively. Muscle signals were observed in every recording after 29 days post-operatively (see fig. 2.17). At 58 days post operatively SNR peaked at 6.64 , at 12 weeks post operatively SNR was 4.27.

2.3.3.3 Force Plate Analysis

Pre-operatively no significant difference in F_{max}/weight was observed between the left and right legs ($p = 0.478$). For the first month following TMR the force was significantly different between limbs and the difference showed an increasing trend with time ($p < 0.006$, $p_{cut} > 0.007$). From 45 days post-operatively the force was not significantly different between the legs ($p > 0.039$, $p_{cut} < 0.024$). The normalised force

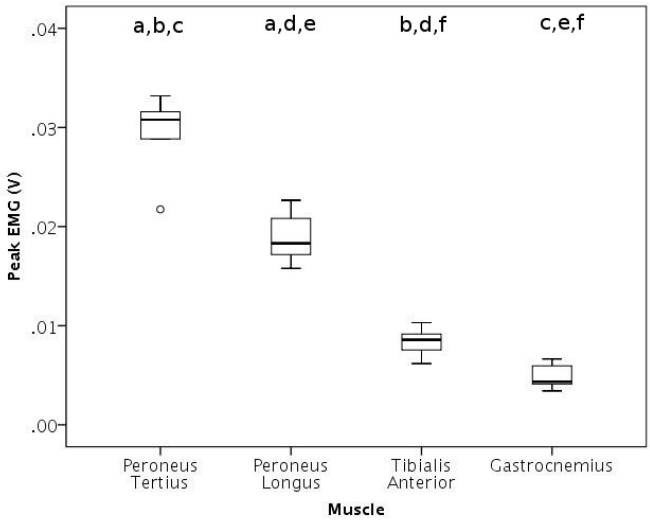

Figure 2.14: Peak EMG signal during selective muscle stimulation, n = 1. Recordings taken epimysially overlying the peroneus tertius, muscles stimulated individually at nerve supply using a 1 mA pulse. Significant differences are indicated by paired letters: a, p = 0.004; b,c,d, p = 0.002; e, p = 0.001; f, p = 0.003.

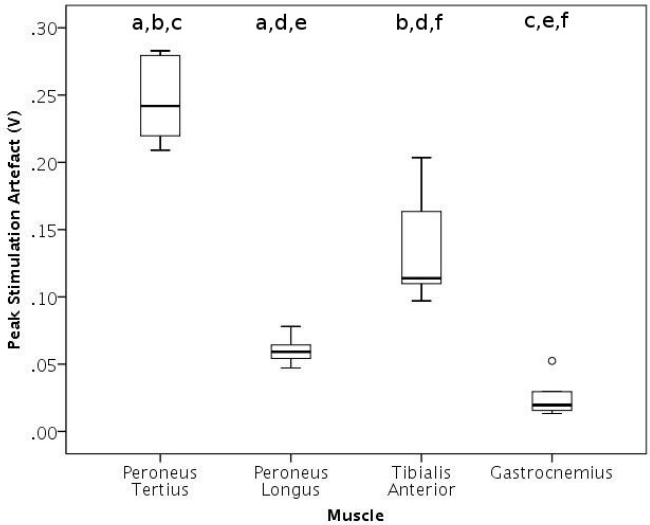

Figure 2.15: Peak stimulus artefact during selective muscle stimulation, n = 1. Recordings taken from the epimysial electrode overlying the peroneus tertius, muscles stimulated individually at nerve supply using a 1 mA pulse. Significant differences are indicated by paired letters: a,b,c,d,f, p = 0.002; e, p = 0.004.

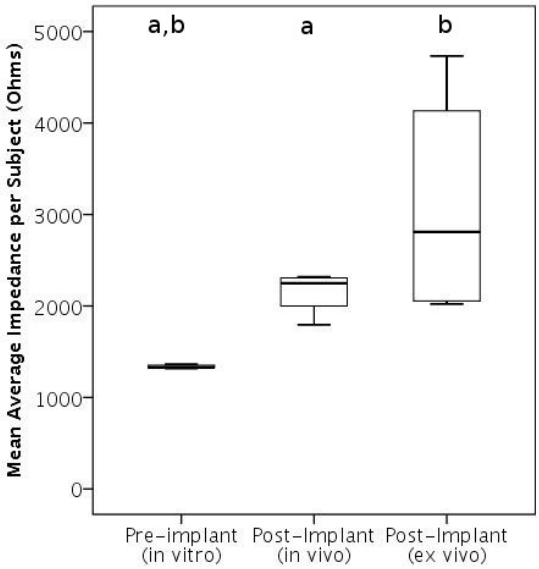

Figure 2.16: Mean 1kHz impedance change of epimysial electrodes following 19 weeks implantation, n = 6. A single mean value for each subject is reported. Significant differences are indicated by paired letters: a, p = 0.003; b, p = 0.008.

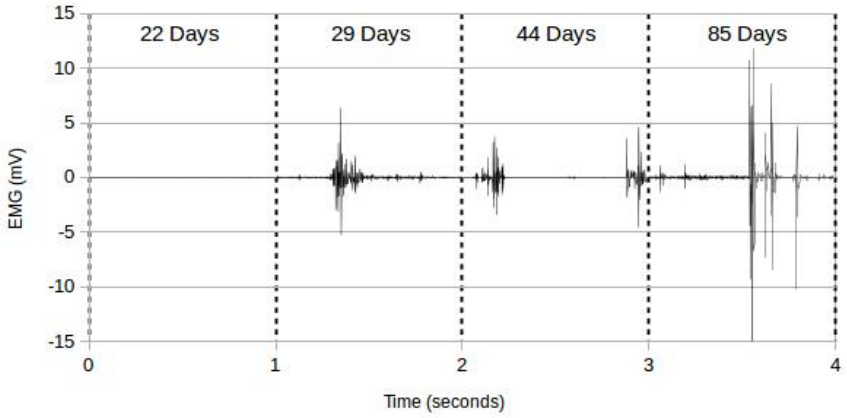

Figure 2.17: Representative EMG recordings following TMR, showing recovery of activations at 29 days post operatively and activations at recording sessions up to 12 weeks (85 days) post-operatively.

is reported in fig. 2.18.

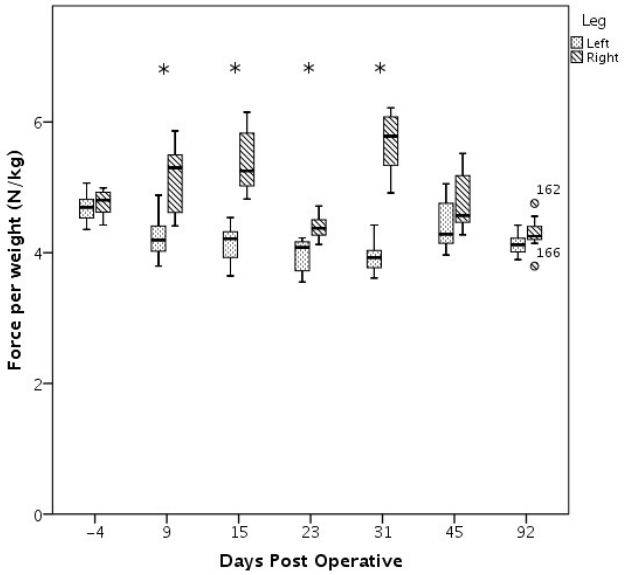

Figure 2.18: Force per sheep weight following targeted muscle reinnervation, n = 1. The left leg has undergone TMR between n. tibialis anterior and m. peroneus tertius. Significantly different pairs are indicated with an asterisk (*).

2.4 Discussion

2.4.1 Implantable Myoelectrodes 1

The 12 week experiment is the first to describe EMG signal recording with a transcutaneous bone-anchored device conduit from a cognisant subject. Over the study period signals could be considered good quality for most recording sessions after 5 weeks [52]. After this the device failed, due to contamination of the external connector caused by the housing environment.

Once the device had been cleared of debris post-explantation impedance could be measured. The impedance values were in the range found in the subsequent (n = 6) study, indicating that the loss of signal quality was due to debris and not internal device failure. Impedance can be expected to be stable following fibrous capsule formation [267]; however, it may be possible to reduce the impedance by selecting more appropriate electrode materials that are more biocompatible and reduce the thickness of the fibrous capsule. Alternative designs may also influence impedance, but it was not the objective of this study to investigate design of epimysial electrodes.

Signals from epimysial electrodes were found to be of better quality than from surface electrodes, however there were a number of potential confounding factors. The comparison surface EMG recordings were only in a single animal at a single time point shortly (2 weeks) following surgery. In addition the sheep model is not optimal for surface recordings, it is difficult to sufficiently shave the leg for electrode attachment and the extent of skin movement around the ankle joint may create artefact or move the

electrodes from optimal placement over the muscle.

The chosen design is an improvement on previous designs, which required a hole to be made through the bone cortex through which to pass the recording wire [241]. In an amputation model, the only required hole would be that already present at the distal bone (eg. humeral or femoral) end. In this study early stage bony bridging was observed, however this did not impinge upon the electrode cable. In longer term studies bone growth up to the electrode wire may cause device failure, this is also a criticism of Pitkin et al, where natural healing of the hole in the bone cortex may lead to cable damage. A possible solution to this issue in longer-term studies is a silicone bend protection grommet surrounding the cable until at least the edge of the porous flange.

2.4.2 Implantable Myoelectrodes 2

The 19 week experiment provides a longer implantation time to examine whether: a) signal deterioration occurs over the long term; b) whether the bone-anchor is a robust design.

The bone-anchor was found to be robust, with no failures due to loosening within the bone. In one animal the external socket connection was damaged and recordings could not be made at week 19. This damage was confined to the commercial LEMO socket, the titanium bone-anchored device and sleeve were undamaged, this indicates that a redesign of the sleeve could be made to: better protect the LEMO connector; or provide a fail-safe mechanism that avoids permanent damage to the bone-anchored device if the applied force exceeds a threshold [268]. This may not be an issue with these electrodes in humans where patients would look after the connectors.

After 19 weeks early stage bony bridging was also observed. This did not impinge upon the electrode cable in any of the animals, however, as discussed above cable protection may be needed for longer-term applications.

The skin sieving observed was primarily attributed to skin movement overlying the flange. This may have been compounded by additional factors: following surgery the site was bandaged and compressed, movement caused the bandage to bunch over the proximal area, causing more pressure to be applied; the flanges had a rectangular cross-section with 90° angles between the radial and vertical directions creating a sharp edge underneath the skin; only a thin skin layer was sutured over the flange to allow dermal attachment, because the flange sits removed from the bone this may stretch the skin and result in inadequate soft tissue cover (see. fig. 2.4). A domed type implant as used in animal [239] and human [237] patients may prevent these problems by having soft edges facing the skin interface. In addition, cable protection may allow the implant to be placed closer to the bone reducing skin stretching. Finally, future implants should be placed less proximal to reduce skin movement and consideration should be made to design an implant for use with a healing cap similar to the Poron washer use by human patients [237].

An increase in signal-to-noise ratio with time was observed, with a single exception, over 19 weeks. Signal quality in the first 7 to 8 weeks was lower than observed in the n = 1 study, however signal quality then increased and remained high for 50 days. Signals from epimysial electrodes were found to be significantly better than from skin surface electrodes, although a large variability in epimysial electrode SNR was observed. Targeting electrodes to *m. peroneus tertius* may have reduced crosstalk from adjacent muscles and the level of skin movement in the model, combined with other confounding factors, may have contributed to lower quality surface EMG.

Crosstalk was also investigated directly, by neural stimulation of the local adjacent muscles. Peak EMG (recorded from the epimysial electrode targeted to *m. peroneus tertius*) was found to decrease with increasing distance from the electrode. This is to be expected, firstly because the body can be considered a volume conductor some fraction of the current flow within any given muscle will be present throughout the body, and can therefore be recorded [56]. Second because recorded potential decreases with increased distance from any given muscle fibre [269]. In addition, the tibia can be expected to block current flow from muscles on the opposing side of the leg, attenuating the signal from the *gastrocnemius* [269].

Crosstalk can be reduced by reducing the pick-up volume of the electrodes. The double-differential (true-tripole) electrode and its electrical equivalent the pseudo-tripole can reduce pick-up volume in the presence of resistive tissue layers [160, 270]. In addition reducing interelectrode distance (10 mm in this study) could further reduce pick-up volume [162].

Crosstalk should also be investigated using multiple electrode sites. In this study only the *m. peroneus tertius* was used with a single targeted bipolar electrode. A greater number of electrodes ($\geq$6) should be used targeted over different muscles. In the sheep model the following distinct muscles are available locally within the hind limb (identified by dissection by Y. Al Ajam): tibialis anterior, peroneus tertius, peroneus longus, flexor digitorum longus, gastrocnemius, and soleus. Additional muscles are present, however due to interdigitation or inaccessibility these were discounted as surgically unavailable.

The trend in peak stimulus voltage recorded epimysially over the *m. peroneus tertius* was different to that of peak EMG and can therefore not be fully explained by distance from stimulus site to recording site, although artefact decreases linearly with distance when only one single muscle is considered [271]. The greatest voltages are observed when stimulating *n. peroneus tertius* and *n. tibialis anterior*, which are both branches of the deep peroneal nerve supplying the anterior compartment. *N. peroneus longus* is a superficial peroneal nerve branch supplying the lateral compartment and has the next greatest voltage. Finally the *gastrocnemius* is supplied by a branch of the *n. tibialis*. This leads to a tentative hypothesis that the stimulus artefact is following a conductive pathway along the nerves and that therefore, a greater stimulus artefact voltage is observed when stimulating muscles, which have more similar nerve supplies. As with EMG amplitude, stimulus artefact can be reduced by using a smaller inter-electrode distance

[271].

The change in impedance with implantation for the experiment with 6 sheep was in the range obtained from the initial study where there was one individual, validating the results from that experiment. Again the change in impedance can be attributed to fibrous capsule formation following implantation. Because the impedance value following 12 weeks implantation (2.3 kΩ) is in the range of the values following 19 weeks implantation (2.2 k$\Omega \pm 0.2$ kΩ) a stable fibrous capsule and therefore stable impedance readings may have been reached [267]. The non-significant increase in impedance following explantation may be due to crosslinking of the capsule by the fixative and ionic availability in the different solutions used (interstitial fluid compared with isotonic saline).

2.4.3 Targeted Muscle Reinnervation

Recovery in gait and muscle activity was observed following reinnervation. This supports the use of sheep hind limb as a model for TMR. Muscle recovery was observed after approximately 1 month, this correlates with the peak difference in force distribution between legs. This indicates that *m. peroneus tertius* reinnervation leads to gait recovery, and that reinnervation is required for a return to normal gait. A learning effect may also be key to gait recovery, this could be tested in a 3 group study: one group as per this study; one group *m. peroneus tertius* deinnervated without reinnervation; one group section taken from *n. peroneus tertius* and reversed before coaption back into *n. peroneus tertius*.

The change in gait measured by force plate assessment was not apparent by visual inspection. Following initial surgical recovery no signs of lameness were observed supporting the use of the chosen nerve transfer for TMR studies in the sheep model.

By the end of the study there was no difference in weight bearing between the operated and non operated hind limbs, however muscle activation patterns (fig. 2.17) were qualitatively different from normal muscle (fig. 2.6). This was expected [56], because not all the motor axons present can be expected to reinnervate the nerve, therefore larger groups of muscle fibres will be reinnervated by a single motor axon and act as one unit compared with the more even axon distribution and therefore fibre activations in normal muscle. This leads to the change in signal morphology with fewer larger spikes within the compound trace.

TMR patients may benefit from implantable electrodes, removing the need to wear a waistcoat with skin surface electrodes [227]. This has been investigated using needle electrodes, with offline classification accuracy equivalent to that from surface electrodes [272]. Needle electrodes are not optimal for TMR patients, as reinnervated muscles are sensitive to needle insertion at the reinnervation site. Epimysial electrodes may overcome this issue: the surgeon performing TMR can implant the electrodes during the same procedure as in this study and as others have for RPNI [231], eliminating the need for further surgery. Furthermore, where bipolar needle electrodes have been used [272], the reduced

interelectrode distance and reduced pick up area results in highly variable recordings (of few motor units) from large muscles. Epimysial electrodes can be expected to overcome this problem.

Alternatively to electrode implantation during TMR, the electrode could be implanted once the re-innervated muscles stabilise and demonstrate firing following patient's thought of given limb movements [229], this may be around 6 months after surgery provided the patient is given adequate training [273]. Training includes maximising EMG power from individual re-innervated muscles and practising movements and grasps by mirroring a computer interface. This will allow targeting the implanted electrodes to the relevant muscles and the sites of greatest or most specific EMG signal. In addition, implanting the electrodes during TMR may reduce the rate of reinnervation and cause greater muscle atrophy, while this two step procedure can be expected to limit these potential complications.

Delay prior to reinnervation may adversely effect the rate and success of reinnervation. Following a brief review of the literature, patients were found to undergo TMR between 6 and 17 months following the initial amputation (with a mean of 11 months) [227, 229, 274]. This delay is to allow healing of the skin around the amputation, ensure no complications are present, and to assess patients for TMR. However, the delay may adversely affect reinnervation, following denervation both muscle and nerve can change irreversibly. Muscle undergoes denervation atrophy following long term denervation where myofibrils are reabsorbed or misalign and muscle cells undergo apoptosis-like cell death, although this process and timeline following denervation is not clear in humans [275]. In addition, muscle fibre type changes, collagen fills space left by muscle atrophy and the muscles blood supply reduces: a delay of only 1 month can lead to over 50% loss of reinnervated muscle force. It should be noted that in TMR the chosen muscles are typically denervated immediately prior to reinnervation, however the nerves chosen had been left without a target organ following amputation. Over time the number of axons available for reinnervation may reduce contributing to the loss of muscle force [276]. However, there is evidence that, even following 12 months following nerve transection, individual axons will innervate more muscle fibres than normal and therefore, in healthy muscle such as that used in TMR, lead to a normal number of innervated muscle fibres and normal muscle force [277]. Denervation atrophy may be avoided or reduced in TMR patients by using the recording electrodes for FES while awaiting reinnervation, evidence from spinal cord injury patients has demonstrated that beginning FES usage shortly following injury significantly reduces muscle loss [278].

In addition, reinnervation is expected to be less successful in older patients, to date it has been used successfully in patients over the age of 50 [227], however the nerve is expected to repair more slowly and less effectively [279]. A key finding for improving neural repair in older amputees is that neural debris slows reinnervation, by clearing this debris axon growth and neuromuscular junction formation may be facilitated [280].

In this study, due to cost, time and ethical constraints, there was no delay between nerve transec-

tion and coaption, therefore this can be considered a poor model of TMR as practised in amputees. A prolonged axotomy study similar to that used by Fu and Gordon [277] may be applicable, in the sheep model this would involve transection of *n. peroneus tertius* with targeted reinnervation to *m. peroneus tertius* following a delay of approximately 12 months (to appropriately mirror the case in human TMR patients).

2.4.4 Conclusions

It is concluded that the sheep model chosen is suitable for the transfer of EMG signals using a bone-anchored device in cognisant, moving animals. The model should be refined and extended as discuss above to improve: implant robustness; the skin interface; and the number of recording sites. Once this is carried out the model will lend itself to pre-clinical testing of epimysial electrode designs with hard-wired interfaces.

The findings of this study indicate that a bone-anchored device would be suitable for transcutaneous signal transmission in human patients. The implanted device described above may require significant alteration for human use [237]. A domed flange shape has been discussed above. In addition the bone-anchor and flange will need to be sized to fit the patient.

The implant design presented requires a hole through the centre of the bone-anchored device, breaking the skin barrier created by the porous flange and introducing a route for infection. In this study a medical grade silicone was used to seal the hole; however this may not be suitable for human use. Silicones are often viscous and, even when degassed, form bubbles when injected into samples. Bubbles may weaken the seal or result in no seal forming. For human applications a hermetic seal is suggested, this will prevent water and infection ingress through the lumen of the bone-anchored device. A metal-in-glass or metal-in-ceramic feedthrough is suggested which can be soldered to the body of the bone-anchor. This feed-through should then be sealed with a medical grade silicone on the patient side to provide a second barrier to infection.

Alternative bone-anchored device designs may already be suitable for signal transmission: for patients with a two-part prosthesis [236, 281] the skin penetrating abutment could be removed from the osseointegrated portion and a modified abutment used as a hard-wired transcutaneous pathway, this has been demonstrated recently in human patients (January 2013), following the research described in this chapter (the first experiment began in October 2011, the second experiment began in July 2012) [233]. It should be noted that the abutments described do not have a porous flange design to encourage skin and soft tissue integration, therefore the skin seal, although assumed to be of lower quality, can be broken and reformed around a new implant without requiring significant tissue removal.

This study demonstrates that epimysial electrodes can be placed on a muscle in the same surgical session as TMR and that reinnervation will occur. It is unknown whether the extent and quality of

reinnervation is reduced due to the epimysial experiments. This should be examined in an animal model to determine whether simultaneous TMR and implantation can be suggested for clinical practice.

This chapter presents a technique for accurate 1-to-1 mapping of electrodes and muscles without relative movement. However, untargeted mono-polar electrodes may also perform well [282], some control algorithms show robustness to electrode movement and reduced electrode number [283]. Implanting electrodes may even reduce classification accuracy, however targeting muscle directly during implantation may overcome these issues [284]. Untargeted systems would reduce surgery time and invasiveness, but further work is required to confirm whether the extra time spent targeting electrodes to muscles is beneficial for patients.

This study used passive electrodes with recording equipment sited outside the body. Further work is ongoing to develop active electrodes with signal amplification at the recording site and multiplexing using an active implant. This will enable multiple electrodes to be implanted using a single hard-wired connection. In addition, amplified and digitised signals will be less susceptible to cable artefact and external noise. To account for differing surgical approaches and patient anatomy active implants can be produced with different cable lengths, which are then chosen, connected and sealed during surgery using Craggs connectors [285]. In addition to a mutiplexed recoding system, additional channels could be introduced for sensory feedback by stimulation of nerves within the amputation stump, where stimulation signals are carried using the same hard-wired connection. This has the potential to provide patients with prosthesis attachment, control and sensation.

This study presents a series of *in vivo* experiments with limitations due to the model, including: some anatomical differences; a trans-tibial rather than amputation insertion; the single channel design; and a lack of patient feedback. Some of these issues will be overcome in further work with a more advanced device design; however, it is not ethically feasible to carry out an amputation model and training and control issues can only be considered with a non-human primate or human study.

Chapter 3

In Vitro Neuron Adhesion Studies: Basement Membrane Proteins

3.1 Introduction

Improving neurocompatibility of microchannel surfaces may improve their function. Reducing the adverse foreign body response will prevent channel occlusion and enable the *in vivo* use of smaller diameter microchannels [51, 113, 146].

Microchannel neural interfaces are regenerative electrodes, and must therefore be sutured within a transected peripheral nerve. In order for microchannel electrodes to function axons must regenerate along the *circa* 5 mm gap created between the proximal and the distal nerve endings [59, 113].

The gold standard for neural repair and regeneration following complete nerve transection is the autograft, but taking the graft can lead to donor site morbidity. Synthetic nerve guidance channels (NGCs) have been introduced to overcome donor site morbidity associated with autografts and provide a reproducible off-the-shelf alternative [75, 77, 78, 178, 286]. MNIs can be considered a special case of NGCs, therefore the same strategies to improve neurocompatibility and neural regeneration apply. Furthermore, the challenges in interfacing with chronically amputated nerves make improving regeneration imperative for the clinical use of MNIs. Previous animal models have shown increased inflammatory response to neural interfaces and the formation of benign but often painful neural tumours (neuromas) in the absence of a target organ [287, 288].

Strategies to improve neurocompatibility and neural regeneration within nerve guides include: tailored materials; coatings; scaffolds; topography; release of trophic factors or other signalling molecules; electrical cues; the inclusion of support cells or stem cells; and the development of anisotropically distributed cues [71, 76, 176–180].

For neural electrodes some strategies are unsuitable. MNIs must be made from a flexible insulator, which interfaces with electronic components; suitable materials are medical grade silicones, polyimides and to a lesser extent fluorocarbon polymers [289], therefore materials choice is restricted. This study

will use silicone (Polydimethylsiloxane, PDMS).

Strategies, which lend themselves readily to application within microchannels are the use of coatings, trophic factors, electrical cues and cells. These factors could be isotropically or anisotropically distributed along the axis of regeneration (proximally to distally).

In healthy nerve there is intimate contact between nerve axons, Schwann cells and the endoneurial basement membrane (or Schwann cell basement membrane). Following nerve injury and Wallerian degeneration axons can regrow, guided by the remaining extracellular matrix (ECM) architecture, trophic factors and support cells [71]. It is this natural regeneration pathway that is restored by autografts [178]. Autografts do not contain active neurons or axons, but have active support cells and ECM arranged in the correct micro-environment for axonal regrowth. By making the micro-environment within microchannels similar to that of autografts neural regeneration may be improved.

This chapter will focus on a coating strategy for improving neural regeneration: mimicking the extracellular matrix of the peripheral nervous system.

3.1.1 Endoneurial Basement Membrane

Components of the endoneurial basement membrane (BM) have been shown to improve neurite outgrowth *in vitro*. In addition, ECM gel[1], a mixture of basement membrane proteins and proteoglycans, has been shown to promote neurite outgrowth [290–293]; however, ECM gel is poorly characterised and unlikely to be approved for human implantation [294–296]. This implies that a well-characterised, ECM gel-like, endoneurial basement membrane coating may improve neurite outgrowth *in vitro* and *in vivo*.

Basement membranes are primarily comprised of Collagen-IV (C-IV), Laminins (Ln), Perlecan, Heparan sulphate and Nidogens (Nid) [24, 297]. There are minor components that include fibulin and tenascins [297, 298]. Typical proportions in Engelbreth-Holm-Swarm tumor have been determined as 60% Ln, 30% C-IV, 6% Nid with other proteins present in smaller amounts [299, 300]. Ln expression in the endoneurial basement membrane is primarily the merosin form of Ln, Ln-2 ($\alpha 2\beta 1\gamma 1$) [297,301,302]. Other forms of Ln are expressed in the peripheral nervous system: for example, in the perineurium, Ln-9 ($\alpha 4\beta 2\gamma 1$) and Ln-11 ($\alpha 5\beta 2\gamma 1$); and at neuromuscular junctions Ln-4 ($\alpha 2\beta 2\gamma 1$), Ln-9, and Ln-11 [303]. The $\alpha 2$ chain Ln-2 and Ln-4 are readily extracted from placenta and may be more applicable to neural regeneration than the more commonly used Ln-1 ($\alpha 1\beta 1\gamma 1$) [179].

Recently Ln-2 derived peptides have shown promise *in vivo* and *in vitro* [203, 304]. However, Ln-2 dosing of nerve-derived scaffolds has not been shown to improve neurite outgrowth [305]. Other derived proteins are in regular use, for example RGD (arginyl glycyl aspartic acid), which provides adhesion sites for many integrins, has shown promise for neural regeneration [306, 307].

BM proteins self-assemble *in vitro* (see fig. 3.1) [211, 308–311]. C-IV and Ln form independent

[1] ECM gel is sourced from from Engelbreth-Holm-Swarm sarcoma in mice. It is sold commercially under the following names: Matrigel™ (BD Biosciences), Cultrex® (Trevigen), ECM gel (Sigma-Aldrich), and others.

sheet-like structures. In turn C-IV and Ln are connected by Nid [209] and perlecan [207]. This self-assembled structure may act to present binding domains to cells and therefore should be investigated for use as a coating for neural outgrowth.

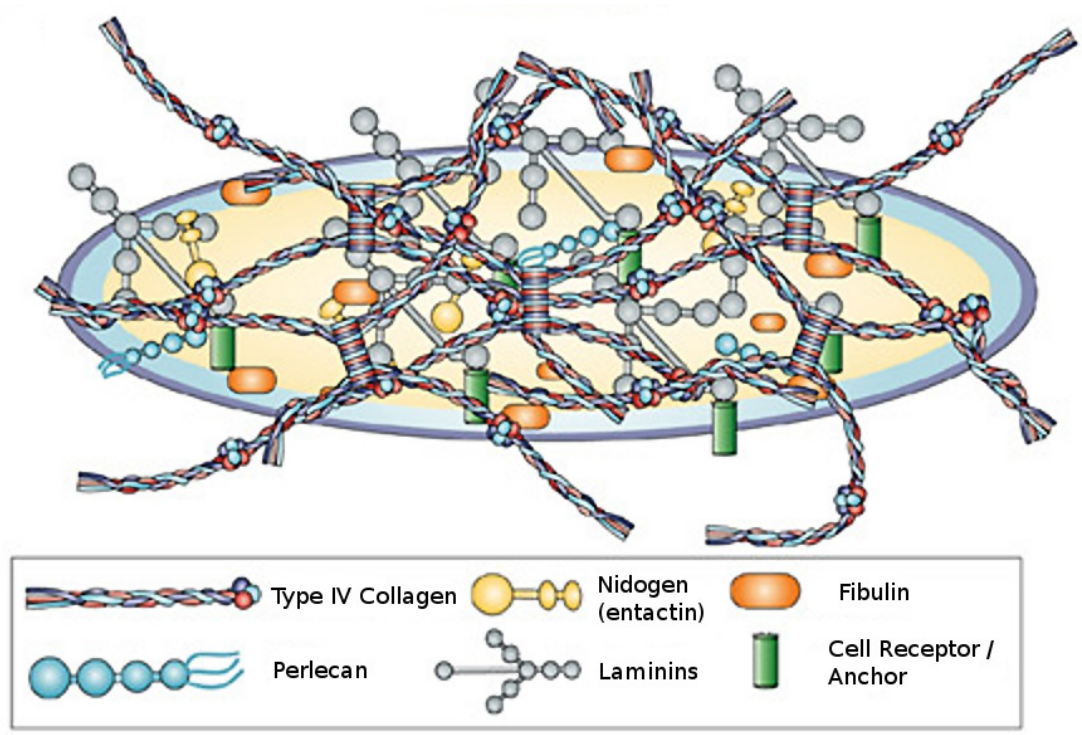

Figure 3.1: Structure of a typical basement membrane (BM). Laminin polymerises at the basolateral cell surface, anchored to cell receptors. Nidogens and perlecans form bridges between the laminin and a network of collagen type-IV. Reprinted by permission from Macmillan Publishers Ltd (Nature Publishing Group): Nature Reviews Cancer [207], ©2003.

3.1.2 Aims and Hypotheses

This chapter presents an *in vitro* study investigating the effect of adsorbed protein surface coatings on neurite outgrowth. The proteins that will be considered are: poly-D-lysine; C-IV; Ln-2,-4; Ln-1; Nid-1; fibronectin and poly-L-orthinine. Because basement membrane preparations are poorly characterised, application specific protein concentrations will be determined for each protein.

The aim of this study is to develop and test a coating that could be applied within a microchannel to improve neural regeneration. Therefore the coating method must be suitable for application within a small diameter ($<$200 μm) tube. In addition the coating should require as few steps to apply as possible.

The hypotheses for this chapter are as follows:

1. Endoneurial basement membrane protein coatings increase neurite outgrowth on silicone surfaces compared with poly-D-lysine (PDL) coated or uncoated controls.

2. Collagen-IV + Laminin + Nidogen multi-protein coatings increase neurite outgrowth on silicone surfaces compared with single protein coatings.

3. Multi-protein coating order does not significantly change neurite outgrowth on silicone surfaces.

4. Multi-protein coatings do not significantly change neurite outgrowth on silicone surfaces compared with ECM gel coatings.

3.2 Methodology

3.2.1 Preparation of Silicone Surfaces for *In Vitro* Assays

Silicone (Sylgard 184, Dow Corning, Midland, MI) was spin coated onto 25 mm $\times$ 75 mm glass slides using a WS-400BZ-6NPP-Lite spin coater (Laurell Technologies). Approximately 2 mL of uncured, 1:1 mixed, silicone was extruded onto the slide using a syringe. The slide was spun at the following speeds: 100 rpm for 20 s; 500 rpm for 30 s; 1000 rpm for 15 s. The coated slide was cured at between 50°C and 75°C for 12 hours.

Spin coated silicone surfaces were prepared for seeding. The samples were UV sterilised for 12 hours. Samples were divided into 1 cm^2 sections, supported on 19 mm diameter glass cover slips (VWR) and placed into 6-well plates. The samples were coated with protein as follows (see also table 3.1).

3.2.1.1 Poly-D-Lysine

Poly-D-lysine (PDL) was supplied as a lyophilized powder (30 kDa to 70 kDa molecular weight). This was allowed to come to room temperature. The PDL was reconstituted in sterile filtered sterile distilled water (SDW) to give a 0.1 mg/ml solution. The solution was separated into 1 ml aliquots and stored at -20°C.

For cell culture flasks 1ml of 0.1 mg/ml PDL solution is sufficient to coat 25 cm^2 (a coating density of 4 $\mu g/cm^2$). To coat a surface sufficient dilute PDL was allowed to come to room temperature (eg. 3 ml for 1 T-75 culture flask). The PDL solution was pipetted onto the surface and full coverage was ensured. The surface was incubated for 20 minutes at 36°C. The PDL solution was removed and the surface washed thoroughly with PBS three times. The surface was placed in an incubator for at least 2 hours to dry.

For silicone surfaces the dilution factor was altered to coat 1 cm^2 with a 150 μl droplet. The PDL solution was micropipetted onto the surface. The surface was incubated for 20 minutes at 36°C. The surface was washed thoroughly with PBS three times. The surface was placed in an incubator at 36°C for at least 2 hours to dry.

3.2.1.2 Collagen-IV

Collagen-IV was supplied as a lyophilized powder. C-IV was reconstituted in sterile PBS to give a 1 mg/ml solution. The solution was separated into 1 ml aliquots and stored at -20°C.

To coat a silicone surface sufficient dilute C-IV was allowed to come to room temperature to coat 1 cm^2 with a 150 μl droplet of the desired concentration. The C-IV solution was micropipetted onto the

surface. The surface was incubated for 1 hour at 36°C. The surface was washed thoroughly with PBS three times. The surface was placed in an incubator at 36°C for at least 2 hours to dry.

3.2.1.3 Laminin-2,-4

Ln-2,(-4) was supplied at a concentration of 0.5 mg/ml in 50 mM Tris-HCL with 150 mM NaCl. This was thawed slowly at 4°C to prevent gelling. Ln was reconstituted in cold (∼4°C) sterile PBS to give a 0.1 mg/ml solution. The solution was separated into 0.5 ml aliquots and stored at -20°C.

To coat a silicone surface sufficient dilute Ln was allowed to come to room temperature to coat 1 cm^2 with a 150 μl droplet of the desired concentration. The Ln solution was micropipetted onto the surface. The surface was incubated for 2 hours at 36°C. The surface was washed thoroughly with PBS three times. The surface was placed in an incubator at 36°C for at least 2 hours to dry.

3.2.1.4 Laminin-1

Ln-1 was supplied was supplied at a concentration of 1 mg/ml in 50 mM Tris-HCL with 150 mM NaCl. This was thawed slowly at 4°C to prevent gelling. The Ln-1 was reconstituted in cold (∼4°C) sterile PBS to give a 0.1 mg/ml solution. The solution was aliquoted into 0.5 ml aliquots and stored at -20°C.

To coat a silicone surface sufficient dilute Ln-1 was allowed to come to room temperature to coat 1 cm^2 with a 150 μl droplet of the desired concentration. The Ln-1 solution was micropipetted onto the surface. The surface was incubated for 2 hours at 36°C. The surface was washed thoroughly with PBS three times. The surface was placed in an incubator at 36°C for at least 2 hours to dry.

3.2.1.5 Nidogen-1

Nid-1 was supplied as a lyophilized powder. Nid-1 was reconstituted in sterile PBS to give a 0.1 mg/ml solution. The solution was separated into 0.1 ml aliquots and stored at -20°C.

To coat a silicone surface sufficient dilute Nid-1 was allowed to come to room temperature to coat 1 cm^2 with a 150 μl droplet of the desired concentration. The Nid-1 solution was micropipetted onto the surface. The surface was incubated for 1 hour at 36°C. The surface was washed thoroughly with PBS three times. The surface was placed in an incubator at 36°C for at least 2 hours to dry.

3.2.1.6 Fibronectin

Fibronectin (Fn) was supplied as a lyophilized powder. This was thawed slowly at 4°C. Fn was reconstituted in sterile PBS to give a 0.1 mg/ml solution. The solution was separated into 0.5 ml aliquots and stored at -20°C.

To coat a silicone surface sufficient dilute Fn was allowed to come to room temperature to coat 1 cm^2 with a 150 μl droplet of the desired concentration. The Fn solution was micropipetted onto the surface. The surface was incubated for 2 hours at 36°C. The surface was washed thoroughly with PBS three times. The surface was placed in an incubator at 36°C for at least 2 hours to dry.

3.2.1.7 ECM Gel

Growth-factor reduced ECM gel (E6909, Sigma-Aldrich) was supplied as a liquid at a concentration of 7 mg/mL to 9 mg/mL, a concentration of 8 mg/mL was assumed. The ECM gel was diluted in in sufficient phosphate buffered saline to coat 1 cm^2 with a 150 μl droplet of the desired concentration. The ECM gel solution was micropipetted onto the surface. The surface was incubated for 2 hours at 36°C. The surface was washed thoroughly with PBS three times. The surface was placed in an incubator at 36°C for at least 2 hours to dry.

3.2.1.8 Poly-L-Orthinine

Poly-L-Orthinine (PLO) was supplied as a lyophilized powder (30 kDa to 70 kDa molecular weight). This was allowed to come to room temperature. The PLO was reconstituted in sterile filtered SDW to give a 1 mg/ml solution. The solution was separated into 1ml aliquots and stored at -20°C.

To coat a silicone surface sufficient dilute PLO was allowed to come to room temperature to coat 1 cm^2 with a 150 μl droplet of the desired concentration. The PLO solution was micropipetted onto the surface and full coverage was ensured. The surface was incubated for 20 minutes at 36°C. The PLO solution was removed and the surface washed thoroughly with PBS three times. The surface was placed in an incubator at 36°C for at least 2 hours to dry.

Protein	**Source**	**Reconstituted in**	**Incubation time (minutes)**
Poly-D-Lysine	P7280, Sigma-Aldrich	Sterile Distilled Water	20
Poly-L-Orthinine	P3655, Sigma-Aldrich	Sterile Distilled Water	20
Collagen-IV	C5533, Sigma-Aldrich	Phosphate Buffered Saline Solution	60
Laminin-2,-4	L6274, Sigma-Aldrich	Phosphate Buffered Saline Solution	120
Laminin-1	L2020, Sigma-Aldrich	Phosphate Buffered Saline Solution	120
Nidogen-1	2570-ND, R&D Systems	Phosphate Buffered Saline Solution	60
Fibronectin	F2006, Sigma-Aldrich	Phosphate Buffered Saline Solution	120
ECM Gel	E6909, Sigma-Aldrich	Phosphate Buffered Saline Solution	120

Table 3.1: Protein sources, solvents and incubation conditions.

3.2.2 Protein Coating of Silicone Surfaces

3.2.2.1 Protein concentration optimisation

Firstly the optimal concentration of the chosen proteins was determined. Silicone surfaces were prepared and coated using the above procedures at the concentrations shown in table 3.2. The optimal concentrations determined are shown in table 3.2. Where an doubling (or greater) in protein concentration did not result in a significant increase in neurite outgrowth measures the lower concentration was considered optimal.

3.2.2.2 Laminin-2,(-4) and Laminin-1

Laminin-2,-4 was compared with Laminin-1 at the same concentration. The optimal concentration determined was used (1 μg/cm^2, see table 3.2).

3.2.2.3 Comparison of Optimal Concentrations

The optimal coating concentrations of PDL, Ln-2,-4, and C-IV were compared with a basement membrane mimicking surface coating.

To mimic basement membrane *in vitro* multi-protein surface coatings were used. Optimal concentrations determined with single-protein coatings were used (see table 3.2). Nid-1 coating concentration was determined using a 1:1 molar ratio of Ln-2,-4 to Nid-1 [210]. The molecular masses of Ln-1, Ln-2 and Ln-4 are highly similar (850 kDa) and the molecular mass of Nid-1 is known (150 kDa) [209]. Therefore a 1:1 molar ratio of Ln-2,-4 to Nid-1 will have a mass ratio of 1:0.176 (1:0.175 was used in this study).

To form a C-IV + Nid-1 + Ln-2,-4 layer-by-layer coating (CNL) surfaces were coated with the optimal C-IV coating concentration, washed and dried as described above. Surfaces were coated with Nid-1, washed and dried as described above. Finally, surfaces were coated with Ln-2,-4, washed and dried as described above.

3.2.2.4 Comparison of Multi-Protein Coatings: Experiment 1

Different methods for forming multi-protein coatings were evaluated and compared with CNL coatings and commercial standard ECM gel coatings as described above.

To form an alternative Ln-2,-4 + Nid-1 + C-IV layer-by-layer coating (LNC) surfaces were first coated with the optimal Ln-2,-4 coating concentration, washed and dried as described above, followed by Nid-1 and finally C-IV.

An all-in-one procedure was developed. C-IV, Nid-1 and Ln-2,-4 were diluted and mixed to give an optimal coating concentration of each protein in a single 150 μl droplet. The surface was incubated for 2 hours at 36°C. The surface was washed thoroughly with PBS three times. The surface was placed in an incubator at 36°C for at least 2 hours to dry.

	Surface Coating	Concentration(s) (μg/cm^2)	Abbreviation
Optimisation	Poly-D-Lysine	2, 4, 10, 20	PDL
	Poly-L-Orthinine	1, 5, 10, 20, 40	PLO
	Collagen-IV	1, 5, 10, 20, 40	C-IV
	Laminin-2,-4	0.1, 0.5, 1, 2, 5	Ln-2,-4
	Fibronectin	1, 2, 5	Fn
	Nidogen-1	0.5, 1, 2	Nid-1
Laminin-2,(-4) and Laminin-1	Laminin-2,-4	1	Ln-2,-4
	Laminin-1	1	Ln-1
Comparison of Optima	Poly-D-Lysine	10	PDL
	Collagen-IV	10	C-IV
	Laminin-2,-4	1	Ln-2,-4
	Nidogen-1	N/A	Nid-1
	Layer-by-Layer (Collagen-IV + Nidogen-1 + Laminin-2,-4)	10 + 0.175 + 1	CNL
	Uncoated	N/A	Uncoated
Comparison of Multi-Protein Coatings: Experiment 1	Layer-by-Layer (Collagen-IV + Nidogen-1 + Laminin-2,-4)	10 + 0.175 + 1	CNL
	Layer-by-Layer (Laminin-2,-4 + Nidogen-1 + Collagen-IV)	1 + 0.175 + 10	LNC
	All-in-One (Collagen-IV + Nidogen-1 + Laminin-2,-4)	10 + 0.175 + 1	All-in-One
	ECM Gel	11.175	ECM Gel
Comparison of Multi-Protein Coatings: Experiment 2	Layer-by-Layer (Collagen-IV + Laminin-2,-4)	10 + 1	CL
	Layer-by-Layer (Laminin-2,-4 + Collagen-IV)	1 + 10	LC
	All-in-One (Collagen-IV + Laminin-2,-4)	10 + 1	CL All-in-One
	All-in-One (Collagen-IV + Nidogen-1 + Laminin-2,-4)	10 + 0.175 + 1	All-in-One
	ECM Gel	11.175	ECM Gel
	Collagen-IV	10	C-IV

Table 3.2: Protein coating concentrations used for each experiment or group of experiments.

3.2.2.5 Comparison of Multi-Protein Coatings: Experiment 2

The effect of different constituents in the multi-protein coatings were evaluated. The all-in-one, ECM gel and 10 μg/cm^2 C-IV coatings were formed as described above. Coatings without Nid-1 were developed.

To form Ln-2,-4 + C-IV layer-by-layer coatings (LC) surfaces were first coated with the optimal

Ln-2,-4 coating concentration, washed and dried as described above, followed by C-IV.

To form C-IV + Ln-2,-4 layer-by-layer coatings (CL) surfaces were first coated with the optimal C-IV coating concentration, washed and dried as described above, followed by Ln-2,-4.

To form C-IV + Ln-2,-4 all-in-one coatings (CL all-in-one) C-IV and Ln-2,-4 were diluted and mixed to give an optimal coating concentration of each protein in a single 150 μl droplet. The surface was incubated for 2 hours at 36°C. The surface was washed thoroughly with PBS three times. The surface was placed in an incubator at 36°C for at least 2 hours to dry.

3.2.3 Analysis of Coating by Raman Microscopy

In addition to cell seeding surfaces, n=2 samples were prepared for additional analysis by freeze drying. Once dry, the samples were transferred to a Raman microscope for analysis. Spectrographs of surfaces with and without protein coatings were taken and analysed. Raman Microscopic images were taken using a Labram 300 (Horiba Jobin Yvon, at the UCL Eastman Dental Institute) with a HeNe (633 nm) laser. 100 spectra were captured for 2 seconds each and averaged.

3.2.4 Analysis of Coating by BCA Assay

Separate surfaces were prepared by dropping 50 μl PDMS into each well of a 98 well plate, giving a PDMS surface area of 0.31 cm^2. PDMS was prepared under particle free conditions and well plates were coated under aseptic conditions. Well plates were placed on a plate shaker for at least 12 hours at 37°C to ensure complete coating of the well surface. Wells were checked under an optical microscope, in all cases the well surface was completely covered with PDMS.

Surfaces were coated with proteins (n = 3) as above (table 3.2) using 100 μl droplets. Surfaces were washed 3 times with PBS. Washed PDMS surfaces were allowed to dry in an incubator at 36°C.

3.2.4.1 BCA Assay

Protein concentrations on surfaces were analysed using a micro BCA assay (bicinchoninic acid assay, Pierce Micro BCA Protein Assay Kit, Thermo Fisher Scientific Inc.) [312]. The BCA assay is a variation on the Lowry assay, and detects cuprous ions generated from a reaction of cupric ions with protein. Because the assay detects ions in solution, rather than the formation of a chromophore following reagent–protein binding, it is valid for the measurement of adsorbed or bound proteins [313].

A bovine serum albumin standard (BSA) curve was used. BSA was diluted in PBS to form concentrations from 0.001 mg/ml to 0.04 mg/ml. 100 μl droplets of protein were placed into PDMS coated well plates, the surfaces were not washed, surfaces were allowed to dry in an incubator.

150 μl BCA working reagent was added to each well including standards and blank reference. The well plate was sealed and placed on a plate shaker for 2 hours at 37°C.

The plate was allowed to cool and absorbance was measured at 562 nm using a NanoDrop1000 spectrophotometer (Thermo Scientific). Protein concentrations were calculated using the interpolation

lines given by the standard curve. Amount of protein per well plate, and therefore per cm^2 was calculated for each sample.

3.2.5 Cell Line

All *in vitro* assays were carried out using the PC-12 cell line (European Collection of Cell Cultures, Porton Down, UK (catalogue number: 88022401).

Within any single experiment cells from a single population (passage) were used to reduce experimental error. Previous studies have suggested that the line should be used before passages 6 to 10 to avoid senescence [198, 199, 314]. However, this was not feasible because the PC-12 cells were received at passage 7. Therefore the cells were used within 6 passages (passage $\leq$ 12).

Cells were culture expanded in 25 cm^2 cell culture flasks (Corning) coated with 4 $\mu g/cm^2$ Poly-D-Lysine (PDL). PDL was chosen as the cell adhesion coating for culture expansion because it interacts electrostatically with cell membranes, and therefore is unlikely to upregulate the expression of specific cell adhesion molecules [315].

The following cell culture media was used: RPMI 1640 (R8758, Sigma) + 10 mM HEPES Buffer + 1 mM Sodium Pyruvate + 1% penicillin-streptomycin + 10% Horse Serum + 5% Foetal Bovine Serum (FBS). Standard subculture technique was used: cells were detached using trypsin-EDTA (Gibco) and agitation, centrifuged to form a cell pellet, resuspended as a single-cell suspension using a small diameter needle and seeded onto 2 new PDL coated flasks.

Prior to seeding onto test surfaces cells were primed by culturing with NGF 7S (50 ng/mL) in complete media for at least 7 days. Priming with NGF enhances the rate of neurite outgrowth following seeding [316].

3.2.6 Cell Seeding

Cells were seeded at a rate of 5,000 cells per cm^2. Cells were detached from culture flasks using trypsin-EDTA and agitation, centrifuged to form a cell pellet and resuspended in media + 50 ng/mL NGF to give single-cell suspension at 50,000 cells/mL. Cells were dropped onto the silicone sample surface in a 100 μL droplet using a gilson pipette. Samples were place in an incubator at 37°C, 5% CO_2, for 1 hour to adhere to the sample surface. The samples were then flooded with 2 mL media + 50 ng/mL NGF and incubated for 96 hours with a single media change after 48 hours.

3.2.7 Neurite Outgrowth Assay

3.2.7.1 Scanning Electron Microscopy

After 96 hours incubation cells (n=6 samples) were prepared for scanning electron microscopy (SEM). Media was removed from each sample. 2 ml 2.5% gluteraldehyde fixative in 0.1M sodium cacodylate buffer (pH 7.4) was added to each sample. After 30 minutes the fixative was removed and the samples

Alcohol	Concentration (vol.% Alcohol in dH_2O)	Time (minutes)	Number of repeats
IMS	20	5	2
IMS	30	5	2
IMS	40	5	2
IMS	50	5	2
IMS	60	5	2
EtOH	90	5	2
EtOH	96	10	2
EtOH	100	15	2

Table 3.3: Alcohol series used for dehydration of cell monolayers on silicone sample. IMS = industrial methylated spirits. EtOH = Ethanol. Alcohol diluted in distilled water.

were washed in 0.1M sodium cacodylate buffer (pH 7.4). The samples were dehydrated in ascending alcohol series (see table 3.3). The samples were covered with a loose lid and air dried for at least 12 hours. The transition solvent hexamethyldisilazane caused the silicone samples to swell and curl, damaging or detaching the cell layer, therefore no transition solvent was used.

Dry samples were mounted onto aluminium stubs using double sided carbon tape. Samples were sputter coated with Au/Pd for 2.5 minutes at 20 mA using an Emitech K550 sputter coater. Conductive paint was used to create a conductive bridge between the sample and the aluminium stub. Prepared samples were image under a scanning electron microscope at 15 keV and 20 keV (JEOL JSM 5500 LV, JEOL, Welwyn Garden City, UK). 6 images were taken of each sample at 400× magnification. Images were taken approximately equidistantly across the sample surface. In addition representative images were taken at 40×, 100× and 200×.

3.2.7.2 Immunoflourescence Microscopy

To visualise the actin cytoskeleton immunflourescent staining was used. This allowed confirmation that the processes observed under SEM are cellular and not image artefact.

After 96 hours incubation cells (n=1 samples) were prepared for fluorescence microscopy. Media was removed from each sample. 2 ml 4% formalin in phosphate buffered saline was added to each sample. After 30 minutes the fixative was removed and the samples were washed in PBS. Cells were permeabilised using 0.1% Triton-X (Sigma-Aldrich) in PBS for 15 minutes. Samples were washed 3 times with PBS and 1% phalloidin-FITC was added to each sample. Samples were incubated at room temperature for 1 hour. Samples were washed 3 times with PBS and stained with 0.1% Hoechst 33258 (Sigma-Aldrich) in PBS for 15 minutes. Samples were washed and stored under PBS prior to imaging.

Samples were imaged using an Axioskop 2 Plus light microscope (Zeiss) with FITC and DAPI filters and images were recorded using Axiovision software (Zeiss).

3.2.7.3 Neurite Length and Number

Neurite length and Neurite number were determined from 400x electron micrographs using ImageJ software (version 1.46r to version 1.49m, NIH, USA) [317, 318]. Linear extensions from the cell were measured for all cells exhibiting extensions fully within the field of view. Extensions were considered neurites when they extended at least 1 cell diameter from the cell edge. The number of neurites per cell exhibiting neurites was recorded.

3.2.8 Data Analysis

Analysis of neurite number and neurite length was carried out using SPSS 21.0, Mac and Linux versions (SPSS Inc., IBM, Chicago, IL). Data were tested for normality using the Kolmogorov-Smirnov test. Data were not found to be normally distributed, therefore non-parametric statistical analyses were performed.

For each experiment neurite number and neurite length for all groups were compared using the Kruskal-Wallis one-way analysis of variance test. If a significant difference was observed pair-wise Mann-Whitney U tests were performed to identify differences between groups. If no significant difference was found using the Kruskal-Wallis test the p-value was reported and no further statistical tests were carried out. Differences were considered significant at the $\alpha \leq 0.05$ level.

Pair-wise tests were corrected for multiple comparisons using Holm-Bonferroni correction [319]. This is intended to reduce the likelihood of type I errors.

3.3 Results

Data are reported as mean $\pm$ standard deviation to 3 significant figures unless otherwise stated. Neurite outgrowth data are plotted as median, interquartile range and inner fences (1.5 times interquartile range). Where data are highly skewed a log scale is used. p-values are tabulated in the appendix.

3.3.1 Raman Microscopy

All results for the Raman microscopy showed the PDMS spectrum predominating (example fig. 3.2). No protein signatures were visible due to the relative thickness of the PDMS and protein layers. Even with the normalisation for the PDMS spectrum protein signatures were not observed.

3.3.2 BCA Assay

Comparisons between protein types may not be valid due to the differing reaction characteristics for each protein. In addition statistical comparisons were not made due to the low number of measurements for each group (n = 3).

The results demonstrate that for increasing protein concentration applied, concentration on the PDMS surface increases for C-IV, Fn and Ln-2,-4. For PDL and PLO this trend was not observed. Nid-1 was tested at one concentration due to cost constraints and showed the least consistent readings across n = 3 samples. The trend fitted well to a linear model for C-IV (R^2 = 0.917) and Fn (R^2 = 0.948).

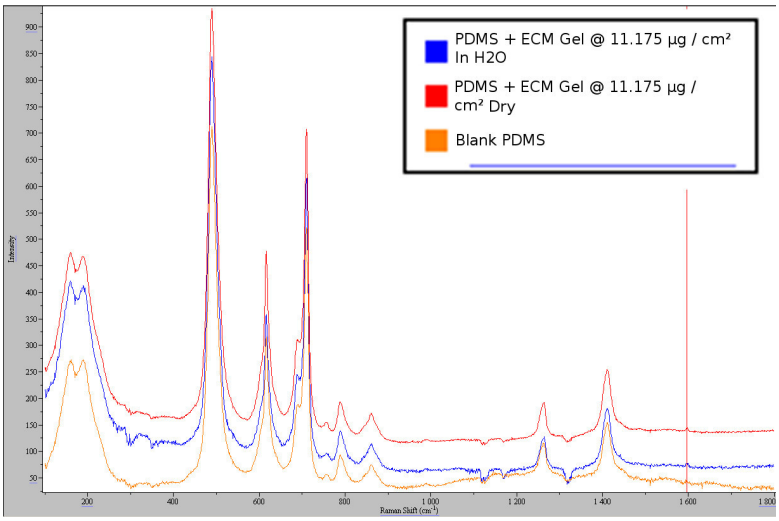

Figure 3.2: Raman Microscope Spectra of protein coated and uncoated PDMS surfaces. Averages of 100 x 2 second spectra. Observable spectra are for coated and uncoated PDMS.

For Ln-2,-4 a logarithmic model fitted the data more closely (R^2(linear) = 0.885, R^2(log) = 0.933). For Ln-2,-4 with an applied concentration $\leq$ 2 μg/cm^2 a linear model fitted the data more closely (R^2(linear) = 0.975, R^2(log) = 0.908).

There was no consistent trend with coating order for multi-protein coatings. LNC layer-by-layer coatings had a lower concentration than CNL layer-by-layer coatings, however LC layer-by-layer coatings had a higher concentration than CL layer-by-layer coatings.

3.3.3 Protein Concentration Optimisation

3.3.3.1 Poly-D-Lysine Concentration

PC-12 cells adhered to PDL coated surfaces. The cells also extended neurites. Results are plotted in figs. 3.4a and 3.4b. The optimum concentration of PDL observed was 10 μg/cm^2.

The number of neurites per cell was greatest on surfaces coated with 10 μg/cm^2 PDL (1.79 $\pm$ 1.36 neurites). Fewer neurites per cell were observed on surfaces coated with 20 μg/cm^2 (1.71 $\pm$ 1.12 neurites), 4 μg/cm^2 (1.34 $\pm$ 0.55 neurites) and 2 μg/cm^2 (1.28 $\pm$ 0.60 neurites) of PDL. None of the differences observed were statistically significant (Kruskal-Wallis p value = 0.078).

Cells extended the longest neurites on surfaces coated with 10 μg/cm^2 PDL (59.1 $\pm$ 42.2 μm). Significantly shorter neurites were observed on surfaces coated with 20 μg/cm^2 (22.8 $\pm$ 9.43 μm, p $\leq$ 0.001) and 2 μg/cm^2 (32.2 $\pm$ 23.6 μm, p = 0.002). PC-12 cells on surfaces coated with 4 μg/cm^2 extended shorter neurites (36.2 $\pm$ 23.6 μm), however this was not significantly different to the neurite length on surfaces coated with 10 μg/cm^2 PDL (p = 0.093). No other significant differences were observed (p $\geq$ 0.019, p_{cut} = 0.016).

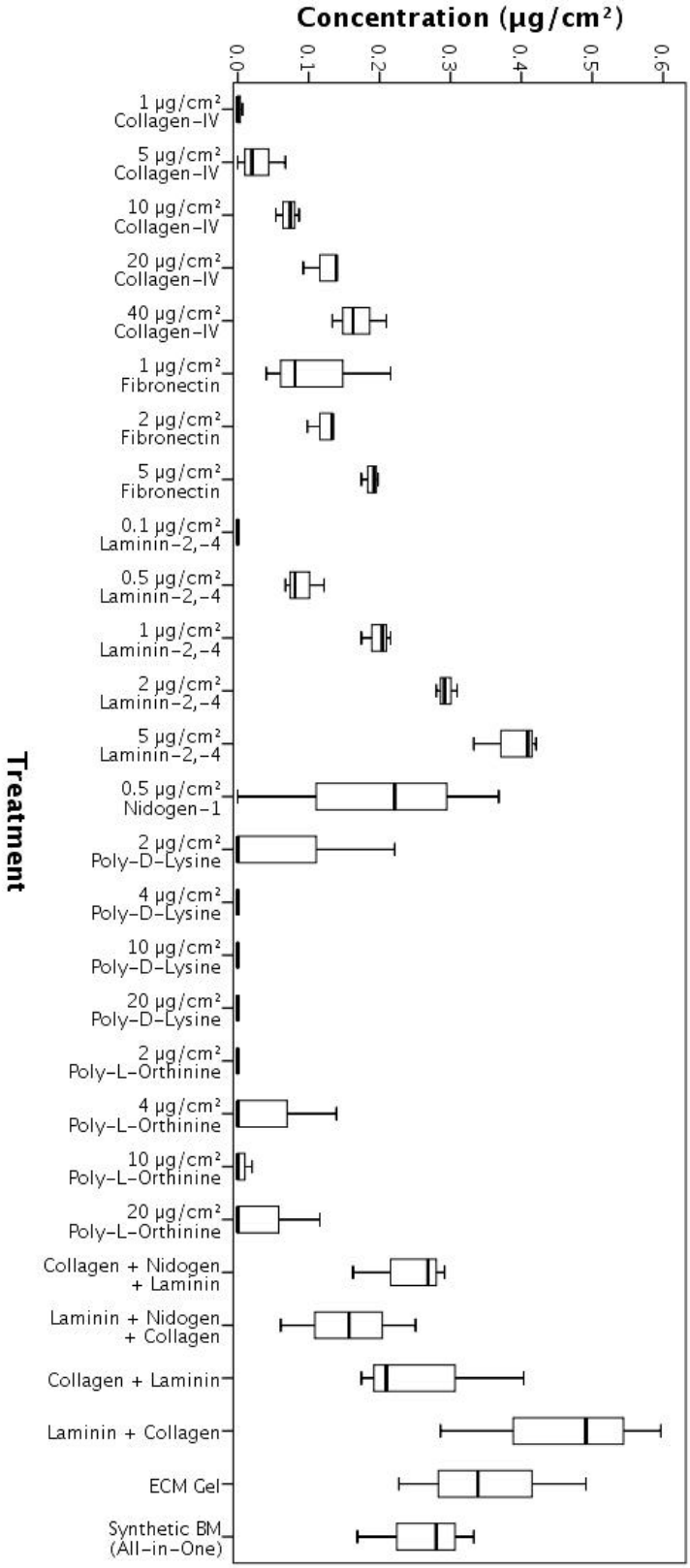

Figure 3.3: Concentration of proteins on PDMS following 3 PBS washes. Determined using a micro BCA assay (n=3).

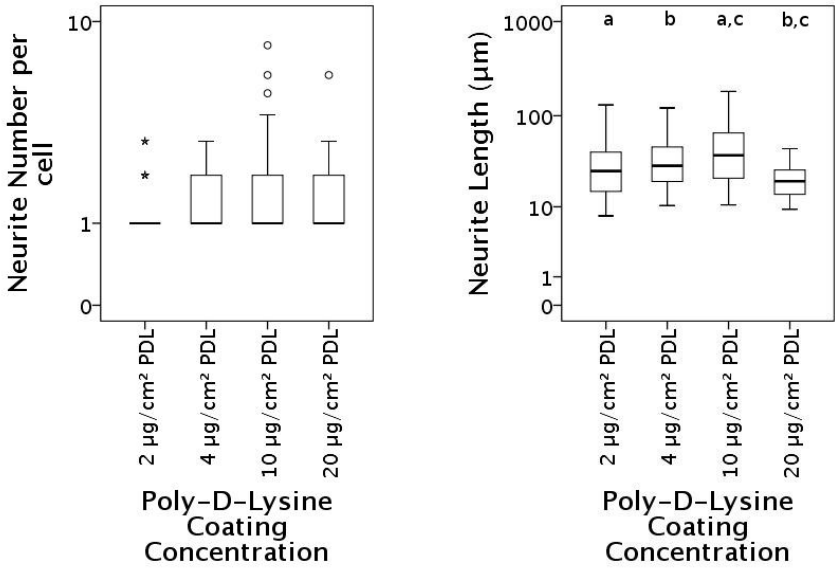

(a) PC-12 cell neurite number on Poly-D-Lysine coated samples. Data displayed on a logarithmic scale. Differences not significant, p = 0.078.

(b) PC-12 cell neurite length on Poly-D-Lysine coated samples. Data displayed on a logarithmic scale. Significant differences are indicated by paired letters: a, p = 0.002; b, p = 0.001; c, p <0.001.

Figure 3.4: PC-12 cell neurite outgrowth data for silicone samples coated with Poly-D-Lysine at the following concentrations: 20 μg/cm^2; 10 μg/cm^2; 4 μg/cm^2; 2 μg/cm^2.

3.3.3.2 Poly-L-Orthinine Concentration

PC-12 cells adhered well to PLO coated surfaces, however the coating was non-uniform, with large areas of the surface showing low cell attachment, while cells attached in small areas, typically forming a striped pattern. Cells did extend neurites that could be measured, however the coating was inconsistent therefore PLO was discounted and no measurements were made.

3.3.3.3 Collagen IV Concentration

PC-12 cells adhered to C-IV coated surfaces and extended measurable neurites at every concentration tested. Two experiments were carried out to determine the optimal C-IV concentration: the first experiment used 10, 5 and 1 μg/cm^2 C-IV, the results did not appear to plateau within this range therefore the concentrations were extended. The second experiment used 40, 20 and 10 μg/cm^2 C-IV, a plateau was found within this range therefore no further experiments were needed. The optimum concentration of C-IV observed was 10 μg/cm^2.

Collagen IV Concentration: Experiment 1 Results are plotted in figs. 3.5a and 3.5b. No significant difference in neurite number was observed between the samples tested (Kruskal-Wallis p value = 0.217). A maximum number of neurites was observed on surfaces coated with 5 μg/cm^2 C-IV (2.48 $\pm$ 1.39 neurites). Fewer neurites were observed on surfaces coated with 10 μg/cm^2 C-IV (2.31 $\pm$ 1.16 neurites) and 1 μg/cm^2 C-IV (2.20 $\pm$ 1.17 neurites).

Significantly longer neurites were observed on surfaces coated with 10 μg/cm^2 C-IV compared with all other samples (41.7 $\pm$ 30.4 μm, p $<$0.002). Neurites were significantly longer on surfaces coated with 5 μg/cm^2 C-IV (35.5 $\pm$ 26.6 μm) than on surfaces coated with 1 μg/cm^2 C-IV (19.8 $\pm$ 13.5 μm, p $<$0.001).

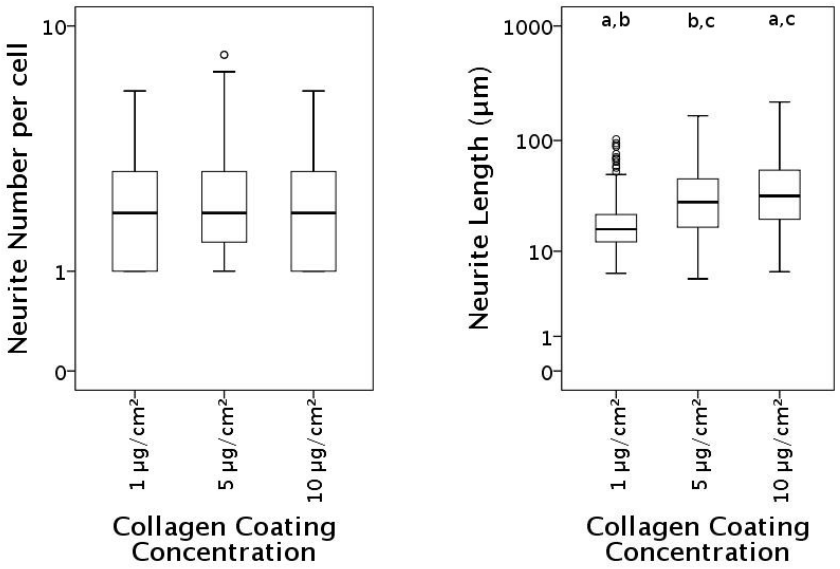

(a) PC-12 cell neurite number on Collagen-IV coated samples. Data displayed on a logarithmic scale. Differences not significant, p = 0.217.

(b) PC-12 cell neurite length on Collagen-IV coated samples. Data displayed on a logarithmic scale. Significant differences are indicated by paired letters: a, p $<$0.001; b, p = 0.001; c, p $<$0.001.

Figure 3.5: PC-12 cell neurite outgrowth data for silicone samples coated with Collagen-IV at the following concentrations: 10 μg/cm^2; 5 μg/cm^2; 1 μg/cm^2.

Collagen IV Concentration: Experiment 2 No significant differences in neurite number (Kruskal-Wallis p value = 0.942) or neurite length (Kruskal-Wallis p value = 0.063) were observed. The results are plotted in figs. 3.6a and 3.6b. Cells expressed the most neurites on surfaces coated with 10 μg/cm^2 C-IV (3.48 $\pm$ 1.74 neurites). Fewer neurites per cell were observed on surfaces with 20 μg/cm^2 C-IV (3.38 $\pm$ 1.88 neurites) and 40 μg/cm^2 C-IV (3.01 $\pm$ 1.81 neurites).

The longest neurites were on surfaces coated with 10 μg/cm^2 C-IV (48.5 $\pm$ 33.7 μm). Neurites were shorter on surfaces with 20 μg/cm^2 C-IV (45.2 $\pm$ 31.9 neurites) and 40 μg/cm^2 C-IV (43.0 $\pm$ 31.8 neurites).

3.3.3.4 Laminin-2 (-4) Concentration

PC-12 cells adhered to Ln-2,-4 coated surfaces and extended measurable neurites on some of the tested coating concentrations. Two experiments were carried out to determine the optimal Ln-2,-4 concentration: the first experiment used 0.1, 0.5 and 1 μg/cm^2 Ln-2,-4, the results did not appear to plateau within this range therefore the concentrations were extended. The second experiment used 1, 2 and 5

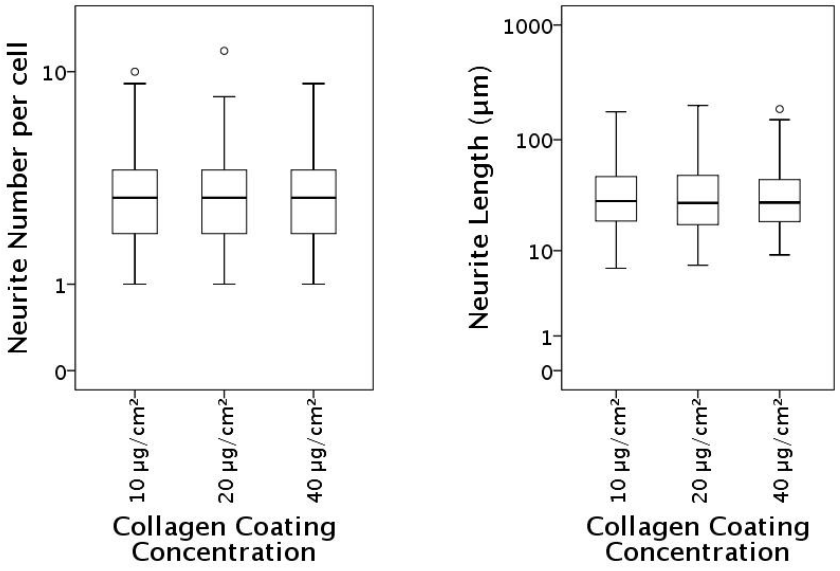

(a) PC-12 cell neurite number on Collagen-IV coated samples. Data displayed on a logarithmic scale. Differences not significant, p = 0.942.

(b) PC-12 cell neurite length on Collagen-IV coated samples. Data displayed on a logarithmic scale. Differences not significant, p = 0.063.

Figure 3.6: PC-12 cell neurite outgrowth data for silicone samples coated with Collagen-IV at the following concentrations: 40 μg/cm^2; 20 μg/cm^2; 10 μg/cm^2.

μg/cm^2 Ln-2,-4, a plateau was found within this range therefore no further experiments were needed. The optimum concentration of Ln-2,-4 observed was 1 μg/cm^2.

Laminin-2 (-4) Concentration: Experiment 1 No cells with neurites were observed on surfaces coated with 0.1 μg/cm^2 Ln-2,-4, therefore these surfaces were not included in the statistical comparisons. The observed data are plotted in figs. 3.7a and 3.7b.

Significantly more neurites per cell were observed on surfaces coated with 1 μg/cm^2 Ln-2,-4 (2.73 $\pm$ 1.73 neurites) compared with surfaces coated with 0.5 μg/cm^2 Ln-2,-4 (1.90 $\pm$ 1.27 neurites, p = 0.0264). Neurites were also longer on surfaces coated with 1 μg/cm^2 Ln-2,-4 (36.4 $\pm$ 28.5 μm) compared with surfaces coated with 0.5 μg/cm^2 Ln-2,-4 (21.6 $\pm$ 10.8 μm, p = 0.0037).

Laminin-2 (-4) Concentration: Experiment 2 The results are plotted in figs. 3.8a and 3.8b. No significant difference in number of neurites per cell was observed between the concentrations tested (Kruskal-Wallis p value = 0.388). The most neurites per PC-12 cell were observed on surfaces coated with 2 μg/cm^2 Ln-2,-4 (3.27 $\pm$ 1.82 neurites). Fewer neurites per cell were observed on surfaces coated with 1 μg/cm^2 Ln-2,-4 (3.17 $\pm$ 1.80 neurites) and 5 μg/cm^2 Ln-2,-4 (3.10 $\pm$ 1.89 neurites).

Neurites were significantly longer on surfaces coated with 1 μg/cm^2 Ln-2,-4 (26.3 $\pm$ 21.8 μm) compared with all other samples (p $<$0.007). Neurite length was not significantly different between surfaces coated with 2 μg/cm^2 Ln-2,-4 (24.3 $\pm$ 21.2 μm) and 5 μg/cm^2 Ln-2,-4 (22.1 $\pm$ 17.4 μm, p = 0.166).

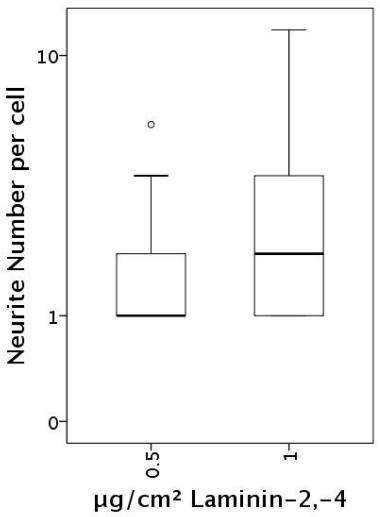

(a) PC-12 cell neurite number on Laminin-2,-4 coated samples. Data displayed on a logarithmic scale. The difference is significant, p = 0.0264.

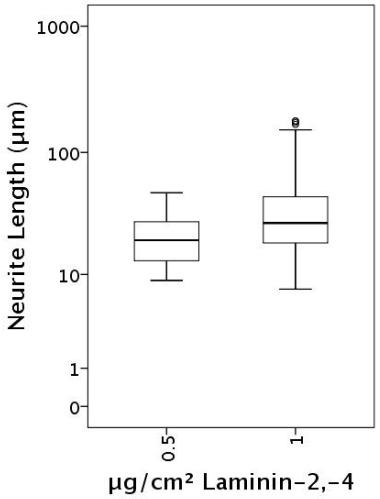

(b) PC-12 cell neurite length on Laminin-2,-4 coated samples. Data displayed on a logarithmic scale. The difference is significant, p = 0.0037.

Figure 3.7: PC-12 cell neurite outgrowth data for silicone samples coated with Laminin-2,-4 at the following concentrations: 0.5 μg/cm^2; 1 μg/cm^2.

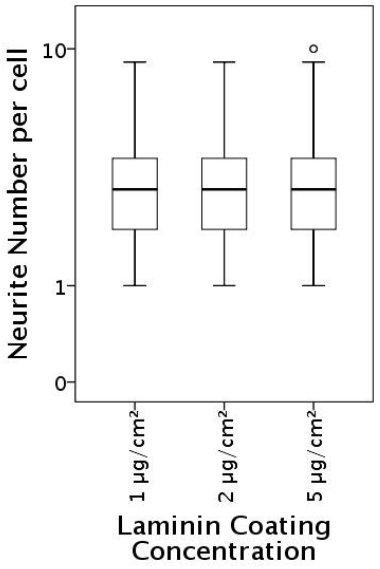

(a) PC-12 cell neurite number on Laminin-2,-4 coated samples. Data displayed on a logarithmic scale. Differences not significant, p = 0.388.

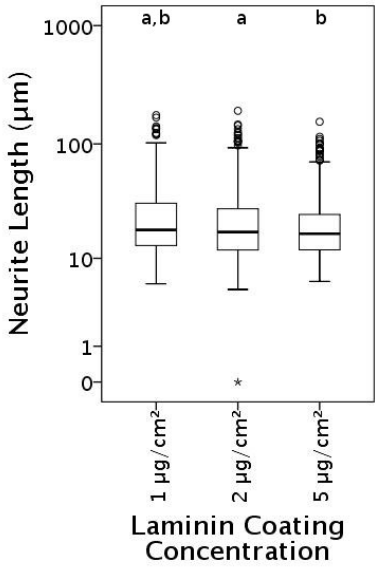

(b) PC-12 cell neurite length on Laminin-2,-4 coated samples. Data displayed on a logarithmic scale. Significant differences are indicated by paired letters: a, p = 0.006; b, p $<$0.001.

Figure 3.8: PC-12 cell neurite outgrowth data for silicone samples coated with Laminin-2,-4 at the following concentrations: 1 μg/cm^2; 2 μg/cm^2; 5 μg/cm^2.

3.3.3.5 Fibronectin Concentration

PC-12 cells adhered to surfaces coated with Fn in the range tested, however neurite outgrowth was not observed therefore an optimum concentration could not be determined. Fn was not used in subsequent

experiments.

3.3.3.6 Nidogen-1 Concentration

Few PC-12 cells adhered to Nid-1 coated surfaces at the concentrations tested, the numbers were not sufficient to quantify neurite outgrowth. Therefore, Nid-1 single protein coatings were not used in subsequent experiments. An optimal coating concentration was calculated using a 1:1 molar ratio of Nid-1:Ln-2,-4.

3.3.4 Laminin-2,(-4) and Laminin-1

Laminin-2,(-4) was compared with Laminin-1 at 1 μg/cm^2. No differences in neurite number (p = 0.0554) or neurite length (p = 0.4396) were observed between the samples. The results are plotted in figs. 3.9a and 3.9b. More neurites per cell were observed on Ln-1 coated surfaces (2.95 $\pm$ 1.81 neurites) compared with Ln-2,-4 coated surfaces (2.42 $\pm$ 1.41 neurites). However, the neurites were longer on Ln-2,-4 coated surfaces (58.7 $\pm$ 36.6 μm) than on Ln-1 coated surfaces (53.5 $\pm$ 29.4 μm).

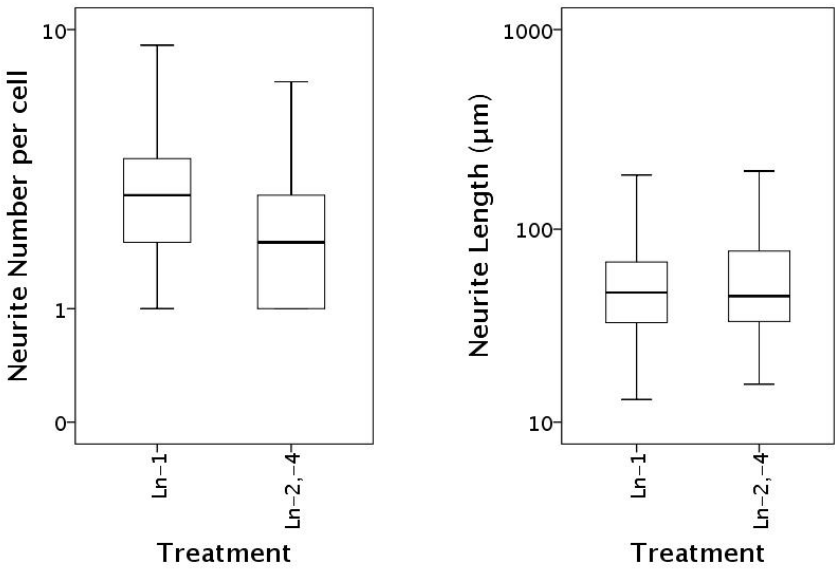

(a) PC-12 cell neurite number on Laminin-2,-4 and Laminin-1 coated samples. Data displayed on a logarithmic scale. The difference is not significant, p = 0.0554.

(b) PC-12 cell neurite length on Laminin-2,-4 and Laminin-1 coated samples. Data displayed on a logarithmic scale. The difference is not significant, p = 0.4396.

Figure 3.9: PC-12 cell neurite outgrowth data for silicone samples coated with 1 μg/cm^2 Laminin-2,-4 compared with 1 μg/cm^2 Laminin-1.

3.3.5 Comparison of Optimal Concentrations

PC-12 cells adhered to surfaces and extended measurable neurites with every coating tested. The results are plotted in figs. 3.10a and 3.10b.

The greatest number of neurites per cell was on layered CNL coating (5.77 $\pm$ 3.30 neurites), this was significantly greater than all other samples (p $<$0.003). No significant difference in neurites per cell

was observed between C-IV (4.34 $\pm$ 2.96 neurites) and Ln-2,-4 (3.65 $\pm$ 1.73 neurites) coated surfaces (p = 0.225). PC-12 cells on PDL coated surfaces exhibited a significantly lower number of neurites per cell (2.14 $\pm$ 0.889 neurites) compared with all other sample (p <0.001).

Neurite length was significantly increased on C-IV coated surfaces (49.3 $\pm$ 35.3 μm) compared with all other sample (p <0.004). PC-12 cells on layered CNL coatings exhibited significantly longer neurites (45.5 $\pm$ 36.6 μm) than cells on Ln-2,-4 (35.8 $\pm$ 26.3 μm, p <0.002) and PDL (25.6 $\pm$ 15.6 μm, p <0.001) coated surfaces. Ln-2,-4 coated surfaces increased neurite length compared with PDL controls (p <0.005).

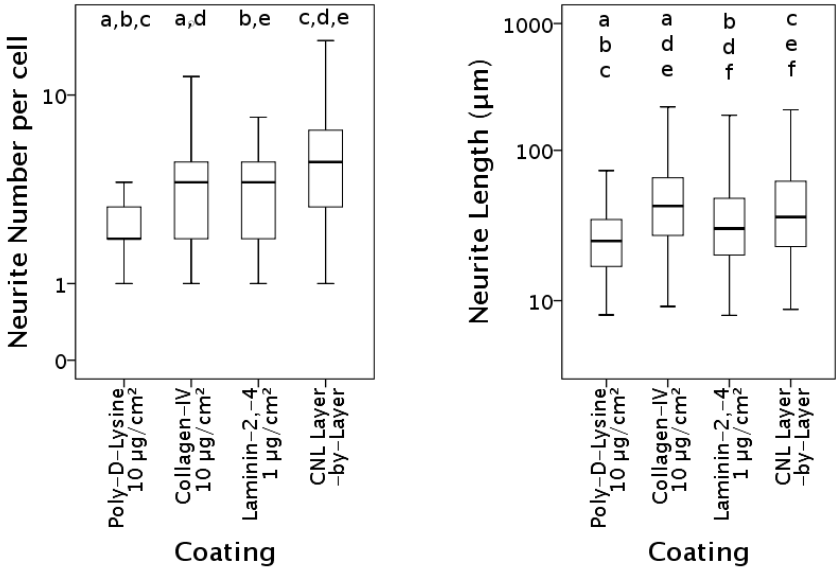

(a) PC-12 cell neurite number per cell. Data are displayed on a log scale. Significant differences are indicated by paired letters: a,b,c,e, p <0.001; d, p = 0.002.

(b) PC-12 cell neurite length. Data are displayed on a log scale. Significant differences are indicated by paired letters: a,c,d, p <0.001; b, p = 0.004; e, p = 0.003; f, p = 0.001.

Figure 3.10: PC-12 cell neurite length and neurite number per cell on protein coated silicone surfaces. CNL Layer-by-Layer is a layered coating of 10 μg/cm^2 collagen-IV + 0.175 μg/cm^2 nidogen-1 + 1 μg/cm^2 laminin-2,-4.

3.3.6 Comparison of Multi-Protein Coatings: Experiment 1

PC-12 cells adhered to surfaces and extended measurable neurites with every coating tested. Results are plotted in figs. 3.11a and 3.11b

Number of neurites per cell was not significantly different between CNL (3.55 $\pm$ 2.67 neurites), ECM gel (3.49 $\pm$ 2.40 neurites), and all-in-one (3.36 $\pm$ 2.07 neurites) coated samples (p $\geq$ 0.843). Significantly fewer neurites per PC-12 cell were observed on LNC coated samples (2.89 $\pm$ 1.80 neurites, p <0.018).

The longest neurites were observed on CNL (28.7 $\pm$ 23.5 μm) coated samples, and neurite lengths on ECM gel (28.6 $\pm$ 26.6 μm) and all-in-one (27.7 $\pm$ 24.2 μm) coated samples were not significantly

lower ($p \geq 0.090$). Significantly shorter neurites were observed on LNC coated samples (23.0 $\pm$ 19.6 μm, $p < 0.001$) compared with all other samples.

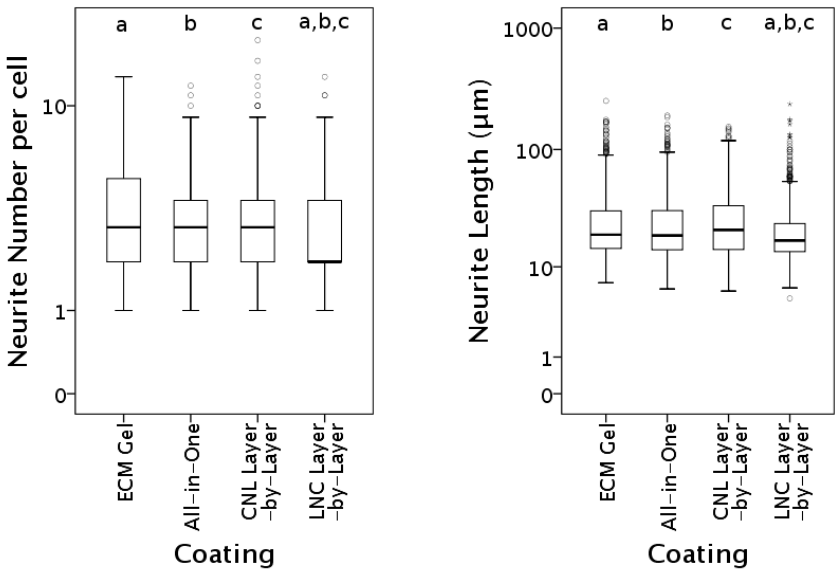

(a) PC-12 cell neurite number per cell. Data are displayed on a log scale. Significant differences are indicated by paired letters: a, p = 0.010; b, p = 0.016; c, p = 0.018.

(b) PC-12 cell neurite length. Data are displayed on a log scale. Significant differences are indicated by paired letters: a,b,c, p $<$0.001.

Figure 3.11: PC-12 cell neurite length and neurite number per cell on protein coated silicone surfaces. ECM Gel is a coating of 11.175 μg/cm^2 ECM Gel (Sigma Aldrich). All-in-One is a mixed coating of 10 μg/cm^2 collagen-IV + 0.175 μg/cm^2 nidogen-1 + 1 μg/cm^2 laminin-2,-4. CNL Layer-by-Layer is a layered coating of 10 μg/cm^2 collagen-IV + 0.175 μg/cm^2 nidogen-1 + 1 μg/cm^2 laminin-2,-4. LNC Layer-by-Layer is a layered coating of 1 μg/cm^2 laminin-2,-4 + 0.175 μg/cm^2 nidogen-1 + 10 μg/cm^2 collagen-IV.

3.3.7 Comparison of Multi-Protein Coatings: Experiment 2

PC-12 cells adhered to surfaces and extended measurable neurites with every coating tested. Results are plotted in figs. 3.12a and 3.12b

Significantly fewer neurites per PC-12 cell were observed on LC layer-by-layer coated surfaces (2.79 $\pm$ 2.23 neurites) compared with ECM gel (3.51 $\pm$ 2.07 neurites, p = 0.0001) and all-in-one (3.49 $\pm$ 2.29 neurites, p = 0.0009) coated surfaces. No other significant differences were observed ($p \geq 0.011$, p_{cut} = 0.004). Neurite number per cell was intermediate on CL layer-by-layer (3.33 $\pm$ 2.35 neurites), CL all-in-one (3.09 $\pm$ 2.40 neurites) and C-IV (3.20 $\pm$ 2.25 neurites) coated surfaces.

The longest neurites were observed on all-in-one coated surfaces (49.3 $\pm$ 30.5 μm), this was significantly longer than on LC layer-by-layer (40.0 $\pm$ 27.1 μm, $p < 0.001$) and CL layer-by layer (43.4 $\pm$ 29.0 μm, $p < 0.001$) coated surfaces. No other significant differences were observed ($p \geq 0.019$, p_{cut} = 0.004). The averages of neurite length on different coatings were: ECM gel (47.3 $\pm$ 34.9 μm), C-IV (45.5 $\pm$ 33.1 μm), and CL all-in-one (44.2 $\pm$ 31.9 μm).

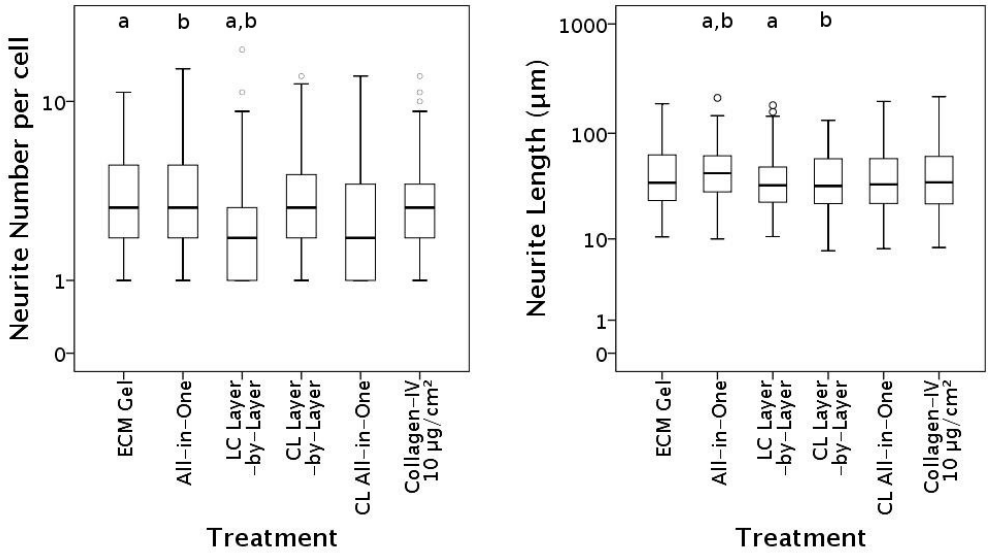

(a) PC-12 cell neurite number per cell. Data are displayed on a log scale. Significant differences are indicated by paired letters: a,b, $p < 0.001$.

(b) PC-12 cell neurite length. Data are displayed on a log scale. Significant differences are indicated by paired letters: a,b, $p < 0.001$.

Figure 3.12: PC-12 cell neurite length and neurite number per cell on protein coated silicone surfaces. ECM Gel is a coating of 11.175 μg/cm^2 ECM Gel (Sigma Aldrich). All-in-One is a mixed coating of 10 μg/cm^2 collagen-IV + 0.175 μg/cm^2 nidogen-1 + 1 μg/cm^2 laminin-2,-4. CL Layer-by-Layer is a layered coating of 10 μg/cm^2 collagen-IV + 1 μg/cm^2 laminin-2,-4. LC Layer-by-Layer is a layered coating of 1 μg/cm^2 laminin-2,-4 + 10 μg/cm^2 collagen-IV. CL All-in-One is a mixed coating of 10 μg/cm^2 collagen-IV + 1 μg/cm^2 laminin-2,-4.

3.3.8 Cell Morphology

Cell morphology varied between surfaces and between cells, representative images are presented in figs. 3.13 and 3.14. Cells did not adhere to uncoated surfaces and very few cells adhered to Nid-1 coated surfaces (figs. 3.13a and 3.13b), and while cells adhered to Fn coated surfaces, cell seeding was uneven and there was no evidence of cell soma spreading (fig. 3.13g). Soma spreading, neurite extension, network formation, uniform cell distribution, and a high proportion of cells exhibiting neuronal phenotype were considered indicators of surface neurocompatibility.

PC-12 cells on PDL adhered and a low proportion of cells exhibited neuronal phenotype (fig. 3.13e), there was little evidence of network formation between neurites. In contrast on Ln-2,-4, C-IV, and PLO coated surfaces the majority of the cells exhibited neurites and highly branched networks formed (figs. 3.13c, 3.13d and 3.13f). In addition, some PC-12 cells on Ln-2,-4 and C-IV coated surfaces exhibited spreading of the cell soma and increased contact with the surface. On PLO coated surfaces cells formed striped or string like patterns in small areas of the substrate, while there was low cell adhesion in most areas, this limited network formation and caused elongated soma and cell polarisation (fig. 3.13f).

PC-12 cell morphology is similar between ECM gel, all-in-one, CL, CL all-in-one and CNL coated samples (figs. 3.14a to 3.14c, 3.14e and 3.14g). Branched neurite networks form and cell soma exhibited

spreading. However, a lower proportion of cells exhibited a neuronal phenotype on LNC samples, and less branching, network forming and soma spreading was observed (fig. 3.14d). On LC coated samples soma spreading, neurite branching and network formation was observed, however neurites appeared shorter (fig. 3.14f).

Immunoflourescence microscopy demonstrated a similar cell morphology, with neurites forming branched networks on C-IV and all-in-one coated surfaces (example images are given in the following chapter, see figs. 4.24a and 4.24b). This confirmed that the observed processes are part of the cells and contain actin cytoskeletons. In all other respects the immunoflourescence microscopy confirmed the results from the SEM images, however the depth of focus was less and image quality was lower. SEM images were used for analysis and are reported.

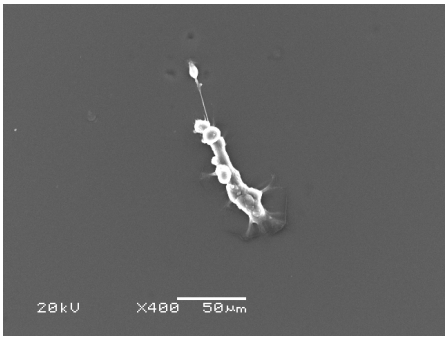

(a) 2 μg/cm^2 Nidogen-1.

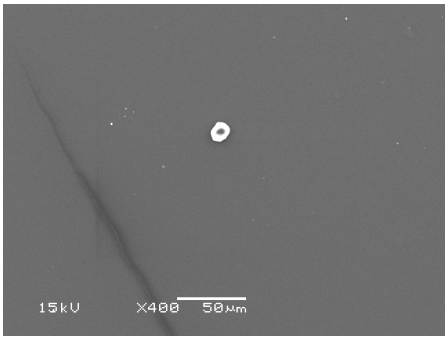

(b) Uncoated Silicone.

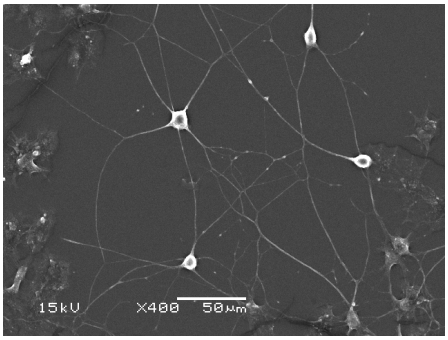

(c) 10 μg/cm^2 Collagen-IV.

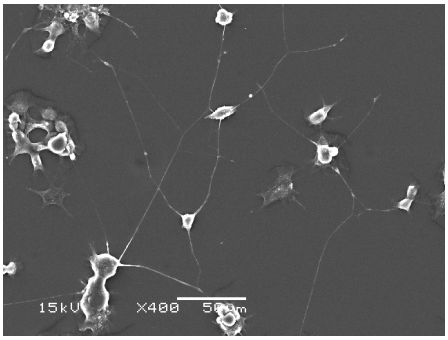

(d) 1 μg/cm^2 Laminin-2,-4.

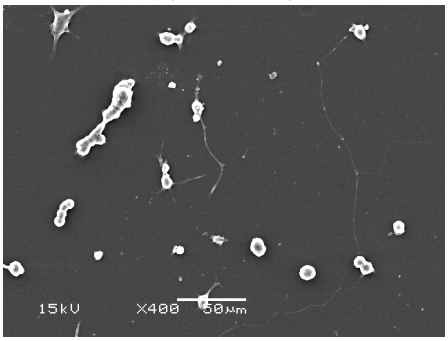

(e) 10 μg/cm^2 Poly-D-Lysine.

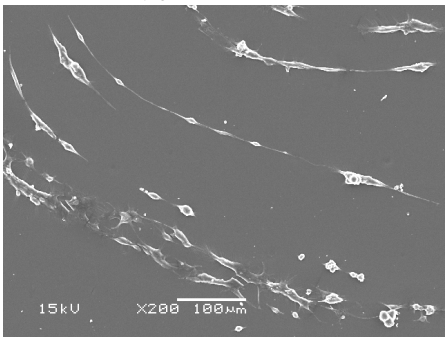

(f) 10 μg/cm^2 Poly-L-Orthinine.

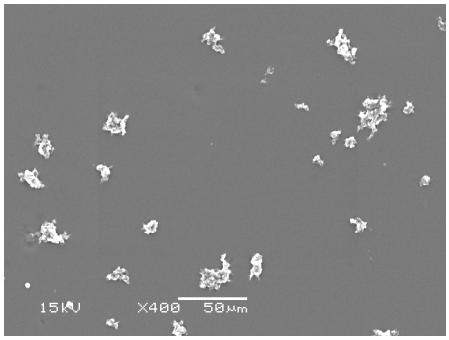

(g) 1 μg/cm^2 Fibronectin.

Figure 3.13: Scanning Electron Micrographs of PC-12 cells on protein coated surfaces following 96 hours incubation: 3.13a) 2 μg/cm^2 Nidogen-1; 3.13b) Uncoated Silicone; 3.13c) 10 μg/cm^2 Collagen-IV; 3.13d) 10 μg/cm^2 Laminin-2,-4; 3.13e) 10 μg/cm^2 Poly-D-Lysine; 3.13f 10 μg/cm^2 Poly-L-Orthinine; 3.13g 1 μg/cm^2 Fibronectin.

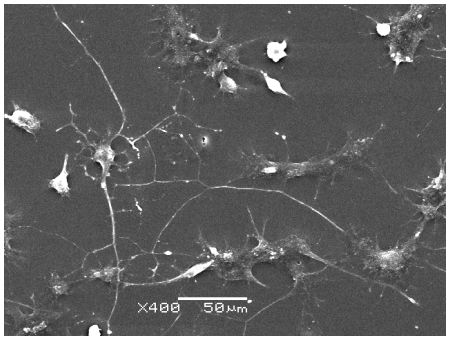

(a) ECM gel coating.

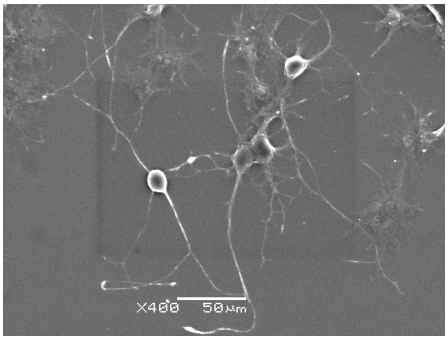

(b) All-in-One coating.

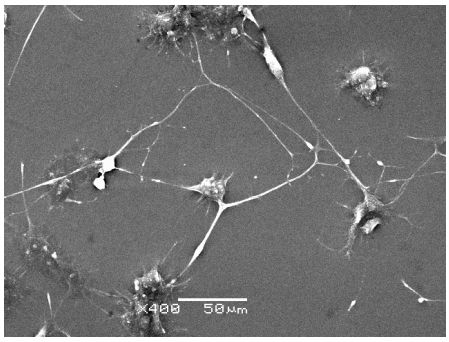

(c) CNL coating.

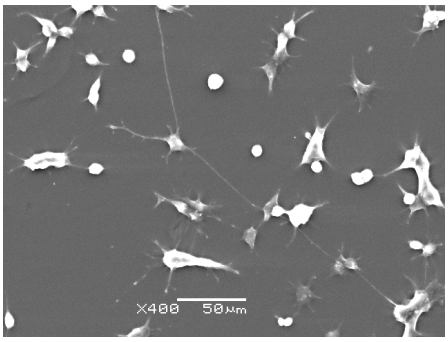

(d) LNC coating.

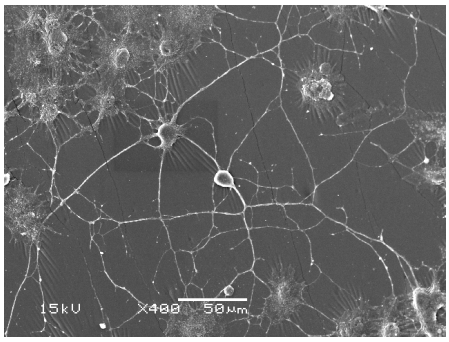

(e) CL coating.

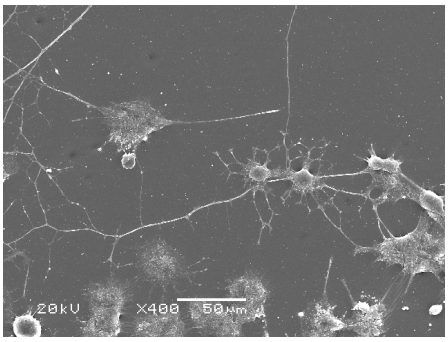

(f) LC coating.

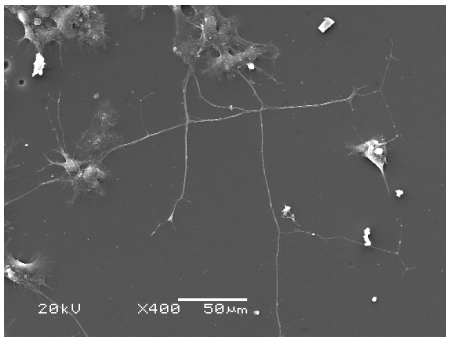

(g) CL all-in-one coating.

Figure 3.14: Scanning Electron Micrographs of PC-12 cells on protein coated surfaces following 96 hours incubation: 3.14a 11.175 μg/cm^2 ECM gel; 3.14b Collagen-IV + nidogen-1 + laminin-2,-4 all-in-one coating using optimal concentrations; 3.14c Collagen-IV + nidogen-1 + laminin-2,-4 layer-by-layer coating using optimal concentrations; 3.14d Laminin-2,-4 + nidogen-1 + collagen-IV layer-by-layer coating using optimal concentrations; 3.14e Collagen-IV + laminin-2,-4 layer-by-layer coating using optimal concentrations; 3.14f Laminin-2,-4 + collagen-IV layer-by-layer coating using optimal concentrations; 3.14g Collagen-IV + laminin-2,-4 all-in-one coating using optimal concentrations.

3.4 Discussion

3.4.1 Analysis of Coatings by Raman Microscopy and BCA Assay

Previous studies have found 0.13 μg/cm^2 bovine serum albumin adsorbed to steel with large grains (22 μm), while 0.71 μg/cm^2 adsorbed to smaller grained steels (320 nm) [320]. The values observed in this study fall within this range, however the difference in surfaces, proteins and solution concentrations can be expected to alter the results. In contrast protein adsorption on polyurethane hydrogel films has been shown to be in the range 1 μg/cm^2 to 4 μg/cm^2 for bovine serum fibrinogen and 8 μg/cm^2 to 16 μg/cm^2 for bovine serum albumin, depending upon sample hydrophilicity and swelling [321]. In this study surfaces were not modified to improve hydrophilicity, which may improve protein adsorption.

To reduce desorption, and increase initial protein concentration proteins could be attached by silanisation. This has been used for fibronectin, with concentrations of 1.5 μg/cm^2 achieved [322]. For PDL, silanisation has achieved a surface concentration of 2.1 μg/cm^2 [323]. To silanise proteins steps which alter the surface topography may be required, therefore direct comparisons between proteins may not be applicable [324]. The adsorption method does not alter underlying surface topography, avoiding this potential confound.

The BCA assay response is dependent upon the protein composition, with the amino acids cysteine, cystine, tryptophan and tyrosine key to the formation of the coloured product [312]. Two proteins tested in this study did not include these residues (poly-D-lysine, poly-L-orthinine), therefore these could not be measured reliably using the BCA assay. Alternative assays such as the Lowry assay and the Bradford assay are also dependent upon protein composition [325]. For this reason comparisons are only valid within the concentration gradient for a given protein, not between proteins. A standard curve for each protein used would allow this problem to be overcome, however other confounds such including variations in incubation time are likely to make the comparisons invalid between protein types.

Alternative methods for the measurement of protein adsorption include ATR/FTIR (investigated previously) [326], Raman microscopy (investigated in this study), surface plasmon resonance (SPR) [327] and radio-labelling [328]. ATR/FTIR (attenuated total internal reflection/Fourier transform infrared spectroscopy) was discounted in previous work for the same reason Raman microscopy was unsuccessful in this study: the PDMS spectrum predominates the spectrum. Spin coating ultra-thin PDMS surfaces on glass or crystal may overcome this problem and should be investigated in future. SPR would also require spin coating ultra-thin PDMS layers, however the equipment is cost prohibitive, especially since surface regeneration of the SPR chips could not be guaranteed. Radio-labelling was discounted due to the cost for modifying each protein used, potential effects of iodination on protein structure, and the complexity of waste disposal.

3.4.2 Protein Concentration Optimisation

The optimal concentrations found were: 10 μg/cm^2 PDL; 10 μg/cm^2 C-IV; and 1 μg/cm^2 Ln-2,(-4). Optimal concentration was not determined for PLO, Fn or Nid-1. Using the 1:1 molar ratio of Ln to Nid-1 an theoretical optimal concentration of Nid-1 was calculated as 0.175 μg/cm^2 [209, 210].

PC-12 cells did not adhere in sufficient number to PDMS surfaces coated with Nid-1, higher concentrations may have resulted in increased cell adhesion but this was not investigated. Nidogen-1 has been shown to induce process formation and migration of Schwann cells [329]. Therefore, while effects were not observed in this study, they may be present with other cell types or *in vivo*.

The observations for Fn coated PDMS agree with results by Tomaselli et. al., who observed poor attachment and low neurite outgrowth on Fn coated surfaces [330]. In contrast the RGD binding epitope (present in Fn) does improve neurite outgrowth and is effective for improving neural regeneration *in vivo*, although to a lesser extent than the IKVAV domain of laminin [331, 332].

The concentration ranges chosen were either suggest by the supplier or from work by other researchers. Often researchers describe the concentration of protein in a solution used, but not the surface area treated or the volume of protein solution used. For example Soussou et. al. used 50 μg/cm^2 PDL, 50 μg/cm^2 PLO, and 125 μg/cm^2 reconstituted basement membrane on glass cover slips, however they do not measure the actual amount remaining following washing [300]. The supplier, Sigma Aldrich, suggest using between 0.5 ml and 1.0 ml of a 0.1 mg/ml solution to coat 25 cm^2, giving a surface concentration of between 2 μg/cm^2 and 4 μg/cm^2. Therefore, for this work concentrations in this range were chosen. The detail supplied in this thesis will make replication and comparison of results easier for future research.

The peaks or plateaus in neurite outgrowth response observed for PDL, C-IV and Ln-2,(-4) indicate a number of possible explanations.

First, the response may reach an optimum because the concentration at the surface reaches a maximum, and no more protein adsorbs with increased concentration. This is not supported by the BCA assay data which show that C-IV and Ln-2,(-4) surface concentration increases with increasing protein applied. Second, the surface may become saturated, and any additional protein will rest on top of the protein already adsorbed. This explanation presents a further theory, that protein adsorbed as a second protein layer is less tightly bound than protein adsorbed to the PDMS surface, this supports the observation of peak responses rather than plateau responses, and a logarithmic relationship between applied protein and final concentration (observed with Ln-2,-4). Finally, the cell response may be limited to a given number of binding sites per area, therefore increasing the binding site concentration has no effect, or a negative effect on cell response. This is supported by research showing a sigmoidal response between RGD concentration and cell attachment, with a critical maximum density beyond which response is asymptotic to a theoretical maximum number of cells [333].

3.4.3 Laminin-2,(-4) and Laminin-1

Laminin-2,(-4) has been suggested as more suitable for peripheral nerve applications than Laminin-1 [179]. This study found no significant difference in neurite outgrowth between coatings at the same initial concentration. However, neurites were longer and fewer on Ln-2,(-4), this may indicate a time dependent maturation of the cells, with PC-12 cells on Ln-2,(-4) undergoing "whisker trimming" prior to the 96 hour time point in this study, where small non-networked neurite branches are removed in favour of branches in a network with other cells. No conclusions on the relative merits of Ln-1 and Ln-2,(-4) can be drawn at this stage.

Additional factors may affect the results of this experiment. The choice of a neuronal-like cell line may not be representative of peripheral nervous system cells. In addition, there may be differences, which were not observed due to the n = 6 repeats used in this study, although these are likely to be of small effect size and therefore may not be biologically relevant (i.e. translate to the complex *in vivo* environment). A power analysis prior to any future experiments could use this data to indicate a suitable n, however a *post hoc* power analysis of the observed data would not be valid because of the inverse relationship between the p-value and power [334, 335]. Also, the relative cost of Ln-2,(-4) and Ln-1 must be considered (681 and 139 £/mg respectively).

This experimental series focused on Ln-2 due to its role in the endoneurial BM [179]. Other Ln isoforms such as Ln-8, -9, and -11, which are present in the PNS, should be examined *in vitro*.

3.4.4 Comparison of Optimal Concentrations

In this experiment coatings were layered in the order C-IV, Nid-1, LN-2,-4: suggesting that LN-2,-4 will be most prevalent at the coatings surface. Improvements to neurite outgrowth on sBM compared with LN-2,-4 suggest that C-IV and Nid-1: encourage LN-2,-4 recognition site presentation; directly enhance neurite outgrowth; and/or stabilise the coatings.

This work has shown that endoneurial BM protein coatings increase neurite outgrowth on silicone surfaces compared with PDL coated controls. Multi-protein coatings significantly increase number of neurites compared with optimised single layer coatings, and significantly increase neurite length compared with PDL and Ln-2,-4 coated samples. We therefore suggest that a multi-protein coating is promising for the promotion of neural regeneration within microchannels.

3.4.5 Comparison of Multi-Protein Coatings

The well-defined multi-protein coatings developed in this study are as conducive to neurite outgrowth as the tested concentration of ECM gel. Furthermore, a simple, all-in-one mix of basement membrane proteins is one of the most effective coatings, and lends itself better to use in large-scale applications than the time intensive layer-by-layer coatings.

The relative concentration of proteins in the defined multi-protein coatings differed from ECM

gel. In ECM gel major components are present in the following amounts 60% Ln, 30% C-IV, 6% Nid (10:5:1 mass ratio), while in this work the multi-protein coatings used 89.5% C-IV, 8.9% Ln and 1.6% Nid. It should be noted that the relative concentrations of Ln and Nid found by Kleinman *et. al.* agree approximately with a 1:1 molar ratio, however the difference may be due to some Nid remaining bound to the Ln therefore slightly increasing the Ln concentration [299]. This study used growth factor reduced ECM gel. This aims to reduce the abundance of growth factors including nerve growth factor and epidermal growth factor [294]. As a result growth factor reduction increases the relative abundance of structural proteins, such as laminin, nidogen and fibronectin [296].

In this study, the ECM gel concentration used was not optimised, an equal concentration to the multi-protein coatings was chosen, C-IV and Ln are major components of ECM gel; however, their concentration is likely to have been reduced due to the presence of other ECM molecules. The ECM gel concentration could be further optimised. The three-protein coating developed in this work lends itself well to a factorial analysis of the effect of changing single protein concentrations within a multi-protein coating. Optimising multi-protein coatings may further improve neurocompatibility, and would allow a test of a 10:5:1 mass ratio of Ln:C-IV:Nid, more similar to that found in reconsitituted BM.

The LNC layer-by-layer and LC layer-by-layer coatings are less effective at promoting neurite outgrowth than other multi-protein coatings. This may be because to C-IV sheet formation *in vitro* creates a suitable scaffold for smaller basement membrane proteins [308]. Alternatively, correctly presented Ln binding sites may best promote neurite outgrowth. Competitive protein adsorption on surfaces from mixtures follows a process called the Vroman effect: proteins adsorb to and desorb from surfaces at random, over time proteins with higher affinity for the surface replace lower-affinity proteins. Smaller proteins typically diffuse through solution more quickly, so adsorb more rapidly, however larger proteins have more sites for bonding with surfaces, and therefore larger proteins typically have a higher affinity for surfaces [336]. It is possible that, the Vroman effect may lead to partial Ln displacement by larger C-IV proteins, creating a disordered transient structure [336,337]; therefore, a longer final incubation time may lead to complete coating remodelling, forming a structure similar to an all-in-one mixed coating. It is possible that the long macromolecular fibril structure of C-IV is responsible for increased neurite length on C-IV coated surfaces compared to multi-protein coated surfaces, and that competitive displacement during multi-protein coating partially disorders *in vitro* C-IV sheets leading to reduced neurite length.

Coatings without Nid-1 (CL layer-by-layer and CL all-in-one) were shown to induce less neurite outgrowth than the best coatings with Nid-1 (All-in-one, ECM gel). These differences were not significant in all cases. However, this may indicate a trend, supporting the use of Nid-1 as a binding protein to ensure the correct presentation of binding sites on Ln.

3.4.6 General Discussion

The data show that endoneurial BM proteins enhance neurite outgrowth compared with controls. However, Nid-1 did not support PC-12 cell attachment at the coating concentrations tested, and is cost prohibitive at higher concentrations. C-IV and All-in-one are the coatings indicated to most improve neural regeneration within microchannels in this study. The all-in-one coating will be used within microchannels in a following chapter, and the results of *in vivo* testing are presented in this thesis.

This work may be applicable to other nerve guidance conduits, especially where scaffolds mimicking the fascicular or endoneurial structure are used, for example multichannel collagen conduits [338]. As part of a hierarchical design endoneurial proteins may improve axonal guidance and reduce the disorganisation associated with neural repair.

These findings support evidence by Tonge et. al. [292] who found that ECM gel, C-IV and Ln support neurite outgrowth *in vitro*. The results of this study suggest that C-IV is more conducive to neural regeneration than Ln and that C-IV contributes most to the induction of neural outgrowth by ECM gel. In line with previous research a summation of the effects of Ln and C-IV was not observed [292]. In contrast, additive combinatorial effects of Ln and C-IV have been described [339], suggesting that, in this case, protein-protein interactions in the basement membrane reduce, rather than increase, the availability of binding sites to cells.

At time points longer than those tested in this study (15 days) neurite outgrowth on Ln (unspecified form) is greater than on C-IV, and the addition of heparan-sulphate to a collagen-Ln co-coating has been shown to increase neurite outgrowth [340]. This suggests an application for the investigated proteins as part of a proteoglycan hydrogel filler for nerve guidance conduits.

To reduce upregulation of cell-adhesion molecules for a specific ECM protein PC-12 cells were culture expanded in PDL coated flasks. However, supplier guidelines suggest culture-expansion on C-IV coated surfaces or in suspension[2]. Therefore the cells may have been pre-selected for affinity to C-IV coated surfaces by the supplier prior to delivery.

Although PC-12 cells are a well-established cell line for *in vitro* investigation of neurocompatibility, a more complete *in vitro* model of neural outgrowth could be used to improve translation to the *in vivo* environment. For example, dorsal root ganglion primary cells have been used for *in vitro* investigation of neurite outgrowth [341]. During neural regeneration Schwann cell recruitment is crucial for directing axonal growth [71, 76]; therefore these surfaces should additionally be tested for either Schwann cell compatibility or using a neuron/Schwann cell co-culture.

ECM gel-like protein matrices can be derived from cells *in vitro* [311], and it has been shown that tissue matched ECM gels improve cell adhesion, proliferation and function *in vitro* [342]. Decellularised

[2]Information from the supplier indicates that PC-12 cells are "routinely cultured on Collagen-IV coated flasks"; however, cells supplied as growing cultures are "grown and dispatched in suspension". In this study the PC-12 cells used were supplied cryopreserved.

ECM from Schwann cell culture may provide an alternative to recombinant or xenogenic protein mixes.

It should be noted that the lack of significant differences between multi-protein coated surfaces does not imply the results are the same. Observed, insignificant, differences may have been below the effect size allowed for in this study. However, the results do support the use of multi-protein coatings as any effect is small in comparison to the difference when compared with single protein coatings.

This study determined optimal coating concentrations for single proteins and assumed that this would translate to multi-protein coatings. However, interactions between the chosen ECM proteins are likely to alter the effect of concentration upon neurite outgrowth, a hypothesis supported by the absence of summation in effects seen in this study. A factorial study design testing multi-protein coatings should be carried out to determine combinatorial effects

The results presented support the initial hypotheses with a few exceptions:

1. Endoneurial basement membrane protein coatings increase neurite outgrowth on silicone surfaces compared with poly-D-lysine coated controls. However, PC-12 cells do not adhere to nidogen-1 coated or uncoated silicone surfaces.

2. Collagen-IV + Laminin + Nidogen multi-protein coatings increase neurite outgrowth on silicone surfaces compared with most single protein coatings. However, neurite length is significantly greater on collagen-IV coatings.

3. Multi-protein coating order significantly affects neurite outgrowth on silicone surfaces. Layer-by-layer coatings starting with laminin significantly reduce neurite outgrowth compared with other multi-protein coatings. However, layer-by-layer coatings starting with collagen-IV are as good as all-in-one mixed coatings.

4. Collagen-IV + Laminin + Nidogen multi-protein coatings increase neurite outgrowth on silicone surfaces compared with Collagen-IV + Laminin multi-protein coatings.

5. Optimal multi-protein coatings do not significantly change neurite outgrowth on silicone surfaces compared with ECM gel coatings.

Chapter 4

In Vitro Neuron Adhesion Studies: Topography

4.1 Introduction and Hypotheses

The success of microchannel neural interfaces depends upon neural regeneration through the channels. Enhanced regeneration can include increased number of axons per microchannel, reduced fibrotic capsule width, or reduced channel diameter without causing fibrotic occlusion [113].

Topographical cues in a cell's environment can alter cell response [196]. Regenerating axons demonstrate substrate mediated responses following severe crush injuries, where Wallarian degeneration of axons occurs but the myelin sheath remains in continuity (2° Sunderland Injury, [65]). In this case regeneration is directed along the original endoneurial tube and the pattern of innervation is identical with the original structure [64]. However, when a nerve is completely transected (for example in microchannel neural interface implantation) these structural cues are lost, and the resulting nerve regeneration becomes frustrated and disorganised. In nerve repair long gaps (over 5 mm) must be repaired using autograft or a nerve guidance conduit (NGC) [71, 75–78].

NGCs aim to provide the structural, topographical, and in some cases molecular and cellular, cues to enhance regeneration, and reduce incorrect patterns of reinnervation [26]. A MNI using successful NGC strategies could enhance regeneration and encourage axonal growth towards the electrodes within neural interfaces and therefore improve the implant function.

In this chapter two different topographies will be considered. Grooves, or ridges, have been shown to cause 'contact guidance' of cells, a strategy, which may help provide directional cues to regenerating axons and reduce disorganisation. Roughened surfaces have also been shown to alter cell response, increasing cell adhesion and enhancing axon growth. Moreover, a combination of these topographical cues may prove optimal for guiding and enhancing neural regeneration.

4.1.1 Contact Guidance and Groove Dimensions

Grooved topographies can cause 'contact guidance' of cells [190, 191]. Contact guidance is the directional response by cells to a given surface, with preference to a given direction of movement, cell orientation, or elongation. Contact guidance has been demonstrated with many cell types, in particular neural cells where alignment with respect to a substrate is readily determined from neurite angle [192–196]. In this chapter neurite orientation will be considered.

Dimensions of interest for contact guidance topographies are in the cell, axon and subcellular ranges. Neuron cell bodies are typically 5 μm to 20 μm diameter and axons vary from $<$1 μm to 20 μm diameter and extend from μm to cm long [53]. PC-12 cells, used in this chapter, are typically at the lower end of these dimensions, although it should be noted that cells will respond to cues outside these ranges.

Neurites have been shown to align parallel to grooves between 1 μm and 100 μm wide [42, 343–358]. There is high variability between cell types and the surfaces used; however, consensus is emerging that features with an aspect ratio (depth / width) above a critical value of 0.1 induce more alignment, and that increasing aspect ratio increases alignment [352, 359–362]. An overview of studies looking at contact guidance of neuronal and other cell types is given in table 32 in the appendix.

Small groove sizes ($<$1 μm wide) are both less effective at aligning neurites, but can also cause perpendicular alignment in some cell types [354–356]. Grooves can have other unexpected, but beneficial, effects: inducing neuronal phenotype in cells [358, 363, 364]; reducing fibroblast adhesion while maintaining Schwann cell adhesion [346]; and aligning neural support cells, enhancing neurite alignment [353].

Grooves are an artificial environment, alternative, more physiologically relevant, topographies have been used to guide extending neurites. Schwann Cell-like topographies — imprints from aligned *in vitro* Schwann cell culture and Schwann cell inspired artificial topographies — cause neurite alignment and enhance neurite outgrowth from dorsal root ganglion cells [341, 365]. More complex groove topographies also cause guidance, with neurons on zig-zag grooves extending longer, more aligned neurites [366] and grooves with a gradient in width improving alignment compared with continual cross-section grooves [226].

Recent *in vivo* studies have lent support to the use of alignment for nerve regeneration, with aligned 250 nm diameter polycaprolactone fibres and aligned peptide amphiphile nanofibres supporting successful sciatic nerve regeneration [367, 368]. However, highly variable findings *in vitro* mean that any intended topography and method must be tested both *in vitro* and also *in vivo* before conclusions can be drawn.

4.1.2 Roughened Surfaces and the Neural Extracellular Matrix

Surface topographies with similar roughness to extracellular matrix (ECM) may prove to be beneficial for *in vitro* cell culture. Healthy nerve fascicles are compartmentalised by perineurial basement membrane, which ensheaths individual fascicles [71, 178]. Basement membrane has a complex porous structure, which cannot be mimicked due to the constraints on porosity imposed by the microchannel design, however basement membrane feature size can be considered. Basement membrane features range in size from 10 nm to 350 nm, with most features falling in the range 50 nm to 250 nm [369, 370]. Perineurial basement membrane structure has not been studied; however, repeated protein configurations on the order of 70 nm can be expected (due to laminin polymerisation) [371, 372].

In vitro these structures can be mimicked through surface roughness. Optimal values have been found between 20 nm and 70 nm R_a, which enhance neural adhesion and neurite outgrowth [197, 198]. Importantly, coating surfaces with a protein layer may negate the effect of a roughened surface, possibly because the features of interest are 'hidden' by the protein [198]. Basement membrane structures can also be replicated accurately using polymer casting [373]. The complex porous structure may also be key to cell response [374], however this study is limited to non-porous surfaces.

Roughened surfaces also affect cells involved in fibrotic capsule formation and microchannel occlusion. Nanorough surfaces reduce fibroblast proliferation, and nano-porous surfaces can reduce astrocyte adhesion, while maintaining neuronal cell activity [27, 199, 375].

Additional substrate factors alter cell response *in vitro* and *in vivo*, for example substrate stiffness [184]. In neural cells substrate modulus affects alignment [185] and neurite branching [186]. *In vivo* it is hypothesised that flexible electrodes will lower stress concentrations and micromotion at the electrode-tissue interface, reducing tissue damage and the foreign body response [182, 183]. Stiffness of neural interface materials is discussed in more details in chapter 5.

4.1.3 Multiscale Topographies

Implementing both micron scale grooves and nanoscale roughness will form a hierarchical structure, with controlled features at both the μm and nm scales [376], mimicking the organisation of tissue over different length scales [377]. The use of multiscale substrates has been shown to promote myogenesis in human mesenchymal stem cells [376], alignment of mouse skeletal myoblasts [378] and alignment of mouse embryonic fibroblasts [379]. For neurons this would allow the inclusion of outgrowth enhancing sub-μm scale features or roughness and μm scale contact guidance patterns.

4.1.4 Aims and Hypotheses

This chapter presents an *in vitro* study looking at the effect of two different changes in surface topography on neurite outgrowth. The two topographical changes considered are surface roughness and grooves.

The aim of this study is to develop and test a surface that could be applied within a microchannel

to improve neural regeneration. Therefore limitations are placed upon the study: the structure must be non-porous; any structures must fit within a microchannel without greatly altering its dimensions; and it must be possible to create the structures using a simple manufacturing method.

To assess the extent to which neurites align with grooved surfaces the normalised cumulative periodogram criterion is used [380, 381]. This provides an angle of alignment, the point at which the distribution of angles is considered to diverge from that of a randomly distributed sample. For more aligned samples the angle of alignment is expected to be nearer 0°.

The hypotheses for this chapter are as follows:

- Increased roughness will improve *in vitro* neurite outgrowth on silicone substrates compared with relatively smooth controls.
- PC-12 cells will exhibit increased alignment with cell scale surface grooves compared with smooth controls.
- A combination of grooves and nanoscale roughening will: increase neurite outgrowth compared with grooved samples; and increase neurite alignment compared with roughened samples.
- A combination of multiscale topography and nerve specific mixed-protein coatings will increase neurite outgrowth compared with multiscale topography and single-protein coatings.

4.2 Methodology

4.2.1 Fabrication of Patterned Templates

Turned medical grade Ti-6Al-4V discs, 10 mm diameter, 5 mm thickness, were polished. An abrasive paper series: P600; P1200; P2500; and P4000 was used, followed by buffing using an AP-A (agglomerated alpha alumina) suspension (Struers Ltd, Rotherham, UK) and a polishing cloth. Surface roughness was determined using surface profilometry, and surfaces with R_a <0.03 μm were accepted.

Discs were degreased in an ultrasound bath in 10% Decon90 (Decon Laboratories Ltd., Hove, UK) for 10 minutes, rinsed in distilled water, and cleaned by an ultrasound bath in acetone for 10 minutes.

Cleaned, polished discs were patterned to create a negative topography that would act as a template for silicone samples.

4.2.1.1 HF Etched Samples

Polished titanium discs were immersed in 2.5% hydrofluoric acid (HF). Surface roughness was found to be linearly dependent upon time in HF up to 4 minutes, after 4 minutes no change in Ra was observed. 1 minute and 4 minute immersion in HF was chosen.

Surface	Groove Width (μm)	Groove Spacing (μm)	Groove Depth (μm)	Aspect Ratio
30/30/10	30	30	10	0.33
30/30/5	30	30	5	0.17
15/30/10	15	30	10	0.67

Table 4.1: Groove geometries achieved in silicone using laser patterned Ti-6Al-4V templates. The values refer to the positive, silicone samples. Aspect ratios are reported to 2 significant figures.

4.2.1.2 Grooved Samples

Parallel grooves were created by direct laser writing using a ClassIV Nd:YAG laser (Violino-2, Laservall, Laser Lines Ltd, Oxon, UK). Polished titanium discs were cleaned by ultrasonification in acetone for one minute immediately prior to laser etching. Discs were etched using a power of 50 % (40 kW peak, 10 W mean average), shot frequency of 10 kHz, write speed of 200 mm/s and a pulse width of 12 ns. Laser spot size was 30 μm. To achieve greater groove depth a greater number of passes was used: two passes for 5 μm deep grooves and five passes for 10 μm deep grooves. The groove geometries achieved are listed in table 4.1. During the direct laser writing a HEPA filtered, rapid airflow was passed over the surface of the discs to prevent sputtered particles from settling back on the disc surface.

4.2.1.3 Multiscale Samples

To form multiscale surface topographies polished Ti-6Al-4V discs were first grooved and and then HF etched as described.

Multiscale surfaces were compared with smooth controls, etched samples and grooved samples.

4.2.2 Fabrication of Patterned Silicone Substrates

Silicone (Sylgard 184, Dow Corning, Midland, MI) was cast onto the Ti-6Al-4V templates as follows. Silicone was speed mixed for two minutes at 2000 rpm with a speed mixer (DAC 150 FVZ-K, Synergy Devices Ltd, High Wycombe, UK). Mixed silicone was degassed in a vacuum centrifuge for two minutes at approximately 30 mbar and 500 rpm. Titanium samples and glass coverslips (borosilicate glass, 20 mm x 20 mm, VWR) were cleaned by ultrasonification in acetone for five minutes immediately prior to casting. Discs were placed in a solution of HAEMO-SOL detergent (Cox Surgical, Surrey, UK) in distilled water for 10 seconds and agitated to form a release layer. Discs were dried under vacuum. Approximately 0.5 ml silicone was syringed onto the patterned surface each template, and a coverslip placed on top of the silicone. Samples were placed in a dry oven at 150°C for 1 hour. Templates were soaked in ELGA distilled water for up to 30 minutes and gently removed to leave patterned silicone adhered to glass coverslips.

4.2.3 Vertical Scanning Interferometry

Surface roughness and groove dimensions were assessed using vertical scanning interferometry. Samples were places in an interferometer (Contour GT, Bruker) and images were recorded using Vision64 software (Release v5.30, Bruker). Vertical travel was adjusted depending upon sample profile from 20 μm to 70 μm. An area 0.598 mm by 0.442 mm was imaged at 20x magnification.

4.2.4 Water Contact Angles

To determine surface hydrophilicity water contact angles were measured using sessile drop goniometry. A 10 μL droplet of deionised water was placed onto the surface of each sample and the droplet imaged using a Nikon D90 digital camera and background lighting. 6 contact angle measurements were taken per sample with the sample dried using a lint-free cloth between each measurement. For grooved samples images were taken of angles parallel to and perpendicular to the groove direction to account for directional spreading. Contact angles were measured using ImageJ software as shown diagrammatically in fig. 4.1.

4.2.5 Surface Functionalisation

Prior to cell culture silicone substrates were washed three times for 5 minutes with 70% Industrial Methylated Spirits, followed by rinsing three times for 5 minutes with phosphate buffered saline. Samples were sterilised under UV for 12 hours.

Surfaces were coated with Collagen-IV to improve PC-12 cell adhesion. One 100 μl droplet of Collagen-IV dissolved in phosphate buffered saline was pipetted onto each sample to give a coating concentration of 10 μg/cm^2. Samples were incubated for one hour at 37°C, 5% CO_2, and washed three times with phosphate buffered saline and incubated again for at least a further two hours to dry.

In addition successful surfaces were coated with a mixed protein coating: 10 μg/cm^2 Collagen-IV; 0.175 μg/cm^2 Nidogen-1; 1 μg/cm^2 Laminin-2,-4. Proteins were mixed in a 100 μl droplet of phosphate buffered saline to give the required final surface concentration. Samples were incubated for 1 hour at 37°C, 5% CO_2, and washed three times with phosphate buffered saline and incubated again for at least a further two hours to dry.

Figure 4.1: A diagram of water contact angle measurement, as seen in sessile liquid drop goniometry on smooth solid surfaces. ©2013 Springer-Verlag, with permission [382]. REDACT IN ONLINE COPY.

4.2.6 Analysis of Coating by Bicinchoninic Acid (BCA) Assay

Substrates (n = 3) were prepared for a protein assay. Polished control, 4 minute HF etched, 15/30/10 grooved and 15/30/10 grooved + 4 minute HF etched silicone surfaces were prepared as above.

Surfaces were coated with Collagen-IV as above using 100 μl droplets. Substrates were washed 3 times with PBS. Washed substrates were allowed to dry in an incubator.

4.2.6.1 BCA Assay

Protein concentrations on surfaces were analysed using a micro BCA assay (Pierce Micro BCA Protein Assay Kit, Thermo Fisher Scientific Inc.) [312].

A bovine serum albumin solutions (BSA) were used to construct a standard curve. BSA was diluted in PBS to form concentrations from 0.001 mg/ml to 0.04 mg/ml. 100 μl droplets of each BSA standard were placed onto control substrates, the surfaces were not washed, surfaces were allowed to dry in an incubator.

100 μl BCA working reagent was placed on each surface including standards and blank reference. The well plate was sealed and incubated for 2 hours at 37°C.

The plate was allowed to cool and adsorbance was measured at 562nm using a NanoDrop1000 spectrophotometer (Thermo Scientific). Protein concentrations were calculated using the interpolation lines given by the standard curve. Amount of protein per substrate, and therefore per cm^2 was calculated for each sample.

4.2.7 Cell Line

All *in vitro* assays were carried out using the PC-12 cell line (ECACC, catalogue number: 88022401).

Within any single experiment cells from a single population (passage) were used to reduce experimental error. Previous studies have suggested that the line should be used at passage 6 to 10 to avoid senescence [198, 199, 314]. However, this was not feasible because the PC-12 cells were received at passage 7. Therefore the cells were used within 6 passages (passage $\leq$ 12). Senescence of neurite outgrowth was not observed with cells at $\leq$ passage 12.

Cells were culture expanded in 25 cm^2 cell culture flasks (Corning) coated with 4 μg/cm^2 Poly-D-Lysine (PDL). PDL was chosen as the cell adhesion coating for culture expansion because it interacts electrostatically with cell membranes [315], and therefore is unlikely to up-regulate the expression of specific cell adhesion molecules.

The following cell culture media was used: RPMI 1640 (R8758, Sigma) + 10 mM HEPES Buffer + 1 mM Sodium Pyruvate + 1% penicillin-streptomycin + 10% Horse Serum + 5% Foetal Bovine Serum (FBS). Standard subculture technique was used. Cells were detached using trypsin-EDTA (Gibco) and agitation, centrifuged to form a cell pellet, resuspended as a single-cell suspension using a small diameter needle and seeded onto 2 new PDL coated flasks.

Alcohol	Concentration (vol.% Alcohol in dH_2O)	Time (minutes)	Number of repeats
IMS	20	5	2
IMS	30	5	2
IMS	40	5	2
IMS	50	5	2
IMS	60	5	2
EtOH	90	5	2
EtOH	96	10	2
EtOH	100	15	2

Table 4.2: Alcohol series used for dehydration of cell monolayers on silicone sample for scanning electron microscopy. IMS = industrial methylated spirits. EtOH = Ethanol. Alcohol diluted in distilled water.

Prior to seeding onto test surfaces cells were primed by culturing with NGF 7S (50 ng/mL) in complete media for at least 7 days. Priming with NGF enhances the rate of neurite outgrowth following seeding [316].

4.2.8 Cell Seeding

Cells were seeded at 5,000 cells per sample (approximately 6350 cells/cm^2). Cells were detached from culture flasks using trypsin-EDTA and agitation, centrifuged to form a cell pellet and resuspended in media + 50 ng/mL NGF to give single-cell suspension at 50,000 cells/mL. Cells were dropped onto the silicone sample surface in a 100 μL droplet using a Gilson pipette. Samples were place in an incubator at 37°C, 5% CO_2, for 1 hour to adhere to the sample surface. The samples were then flooded with 2 ml media + 50 ng/ml NGF and incubated for 96 hours with a single media change after 48 hours.

4.2.9 Scanning Electron Microscopy

The media was completely removed from the samples prior to processing. 2 ml 2.5% gluteraldehyde fixative in 0.1M sodium cacodylate buffer (pH 7.4) was added to each sample. After 30 minutes the fixative was removed and the samples were washed twice in 0.1M sodium cacodylate buffer (pH 7.4). The samples were dehydrated in ascending alcohol series (see table 4.2). The samples were covered with a loose lid and air-dried for at least 12 hours.

Dry samples were mounted onto aluminium stubs using double-sided carbon tape. Samples were sputter coated with Au/Pd for 2.5 minutes at 20 mA using an Emitech K550 sputter coater. Conductive paint was used to create a conductive bridge between the sample and the aluminium stub.

Prepared samples were imaged using a JEOL JSM 5500 LV scanning electron microscope (JEOL, Welwyn Garden City, UK). 6 images were taken of each sample at 400× magnification. Images were taken approximately equidistantly across the sample surface. In addition representative images were taken at 200×.

4.2.10 Immunoflourescence Microscopy

4.2.10.1 Vinculin

After 96 hours incubation cells (n=1 samples) were prepared for fluorescence microscopy. Media was removed from each sample. 2 ml of 4% formalin in phosphate buffered saline was added to each sample. After 30 minutes the fixative was removed and the samples were washed in PBS. Primary antibody (Primary anti-vinculin mouse monoclonal Antibody (V9131, Sigma-Aldrich, UK), dilution of 1:200 with PBS and 0.0025% Triton X) was added to each sample and incubated at room temperature for 1 hour. Samples were washed 3 times with PBS. The underside of each substrate was dried and placed in a clean, dry welled-plate. The secondary antibody (Alexa Fluor 488 chicken anti-mouse IgG antibody (A21200, Invitrogen, UK), dilution 1:1000 with PBS) was added to each sample and incubated for 2 hours at room temperature in the dark. Samples were washed 3 times with PBS and stored under PBS prior to imaging.

Samples were imaged using an Axioskop 2 Plus light microscope (Zeiss) with a FITC filter and images were recorded using Axiovision software (Zeiss).

4.2.10.2 Actin

After 96 hours incubation cells (n=1 samples) were prepared for fluorescence microscopy. Media was removed from each sample. 2 ml 4% formalin in phosphate buffered saline was added to each sample. After 30 minutes the fixative was removed and the samples were washed in PBS. Cells were permeabilised using 0.1% Triton-X (Sigma-Aldrich) in PBS for 15 minutes. Samples were washed 3 times with PBS and 1% phalloidin-FITC was added to each sample. Samples were incubated at room temperature for 1 hour. Samples were washed 3 times with PBS and stained with 0.1% Hoechst 33258 (Sigma-Aldrich) in PBS for 15 minutes. Samples were washed and stored under PBS prior to imaging.

Samples were imaged using an Axioskop 2 Plus light microscope (Zeiss) with FITC and DAPI filters and images were recorded using Axiovision software (Zeiss).

4.2.11 Image Analysis

4.2.11.1 Cell Number

Cell number was determined from 200x images using ImageJ software (version 1.46r and version 1.46a, NIH, USA) [317, 318] and the cell counter plugin.

4.2.11.2 Neurite Length and Number

Neurite length and neurite number were determined from 400x images using ImageJ software. Linear extensions from the cell were measured for all cells exhibiting extensions fully within the field of view. Extensions were considered neurites when they extended at least 1 cell diameter from the cell edge. The number of neurites per cell exhibiting neurites was recorded.

4.2.11.3 Neurite Angle

Neurite deviation (angle) from grooves was determined relative to the sample surface. 0° indicates alignment parallel to grooves, 90° indicates alignment perpendicular to grooves. For un-grooved samples deviation was calculated relative to the lower edge of the field of view.

4.2.12 Data Analysis

Prior to the following statistical analyses a randomly selected 10% of the micrographs were assessed by a second investigator and the intra-class correlation coefficient was calculated. Correlation coefficient minimum was set at 0.7 [383].

Analysis of cell number, neurite number, neurite length and neurite angle was carried out using SPSS 21.0, Mac and Linux versions (SPSS Inc., IBM, Chicago, IL). Data were tested for normality using the Kolmogorov-Smirnov test. Data were not found to be normally distributed, therefore non-parametric statistical tests were used.

For each experiment cell number, neurite number, neurite length and neurite angle for all groups were compared using the Kruskal-Wallis one-way analysis of variance test. If a significant difference was observed pair-wise Mann-Whitney U tests were performed to identify differences between groups. If no significant difference was found by Kruskal-Wallis test the p-value was reported and no further statistical tests were used. Differences were considered significant at the alpha ≤ 0.05 level.

Pair-wise tests were corrected for multiple comparisons using Holm-Bonferroni correction [319]. This is intended to reduce the likelihood of type I errors.

4.2.12.1 Normalised Cumulative Periodogram

To compare alignment of cells on substrates the normalised cumulative periodogram (NCP) criterion was used. The NCP criterion determines an angle of alignment for a given group of neurites. The NCP was determined using MATLAB (MATLAB R2011b for Linux, Mathworks) as previously described [380]. Two versions of the NCP were used: firstly, as described in [380], where NCP divergence was tested for every 5th angle 'k' (k=5); and second, a more sensitive version, where divergence was calculated for every angle 'k' (k=1). For each method each sample was treated separated and data were reported as median and range. In addition for k=1 a single NCP value for each surface was calculated using all datapoints. The MATLAB script for the NCP written for this work is given in the appendix.

4.3 Results

Data are reported as mean ± standard deviation to 3 significant figures unless otherwise stated. Neurite outgrowth data are plotted as median, interquartile range and inner fences (1.5 times interquartile range). Where data are highly skewed a log scale is used. Neurite alignment data are plotted as histograms with 10° bins. All p-values are tabulated in the appendix.

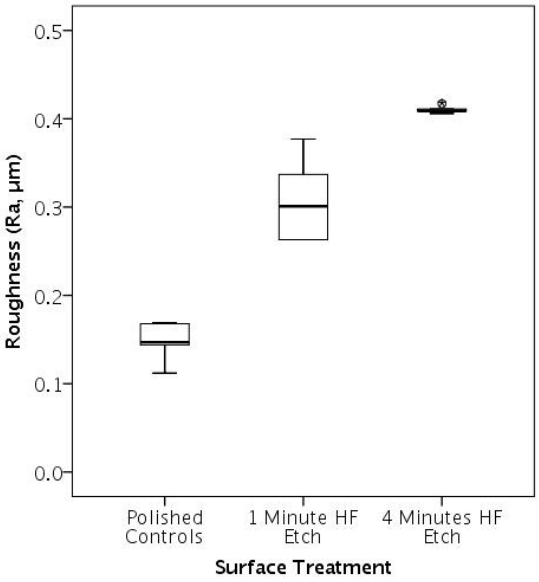

Figure 4.2: Change in R_a with HF etching time. Silicone samples patterned using etched Ti-6Al-4V discs. All differences are significant, $p \leq 0.001$.

4.3.1 Surface Roughness by Vertical Scanning Interferometry

The following surface roughnesses (R_a) were achieved (median, range): polished controls (147 nm, 112 nm to 169 nm); 1 minute HF etch (301 nm, 263 nm to 377 nm); 4 minute HF etch (409 nm, 406 nm to 418 nm). A significant difference in roughness was found by Kruskal Wallis test ($p \leq 0.001$). Samples etched for 1 minute were significantly rougher than polished controls ($p \leq 0.001$). Samples etched for 4 minutes were significantly rougher than controls and samples etched for 1 minute ($p \leq 0.001$). No increase in roughness was detected if longer etching times were used beyond 4 minutes, in a single sample test etching for 8 minutes gave a roughness 4% lower than that for a 4 minute etched sample. R_a values are plotted in fig. 4.2.

The interferometry images show some non-uniformity on the polished surfaces, while the HF etched surfaces are more uniform with evenly spread peaks and troughs.

4.3.2 Surface Topography by Vertical Scanning Interferometry

Due to high aspect ratio, steep side walls and possible overhangs created by the direct laser writing, vertical scanning interferometry created a low resolution image of the surface indicating groove size and the roughness profile of the base of grooves and top of ridges (figs. 4.3 to 4.10).

4.3.3 Water Contact Angles

Water contact angles are reported in fig. 4.11. Water contact angle increased on HF etched surfaces compared with controls. The largest median water contact angles were observed on deep, narrow grooves following etching. In contrast etching shallow, wide grooves reduced water contact angle. Droplet spreading parallel to the grooves was observed on etched shallow, wide grooves, but was not observed

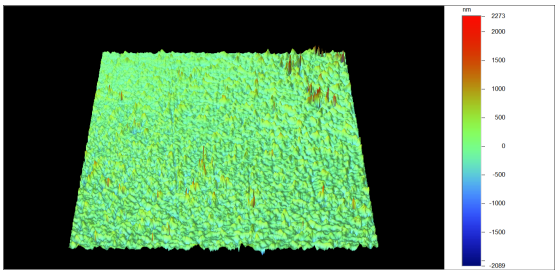

Figure 4.3: Vertical Scanning Interferometry profile of an example polished control silicone control surface. Area: 0.598 mm by 0.442 mm. Magnification: 20x.

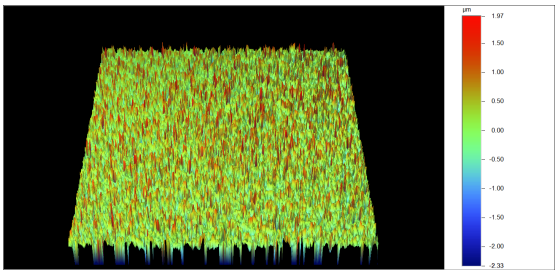

Figure 4.4: Vertical Scanning Interferometry profile of an example 1 minute HF etched silicone surface. Area: 0.598 mm by 0.442 mm. Magnification: 20x.

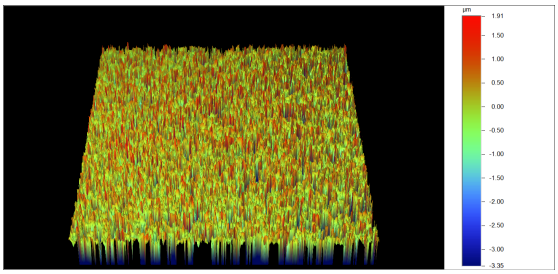

Figure 4.5: Vertical Scanning Interferometry profile of an example 4 minute HF etched silicone surface. Area: 0.598 mm by 0.442 mm. Magnification: 20x.

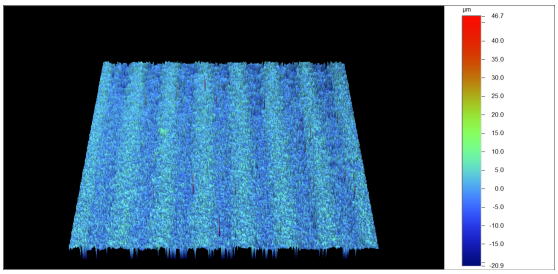

Figure 4.6: Vertical Scanning Interferometry profile of an example 30/30/5 grooved silicone surface. Area: 0.598 mm by 0.442 mm. Magnification: 20x.

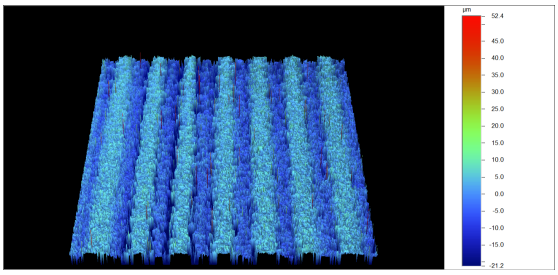

Figure 4.7: Vertical Scanning Interferometry profile of an example 30/30/10 grooved silicone surface. Area: 0.598 mm by 0.442 mm. Magnification: 20x.

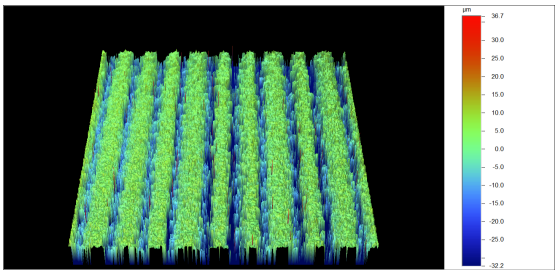

Figure 4.8: Vertical Scanning Interferometry profile of an example 15/30/10 grooved silicone surface. Area: 0.598 mm by 0.442 mm. Magnification: 20x.

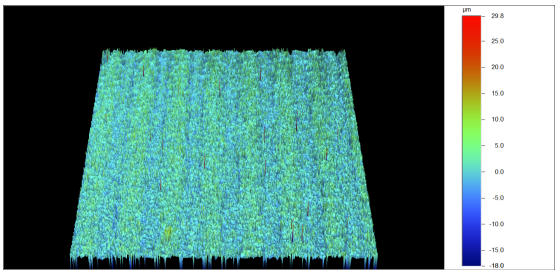

Figure 4.9: Vertical Scanning Interferometry profile of an example multiscale 30/30/5 grooved + 1 minute HF etched surface. Area: 0.598 mm by 0.442 mm. Magnification: 20x.

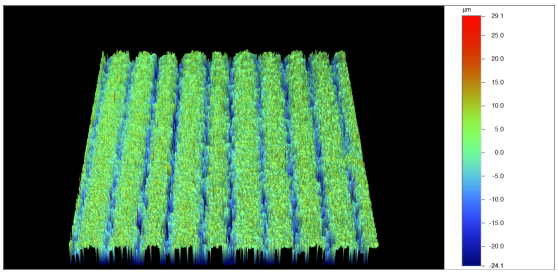

Figure 4.10: Vertical Scanning Interferometry profile of an example multiscale 15/30/10 grooved + 4 minute HF etched surface. Area: 0.598 mm by 0.442 mm. Magnification: 20x.

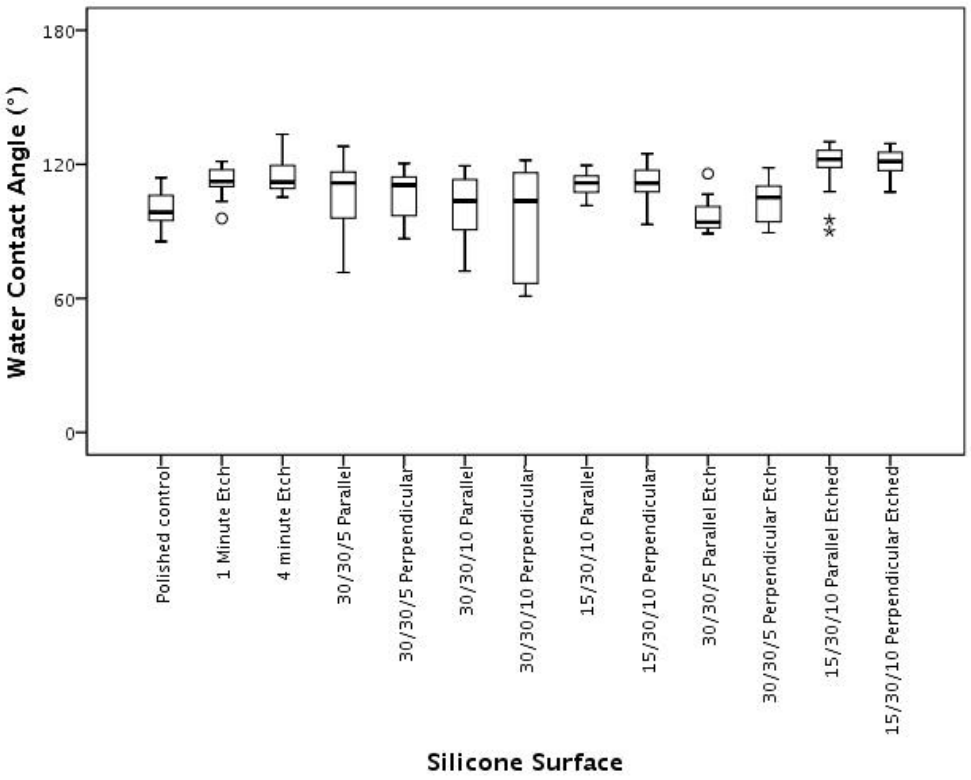

Figure 4.11: Water contact angles for smooth, HF etched, grooved and multiscale silicone surfaces.

on other grooved surfaces.

4.3.4 BCA Assay

The lowest protein concentration was observed on control surfaces (0.479 ± 0.161 μg/cm^2, see fig. 4.12). The protein concentration was greater on 4 minute HF etched surfaces (0.586 ± 0.012 μg/cm^2), and greatest on 15/30/10 grooved surfaces (0.779 ± 0.061 μg/cm^2). An intermediate protein concentration was observed on multiscale surfaces (0.659 ± 0.042 μg/cm^2).

4.3.5 Intraclass correlation

Intraclass correlation coefficients were greater than the minimum level set, ICC(3,1) = 0.702, ICC(3,k) = 0.845. Therefore results were considered reliable between observers.

4.3.6 HF Etched Surfaces

Nano-scale roughening by HF treatment significantly increased number of cells per area compared with control samples: 1 minute HF etch ($p = 0.017$); 4 minutes HF etch ($p = 0.011$). No significant difference in number of cells per area was observed between the two etched sample groups.

Number of neurites per cell was significantly increased on surfaces that had been etched for 4 minutes (3.28 ± 1.66 neurites) compared with all other samples ($p \leq 0.001$). Etching for 1 minute did not significantly increase neurite number compared with control samples ($p = 0.558$): 2.82 ± 1.65 neurites; and 2.76 ± 1.63 neurites respectively, fig. 4.13a.

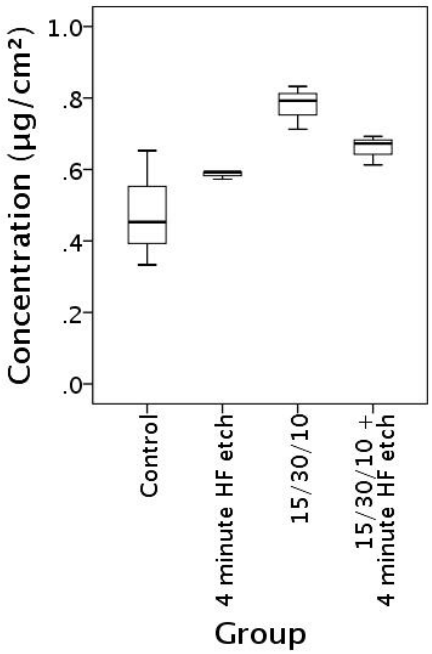

Figure 4.12: Protein concentration on polished control, HF etched, grooved and multiscale silicone surfaces. Determined using a micro-BCA assay.

Etching surfaces for 1 minute significantly increased neurite length compared with control samples ($p \leq 0.001$): 21.5 ± 16.4 μm; and 20.8 ± 19.1 μm respectively. Etching for 4 minutes significantly reduced neurite length compared with all other samples (16.9 ± 13.1 μm, $p \leq 0.001$), fig. 4.13b.

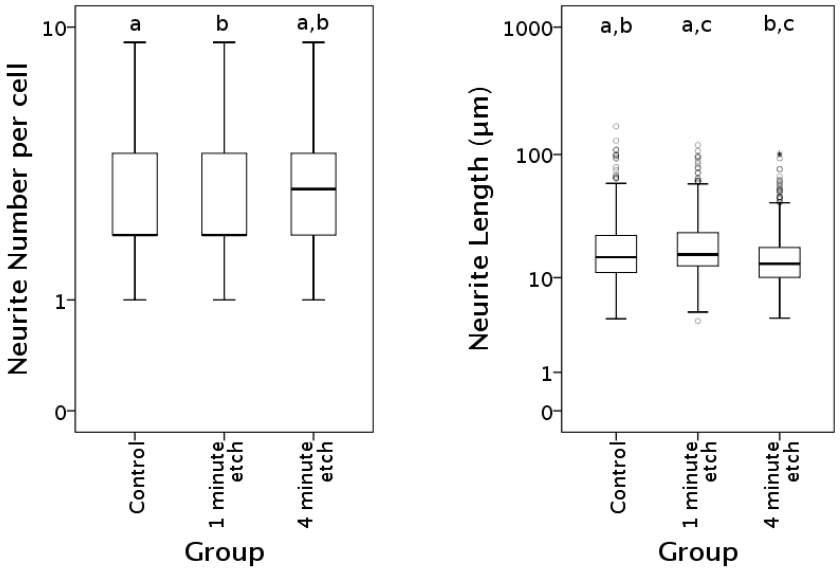

(a) PC-12 cell neurite number on HF etched samples. Data displayed on a logarithmic scale. Significant differences are indicated by paired letters: a,b, $p \leq 0.001$.

(b) PC-12 cell neurite length on HF etched samples. Data displayed on a logarithmic scale. Significant differences are indicated by paired letters: a,b,c, $p \leq 0.001$.

Figure 4.13: PC-12 cell neurite outgrowth data for silicone samples templated using Ti-6Al-4V samples with the following surface treatments: polished controls; 1 minute HF etch; 4 minutes HF etch.

Surface	Median Angle of Alignment ° (range), n=6, k=1	Median Angle of Alignment ° (range), n=6, k=5	Angle of Alignment ° n=1, k=1
15/30/10	48.0565 (10.188,90)	90 (6.8,90)	0.59
30/30/10	87.433 (1.233,90)	43.195 (38.97,90)	2.574

Table 4.3: Angles of neurite alignment on grooved silicone surfaces calculated using the NCP criterion.

4.3.7 Grooved Surfaces

Significantly fewer PC-12 cells were observed on samples with deep grooves (10 μm) compared with control samples ($p \leq 0.007$). There was no significant difference in number of cells per area between the different grooved samples ($p \geq 0.143$). Samples with shallower grooves (5 μm) did not have a significantly different number of cells per area compared with control samples ($p = 0.045$, $p_{cut} = 0.0125$).

The number of neurites per cell was significantly reduced on the deep, narrow 15/30/10 grooved samples (1.97 $\pm$ 1.05 neurites) compared with all other samples ($p \leq 0.001$). The number of neurites per cell did not change significantly between wider 30/30/10 samples (2.31 $\pm$ 1.42 neurites), shallower 30/30/5 samples (2.34 $\pm$ 1.43 neurites) and smooth controls (2.56 $\pm$ 1.70 neurites), fig. 4.14a.

The longest neurites were observed on shallow grooved 30/30/5 samples (23.5 $\pm$ 20.8 μm) these were significantly longer than the neurites observed on 30/30/10 samples (21.5 $\pm$ 19.3 μm) and control surfaces (21.5 $\pm$ 20.7 μm, $p \leq 0.001$). Neurites expressed on 15/30/10 samples were of intermediate length (22.2 $\pm$ 17.0 μm) and were not significantly different compared with all other sample groups ($p \geq 0.038$, $p_{cut} = 0.025$). The observed neurite lengths were not significantly different ($p = 0.947$) between 30/30/10 grooved samples and smooth control samples, where cells with the shortest neurites were found fig. 4.14b.

Neurites on the deep, narrow 15/30/10 grooved samples were more aligned (31.6° $\pm$ 25.6°) compared with all other samples ($p \leq 0.001$). Neurites were also more aligned on deep, wide 30/30/10 grooved surfaces (41.1° $\pm$ 26.0°) compared with smooth controls (46.6° $\pm$ 26.7°, $p \leq 0.001$) and shallow 30/30/5 grooved surfaces (45.3° $\pm$ 25.5°, $p \leq 0.001$). PC-12 cells on shallow 30/30/5 grooved samples did not align compared with smooth samples ($p = 0.168$). Neurite alignment is displayed as a series of histograms with 10° bins, fig. 4.15. Angles of alignment are shown in table 4.3.

4.3.8 Multiscale Surfaces: Experiment 1

A first series of experiments was carried out using shallow 30/30/5 grooves and 1 minute HF etching. These treatments were carried out in combination (multiscale) and separately and compared with polished controls.

No significant difference in cell number per area between samples was found by Kruskall Wallis Test ($p = 0.064$), therefore Mann-Whitney U tests were not carried out.

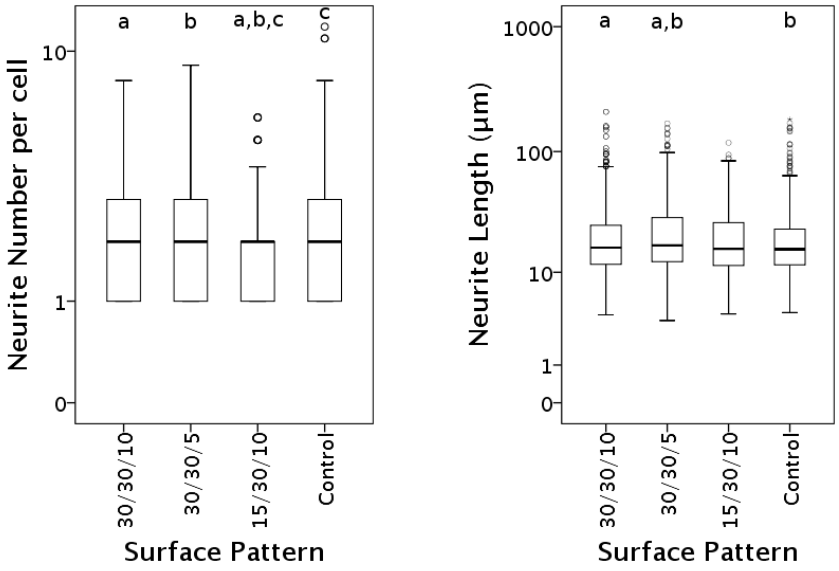

(a) PC-12 cell neurite number on grooved samples. Data displayed on a logarithmic scale. Significant differences are indicated by paired letters: a,b,c, $p \leq 0.001$.

(b) PC-12 cell neurite length on grooved samples. Data displayed on a logarithmic scale. Significant differences are indicated by paired letters: a,b, $p \leq 0.001$.

Figure 4.14: PC-12 cell neurite outgrowth data for silicone samples templated using Ti-6Al-4V samples with the following laser patterned grooves: 30 μm wide, 30 μm spacing, 5 μm deep (30/30/5); 30 μm wide, 30 μm spacing, 10 μm deep (30/30/10); 15 μm wide, 30 μm spacing, 10 μm deep (15/30/10).

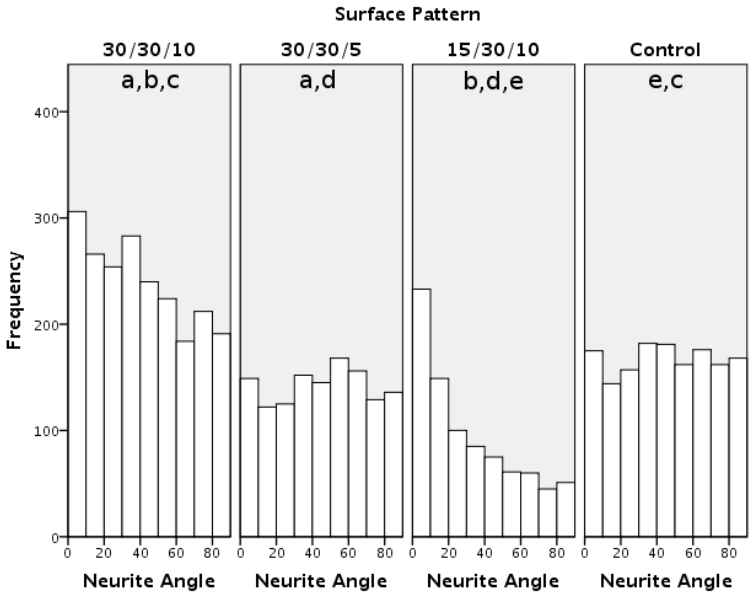

Figure 4.15: Histograms of PC-12 cell neurite angles on grooved samples. Neurites are most aligned on 15/30/10 samples, and also aligned on 30/30/10 samples. 10° bins. N.B. total number of angles is not equal between samples. Significant differences are indicated by paired letters: a,b,c,d,e, $p \leq 0.001$.

Neurite number per cell was significantly reduced on 30/30/5 grooved (2.01 ± 1.30) compared with controls (2.17 ± 1.29, $p \leq 0.001$) and etched samples (2.31 ± 1.31, $p \leq 0.001$). In addition, neurite number was significantly reduced on grooved and etched samples (1.92 ± 1.12) compared with controls

(p = 0.002) and etched samples (p $\leq$ 0.001). Neurite number was significantly increased on surfaces templated with titanium alloy discs which were etched for 1 minute compared with smooth control surfaces (p = 0.011). No significant difference in neurite number was observed between 30/30/5 grooved and grooved and etched samples (p = 0.548), fig. 4.16a.

Neurite length was reduced significantly on 30/30/5 grooved (13.7 $\pm$ 9.02 μm) and multiscale surfaces (15.0 $\pm$ 12.1 μm) compared with 1 minute HF etched surfaces (15.1 $\pm$ 10.1 μm) and polished controls (14.8 $\pm$ 9.46 μm,p $\leq$ 0.003). PC-12 cells on multiscale surfaces exhibited significantly longer neurites than on grooved surfaces (p = 0.014, p_{cut} = 0.025). No significant difference in neurite length was observed between 1 minute HF etched and polished control samples (p = 0.742), fig. 4.16b.

Neurites did not align on shallow 30/30/5 grooved multiscale surfaces (p = 0.774, fig. 4.17), therefore angles of alignment were not calculated.

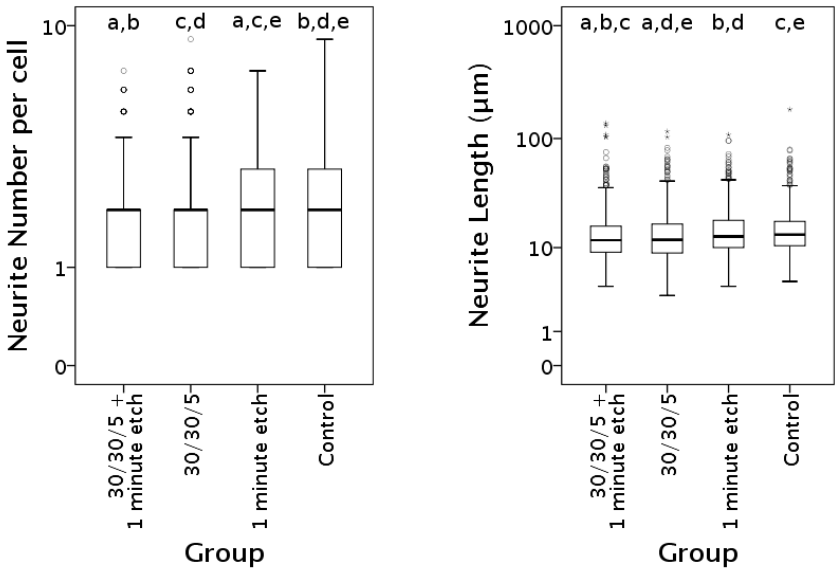

(a) PC-12 cell neurite number on grooved and etched samples. Data displayed on a logarithmic scale. Significant differences are indicated by paired letters: a,c,d, p $\leq$ 0.001; b, p = 0.002; e = 0.011.

(b) PC-12 cell neurite length on grooved and etched samples. Data displayed on a logarithmic scale. Significant differences are indicated by paired letters: a, p = 0.014; b, p = 0.003; c,d,e, p $\leq$ 0.001.

Figure 4.16: PC-12 cell neurite outgrowth data for silicone samples templated using Ti-6Al-4V samples with the following surface treatments: polished controls; 1 minute HF etch; 30 μm wide, 30 μm spacing, 5 μm deep laser patterned grooves (30/30/5); multiscale 30/30/5 laser patterned grooves + 1 minute HF etch.

4.3.9 Multiscale Surfaces: Experiment 2

A second series of experiments was carried out using deep, narrow 15/30/10 grooves and 4 minute HF etching. These treatments were carried out in combination (multiscale), separately and compared with smooth controls.

PC-12 cell number per area was significantly reduced on etched surfaces compared with 15/30/10

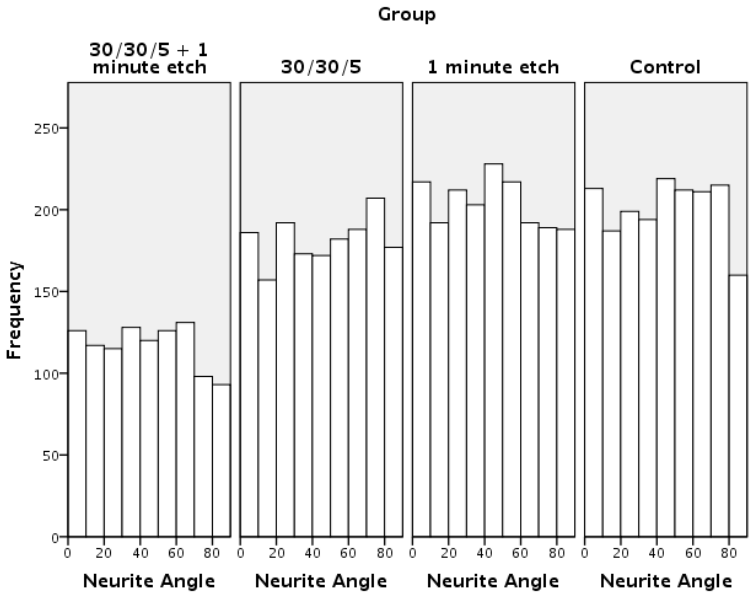

Figure 4.17: Histograms of PC-12 cell neurite angles on grooved and etched samples. Neurites are not significantly aligned on any samples. 10° bins. N.B. total number of angles is not equal between samples. Differences are not significant, p = 0.774.

grooved and multiscale surfaces ($p \leq 0.008$). There were significantly more cells per area on 15/30/10 grooved samples compared with controls (p = 0.006). No other significant differences were observed ($p \geq 0.055$).

Significantly fewer neurites were observed on 15/30/10 grooved samples (1.60 ± 0.893) compared with all other samples ($p \leq 0.006$, $p_{cut} \geq 0.008$). Neurite number was significantly reduced on multiscale samples (1.77 ± 0.977) compared with etched (2.40 ± 1.50) and control samples (2.19 ± 1.23, $p \leq 0.001$). No significant difference in neurite number was observed between etched and control samples (p = 0.192), fig. 4.18a.

Neurite length was significantly increased on all samples compared with control (16.5 ± 11.9 μm, $p \leq 0.001$). PC-12 cells expressed significantly longer neurites on multiscale surfaces (21.1 ± 14.1 μm) compared with etched surfaces (20.1 ± 17.6 μm, p = 0.001). No significant differences in neurite length were observed between: grooved (21.2 ± 15.8 μm) and multiscale surfaces (p = 0.231); and grooved and etched surfaces (p = 0.044, p_{cut} = 0.025), fig. 4.18b.

Neurites were more aligned on multiscale ($39.9° \pm 25.7°$) and grooved samples ($37.3° \pm 26.7°$) compared with samples without grooves ($p \leq 0.01$). There was no significant difference in alignment between multiscale and grooved surfaces (p = 0.05, p_{cut} = 0.025). Cells did not align on etched surfaces ($43.3° \pm 25.8°$) compared with controls ($43.4° \pm 26.1°$, p = 0.917), fig. 4.19. Angles of alignment are shown in table 4.4.

Surface	Median Angle of Alignment ° (range), n=6, k=1	Median Angle of Alignment ° (range), n=6, k=5	Angle of Alignment ° n=1, k=1
15/30/10	90 (3.59,90)	90 (1.57,90)	2.6
15/30/10 + 4 minute HF etch	90 (8.53,90)	90 (14.71,90)	90

Table 4.4: Angles of neurite alignment on grooved and multiscale silicone surfaces calculated using the NCP criterion.

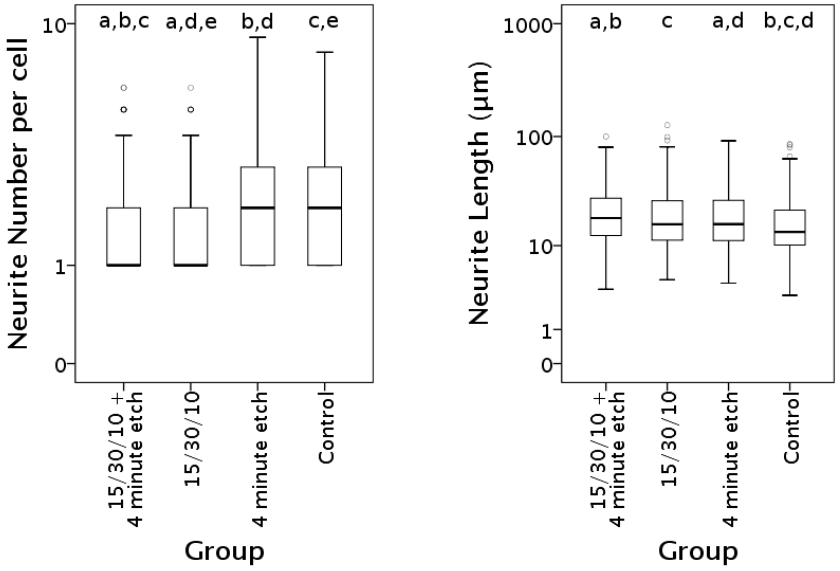

(a) PC-12 cell neurite number on grooved and etched samples. Data displayed on a logarithmic scale. Significant differences are indicated by paired letters: a, p = 0.006; b,c,d,e, p $\leq$ 0.001.

(b) PC-12 cell neurite length on grooved and etched samples. Data displayed on a logarithmic scale. Significant differences are indicated by paired letters: a,b,c,d, p $\leq$ 0.001.

Figure 4.18: PC-12 cell neurite outgrowth data for silicone samples templated using Ti-6Al-4V samples with the following surface treatments: polished controls; 4 minute HF etch; 15 μm wide, 30 μm spacing, 10 μm deep laser patterned grooves (15/30/10); multiscale 15/30/10 laser patterned grooves + 4 minute HF etch.

4.3.10 Protein Mixes on Multiscale Surfaces

Experiments were carried out to compare multiscale surfaces with Collagen-IV (CIV) and Collagen-IV - Laminin-2-4 - Nidogen-1 (All-in-one / All) coatings. These treatments were applied to control, 4 minute HF etched, 15/30/10 grooved and multiscale silicone (PDMS) surfaces.

PC-12 cell number per area was significantly reduced on collagen-IV grooved samples compared with collagen-IV coated control, etched and multiscale samples ($p < 0.001$). Number of cells per area reduced significantly on all-in-one coated grooved samples compared with all-in-one coated control samples ($p < 0.001$). No other significant differences were observed, although overall fewer cells were observed on grooved samples, more on grooved and etched samples, and the greatest density of cells was

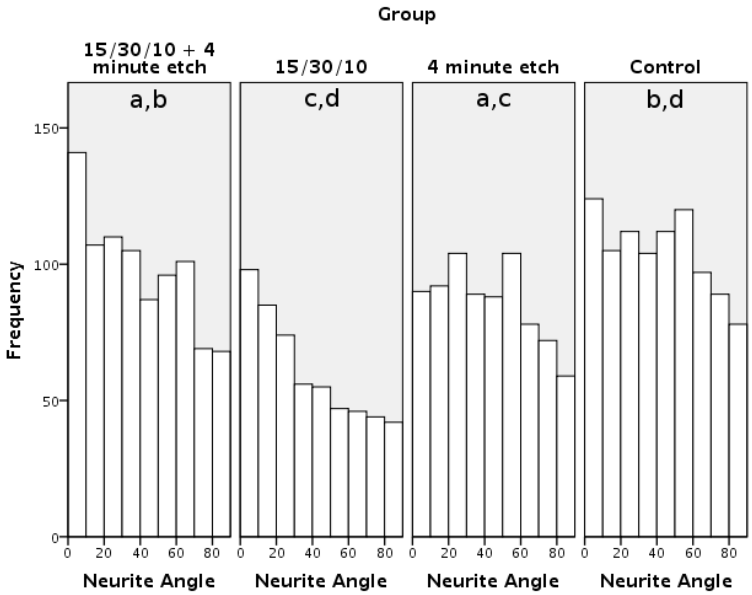

Figure 4.19: Histograms of PC-12 cell neurite angles on grooved and etched samples. Neurites are most aligned on 15/30/10 samples, and also aligned on 15/30/10 + 4 minute etch samples. 10° bins. N.B. total number of angles is not equal between samples. Significant differences are indicated by paired letters: a, p = 0.01; b, p = 0.005; c,d, p $\leq$ 0.001.

observed on control and HF etched surfaces.

Significantly fewer neurites were observed on collagen coated 15/30/10 grooved samples (1.86 $\pm$ 1.08) compared with etched (3.49 $\pm$ 1.78) or control (3.03 $\pm$ 1.64) collagen coated samples (p $<$0.001). Neurite number was significantly reduced on all-in-one 15/30/10 samples (2.19 $\pm$ 1.25) compared with control all-in-one samples (2.75 $\pm$ 1.53) (p $<$0.004), but not compared on all-in-one multiscale samples (2.55 $\pm$ 1.32) compared with control samples (p = 0.481). Multiscale collagen coated samples (2.15 $\pm$ 1.01) had reduced neurite number compared with roughened collagen coated samples (3.49 $\pm$ 1.78) (p $<$0.001). The addition of laminin and nidogen reduced neurite number only for all-in-one roughened samples (2.67 $\pm$ 1.51) (p $<$0.002) and otherwise had no significant effect. More neurites were observed on multiscale surfaces than grooved surfaces with both coatings, though this difference was not significant. Neurite number was increased (not significantly) by the addition of laminin and nidogen to coatings on multiscale samples, fig. 4.20a.

Neurites were longer on collagen coated grooved (43.4 $\pm$ 29.2 μm) and multiscale (37.7 $\pm$ 16.4 μm) samples compared with collagen coated etched (28.72 $\pm$ 17.1 μm) and control (33.9 $\pm$ 23.2 μm) samples (p $<$0.002). Neurites on multiscale samples coated with collagen, laminin and nidogen (54.0 $\pm$ 37.8 μm) were longer than control, roughened and grooved samples coated with the same proteins (36.1 $\pm$ 23.2 μm, 24.3 $\pm$ 14.1 μm and 36.2 $\pm$ 23.5 μm respectively, p $<$0.001). No significant difference in neurite length was observed between control and grooved samples with all-in-one coatings (p = 0.539), although the all-in-one coated grooved sample neurites were significantly longer than on the respective

HF etched samples ($p < 0.001$). Neurites were significantly shorter on HF etched samples compared with controls with both protein coatings ($p < 0.001$). The mixed protein coatings altered neurite length significantly compared with collagen coated samples in one case: with grooved samples ($p = 0.001$). fig. 4.20b.

In all cases neurites were significantly more aligned on grooved and multiscale samples compared with etched and control samples ($p < 0.001$), fig. 4.21. All etched and control samples had mean average angles in the range 42.2° to 48.8°, while grooved and multiscale sample means fall in the range 21.0° to 33.6°. No significant alignment was observed on surfaces with random roughness. Alignment was significantly reduced on all-in-one multiscale surfaces compared with all-in-one grooved surfaces ($p = 0.002$), the same effect was not observed on collagen coated grooved and multiscale surfaces ($p = 0.017$, $p_{cut} = 0.008$).

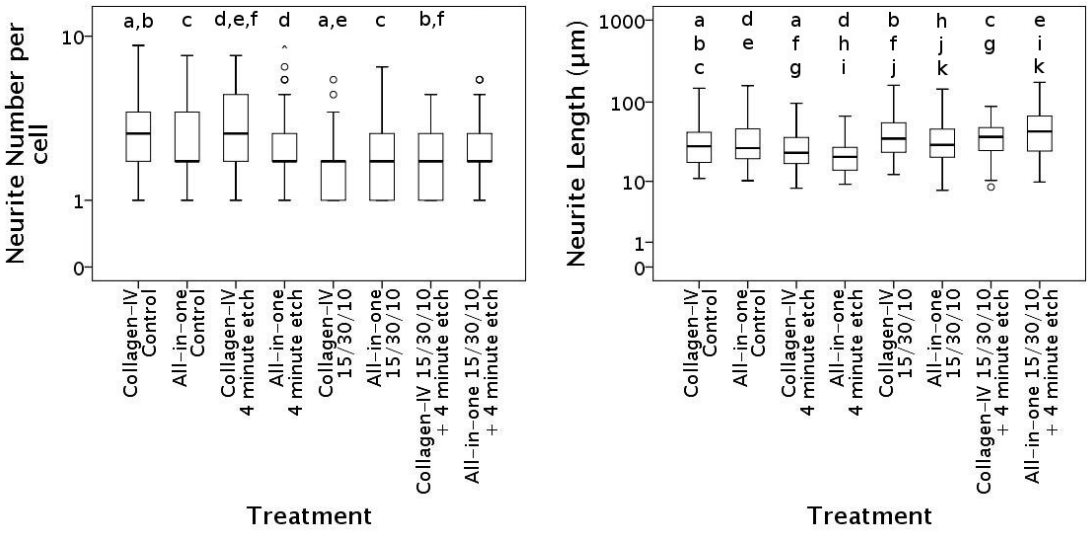

(a) PC-12 cell neurite number on protein coated grooved and etched samples. Data displayed on a logarithmic scale. Significant differences are indicated by paired letters: a,b,d,e,f, $p \leq 0.001$; c, $p = 0.004$.

(b) PC-12 cell neurite length on protein coated grooved and etched samples. Data displayed on a logarithmic scale. Significant differences are indicated by paired letters: a,c,d,e,f,g,h,i,k, $p \leq 0.001$; b,j, $p = 0.001$.

Figure 4.20: PC-12 cell neurite outgrowth data for silicone samples templated using Ti-6Al-4V samples with the following surface treatments: polished controls; 4 minute HF etch; 15 μm wide, 30 μm spacing, 10 μm deep laser patterned grooves (15/30/10); multiscale 15/30/10 laser patterned grooves + 4 minute HF etch. Each substrate is coated with either collagen-IV or a mixed (all-in-one) collagen-IV - laminin-2,-4 - nidogen coating.

4.3.11 Cell Morphology

Cell morphology was affected by the surfaces that they were attached to, see figs. 4.22a to 4.22h. Although the images are representative the high variability between cell morphology means the images are difficult to interpret without statistical analysis. However, cells on grooved samples, in particular those with deeper grooves, appear to exhibit fewer, longer neurites, an observation supported by the statistical analyses. Observations, not quantified, indicate that neurites grow preferentially along the top of ridges.

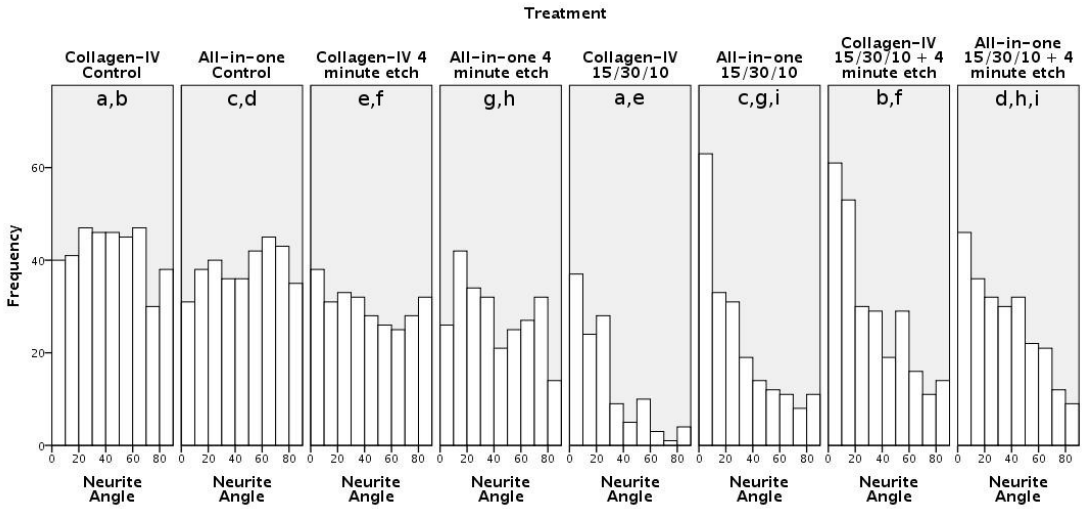

Figure 4.21: Histograms of PC-12 cell neurite angles on protein coated grooved and etched samples. 10° bins. N.B. total number of angles is not equal between samples. Significant differences are indicated by paired letters: a,b,c,d,e,f,g,h, $p \leq 0.001$; i, $p = 0.002$.

Neurite-neurite interactions were observed on all surfaces. The exhibition of these interactions was partly dependent upon the neurite length, with longer neurites more likely to encounter other neurites, but also dependent upon the random local seeding density of PC-12 cells. Therefore the neurite-neurite interations shown are not a strong indicator of surface suitability.

Immunoflourescence microscopy showed vinculin markers on some cells, indicating focal adhesion formation (figs. 4.23a and 4.23b). In addition neurites could be observed using vinculin staining, this indicated that non-specific binding was taking place. Furthermore, fluorescent antibodies adsorbed to the modified substrates and the depth of focus was not sufficient for neurites to be imaged in high quality. Therefore vinculin stains were not used for analysis and cell adhesion could not be quantified using vinculin markers.

Immunoflourescence microscopy using actin staining was more successful, with low levels of non-specific binding and adsorption to the substrate surface. Aligned neurites were observed on grooved samples and cells on roughened samples appeared to express more, shorter neurites. Example images are given in figs. 4.24a to 4.24h.

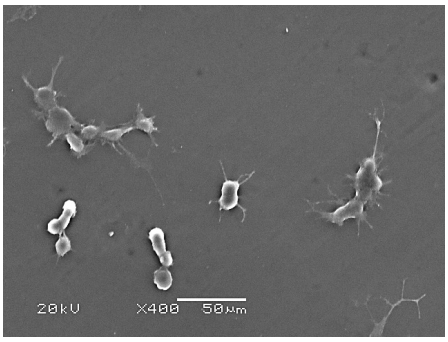

(a) Smooth Control Surfaces. 400x.

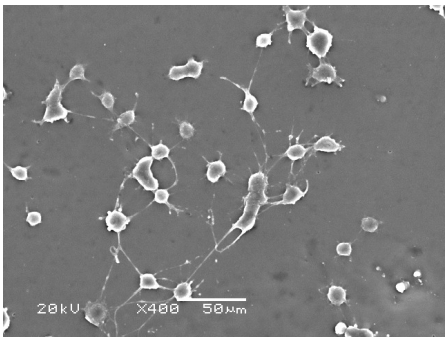

(b) 1 minute HF etched Surfaces. 400x.

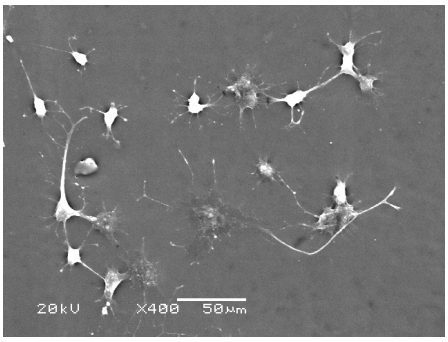

(c) 4 minute HF etched Surfaces. 400x.

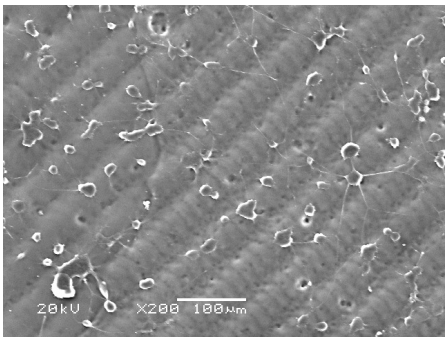

(d) 30/30/5 Grooved Surfaces. 200x.

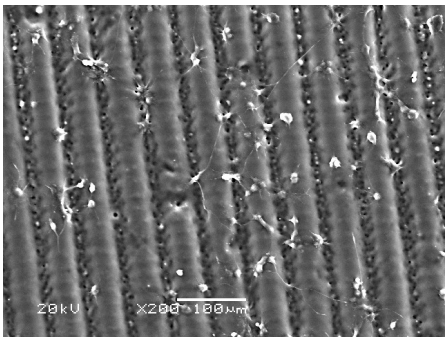

(e) 30/30/10 Grooved Surfaces. 200x.

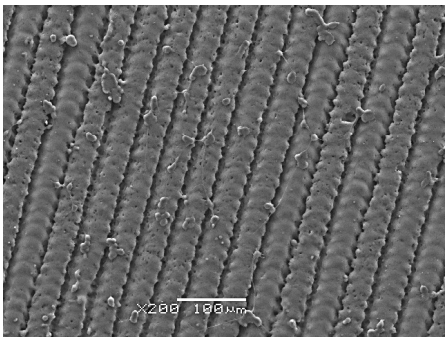

(f) 15/30/10 Grooved Surfaces. 200x.

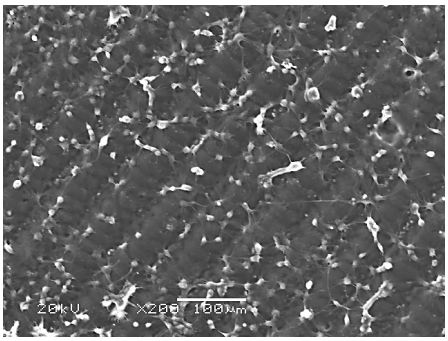

(g) 30/30/5 Grooved Surfaces with 1 minute HF etch. 200x.

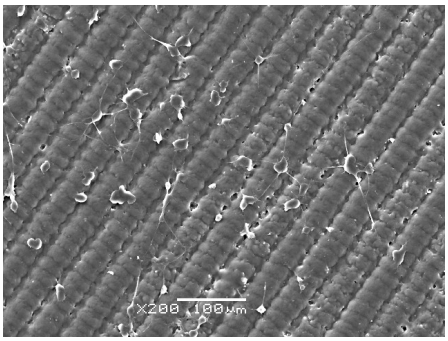

(h) 15/30/10 Grooved Surfaces with 4 minute HF etch. 200x.

Figure 4.22: Scanning Electron Micrographs of PC-12 cell neurite outgrowth on surfaces tested. Scale bar length and magnification is specified for each image.

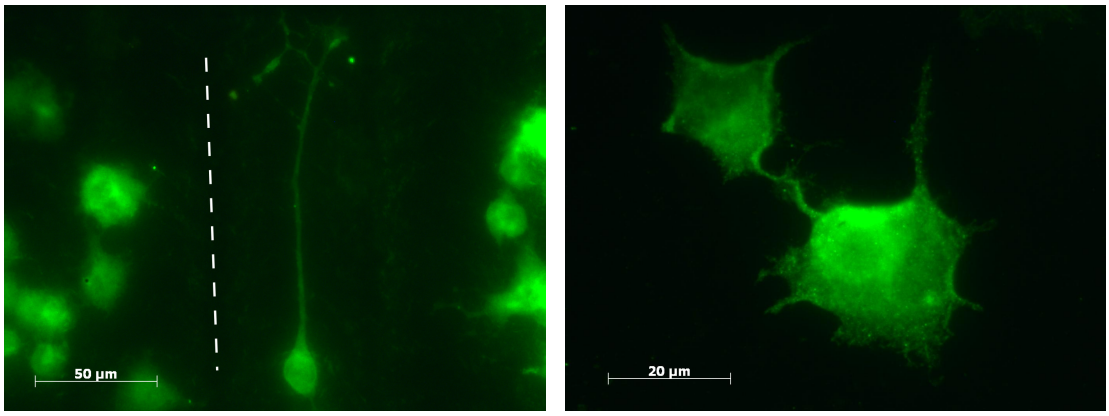

(a) PC-12 cells on a 15/30/10 Grooved Surface. Vinculin markers are not readily distinguished and background fluorescence is visible. Groove angle is indicated by dashed line. 40x magnification.

(b) PC-12 cells on a control surface. Vinculin markers are visible, but not readily distinguished from cell background fluorescence. 100x magnification.

Figure 4.23: Vinculin stained PC-12 cells on modified topographies. Scale bar length and magnification is specified for each image.

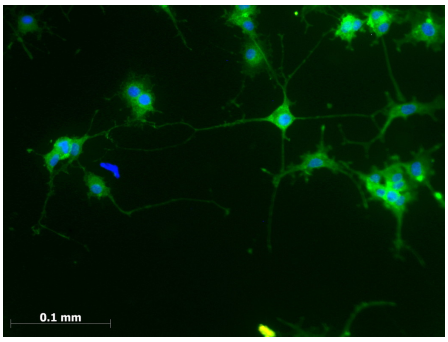

(a) Smooth Control Surfaces coated with Collagen.

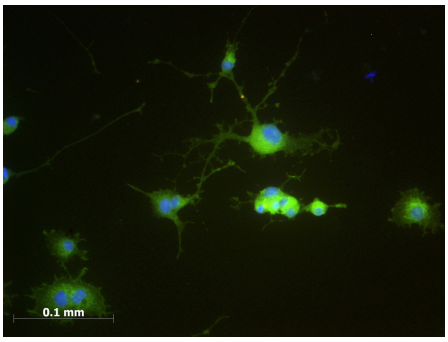

(b) Smooth Control Surfaces coated with all-in-one.

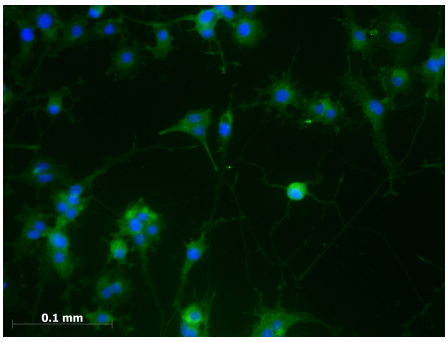

(c) 4 minute HF etched surfaces coated with Collagen.

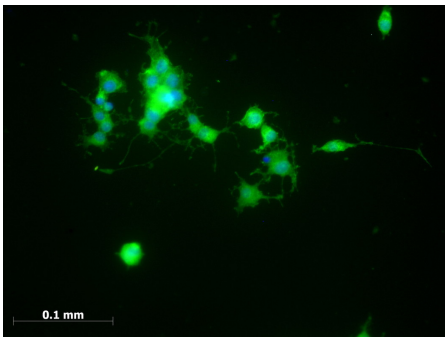

(d) 4 minute HF etched surfaces coated with all-in-one.

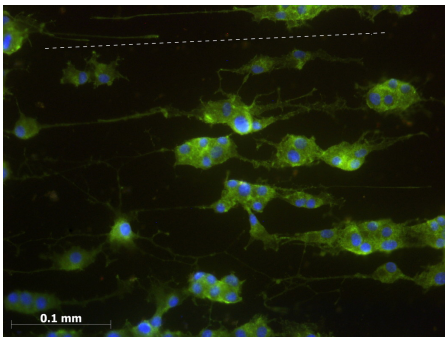

(e) 15/30/10 Grooved Surfaces coated with Collagen.

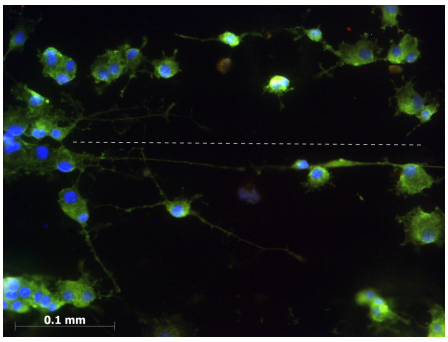

(f) 15/30/10 Grooved Surfaces coated with all-in-one.

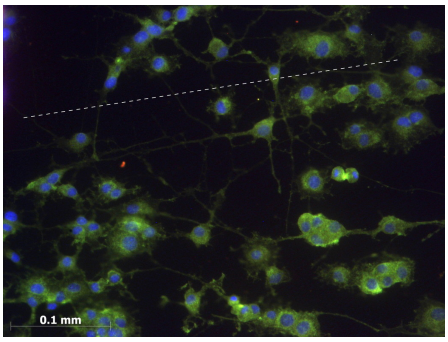

(g) 15/30/10 Grooved Surfaces with 4 minute HF etch coated with Collagen.

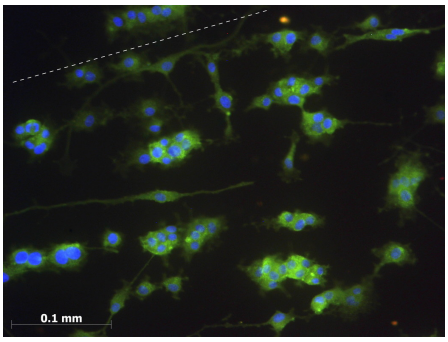

(h) 15/30/10 Grooved Surfaces with 4 minute HF etch coated with all-in-one.

Figure 4.24: Actin stained PC-12 cells on modified topographies with collagen-IV (10 μg/cm^2) or all-in-one coatings (10 μg/cm^2 collagen-IV, 1 μg/cm^2 laminin-2,-4, 0.175 μg/cm^2 Nidogen). All images were counter-stained with Hoechst 33258 and taken at 20x magnification. Where substrates are grooved, groove angle is indicated by dashed line.

4.4 Discussion

In all the conditions assessed in this study PC-12 cell growth was supported and neurites were observed.

4.4.1 Water Contact Angles

The observed surfaces fall within the hydrophobic region (>90°). Due to the surface hydrophobicity, increased geometric surface area and a rough profile, air may be present trapped between the water droplet and the surface. This increase in hydrophobicity, and possible trapped air, may influence collagen adhesion. This work uses FBS (and HS) supplemented media, it has been shown that cell adhesion from FBS supplemented suspension is reduced on hydrophobic regions, whether or not trapped air is removed [384]. This hydrophobicity presents a challenge for the use of PDMS as a neural biomaterial; however, surface modifications may be able to overcome this problem and increase cell adhesion.

4.4.2 BCA Assay

Increasing surface roughness increased the concentration of collagen-IV adsorbed to the surface. Grooves further increase the true surface area for adsorption without increasing the geometrical area, explaining the high protein concentration observed on 15/30/10 grooved surfaces. HF etching of grooved surfaces can be expected to smooth rough edges, reducing true surface area for adsorption and explaining the reduction in adsorbed protein.

These findings are supported by the literature. Increasing surface roughness (R_q) from 2 nm to 32.9 nm (approximately 16x increase) increases surface fibrinogen saturation by about 70% and bovine serum albumin saturation by about 30% [385]. Studies on poly-urethanes have shown that increasing roughness from 7 nm to 117 nm (approximately 17x increase) increases bovine serum albumin saturation by about 35% [321]. However, no difference in bovine serum albumin adsorption was seen on surfaces with R_a from 0.22 μm to 1.74 μm (approximately 7x increase), while a 50% increase in osteoblast number was observed [386]. Changes in protein self assembly may also occur, with bovine serum albumin spreading more evenly, and forming a dendritic rather than island structure on small (300 nm) compared with large (>1 μm) stainless steel grain size. [387], it should be noted that surface roughness was constant with change in grain size.

4.4.3 HF Etched Surfaces

Roughness's in the range of basement membrane (10 nm to 350 nm) are achieved on polished controls and following 1 minute HF etching. 4 minutes HF etching creates rougher surfaces; however, Raffa et. al. show that even with differences in roughness collagen coating can eliminate difference in cell adhesion [198]. Due to the topography of the polished surfaces the lowest roughnesses presented in the literature (<100 nm R_a) could not be achieved, alternative materials such as silicon could be used to

create smoother surfaces.

In these experiments more cells were observed on HF etched surfaces compared with less rough controls. This contrasts with results in the literature which showed that there is an optimal R_a value between 20 nm and 70 nm, and that cell adhesion reduces on surfaces above 80 nm [197, 198, 388]. This study contrasts with the literature, using collagen-IV coated silicone rather than silicon. The different method of roughening, resulted in a rougher surface, mimicking nanoporous surfaces which have been shown to improve PC-12 cell adhesion [199]. In this study rougher surfaces were found to adsorb more collagen-IV, and an increase in collagen can be expected to support more cells as observed.

Neurite outgrowth was observed on all surfaces, with more, shorter neurites on the roughest surfaces and the longest neurites observed on surfaces etched for 1 minute. Previous studies have shown increased neurite outgrowth on lower roughness values (25 nm) [388]. Again, the results of this study are more similar to those found by Moxon et. al., where 100 nm scale nanoporosity increased the number of neurites expressed [199]. Cells exhibiting fewer, longer neurites can be considered to be more mature, indicating that after 96 hours cells on smooth surfaces and the roughest surfaces were still in an immature state, expressing large numbers of pathfinding neurites. PC-12 cells were mature and expressed few longer neurites indicating a reduction in neurite architecture following path-finding.

It can be hypothesised that there is a synergistic effect of cell density, neurite number, and neurite length. Increased cell density will increase the likelihood of neurite junctions forming, at which point neurites typically stop extending and thicken. High levels of junction formation may result in greater numbers of shorter neurites, as observed on the roughest surfaces. To reduce the effect of junction formation cells must be seeded at a lower density.

4.4.4 Grooved Surfaces

On the deepest grooved samples cells resided mostly on the tops of ridges, this reduced the percentage area available for cell adhesion, reducing cell number. On shallower grooved surfaces cells were observed both in the valleys and on ridges. By confining PC-12 cells onto ridges the cells express fewer neurites which align with the underlying architecture. This change agrees with previous research showing reduced neurite architecture when cells are confined in channels [350]. PC-12 cells formed the fewest neurites on the narrowest features, where the cells were expected to be most confined.

Neurite length results do not agree with previous studies. Cells confined on narrower grooved samples were expected to form longer neurites [350, 358]; however, in this study the longest neurites were observed on shallow, undulating grooves. Intermediate lengths were observed on deep, narrow grooves, following the expected trend compared with the control surfaces. Cell morphology on the shallow grooves (fig. 4.22d) showed long neurites expressed radially around cell soma, the traction forces exerted by filopodia extending over the slightly convex ridge edges may encourage neurite extension

[350]. So, while cells on grooves express long neurites, it can be hypothesised that a slight convex surface would provide an alternative optimal surface for neurite outgrowth. Due to the nature of microchannels (concave) this possibility cannot be exploited in this case.

Neurites aligned on deep grooves only with a groove aspect ratio >0.3, this is greater than the 0.05 or 0.1 values predicted in the literature [359]. In this research shallow grooves formed an undulating surface, without sharp edges between grooves and ridges. Sharper grooves are expected to reduce the aspect ratio required for alignment. To achieve sharper edges a smaller laser spot size could be used, the 30 μm spot size has a variation in intensity across its width, creating 'U' shaped negative groove profile, leading to an 'n' shaped silicone ridge profile. Reich *et. al.* used femtosecond lasers to achieve direct writing of 10 μm groove widths [226]. Alternatively photolithography can be used to pattern materials with μm and nm scale precision [358, 360, 389].

The NCP criterion analysis was used to further characterise the extent of neurite alignment. In this case the angles of alignment calculated for each sample using k = 5 and k = 1 disagree. In addition the angles of alignment calculated using data from all samples, although giving the correct rank to the samples provide unrealistically low values. Although reported for some later experiments, angles of alignment will not be discussed hereafter.

4.4.5 Multiscale Surfaces: Experiment 1

To test for synergistic effects of μm scale grooving and nm scale roughening two groups were combined: shallow 30/30/5 grooves and 1 minute HF etching.

Etching for 1 minute was not found to alter the number of cells on the surface, in contrast with the results previously observed for HF etching. In addition fewer PC-12 cells were observed on shallow grooved samples, in contrast with previous results.

Etching samples increased the number of neurites compared with controls, although not significant in previous results the same trend was observed. The addition of grooves to samples reduced neurite number in this experiment, again previous results did not see a significant reduction but the same trend was observed. The reduction in neurite number observed on the multiscale surfaces is accounted for by the effects of grooving, with the addition of etching causing no increase in neurite number.

In this experiment neurite length was reduced on shallow grooves, this contrasts with results previously observed. However, the addition of etching to grooved samples increased neurite length, indicating that roughening is counteracting the negative effect grooving has on neurite outgrowth.

As shown previously neurites did not align on the shallow grooves with cells exhibiting extensions radially around the soma.

4.4.6 Multiscale Surfaces: Experiment 2

To test for synergistic effects of μm scale grooving and nm scale roughening two groups were combined in a further experiment where alignment was expected: 15/30/10 grooves and 4 minute HF etching.

Data on cells per area contrasted with all previous results in this study, finding that increasing roughness reduces cell number and that more cells are attached to samples with deep grooves.

Deep grooves reduced numbers of neurites, a phenomenon previously observed and discussed. Furthermore, the addition of roughening to grooved surfaces caused an increase in neurite number, although not to the control level. This indicates an additive effect where roughening is counteracting the negative effect grooving has on neurite outgrowth.

Previously it was shown that etching for 4 minutes increased neurite number compared with controls, this trend was observed in this experiment although it was not significant.

By roughening samples neurite length was increased, and this was true for grooved samples and polished samples. Previously, roughening for 4 minutes was shown to reduce neurite length, a finding disputed by the results of this experiment. As before longer neurites formed on grooved samples compared with controls. The effect seen here implies a synergistic effect, where roughening and grooving increase neurite length independently, and have an additive effect when combined.

Neurite alignment was observed on both grooved and multiscale surfaces. This agrees with previous studies which have shown alignment on μm scale grooves in the presence of underlying isotropy [376, 378].

4.4.7 Protein mixes on Multiscale Surfaces

To examine the effects of differing protein coatings collagen-IV and mixed protein coatings were applied to multiscale surfaces and relevant controls.

As with previous studies samples with deep grooves have a lower cell density. Roughening these surfaces increases the number of cells per area indicating that this counteracts the negative effects of grooving.

Cells expressed fewer neurites on grooved and multiscale surfaces compared with control or roughened samples, as was previously observed. Again an additive effect, increasing neurite number with roughening of grooved samples, was observed. In this case adding proteins to the coating tended to reduce the neurite number on control or roughened surfaces, but increases it on grooved and multiscale surfaces. The additional proteins may cause maturation and polarisation of cells on un-grooved surfaces, but encourage neurite outgrowth in cases where cells are already polarised by the underlying topography. This effect should be further examined, and protein expression at neurite ends could be characterised to indicate growing and maturing neurites.

In this experiment, as shown previously, neurite length was reduced on roughened samples. Longer

neurites were observed on grooved and multiscale samples, agreeing with previous results. For all-in-one coated surfaces etching of grooved samples further increased neurite length, in agreement with the previous results; however, this effect was not observed with collagen coated samples.

Alignment was observed on grooved and multiscale surfaces. The alignment effect is reduced on multiscale samples with all-in-one coatings, possibly because cells with increased neurite number are less polarised, so factors such as proteins, which increase neurite number will negatively impact neurite alignment. This contrasts with studies that have shown greater neurite alignment and fewer neurites on laminin peptide coatings compared with collagen-I coatings [351], however, in this study the complete laminin protein was used, so the epitope concentration may be lower.

4.4.8 Conclusions

It is concluded that multiscale surfaces are optimal for the promotion of neurite outgrowth and alignment *in vitro*. A synergistic effect of increasing neurite length and counteracting negative effects on neurite number was observed.

The findings of this study support the generation of a further hypothesis: multiscale surfaces will enhance neural regeneration within *in vivo* microchannels. Given the results presented in this chapter then it may be possible that surfaces with roughnesses in the range of basement membrane may encourage increased cell attachment and an increase in the number and length of neural extensions. Meanwhile grooves may guide extending axons and support cells along the length of a microchannel reducing the extent of fascicular misalignment. Grooves may also enhance neural extension length *in vivo* reducing the time in which regeneration takes place.

The addition of proteins to these surfaces to create an environment more representative of the neural basement membrane has little effect on PC-12 cell neurite expression. Significant differences are more regular and pronounced between topographies rather than with different proteins on the same topography. A cell line or primary cell source from the peripheral nerve may alter this balance, demonstrating differences with protein coatings. This is unexpected, because previous research suggests that proteins obscure small scale roughness changes ($<$300 nm feature size) [198]. In this study feature sizes on roughened surfaces ranged from 100 nm to 2 μm peak-to-peak, therefore surface structures were not 'hidden' by a protein coating with fibrils in the $<$100 nm range.

It is also proposed, based on the literature, that multiscale surfaces will alter the action of support cells (Schwann cells) and cells associated with fibrosis *in vivo*. This may lead to reduced occlusion within microchannels and a more stable nerve interface. In a best case scenario the roughened surface would be accepted by the nerve as a perineural membrane, and a complete fascicle will regenerate within a microchannel with minimal fibrotic tissue.

The surfaces developed fulfil the limitations set down for the study. None of the tested surfaces are

porous. The largest structure tested has a periodicity of 60 μm, indicating that from 1 to 3 repeats could fit on one wall of a microchannel. The structure indicated for further investigation has a periodicity of 45 μm, indicating that from 2 to 4 repeats could fit on one wall of a microchannel. Finally the structures are manufactured by a simple negative printing process which could be readily be patterned on one or two surfaces of a square cross-section microchannel by spin casting.

To create more defined structures, both roughnesses and grooves, silicon templates could be used. This would allow nm to μm scale grooving by photolithography and reactive ion etching. Etching processes on silicon can create controlled nm scale roughnesses from the 1 nm to 100 nm R_a scale.

This study has presented modifications aimed at the internal surfaces of microchannels, further work could examine the effect of topographical changes on electrode surfaces. Patterning and roughening electrodes is of interest to improve the impedance and charge injection properties [390]. Having differing surface structures on the electrodes compared with the encapsulating silicone microchannel may cause preferential attachment of cells to one or other of the surfaces [169, 391].

This study presents a series of *in vitro* experiments, using a neuron-like cell line. In the complex *in vivo* environment additional factors will be present: other cell types; 3D structure; foreign body response; etc.. Caution should be taken extrapolating the findings of this study to the *in vivo* environment without further investigation using either more representative *in vitro* models or *in vivo* models.

Chapter 5

The Manufacture of Microchannel Neural Interfaces

5.1 Introduction and Hypotheses

Implantable neural interfaces must be small, both to communicate selectively with micron-scale neural structures and to reduce harm to the host during electrode implantation [42]. This chapter describes four methods for manufacturing microchannel neural interfaces.

The neural interfaces investigated in this chapter of this thesis can be divided generally into groups by design and by manufacturing processes [392]. Neural interface designs have been discussed in chapter 1 of this thesis. Interfaces are grouped by their extent of invasiveness [55, 79]. Typically these designs are: extraneural interfaces; interfascicular interfaces; and intrafascicular interfaces. Intrafascicular interfaces include microwires, microelectrode arrays and regenerative interfaces. Microchannel neural interfaces are regenerative interfaces with longitudinal insulating microchannels. This chapter will discuss manufacturing processes used to create neural interfaces.

5.1.1 Microfabrication Techniques for Neural Interfaces

Processes will be considered in terms of their manufacturability and resulting materials properties. Manufacturability is the ease with which the interface can be manufactured and the potential to scale up the design, both physically to achieve more recording/stimulating channel and for mass or batch production. Materials properties are a concern for any implantable device. One key consideration is reducing damage to the implantation site by reducing mechanical property mismatch [102, 126, 181]. Tissues in the peripheral or central nervous system are soft and flexible; Young's modulus values for nerve under tension range between 0.5 MPa and 30 MPa, for the central nervous system the magnitudes of these properties are even lower, with cortical tissue having shear modulus between 0.5 kPa and 10 kPa [393]. To avoid relative micromotion between an interface and soft tissues, materials should be chosen with elastic moduli as close to these tissues as possible.

Examples of materials stiffnesses are given in table 5.1. Traditional electrode designs are hard and stiff, intended for needle-like insertion into the tissue of interest [42]. The most basic electrode design, a $<$100 μm microwire, can be made from a variety of metals: stainless steel, gold, platinum alloys, tungsten and others [57]. Microwires can be formed into arrays [120] using intermediate PCBs and stacked, in this manner arrays of up to 250 wires have been formed, with electrode pitch of 250 μm within layers and approximately 500 μm between layers [121,122]. These designs are scalable, however failure rates of the microwires are 40% over 18 months due to tissue reactions, impedance changes and other unidentified causes [57, 121]. Thin film interfaces (discussed below) have also been stacked in a similar manner [123].

Silicon based electrode designs allow for micron and sub-micron features to be manufactured using repeatable and automated processes [102]. Typically planar photolithography and etching are used, however techniques including laser cutting and micromachining are also in use. These stiff arrays have an advantage when recording in 3-dimensions; the relative locations of electrode sites are known due to the low deformation of the interface. In addition, application-specific integrated circuits (ASICs) can be included within silicon interfaces using standard chip processing techniques.

The Utah Array and its derivatives are stiff spike arrays formed from $>$1 mm thick silicon wafers [105,130,394], intended for cortical application they have been applied to the peripheral nervous system [135]. The spike arrays are implanted at high speed using a pneumatic pulse [130]. The Michigan array is formed as a planar design from thin silicon wafers, which can be assembled modularly to create multi-site arrays [139, 395]. A single Michigan array can have many spike-like shanks along which multiple electrode sites (4 is typical) are aligned. Other planar arrays have been developed using deep reactive ion etching and direct laser writing to produce 64 channel systems on an array of $<$50 μm diameter shanks allowing control over the final shank thickness [396,397]. Shanks can also be machined to create thinner tips, requiring lower insertion forces [398]. Instead of machining down into a block precursor, shank arrays have also been produced by electro-depositing a tapered, solid shank $<$1 μm over thin plasma-enhanced chemical vapour deposited silicon nitride and electron beam sputtered platinum layers [399]. Titanium substrates have also been used as a machinable support for chemical vapour deposition of silicon devices, which resist buckling on implantation and can therefore be made smaller than corresponding block silicon neural interfaces [400].

Ceramics and glasses are often used in active implants due to their hermetic properties, they can resist moisture ingress to electronic components for months to years [392, 401]. New developments in ceramic feedthroughs have led to High-Temperature Cofired Ceramics (HTCC) which allow the implementation of large numbers of electrode sites immediately situated on the feedthrough surface [166, 169, 250]. Ceramic materials can also take the place of silicon as a stiff substrate for photopatterned electrodes [402].

Polymeric materials present options for designing soft, flexible implants using cost effective and varied polymer processing techniques. Electrically active parts of implants must be encapsulated in a dielectric and this can be achieved simply using polymer moulding [167,403]. Encapsulation can also be achieved by spin coating or dip coating to form thin layers, which conform to the device. Encapsulation methods can be modified with sacrificial mould parts, or some encapsulant removal, to leave exposed electrodes or complex structures [113, 404]. In this manner, using removable nylon filaments wrapped with metal wires, microchannels of the filament dimension were produced with electrode sites created by the wrapped wire [146].

5.1.2 Conductive Polymers

Instead of directly interfacing with the nervous system using a hard, stiff metal or alloy, compliant conductors can be used as coatings or instead of metal tracks in neural interfaces [60, 425]. Elastic moduli of typically conductive polymers are given in table 5.1. These conductors can be micro-patterned and electrospun to form controlled topographies [426], the polymers can also be electrodeposited onto electrode sites with controlled thickness, topography and electrical properties [205]. Metal-silicone composites have been used to create compliant conductive tracks and electrodes [126].

In addition to reducing the potential harm through relative micromotion, conductive polymers can reduce electrode impedance by 1 to 3 orders of magnitude [60]. Conductive polymers can also be doped with bioactive molecules to modify cell reactions *in vitro* and *in vivo*, these materials show promise, however research has yet to demonstrate that these are effective at improving *in vivo* electrode performance [426]. Currently conductive polymers are not sufficiently developed for use in long-term devices, with poor mechanical and electrical stability (some coatings fail after 10 days *in vivo*) [60,205]. Compliant conductors will not be considered further in this work, but are expect to become useful once current challenges are overcome.

5.1.3 Thin film electrode arrays

Thin film electrode arrays are one way to increase neural interface compliance; the thin films are typically flexible and can be designed in a variety of forms depending upon application [427]. The basic thin-film design principle is presented in fig. 5.1.

Thin-film arrays include the TIME (transverse intrafascicular multichannel electrode) and tf-LIFE (thin-film longitudinal intrafascicular electrode) [109, 428]. Fabrication of these devices is a wafer process, meaning a silicon wafer is used as a substrate. A layer of polyimide is spin coated onto the wafer, platinum is sputter coated on top of the polyimide, the platinum is coated with another polyimide layer and the electrode sites are opened by reactive ion etching. This forms structures approximately 10 μm thick with exposed microelectrodes and track buried within polyimide insulator. The poly-imide used in this application is formed biphenyl dianhydride (BPDA) and p -phenilene diamine (PPD) precursors

Table 5.1: Young's Modulus (E, elastic modulus) values for example neural interface materials and approximate modulus mismatch with neural tissue. Measurements were cross referenced against Ashby and Jones, 2005 [405] where possible, to check for inaccuracies, no notable discrepancies were found.

Material	Young's Modulus	Modulus Mismatch (Orders of magnitude)	References
316L Stainless Steel (Annealed)	193 GPa	7	[406]
Alumina Ceramic (99.5%)	370 GPa	7	[407]
Benzocyclobutene (Cyclotene 4026, Dow Chem.)	2.70 GPa to 3.10 GPa	5	[408]
Gold	77.2 GPa	7	[409]
Iridium	516 to 528 GPa	8	[410]
Parylene C (SCS Inc.)	2.7 GPa	5	[411]
Platinum (Annealed)	171 GPa	7	[412]
Platinum / 10% Iridium (Annealed)	164.8 GPa	7	[413]
Poly(3,4-ethylenedioxythiophene) (PEDOT)	1 GPa to 2.7 GPa	5	[414]
Polyaniline (PAni)	0.7 GPa to 1.5 GPa	5	[415]
Polyimide (Durimide 7000 series, FujiFilm)	2.9 GPa	5	[416]
Polyimide (Pyralin 2611, HD MicroSystems)	8.5 GPa	6	[417]
Polypyrrole (PPy)	1.2 GPa to 3.7 GPa	5	[418]
Silicon	112.4 GPa	7	[419]
Silicone (Sylgard 184, Dow Corning)	1.32 MPa to 2.97 MPa,	2	[420]
Silicone (MED-1000, NuSil)	0.8 MPa	2	[421]
SU-8 Photoresist	2.2 GPa to 4.0 GPa	5	[422, 423]
Tungsten (Drawn)	400 GPa	7	[424]

which are robust due to their low water uptake *in vivo*.

Thin polyimide layers can be bonded to a substrate to form a penetrating device, polyurethane cylinders have been used to create a 16 electrode cortical interface [429]. Alternatively stiff substrates can be included within the thin films to allow for penetration [430, 431]. However, polyimides may be unsuitable for long-term applications because they adhere poorly to metal layers, causing rapid electrode failure in a wet environment [427].

An alternative thin-film substrate is parylene-C, a poly(p-xylene chloride) which has been used to form flexible neural probes [432]. Parylene is USP class-VI approved[1], however cracking of coating layers has been observed *in vivo* and delamination of parylene-metal bonds can occur in less than a week *in vitro* [433, 434]. In addition, although flexible, both parylene-C and polyimide are non-stretchable [427]. Stretchable, flexible implants would further reduce relative micromotion with tissue by better mimicking tissue properties.

Thin-film interfaces have also been produced using Benzocyclobutene (BCB) a polymer with very low water uptake. BCB is typically used as a spin coated dielectric on a silicon backing. Without silicon BCB has have been used to provide flexibility aiming to reduce relative micromotion [408, 435–437]. To overcome handling issues with BCB, temporary stiffeners (e.g. crystalline glucose) have been used and show promise [438], this may be applicable to other electrode types.

SU-8 negative photoresist may be advantageous for thin-film interfaces because it can be patterned to form variable thickness films [439]. The biocompatibility of SU-8 has been demonstrated to a superficial level, however it is not approved for medical devices [440]. Neural implants using SU-8 have been designed and tested for up to 1 year in rats [142], indicating good neurocompatibility.

Silicones (or PDMS, polydimethylsiloxanes) have been used for a wide range of implants from catheters and cosmetic prostheses to encapsulants for implanted electronics [187]. Many silicones with a range of properties have USP class-VI approval and can be easily spin coated to a range of thicknesses. Silicones are typically flexible and stretchable, this can present problems when coupled with a stiff metallisation layer: the PDMS looses adhesion, and stretching the weak rubber can lead to tearing or tracks breaking. Thin reinforcing layers of parylene have been suggested for silicone thin films to absorb stretching forces [427].

5.1.3.1 The metal foil process

Early silicone based thin-film interfaces were formed by bonding separate sheets or by block moulding silicone around metal electrodes and then exposing pads [441]. An automated manufacturing process for smaller scale thin-films using silicone encapsulation was presented by Schuettler et. al. [442, 443], based on work by Mortimer and by Naples et. al. [444, 445].

[1] United States Pharmacopoeia plastics designation VI is the most stringent test of biological reactivity in the USP classes. The class includes *in vivo* implantation testing for toxicity.

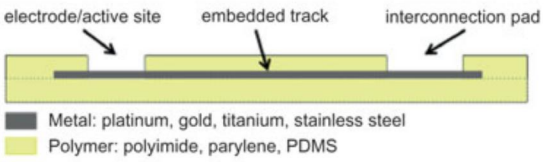

Figure 5.1: Schematic representation of a thin-film electrode array. Reproduced from [427], with kind permission from Cambridge University Press.

The process uses thin metal foil instead of sputter coated metallisation, this creates thicker metal tracks, reducing flexibility, but increasing the choice of metals available. Metal foils are typically 12.5 μm thick, however 5 μm to 25 μm foils can be used to increase flexibility or stability. Metal foils and silicone rubber layers are laser structured to create metal tracks embedded within silicone encapsulant and exposed at electrode sites. Any stiff substrate can be used instead of a silicon wafer, glass slides are commonly used due to reduce costs. The technique has been expanded to form multi-layered devices whereby more electrodes can be included per area (around 4.5 per mm^2). This overcomes one limitation to the number of electrodes by separating electrode tracks in 3-dimensions rather than the usual 2-dimensions of thin-film processes [446]. These arrays have been used *in vivo* for a variety of applications including cortical and retinal prostheses [427].

5.1.3.2 Flexible and Stretchable Track Designs

Thin-film designs with unstretchable substrates and designs using straight ribbons of metallisation typically cannot be elastically extended. Silicones are stretchable elastomers and it is desirable to design a metallisation layer, which will stretch with the substrate.

Meander shaped tracks have been successfully used with 12.5 μm platinum foils to create structures that can elongate over 20% before breaking [421]. With foils this comes at the expense of lower strength and increased track area. This concept is similar to the design of Cooper cable, a coiled structure which can survive millions of flexion cycles [285, 447].

Alternative methods have been developed for use with sputtered metal layers, previously metal films fractured at as low as 1% strain and required non-stretchable substrates to prevent breakage [427, 448]. Compressive stresses can be designed into gold sputtered layers creating wrinkles, which allow up to 10% strain before failure [448–450].

Conducting materials designed to stretch have also been tested including metal nano-particle inks, carbon nanotubes, conductive polymers and graphene layers [425, 451]. The reliability and long term *in vivo* performance of these materials must be better characterised to determine whether they are suitable for implanted neural interfaces. In addition the use of highly compliant designs complicates attachment to soft tissues, especially in mechanically dynamic structures such as peripheral nerves and care should be taken during handling and suturing to avoid stress concentrations or unwanted implant deformation [452].

5.1.3.3 From Thin Films to 3-Dimensions

To record from many neurons at any one time electrodes should be present at multiple sites within or around the nerve. For 2-dimensional films (e.g. tf-LIFE) this means inserting one or more flat arrays within the nerve [428, 453]. More precise spatial offsets can be achieved by stacking flat arrays to create multiple electrode sites in 3-dimensions [395].

Thin films are often rolled to create nerve cuffs. Multi-electrode polyimide cuffs have been designed to be self curling, by curing on a cylindrical former, or by inducing variable stresses in the substrate through stretching and spin coating [444, 454, 455]. Flexible films can be rolled to form ring structures [456] and multilayered coils [149]. By introducing stress to one sheet of PDMS during plasma bonding silicone cuff electrodes can be designed to self-coil [457].

Stacking flexible 2-dimensional films has been achieved in multiple ways. The metal foil process has been modified to create small spatial offsets in 3-dimensions [446]. Musick *et. al.* used plasma bonding to spatially offset rigid thin films using flexible silicone spacers [458]. This technique has since been used to develop 3-dimensional flexible thin film stacks with offsets of around 100 μm [459].

5.1.4 Electrode surface roughening

To reduce impedance electrode surface area should be as large as possible, however neural electrodes should be small to interface with intraneural structures and axons. To overcome this conflict electrodes can be roughened, increasing the effective surface area while maintaining a small geometric surface area.

Controlled microstructures can be formed on electrode surfaces. Gold nanorods can be created on flexible substrates using anodised porous alumina templates, these reduce 1kHz electrode impedance by approximately 25 times, however this requires chip based photolithographic and sputter techniques [460]. More complex 3-dimensional gold structures can also be created which show promise, however, *in vivo* stability of these structures has not been demonstrated [461]. Sputtered platinum, iridium or iridium oxide films can be used to alter electrode impedance, use of a thin titanium interlayer allows the deposition of nano-crystalline or nano-granulated surfaces with good electrical properties for both recording (impedance) and stimulation (charge injection capacity) [455].

Direct current (DC) etching is an effective, simple technique, which increases surface roughness, this has been shown to almost halve impedance using a +2 V current source [462]. Randomised roughness, achieved using low-current pulsated gold electroplating, can reduce electrode impedance by a factor of 100 (3 M Ohms to 30 k Ohms) [463]. Laser patterning can also create random roughness on platinum electrodes using low laser power to ablate only at points of interference, reducing impedance and improving charge injection properties [390]. Alternatively porous electrodes can be fabricated directly through a variety of methods with surface areas more than 3.5 times the geometric surface area [391, 464].

5.1.5 Microchannel Neural Interfaces

To date microchannel neural interfaces have been designed and manufactured using a range of techniques. Work has been carried out on a range of devices at the University of Cambridge, University of Birmingham and EPFL, Switzerland [2]. Single microchannels for *in vitro* testing can be manufactured cost and time effectively by hand. Briefly, wire conductors (e.g. gold) are wrapped around a nylon filament, the filament and wires are encapsulated in silicone and the filament is carefully removed once the silicone is cured [146]. This technique has also been applied for passive *in vivo* interfaces, filaments are spaced using copper grids and encapsulated, removal of the filaments leaves an array of longitudinal microchannels [113, 147]. By embedding microwires within the microchannels an active implant can be formed [147, 148].

To form active interfaces metallisation is required. Ridged polyimide thin films with integrated electrode tracks have been developed, these can be plasma treated and rolled to form microchannel arrays [146, 149, 150]. A 15 μm thick polyimide film is spin coated onto a silicon wafer, followed by deposition and patterning of a 175 nm thick gold layer. Photosensitive polyimide is spin coated to form a 5 μm encapsulating layer and electrodes and pads are opened using photolithography. A thick photosensitive polyimide layer (15 μm to 100 μm) is spin coated and patterned to form microchannels. These open thin film sheets are then plasma treated and rolled up, to form a coiled interface with an array of longitudinal microchannels. Problems with sealing the microchannel caps have been encountered and ongoing research at the University of Birmingham is investigating the use of 10 μm thick PDMS sheets to fully close and therefore electrically isolate the microchannels [151].

Photo patternable PDMS (PP-PDMS) a photosensitive silicone has been used for the development of microchannel interfaces [152]. In a thin-film process on a silicon wafer, a release layer is spin coated followed by thin layer of PDMS. Gold electrodes are evaporated, patterned by a kapton shadow mask. PP-PDMS was spin coated as a 30 μm thick encapsulant and exposed to UV light through a mask. Masked areas did not cure and the uncured PP-PDMS could be removed in a solvent bath. Microchannels were formed separately using an SU-8 mold, and plasma bonded to the thin film electrode sheet [153]. An alternative, thin film, design uses the same basic premise, however a lid is attached to the ridged microchannels during surgery, avoiding the need to section or rhizotomize nerves [154].

The Georgia Tech Regenerative Electrode (GT-RE), developed at Georgia Tech College of Engineering and Emory School of Medicine is a thin film based device [114, 115, 155]. The design concept and development of passive electrodes has been presented. Briefly, a 70 μm silicone layer is spin coated onto glass, silicone is plasma treated and a layer of SU-8 is spin coated. The SU-8 is patterned to form 100 μm by 100 μm microchannels. Finally a second 70 µm silicone layer is plasma bonded to the top of

[2] Additional work is currently ongoing at the University of Texas–Pan American, this group is not a collaborator of Cambridge/Birmingham/EPFL to the knowledge of the author.

the microchannels. In an active implant the 70 μm layers would contain patterned gold electrodes. This forms patterned electrode designs and is promising for the construction of complex microchannel geometries; however, SU-8 is unapproved for medical devices so should be avoided for designs aiming to be first-in-human. In addition to plasma bonding surface silanisation can be used to significantly improve bonding strength and better close microchannels [465].

Microchannel neural interface designs listed above are intended for use with tripolar electrode designs, however different electrode setups can be used. The regenerative microchannel based electrode interface (ReME) is a design developed at the University of North Carolina [157, 158]. Thin-film techniques are used to spin coat a 10 μm layer of parylene, gold electrodes are patterned onto the polymer with a titanium interlayer, and further polymer and electrode layers are patterned and pads are opened using reactive ion etching. Microchannel walls are also patterned from parylene using reactive ion etching and the channels are sealed using a 10 μm silicone (PDMS) layer. This design includes longitudinal and radial aligned electrodes, aimed at providing sense and control functions (recording and stimulating) respectively. The authors suggest this can be created in 2-D or rolled to form a 3-D construct. No *in vitro* or *in vivo* work has been presented with this electrode design, and only *in silico* numerical simulations are presented in the most recent publication. In addition, the stresses applied when rolling parylene may induce cracking, therefore care should be taken to ensure that the electrode design is robust.

5.1.6 Challenges

Current microchannel neural interface manufacturing processes have yet to overcome two limitations. Firstly, where microchannels are insufficiently sealed the electrical isolation between neighbouring channels is reduced. This reduces microchannel selectivity and the signal amplitude [51]. Secondly, rolled and other single layer microchannel neural interfaces have limited numbers of electrodes: the tracks and interconnects take up lateral space, rolled polyimide interfaces have electrode present in just a few microchannels ($<$10%) [51, 150].

5.1.7 Aims and Hypotheses

This chapter describes the manufacture of a microchannel neural interface, see fig. 5.2. The aims of this chapter are as follows:

- To investigate manufacturing processes for microchannel neural interfaces.
- To improve channel sealing and electrode number in microchannel neural interfaces.
- To assess the resulting interface designs and reduce electrode impedances.

It was hypothesised that:

- Direct current etching will significantly reduce electrode impedance and this effect will be apparent after *in vitro* and *in vivo* testing.

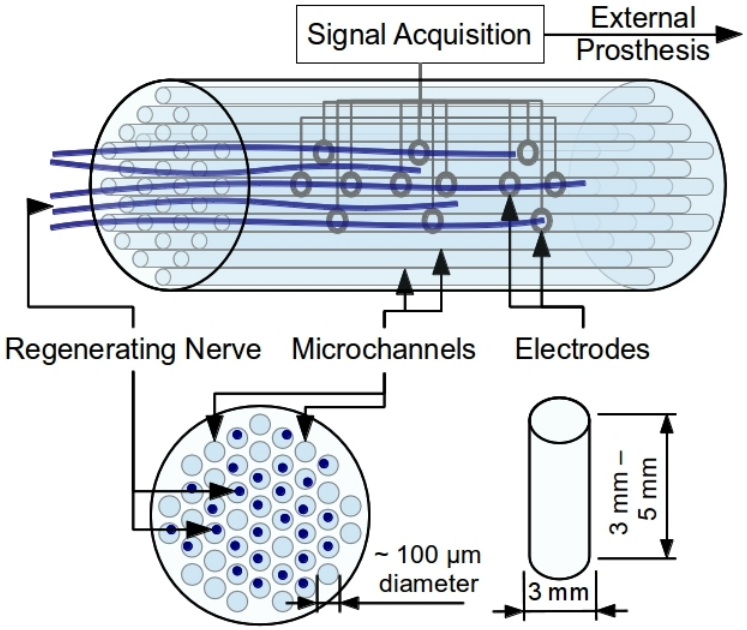

Figure 5.2: A diagram describing the approximate manufacturing aim for a microchannel neural interface.

5.2 Methodology

5.2.1 Microchannel Neural Interface Design

5.2.1.1 3D template method

The first prototype designs were developed using the methods developed by Lacour et. al. and FitzGerald et. al. to develop silicone implants [51, 113].

Nylon monofilament (100 μm to 150 μm) was suspended between TEM grids (Agar Scientific, UK) with grid sizes from between 100 and 50 lines-per-inch. This 3-dimensional template could be used to create a passive microchannel device or metallisation could be introduced using wire wrapped around the nylon filament. The templates were embedded in CF3-2186 silicone elastomer (NuSil) and Sylgard 184 (Dow Corning) and cured for 24 hours at 50°C. The nylon monofilament was removed and the electrodes were dissected into single–electrode blocks.

This method was found to be suitable for creating passive microchannel devices, however there are a number of limitations when wire is introduced. If the wire is wrapped around the filament too tightly it may be pulled into the channel when the filament is removed. Wires, which were not wrapped tightly enough did not consistently contact the channel, resulting in variable exposed surface area and variable impedance. To introduce an electrode to the centre of the array the wire must exit between the filaments forming other channels, if the insulation is damaged and the wire touches an adjacent channel isolation can be lost.

To avoid this limitation the inter-channel spacing was increased, however this reduced the transpar-

ency of the electrode.

Prototype microchannel interfaces were prepared using 100 μm diameter copper wire (enamel coated). The following method were used to remove the enamel coating: mechanical removal with scalpel; flaming in a Bunsen flame for 30 seconds; 6M sulphuric acid for 48 hours at room temperature; 18M sulphuric acid for 5 minutes at 60°C. The wires were examined using scanning electron microscopy.

Single microchannel interfaces were prepared with 2 wire electrodes, 5 mm inter-electrode distance, wire coiled twice per electrode, on 150 μm nylon monofilament. The electrodes were embedded in CF3-2186 silicone elastomer (NuSil) and cured for 24 hours at 50°C. The nylon monofilament was removed and the electrodes were disected into single–electrode blocks.

In order to test the inter-channel isolation (and intra-channel impedances) 4 channel electrodes were produced using a 3D templating process. 150 μm nylon monofilament was arranged between 75 Grid TEM Grids (Agar Scientific, UK). The grid holes were filled alternately. Electrodes were prepared with 2 wire electrodes, 5 mm inter-electrode distance, wire coiled four times per electrode, with 100 μm diameter copper wire stripped using 18M sulphuric acid. The electrodes were embedded in CF3-2186 silicone elastomer and cured.

The microchannels were filled with 0.9% saline in distilled H_2O and impedance values were measured using an EVAL–AD5934EBZ (Analog Devices) (see section 5.2.3). Impedance was measured between two electrode sites within the same microchannel, or electrodes in separate microchannels.

5.2.1.2 Metal negative method

Due to limitations on miniaturisation an alternative electrode design was developed. This alternative design aimed to achieve greater automation and reduce production times for implants. The design is based on a coiled polyimide interface developed and tested previously [51, 149]. The manufacture of the polyimide microchannel electrodes is cost prohibitive due to the manufacturing techniques used, therefore an alternative method was developed which could be carried out with the available equipment using silicone rather than polyimide encapsulants. This process is based upon the metal foil process previously described [442, 443], the process is summarised in fig. 5.3.

A Laserval Violino-2 1064 nm laser was used with a spot size of 30 μm. Laservall Smartist 4.1 software on Windows XP was used to control the laser system. Laser power was 10 W average and 40 kW maximum peak power.

Briefly, grooves were laser written into an Aluminium substrate. To create a release layer Haemosol detergent was used. The substrate was ultrasonicated in a saturated detergent in distilled water solution. The substrate was dried by repeated heating (50°C) and vacuum (50 mbar) cycles.

Silicone (Sylgard 184, Dow Corning) was spin coated over the substrate to a thickness of 30 μm and cured until tacky for 1 hour at 80°C. Pad windows were opened using direct laser writing. Platinum

or stainless steel foil (Advent Research Materials, UK) was placed over the silicone, air was removed under a 50 mbar vacuum for 30 seconds. The foil was patterned by laser cutting and excess was removed manually using. A final layer of silicone encapsulant (30 μm) was spin coated and cured (1 hour at 150°C).

To remove the interface from the substrate the substrate was placed in distilled water for at least 30 minutes. Gentle manipulation was used to remove the ridged microchannel interface. The interface could then be plasma treated using an air plasma for 2 minutes at 2 Torr (forward power 50W, reflected power 10W) and placed in an oven at 80°C to bond once coiled.

Appropriate laser parameters for forming grooves on aluminium were determined from 77 variant settings (7 different power settings and 11 variations of number and spacing of lasered lines, see. tables 5.2 and 5.3). The chosen method created a repeatable ridge of 130 μm height and 75 μm width at the base. The chosen parameters are as follows: 2 parallel lines 10 μm apart; 80% power; 10,000 shot frequency; 100 speed; 1 pass; and 100 repeats. Repeats were achieved by duplicating the line (in a .dxf file) 100 times.

Laser Setting	Power (%)	Shot Freq. (Hz)	Speed (mm/min)	Passes	n (lines)	Passages
1	40	10000	50	1	100	1
2	40	10000	100	1	100	1
3	40	5000	50	1	100	1
4	40	10000	50	1	100	2
5	60	10000	50	1	100	1
6	40	10000	200	1	100	1
7	80	10000	100	1	100	1

Table 5.2: Laser parameters for metal negative method. Passes, n and passages all have the same effect of laser etching the same line multiple times; however, the etching order varies, n was chosen to reduce dust damage from etching adjacent lines.

5.2.1.3 Plasma bonding method

Due to the high failure rate of interfaces produced by the metal negative method an alternative design was developed. This was based on a coiled polyimide interface developed and tested previously [51, 149].

Interfaces were formed in two parts and then joined by plasma bonding. The two parts will be referred to as the electrode layer (Part A), and the microchannel layer (Part B). The process is summarised in fig. 5.4.

First a layer of PSS (561223 Sigma, UK) was spin coated onto a 75 mm by 25 mm glass slide. Slides were spun at 200 rpm for 15 seconds and 2000 rpm for 10 seconds. Slides were then placed in an oven at 60°C for 15 minutes to dry. Silicone (Sylgard 184) was mixed at the standard 10:1 (w:w) ratio and 0.25 parts black pigment (Med-4800-2, Silicone-Polymers) was added to make the silicone less

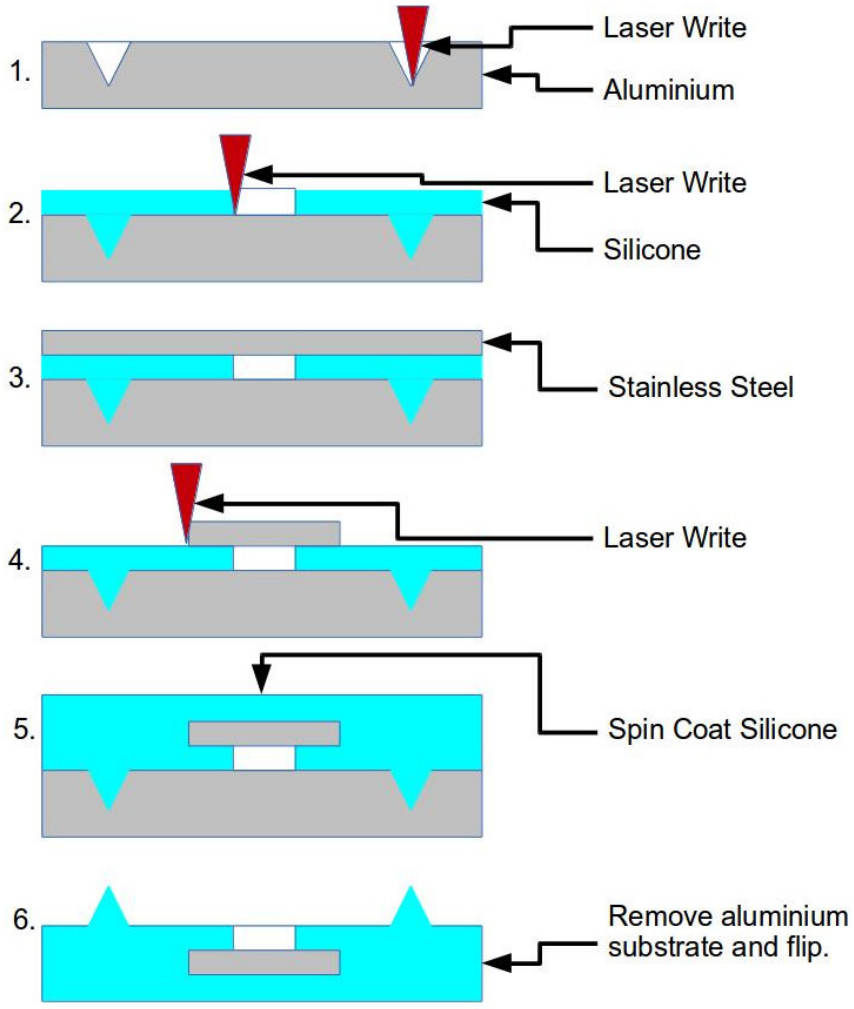

Figure 5.3: An overview of microchannel neural interface manufacture by the metal negative method. 1. Grooved aluminium negative created. 2. Silicone spin coated onto negative and pads opened. 3. Stainless steel foil placed on spin coated silicone layer. 4. Pads and electrodes patterned using laser cutter and excess foil removed. 5. Silicone spin coated onto foil. 6. Negative removed leaving open electrode between ridges. Not to scale.

Variation	Lines per groove	Line Spacing (μm)	Groove Spacing (μm)
1	2	10	200
2	3	10	200
3	4	10	200
4	5	10	200
5	2	20	200
6	3	20	200
7	4	20	200
8	1	0	200
9	2	30	200
10	3	30	200
11	4	30	200

Table 5.3: Groove designs for metal negative method.

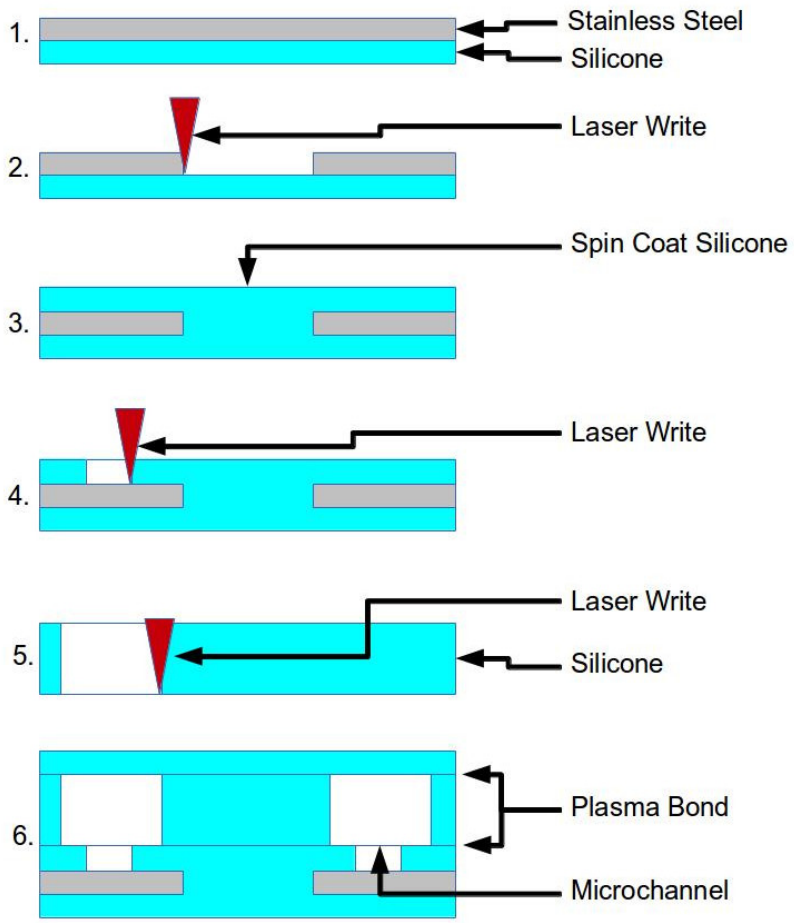

Figure 5.4: An overview of microchannel neural interface manufacture by plasma bonding. 1. Stainless steel foil placed on a spin coated silicone layer. 2. Foil patterned using a laser cutter and excess removed. 3. Silicone spin coated onto patterned foil. 4. Pads and electrodes patterned using laser cutter and silicone removed. This is part A. 5. Microchannels patterned using laser cutter and silicone removed. This is part B. 6. Electrode layer (Part A) and microchannel layer (Part B) plasma bonded. Not to scale.

transparent to laser light and therefore easier to laser pattern. Silicone was speed mixed for 2 minutes at 2500 rpm. Silicone was degassed at 30 mbar in a vacuum centrifuge for 1 minute or until bubbles were no longer visible.

Part A was formed as follows: Silicone was spin coated onto PSS coated slides at 1000 rpm for 45 seconds. The slides were placed in an oven at 60°C for 1 hour to part cure. Metal foil, 12.5 μm stainless steel or platinum (Advent Research Materials, UK), was cut to size using an Nd:YAG laser cutter. Metal foil was cleaned with isopropyl alcohol. Part cured silicone was removed from the oven and allowed to cool for 5 minutes. Metal foil was placed onto the silicone avoiding air bubble formation. Any air bubbles were removed under 50 mbar vacuum for 30 seconds. Electrode designs were cut into the foil using an Nd:YAG laser cutter and excess metal foil was removed. A second layer of silicone was spin coated onto the patterned foil at 1000 rpm for 45 seconds. Slides were cured in an over at 100°C for at least 1 hour. Electrode pads were patterned in the silicone using an Nd:YAG laser cutter. Silicone covering the pads was removed. Slides were returned for the oven for at least 1 hour at 100°C to fully cure.

Part B was formed as follows: Silicone was spin coated onto PSS coated slides at 500 rpm for 45 seconds. The slides were placed in an oven at 100°C for at least 1 hour to cure. Microchannels were patterned in the silicone using an Nd:YAG laser cutter. Silicone strips remaining in the microchannels were removed. Slides were returned for the oven for at least 1 hour at 100°C to fully cure.

Part A and part B were bonded as follows: Both parts were cleaned with isopropyl alcohol and air dried. Excess silicone surrounding the patterned metal or microchannel areas was removed to within 5 mm of the area of interest. The surfaces for bonding remained uppermost on the glass slide. Slides were placed in a plasma oven. Silicone surfaces were plasma treated using air plasma for 2 minutes at 2 Torr, forward power was 50W and reflected power was 10W. Samples were removed from the plasma oven and immediately aligned and bonded. At least 1 kg force was applied to deform the surfaces and ensure adhesion across the entire sample. Samples were placed in an oven at 80°C for at least 1 hour to bond. To lift samples off the substrate slides were placed in distilled water for 30 minutes to dissolve the PSS. Gentle rocking typically removed the glass slide from part B, leaving parts A and B adhered to only one glass slide. Samples could be removed full by longer immersion in distilled water.

Prior to coiling microchannel neural interfaces were cleaned with isopropyl alcohol and air dried. Interfaces were placed with part B uppermost and were plasma treated using an air plasma for 2 minutes at 2 Torr, forward power was 50W and reflected power was 10W. Samples were removed from the plasma oven and immediately coiled and bonded. A clamp was used to hold the coil in place and coils were placed in an oven at 80°C for at least 1 hour to bond.

5.2.1.4 Stacking method

Due to difficulties rolling interfaces with patterned platinum or stainless steel foil electrodes an alternative design was developed. This design is based on the plasma bonding method but sections are stacked and bonded to form a 3D structure. The process is summarised in fig. 5.5.

Parts A and B were formed and bonded as above to create multiple small microchannel sections.

Two bonded sections were placed on PTFE slides, one with part A uppermost, the other with part B uppermost. Slides were placed in a plasma oven. Silicone surfaces were plasma treated using an air plasma for 2 minutes at 2 Torr, forward power was 50W and reflected power was 10W.

Samples were removed from the plasma oven and immediately aligned and bonded. At least 1 kg force was applied to deform the surfaces and ensure adhesion across the entire sample. Samples were placed in an oven at 80°C for at least 1 hour to bond.

5.2.2 Connecting to Microchannel Neural Interfaces

To form an electrical connection between the interfaces' contact pads and recording or stimulating equipment, a spring loaded connector was used. Crosscut sprung pin probes (RS Components, UK) were arrayed on a 2 mm pitch to match the connection pad design on the interface and attached to a Perspex dowel. Before connection a stiff layer was placed underneath the interface, e.g. a ruler or a glass slide, and the pin probes were pressed gently into contact with the interface.

5.2.3 Impedance Reduction by Electroetching

To reduce electrode impedance the surface area was increased, and oxidised layers were removed, by electro-etching.

Impedance of stacked MNI electrodes was analysed in 0.9% saline using a Wayne Kerr 6500B Precision Impedance Analyser (Wayne Kerr Electronics, UK). A 50 mV alternating source was used, with a frequency sweep from 20 Hz to 1 MHz composed of 200 data points.

Additional *in vitro* impedance measurements for validation (not reported) were made using an EVAL–AD5934EBZ (Analog Devices), 1kHz-77kHz, 0.4 Vp-p, 100kΩ calibration resistor. The board was modified to include a switchable AD820ARZ operational amplifier (Analog Devices) with a signal attenuation of 1/4, this allows small impedance values ($Z_{UNKNOWN}$) of <500Ω to be measured. This increases the range of the impedance monitor to $100\Omega < Z_{UNKNOWN} < 1M\Omega$. The standard frequency range for the EVAL–AD5934EBZ is 10^3–10^5Hz.

Electrode impedance and phase was recorded before etching. Electrodes were placed in 0.9% saline with a large (approximately 4 cm^2) stainless steel ground electrode. The saline was degassed under vacuum at 25 mbar for 5 minutes, followed by ultrasonication for 1 minute, and remaining bubbles on or around the electrodes were removed using a fine tipped needle. A single electrode was connected to the positive (+ 4 V DC) line of a voltage controlled power supply. The ground electrode was connected to the

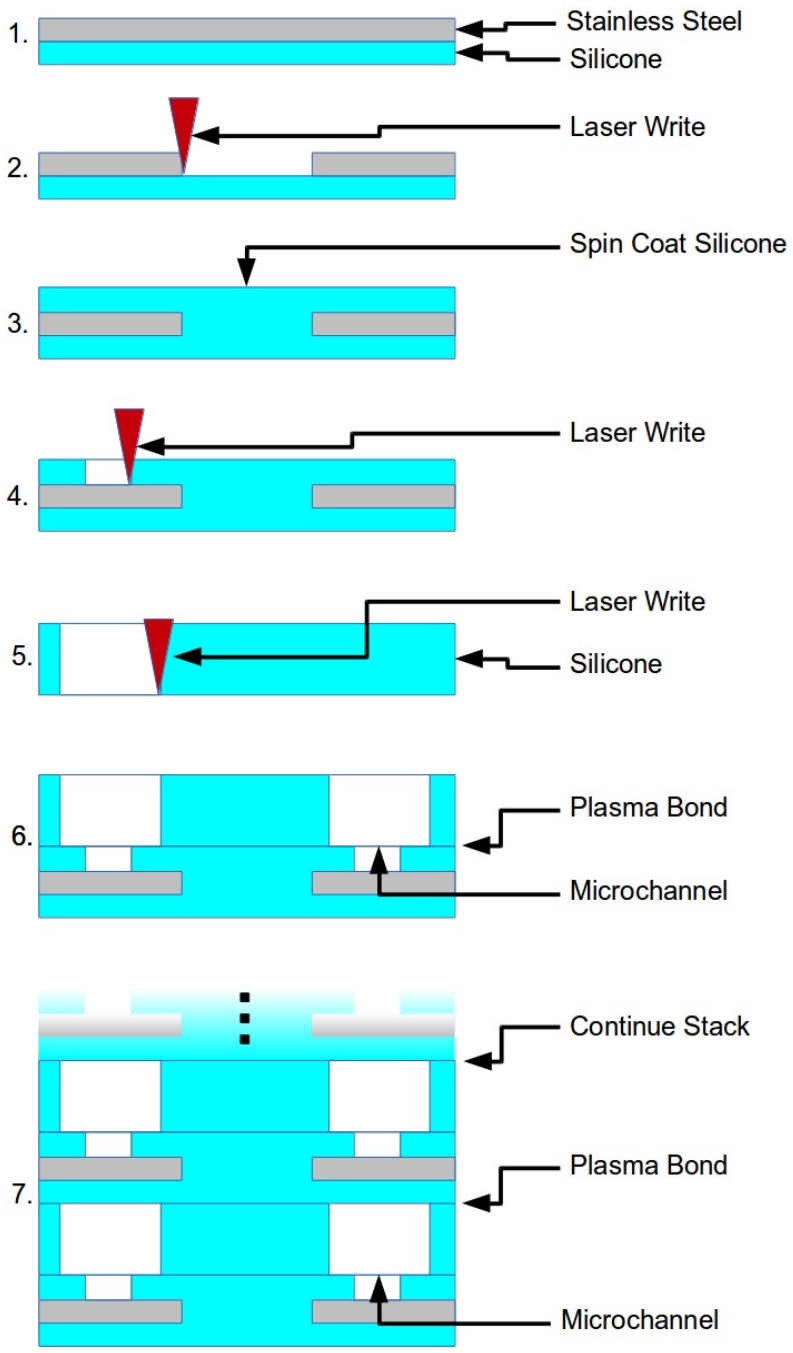

Figure 5.5: An overview of microchannel neural interface manufacture by stacking. Steps 1 to 6 are replicated from the plasma bonding method. 1. Stainless steel foil placed on a spin coated silicone layer. 2. Foil patterned using a laser cutter and excess removed. 3. Silicone spin coated onto patterned foil. 4. Pads and electrodes patterned using laser cutter and silicone removed. This is part A. 5. Microchannels patterned using laser cutter and silicone removed. This is part B. 6. Electrode layer (Part A) and microchannel layer (Part B) plasma bonded. This is a microchannel section. 7. Two microchannel sections are plasma bonded, part A to part B. This is repeated to form a stack. Not to scale.

ground (0 V DC) and negative lines of a voltage controlled power supply. Current was passed through the electrode setup for 5 minutes. The solution was refreshed (0.9% saline) and electrode impedance and phase were recorded. Samples were placed in fresh 0.9% saline for 24 hours, after which the saline was degassed under vacuum at 25 mbar for 5 minutes and electrode impedance and phase was recorded.

5.3 Results

5.3.1 3D template method

The 3D template method was used successfully to create microchannel structures without electrodes (figs. 5.6a and 5.6b). However a range of challenges were encountered.

High density designs typically had non-uniform microchannel alignment, and occasionally nylon filaments touched creating windows between microchannels (figs. 5.6c and 5.6d). In addition, high density designs trapped air between the nylon, this was mostly removed using a vacuum centrifuge, however degasing was limited by the fragility of the design (fig. 5.6d). The PDMS tended to adhere to the nylon filaments and occasionally structures would tear when the filament was removed, this was particularly common for high channel density designs.

Mechanical removal with a scalpel was chosen to remove the enamel coating from the wire for prototype interfaces. Electrical isolation between channels was demonstrated for low microchannel density designs. However, when microchannel density was increased wires tended to be exposed to multiple microchannels and electrical isolation could not be guaranteed.

A key advantage of this design was the low setup cost, however the process could not be carried out in batches and was very time intensive.

5.3.2 Metal negative method

The metal negative method was used to successfully create microchannel structures without electrodes. Microchannel structures with electrodes were formed (figs. 5.7a and 5.7b), however a number of challenges were encountered.

The first challenge was removal of the microchannel structures from the template. Haemosol surfactant was used to provide a release layer, however electrode removal was not consistent and the silicone often tore. Alternative substrates were considered, in particular a black medical grade PTFE would be suitable, allowing laser cutting while ensuring silicone could be readily removed, due to time constraints no alternative materials could be tested.

In addition, introducing electrode pads into the design was a challenge. The chosen method required first spin coating the microchannel layer, then laser cutting pads, followed by applying and laser cutting the metal foil layer. When applying the final silicone layer care was taken to prevent silicone passing into the pads. Furthermore the pads were created while the silicone was still tacky (in order for the metal

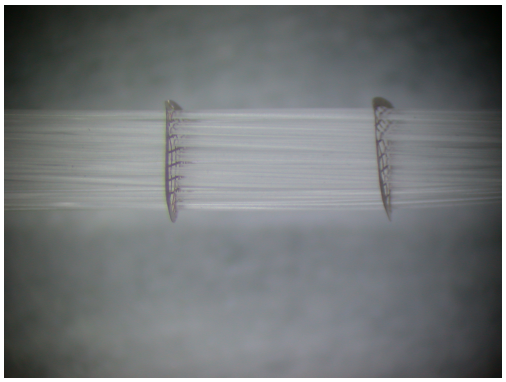

(a) Light micrograph of the 3D templating method. TEM grids and nylon filaments are visible.

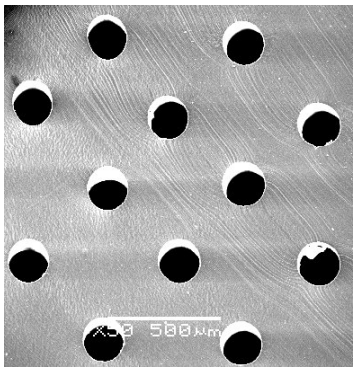

(b) Scanning electron micrograph of 3D templated microchannels formed in PDMS.

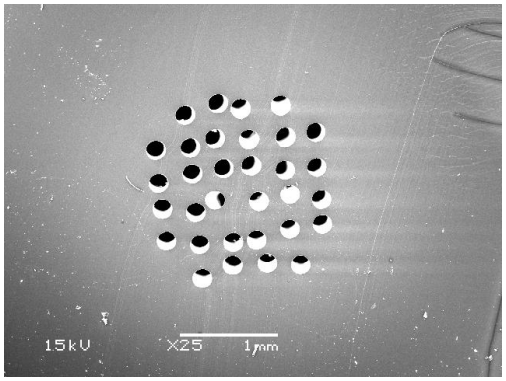

(c) Scanning electron micrograph of 3D templated microchannels formed in PDMS. Non-uniform channel arrangement can be seen.

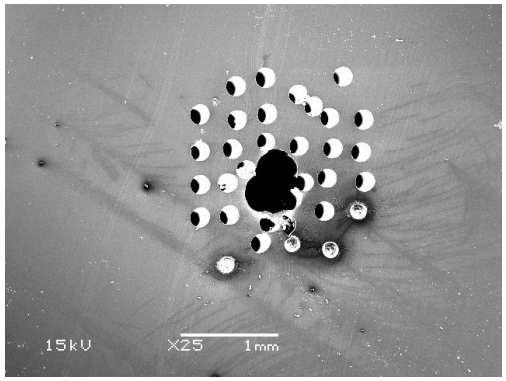

(d) Scanning electron micrograph of 3D templated microchannels formed in PDMS. Pores formed by trapped air can be seen in the centre of the channel array. Channels to the lower right are occulded by non-removed nylon filaments.

Figure 5.6: Light micrographs and scanning electron micrographs of processing steps and results in the 3D templating method.

foil to stick), therefore some silicone did flow into the pads occluding them in some cases.

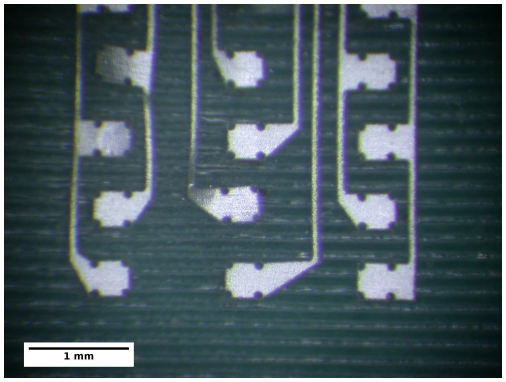

(a) Light micrograph of metal negative method microchannel interface: base view. Ridged microchannels can be clearly seen below the electrode layer.

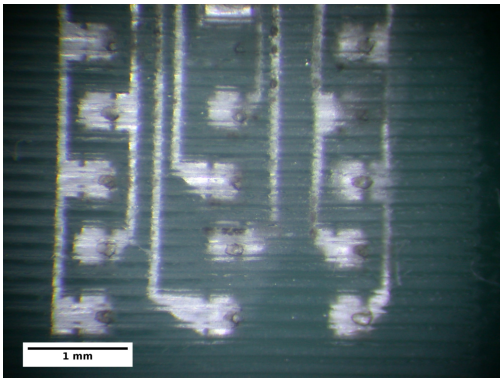

(b) Light micrograph of metal negative method microchannel interface: top view. Ridged microchannels can be clearly seen and electrode holes are visible. A slight misalignment is present.

Figure 5.7: Light micrographs of a microchannel interface formed by the metal negative method.

5.3.2.1 The Effect of Laser Parameters on Groove Profile

Laser parameters (table 5.2) and groove designs (table 5.3) were varied to find a suitable groove profile in the metal template. The resulting sizes are plotted in fig. 5.8. The chosen design used laser parameter 1 and groove design 7. This provided consistent groove profiles in the size range required. Groove height was 130 μm and groove base width was 75 μm. Grooves formed a triangular cross section which could be readily imaged by cutting across the ridges and laying against a glass slide end-on, see fig. 5.9a.

5.3.3 Plasma bonding method

Passive, non-electroded microchannel neural interfaces were successfully manufactured using the plasma bonding method. However, a few challenges had to be overcome. Pressure and heat were required to ensure strong bonding between plasma treated surfaces. 1 kg was found to be insufficient, therefore mini-G-clamps were used to hold parts A and B together in an 80°C dry oven.

Forming electrode containing microchannel neural interfaces was partly successful figs. 5.10a and 5.10b. A challenge not overcome was the stiffness of the metal foil layer. The choice of 12.5 μm stainless steel foil created a flexible, but elastic electrode sheet, which could not be permanently deformed. A malleable metal foil which deforms plastically under stress would be more suitable, for example gold foils are available down to 1 μm thickness. At this thickness issues with handling would be encountered.

The interfaces formed had a high electrode density, with electrodes present in 50% of microchannels fig. 5.10a. This was achieved by using thin, $<50\mu$m, tracks and by connecting the ground electrodes in an alternating pattern.

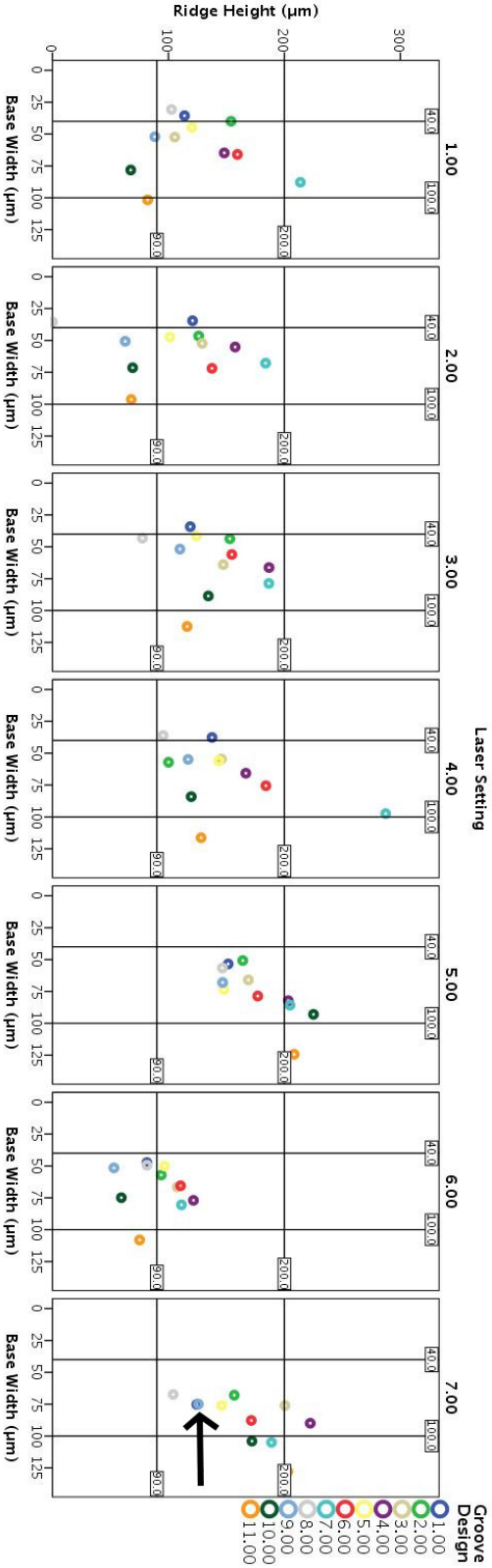

Figure 5.8: Templated silicone ridges formed using laser cutting of 3 mm Aluminium sheet. The chosen parameters are indicated using an arrow.

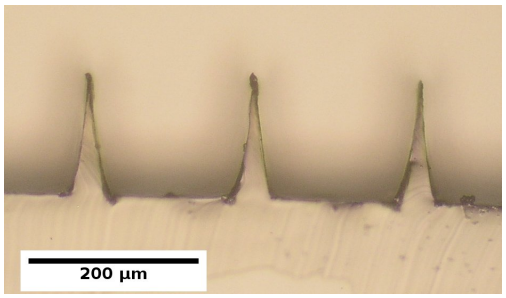

(a) Silicone ridge examples templated from grooves using laser parameter 1 and groove design 7.

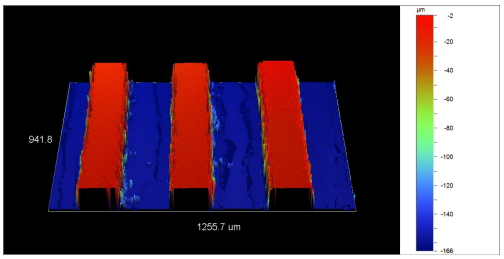

(b) Profile of microchannels produced by cutting silicone. 5X image by scanning interferometry. Microchannels are 150 μm depth, 200 μm width.

Figure 5.9: Microchannel neural interface profiles, in cross section or by white light vertical scanning interferometry.

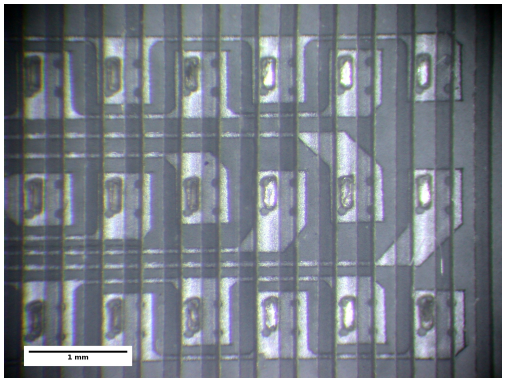

(a) Plasma bonded microchannel neural interface. 6 electroded channels (18 electrodes) are shown. Electrodes to the right of the image have had excess silicone removed.

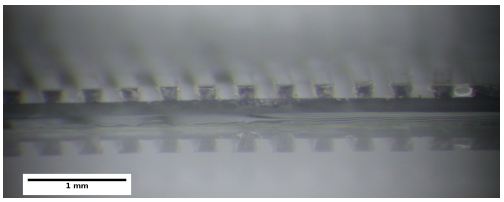

(b) Plasma bonded microchannel neural interface. End view of plasma bonded microchannels.

Figure 5.10: Light micrographs of a microchannel neural interface formed by the plasma bonding method.

5.3.4 Stacking Method

To overcome the problems with coiling electrodes the stacking method was developed. Microchannel neural interfaces were successfully manufactured using the stacking method figs. 5.11g, 5.11h, 5.12a and 5.12b. Additional processing steps are shown in figs. 5.11a to 5.11f.

The microchannel dimensions were determined by the equipment available and handling of the finished neural interface. 200 μm diameter channels were chosen because at this width the PDMS could be reliably cut using the laser without causing the separating ridges to fail. The addition of black pigment to the PDMS was key to accurately cutting silicone to a depth of $>$50 μm. fig. 5.9b shows that channel walls are uniform at 150 μm cutting depth. Once stacked the microchannels have a trapezoid cross section, this is created partly by the laser (a wider heat affected zone is present at the silicone surface) and partly by deformation due to the pressure applied during plasma bonding.

5.3.5 Impedance Reduction by Electroetching

DC etching significantly reduced electrode impedance from 88.9$\pm$66.9 kΩ to 27.2$\pm$19.8 kΩ ($p < 0.001$). Impedance did not significantly increase over the 24 hours after DC etching ($p = 0.766$), with final impedance values of 29.5$\pm$21.0 kΩ.

Surface roughness measurement by vertical scanning interferometry showed a significant increase in electrode pad roughness with DC etching (from 0.248 $\pm$ 0.0579 μm Ra to 0.575 $\pm$ 0.483 μm Ra, $p = 0.009$). After 24 hours there was no significant change in electrode roughness compared with immediately following DC etch (0.6117 $\pm$ 0.534 μm Ra, $p = 1.00$).

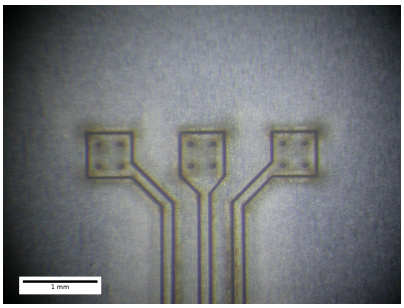

(a) Laser cut foil showing three patterned electrodes and through-holes. Excess foil not removed.

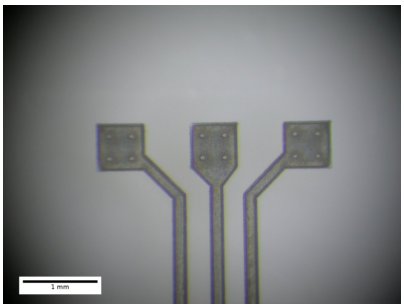

(b) Laser cut foil showing three patterned electrodes and through-holes. Excess foil removed.

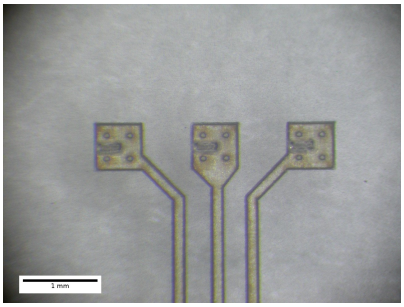

(c) Laser cut silicone electrode openings over stainless steel foil electrodes. A slight misalignment is present. Excess silicone not removed.

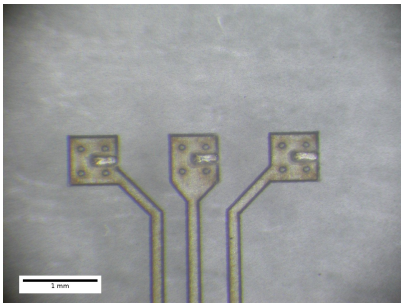

(d) Laser cut silicone electrode openings over stainless steel foil electrodes. A slight misalignment is present. Excess silicone removed. This is a complete Part A.

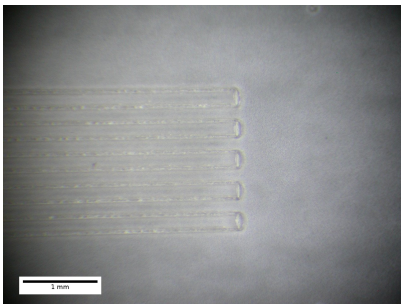

(e) Laser cut silicone microchannels. Excess silicone not removed.

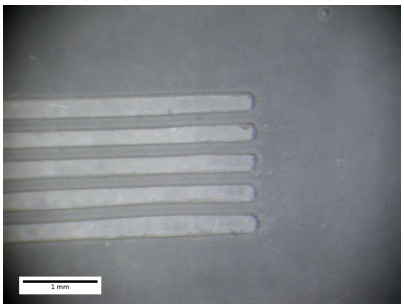

(f) Laser cut silicone microchannels. Excess silicone removed. This is a complete Part B.

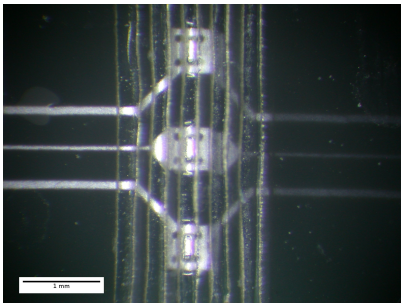

(g) A stacked microchannel interface with the uppermost microchannel layer exposed. A second set of electrode tracks, in another microchannel layer, can be seen to the right.

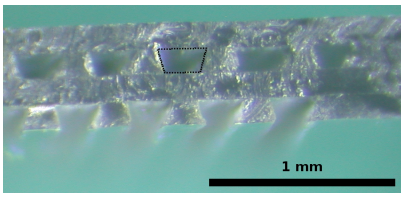

(h) A stacked microchannel interface in cross section with two microchannel layers. The uppermost layer is uncovered.

Figure 5.11: Light micrographs of processing steps in the stacking method.

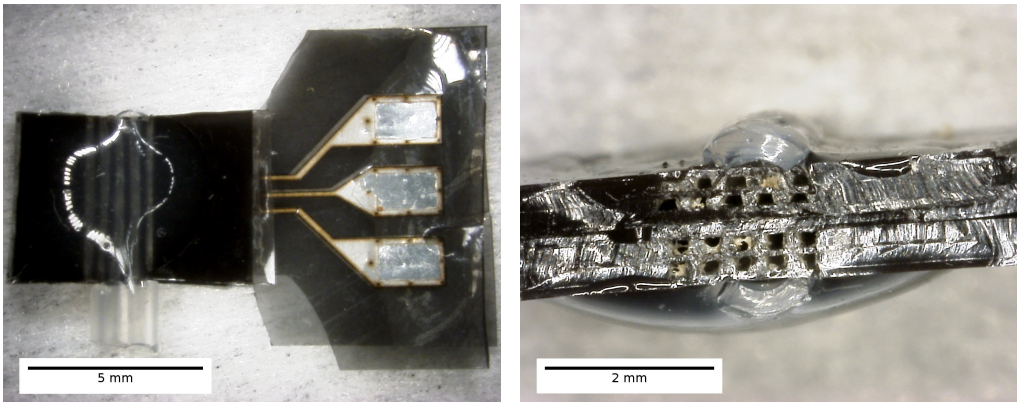

(a) A stacked microchannel neural interface. Oversized connection pads and silicone tubing for suture can be seen. 20x magnification.

(b) A stacked microchannel neural interface in cross section with 4 microchannel layers. 50x magnification.

Figure 5.12: Light micrographs of a microchannel neural interface produced using the stacking method. Images taken after *in vivo* study showing some adherent tissue (white/brown).

5.4 Discussion

5.4.1 Microchannel Neural Interface Design

5.4.1.1 3D template method

The 3D template method has been used successfully in the past, and in this work, to create passive microchannel neural interfaces. The addition of electrodes is simple in a single microchannel design, and has been applied for *in vitro* testing [146]. However, including electrodes in a multi-microchannel design is a challenge, which was not solved in this work.

This manufacturing technique has been applied to regular nerve guidance conduit designs. Longitudinal sacrificial fibres have been used to create large diameter microchannels (410 μm) within cross-linked collagen gels [338, 466]. These designs may be beneficial for nerve regeneration by guiding axon structure in the absence of a normal neural tube or autograft.

5.4.1.2 Metal negative method

The metal negative method was used successfully in this work to create passive microchannel neural interfaces. The first challenge in this method was the creation of a consistent microchannel profile, which was accomplished in an aluminium substrate. Normal substrates for PDMS spin coating were not suitable for laser cutting: medical-grade PTFE was typically white or clear and could not be cut with the laser. Black PTFE may be a suitable alternative and should be tested.

Using black PTFE would help overcome the major challenge of this design, removing the finished interfaces from the substrate. Because the PDMS is very flexible, and there is a large surface area contact between the substrate and the interface, removal is difficult. A surfactant based removal layer helped, however no consistent method was found. In addition, introducing metal tracks to the PDMS meant that the manipulation required to remove the interface involved bending or damaging the tracks. This method could be improved with alternative substrates.

5.4.1.3 Plasma bonding method

The plasma bonding method produced consistent microchannel designs in a batch process. However, the chosen materials were unsuitable for rolling into a coiled design. Stainless steel foil is elastic (springy) and will not consistently deform to allow the microchannel interface to be plasma bonded.

Despite this an alternative track-layer material may make the plasma bonding method most suitable to microchannel manufacture. By creating a separate microchannel layer, the thin film electrode layer can be manufactured using any method which need not be depth dependent. In addition, alternative materials could be used, for example combining a polyimide electrode layer with a PDMS microchannel layer will combine the advantages of photolithography and thin-film metal processing from polyimide

with the stiffness advantages of PDMS.

This method demonstrated a high electrode density (electrodes in 50% of microchannels), using thin tracks and an alternating pattern of connected ground electrodes. The alternating ground electrode design may be useful for determining whether adjacent microchannels are electrically isolated; however, this could not be tested in this case because the interfaces were not coiled and bonded.

5.4.1.4 Stacking method

The stacking method produced consistent microchannel interfaces in a batch process. The main limitation was the minimum workable dimensions. Cutting thick PDMS using a laser created a large heat affected zone, therefore to maintain the microchannel structure channels of 200 μm diameter were chosen. This could be improved by using a laser with a smaller spot size or by further optimising the laser parameters. For thinner silicone smaller size structures can be laser cut consistently, for example the electrode width is typically 80 μm.

Plasma bonding the layers required the surfaces to be in intimate contact, this was achieved using mini g-clamps to press surfaces together. These forces cannot be applied to coiled interface designs, and therefore channel sealing can be poor [51]. In this work, once suitable plasma bonding parameters had been chosen, poor microchannel sealing was not observed. In addition, where poor sealing is present this can be seen under a light microscope following the bonding of one or more microchannel layers and the layer can be rejected.

By stacking electrode layers, the number of electrode containing microchannels is less limited by space compared with a long coil design. This will allow for more channels to include electrodes, up to 50% has been demonstrated in a single layer fig. 5.10a. In this work this advantage was not exploited and layers with electrodes in 20% of microchannels (one of five) where used. To introduce more electrodes a stackable or staggered interconnect is needed, this was not investigated in this work, however, techniques presented in the literature could be adapted for use with a stacked design [150, 467–469].

The stacking method lends itself to the introduction of alternative, stiff materials, such as silicon integrated circuits. Circuits could be used as the electrode layer in a microchannel design, allowing the introduction of recording or stimulating circuitry at the electrode site, and to multiplex signals, overcoming problems with large interconnects [personal correspondence]. Stacking also enables the use of more complex microchannel designs, bifurcating microchannels have been used to direct regenerating axons into channels of 20 μm diameter, with potential benefits in selectivity and action potential amplification [470].

5.4.2 Materials choice

The chosen materials, Sylgard 184 PDMS and 316 Stainless Steel foil are highly suited to prototyping using the manufacturing processes described above. However, for clinical applications alternative ma-

terials should be chosen. Previous work on microchannel interfaces has used Sylgard 184 [113], and it is commonly used for microfluidics applications [471]. For nanometre scale features Sylgard 184 may not be suitable [471], however this work concerned features >10 μm, therefore Sylgard 184 was sufficient. A medical grade silicone (e.g. MED-1000, NuSil) should be used instead of the industrial PDMS for clinical applications.

Stainless Steel was a suitable electrode metal in this case. To lower electrode impedance platinum or platinum/iridium could be used [472], however the cost implications mean that stainless steel is still an economical alternative. In this study interface designs were limited by equipment cost and availability. For human applications, or long term *in vivo* applications alternative electrode materials should be considered. Platinum foil is available and has been used for electrode construction in the metal foil process similar to that described in this work. In clinical applications implant cost is likely to be a small portion of the total cost per patient, for example surgery and rehabilitation would incur high staffing costs.

5.4.3 Impedance Reduction by Electroetching

A reduction in electrode impedance was demonstrated using DC electrode etching. This can be explained by the increase in electrode surface roughness observed. The reduction in impedance (of more than $3\times$) agrees with previous research demonstrating impedance reduction with electrode roughening [390, 391, 462–464]. Increased roughness can be considered similar to increased total surface area (increased surface index), therefore a greater area is available for charge transfer at the electrode electrolyte interface.

5.4.4 Conclusions

This chapter presented manufacturing techniques for microchannel neural interfaces. Microchannel neural interfaces were successfully designed and manufactured using a range of techniques. This chapter presented 4 techniques in progression from least to most successful. It can be concluded that, of the techniques tested in this chapter, the stacking method is most suited to microchannel electrode manufacture. Alternative techniques, such as the plasma bonding method, could be improved by using alternative materials or alternative manufacturing equipment.

It is proposed that microchannel neural interfaces produced by the stacking method will be suitable for *in vivo* testing and that improvements on the designs presented will allow microchannel neural interfaces to undergo clinical trials in patients for prosthesis control. *In vivo* tests of these interfaces will be presented in chapter 6, where additional modifications are made using microchannel protein coatings developed in chapter 3 of this thesis.

Chapter 6

In Vivo testing of Microchannel Neural Interfaces

6.1 Introduction and Hypotheses

The long term performance of neural interfaces depends upon integration with axons and the maintenance of that connection. This is essentially associated with the biology at the interface and for that reason assessment of a regenerative neural interface must be carried out *in vivo* to determine whether the derived signals are appropriate for clinical applications. Work presented previously has shown that *in vitro* neurocompatibility and neurite outgrowth can be enhanced using basement membrane protein coatings (Chapter 3). The microchannel neural interface developed in chapter 5 of this thesis requires neural regeneration for it to function as a neural interface, therefore the implant must be tested in an animal model of neural regeneration. In addition, basement membrane protein coatings should be tested *in vivo* to determine whether they improve regeneration within microchannels.

6.1.1 Neural Interfaces *In Vivo*

Many neural interfaces are primarily designed for cortical implantation (e.g. Utah arrays) and, therefore, the cortical response to implanted devices has been studied extensively [57, 80, 98, 133, 134, 473–476]. This thesis focuses on applications in the peripheral nervous system, where implantation also causes unavoidable injury [4, 55, 58, 103, 254]. *In vivo* tests have tried to assess the extent of this injury and investigate strategies to minimise it.

6.1.1.1 Clinical *In Vivo* Studies

Implantable peripheral nerve interfaces have been in use clinically for functional electrical stimulation since the 1970's (with pioneering experiments in the 1960's) [87, 88, 477], and have demonstrated impressive selectivity over individual muscles over years of testing [478,479]. However, the use of invasive interfaces only entered use for dexterous upper limb prosthesis control in the previous decade. The first reported implantation of a microelectrode array (Utah array) in a human subject was on March 14th,

2002 [131, 132, 480]. Over 96 days recording and stimulation of the median nerve of the left hand was carried out. Control of a wheelchair and an articulated hand with sensory (grip force) feedback were demonstrated. A percutaneous wire bundle was used to transmit signals to a control module, the percutaneous site was closely monitored and no infection was observed. Over the course of the study the connection wires failed due to fatigue and following explantation fibrosis of the array was observed. No functional neural damage was observed over the course of the experiment. A human volunteer was used for the study and the nerve could not be examined histologically for injury which may not have been apparent on functional assessment, however no evidence of neural damage was reported after removal of the array.

Subsequently short term human trials of selective neural interfaces have substantially increased.

Longitudinally implanted intra-fascicular electrodes (LIFEs) and transverse intra-fascicular multichannel electrodes (TIMEs) have been used in trials with upper limb amputees and have demonstrated the survival of motor and sensory function many years after limb-loss [481, 482]. In short term experiments graded motor and sensory signals have been demonstrated [100, 481], allowing patients to control grip force in order to hold soft or fragile objects [124]. These studies have been extended up to four weeks [453, 483], with a decay in efficacy after only 10 days and potentially more serious damage or performance reduction in the long term (not yet tested [484]). Ongoing research is investigating the use of TIME interfaces to treat phantom limb pain [485].

Single channel intrafascicular wire interfaces have been implanted into all major nerves of an amputee patient's upper limb (radial, ulnar and median) [486]. During a short-term ($<$1 day) trial 6 separate interfaces were implanted into the three nerves and 32 nerve activation patterns, controlling 6 different movements, were identified. However, a similar study showed low accuracy in predicting intended movements ($<$2/3 movements predicted correctly) making the system unsuitable for use outside laboratory testing [487].

Longer-term trials are currently ongoing. Nerve cuffs are more common for long term use with upper limb prostheses, where trials have investigated the use of cuffs for sensory feedback. Controlling stimulation intensity and frequency allows the area and strength of the sensation to be varied [117]. Nerve cuffs for sensory feedback have been combined with implanted muscle interfaces for prosthetic control and a bone-anchored transcutaneous interface to allow long-term bi-directional communication with a prosthesis [233]. This hybid design has also been proposed for use with LIFE interfaces alongside EMG or body-powered control [482]. Permanent surgical interventions have also been investigated: targeted sensory reinnervation overcomes issues with selectively stimulating small nerve fascicles by re-routing them to cutaneous nerves, creating a hand map on the skin of a patient [232].

Following amputation, and the loss of afferent and efferent pathways to a limb, the central and peripheral nervous systems reorganise, this reorganisation is a form of neuroplasticity. These neurological

changes may provide benefits and challenges for neuro-prosthetic control [488]. Neuroplasticity can lead to phantom limb pain and other harmful changes; however, it also allows the use of a prosthesis as a rehabilitation tool. Providing motor control and sensory feedback can retrain the nervous system towards embodiment and function use of prosthesis [489].

6.1.1.2 Experimental *In Vivo* Studies

Prior to clinical studies many neural interfaces have been tested in animal models[1]. These models allow problems with peripheral nerve interfaces to be overcome before moving to large (or single case) clinical trials.

Novel cuff designs with increased numbers of electrodes [490,491] or with alternative architectures [116, 118] have been tested in feline and rat nerves. Promising results with fascicle selectivity from multi-electrode cuffs have led to their use for sensory feedback for human patients. However, some designs cause nerve damage in animal trials and have therefore not reached clinical tests.

Utah arrays have been tested in animal models in rats and cats over the short ($<$1 day) and long term (weeks to months) [130,135,136]. The arrays cause axonal damage to rat sciatic nerve which led to gait changes; however, recovery has been demonstrated over 8 weeks *in vivo* [135]. Macrophage activity near the implants and loss in muscle signal strength have been observed [135, 136]. Importantly, studies in cat sciatic nerve showed that surgical technique was critical for interface function, with damage at implantation causing both acute and chronic changes: axons can regenerate following this damage, and following implantation it is important that undamaged fascicles remain normal [106, 137]. The Utah array requires fast pneumatic implantation into soft tissues to reduce elastic deformation, this can be difficult to align correctly prior to insertion, although the use of stereotactic operating equipment can improve accuracy [492]. Utah arrays have been shown to have fascicle selectivity, recruiting individual muscles on sciatic nerve stimulation [493].

TIME and LIFE electrodes show promise in rat sciatic nerve studies, with only mild foreign body reactions occurring [108, 125, 494]. This may be due to the small size and flexibility of these thin film designs. Transverse implantation may damage more nerve fascicles; however, in a porcine model it has been shown to provide more selective stimulation and recruitment, an example of the compromise between invasiveness and selectivity [55, 79, 110].

Regenerative sieve interfaces have been tested in rat sciatic nerve [111, 112]. Axons regenerate; however interfaces with small open areas restrict axon number and size. In some cases the implants can fail over 6 to 12 months, due to micromotion and subsequent fibrotic restriction damaging axons as they pass through the small diameter sieve holes [112]. More open regenerative scaffolds with linear aligned fibres reduce the disruption to rat sciatic nerve regeneration; however these designs only capture signals

[1] This is almost always the case currently; however, early research or small changes to current clinical designs sometimes avoid this step.

from a small subset of axons [114].

6.1.1.3 The Microchannel Neural Interface *In Vivo*

Microchannel neural interfaces were first tested *in vitro* and *in silico*, demonstrating their usefulness for action potential amplification [59, 144, 146, 149, 495]. Advances have since been made *in vitro* [145]. More importantly for clinical applications, *in vivo* testing has demonstrated that axons regenerate through MNIs formed from a variety of materials [51, 113, 147, 148, 153, 154, 156, 470]; however there are challenges with developing highly selective microchannel devices.

The rat model has been used for all the published work to date[2]. Most studies use the sciatic nerve model of neural regeneration [51, 113, 147, 148, 156]; however work has also used teased dorsal rootlets from the vertebral column [153, 154]. Teasing rootlets is advantageous because the nerve remains in continuity and can therefore record complex signals in acute recordings, for example spike trains related to bladder pressure and voiding [153]. Most rootlets survive interface implantation and axons remain for at least 3 months, although myelination reduces dramatically, in contrast where rootlets are cut where they join the spinal cord, both number of axons and myelination reduce by over 90% [154]. If rootlet teasing could be applied to peripheral nerves the requirement for nerves to regenerate within MNIs could be avoided[3].

Studies using the sciatic nerve model are more applicable to this aim which is to use MNIs for control of upper-limb prostheses. In all studies of MNIs in peripheral nerves studies the nerve is severed and allowed to regenerate through the device. The regenerated nerves form "mini-nerves" within the microchannels [51, 113]. These "mini-nerves" have an extra-cellular structure similar to perineurium and endoneurium within the microchannels, and are therefore also refered to as microfascicles [155]. Blood vessels may be present supplying the "mini-nerve", maintaining a population of myelinated and unmyelinated axons [51]. *In vivo* small diameter channels of 50 μm become blocked with fibrous, connective tissue [51, 113, 156]. However, by slowly reducing the channel diameter this may be avoided [470]. In addition, the trauma of implantation and resulting foreign body reaction cause fibrosis, which can either completely occlude microchannels, or reduce the space for axonal regeneration [51, 113].

With the addition of a headstage to a microchannel system axon potentials can be monitored over the course of regeneration [148]. In this case microchannels did not appear to interfere with muscle reinnervation compared with control groups where the nerve was cut and no MNI was interposed. Using recordings during treadmill walking action potentials have been correlated with muscle motor unit activity. In this study there was evidence that the fibrotic response within microchannels was partly due to Schwann cell proliferation, with a layer of S-100 negative cells surrounding a second layer of S-100

[2]Found by standard literature search.

[3]The surgery required to rootlet teasing is complex and detailed; however this does not mean it could not be accomplished for peripheral nerves. The use of a collagenase solution to divide the nerve into fascicles may assist with this surgery [personal correspondence].

positive cells, which in turn surrounded myelinated and unmyelinated axons[4].

Microchannel neural interfaces should be designed such that neural regeneration is encouraged and fibrosis is discouraged.

6.1.2 Assessing Neural Regeneration *In Vivo*

Evaluating peripheral nerve regeneration requires the use of an adequate model and methods [78]. Typically analysis consists of one or more of the following methods: morphology / histology; gait analysis; and electrophysiology. This study will use all three methods to gain a global picture of neural regeneration and function in microchannel neural interfaces.

6.1.2.1 The Animal Model

The choice of animal model is integral to the testing of neural interfaces and nerve guidance conduits [177]. The rat is the most commonly used animal, with approximately 75% of studies using this model [496]. Within this group the majority of studies (>85%) use the sciatic nerve [497]. The length of gap used varies between studies, with up to 100 mm used in large animal models, for rat studies modal gap length is 6 mm to 10 mm. In this work gap length is defined by the electrode design and is kept as long as practical with the electrode design (allowing for suturing this resulted in gaps of 5 mm to 7 mm). It should be noted that nerve regeneration is faster in rodents than in humans due to shorter distances: from the cell bodies to the axon ends; and from any comparable site of injury to the end organ [498].

In addition there are differences in response to neurectomy between rat strains (e.g. Lewis, Sprague–Dawley, Wistar, and others). Lewis rats have a much lower incidence of autotomy (self-mutilation) following sciatic nerve transection than other rat strains, with Wistar rats also exhibiting low autotomy incidence compared with other strains: this makes these strains more suited for studies requiring long term loss of sciatic nerve function [499]. This is important for multiple reasons, primarily ethically: autotomy is an indicator of discomfort and stress. Strain response is also important experimentally: autotomy is an indicator of neuroma formation; and when assessing the sciatic function index autotomy may confound results by shortening toes and therefore toe span. In addition group housing and mixed sex housing has been shown to reduce autotomy rates [500].

6.1.2.2 Peripheral nerve histology

Histology is the most common outcome measure from *in vivo* neural regeneration studies [78, 497]. In 80% of studies regenerated tissue is examined qualitatively, and in 50% of studies the examination includes some quantitative assessment of neuromorphometry [496]. Angius et. al. [496] found that, although there are no standard measures, the most common reported measures of neuromorphometry were: “number of myelinated fibers, total number of nerve fibers, axon diameter, myelin thickness and

[4] S-100 is a Schwann cell marker, therefore S-100 positive cells are Schwann cells and S-100 negative cells are not Schwann cells.

g-ratio [ratio of the inner axonal diameter to the total diameter including myelin]". In addition, proteomic analysis has been proposed, with GAP-43 mRNA levels indicating active neural regeneration [497].

Histological processing techniques for studies of neural regeneration vary widely, and are rarely discussed by authors [496,501]. In basic terms the nerve can be sectioned along different axes: transverse (perpendicular to the direction of regeneration); or longitudinally (along the direction of regeneration). In addition the nerve can be sectioned at different levels: proximal to, within, or distal to the nerve conduit. Stains for axons in the peripheral nervous system include silver impregnation and antibody staining (e.g. anti-neurofilament) [502]. Staining for myelin requires different techniques, mordents (e.g. iron alum) have been added to haemotoxylin staining to achieve myelin staining, toxic reagents including cyanide and osmium tetroxide have also been used [502, 503]. A simple modification for paraffin embedded nerve sections has been developed by Di Scipio et. al. [504], this uses osmium tetroxide to stain myelin, while toluidine, haemotoxylin/eosin or Masson's trichrome can be used for staining cells and connective tissue. In this study we are concerned with regeneration within microchannels, therefore transverse sections stained for myelin and/or haemotoxylin/eosin will allow visualisation of regenerated myelinated and unmyelinated axons as well as quantification of microfascicle formation within microchannels.

Alternative morphometric measures can be taken, including total nerve diameter and target muscle mass. These are typically assessed at the study end point following surgical removal; however magnetic resonance neurography presents a solution for examining neural regeneration non-invasively. Magnetic resonance images can be used to track neural regeneration, observe neuroma formation and evaluate the extent of nerve damage following injury [78]. This presents advantages for clinical applications; however it is cost prohibitive for animal research and does not provide the detail at the axon level given by nerve histology.

6.1.2.3 Gait Analysis

Following sciatic nerve injury or transection in rats normal hind limb gait is lost. The extent of injury and recovery can be measured using biomechanical measures. The sciatic function index (SFI) is a reliable, convenient measure of rat hind limb function, which has been used extensively [78, 368, 503, 505–508]. The SFI was introduced in the 1980's, as a quantitative method for assessing functional recovery following sciatic nerve injury in rats by measuring the change in footprint shape during walking [505]. This was updated by Bain *et. al.* in the late 1980's to define complete sciatic nerve transection with a score of -100 and control or sham operations with a score of 0 [506, 507]. Various methods for recording footprints have been used: x-ray film and developer [506]; bromophenol blue paper [508]; and carbon-black in oil [509].

SFI correlates weakly with other indicators of neural function, possibly indicating functional compensation in addition to regeneration [510]. In addition for severe injuries, and in the first weeks of

recovery, the SFI may not be reliable, but shows the same trends, between observers [508]. Recently more global measures of hind limb function have been achieved using high speed optical tracking [511]. The SFI is considered the only standardised method of functional recovery in the rat model [496].

6.1.2.4 Electrophysiology

Electrophysiology can be used to determine neuromuscular function by monitoring nerve and muscle action potentials. This is of particular interest to implants where the intended use is for recording and/or stimulating nerves and muscles. Approximately 40% of neural regeneration studies examine electrophysiology; however, the measures used vary widely between research groups, making direct comparisons often impossible [496]. Common measures include: compound muscle action potentials; sensory and motor nerve action potentials; reflex tests; and nerve conduction velocities [503].

Typically following nerve injury, muscle action potentials are smaller and the latency (time from stimulus to response) is greater. Nerve conduction velocity is lower where damage to myelin is present; however measurement length and nerve temperature can have large confounding effects on conduction velocities [78]. In addition anaesthesia can alter the results from electrophysiological studies; however, techniques to minimise neural transduction loss may not meet with local ethical approval [512]. Electrophysiology can be carried out serially over the course of an experiment, either under operating conditions, or by using non-invasive or head stage methods: this is of particular interest for neural interfaces [78, 148].

6.1.3 Fibrin Glue

The use of an alternative implantation technique to attach the MNI (fibrin tissue glue) may improve functional recovery through microchannels [513, 514]. Firstly, tissue glue fixation will require less manipulation of the nerve during surgery, reducing damage and allowing the nerve to be placed tension-free in the conduit. In addition, fibrin matrix has been shown to improve neural regeneration within nerve guidance conduits [515], can be used as a carrier for growth factors [516], and can be created from autologous blood [517]. In this study a commercial fibrin will enclose the entire conduit and can be expected to permeate the microchannels by capillary action. Also, tissue glues are available commercially, licensed for use for skin closure / dressing and for internal haemostasis / sealing.

6.1.4 Neural Extracellular Matrix

In chapter 3 of this thesis an experimental series was presented developing and testing a mixture of neural basement membrane proteins for enhancing neural regeneration. The normal regenerative architecture could be partly restored by coating microchannels with neural proteins: microchannels will mimic the physical fascicular or endoneurial structure and the proteins will mimic the small-scale epitope cues present in the endoneurium [71, 178, 338]. The neural basement membrane mixture of collagen-IV, laminin-2,(-4) and nidogen-1 may improve nerural regeneration *in vivo* and should be tested as a

microchannel neural interface coating [179].

6.1.5 Aims and Hypotheses

This chapter presents an *in vivo* study examining stacked microchannel neural interfaces, developed in chapter 5 of this thesis, in a rat sciatic nerve model. The effect of an adsorbed basement membrane protein coating as a modification for microchannel neural interfaces is tested. The coating consists of 10 μg/cm^2 collagen-IV, 1 μg/cm^2 laminin-2,-4, and 0.175 μg/cm^2 nidogen-1 premixed to form an all-in-one coating. The aim of this study is to determine whether the basement membrane protein coating improves the function of a microchannel neural interface.

The hypotheses for this chapter are as follows:

1. Rat sciatic nerve axons regenerate through stacked microchannel neural interfaces *in vivo*.

2. Multi-protein coatings improve functional, histological and electrophysiological outcomes compared with uncoated controls following microchannel neural interfaces implantation in a rat sciatic nerve model.

3. Fibrin glue is a suitable method for *in vivo* fixation of microchannel neural interfaces compared with standard microsurgical suture repair.

6.2 Methodology

All *in vivo* procedures described were carried out in accordance with The Animals (Scientific Procedures) Act UK, 1986 (revised 2013) and local guidance.

6.2.1 Cadaveric implantation of a regenerative neural electrode

Prior to any *in vivo* experimentation a cadaveric test was carried out to determine the surgical approach and the implantation method. One adult male Wistar rat was sacrificed by cervical fracture (procedure carried out for the purposes of a study not discussed in this thesis).

The animal was placed in the right lateral position and the operative site was shaved. An incision was made over the left thigh exposing the Gluteus muscle. Blunt dissection was performed between the Gluteus superficialis and Biceps femoris muscles until the sciatic nerve was identified. The sciatic nerve was freed from surrounding tissue and completely divided.

A dummy implant was interposed between the nerve endings using 9-0 polyamide monofilament suture (Ethicon, W2829). It was decided that 3 epineurial sutures were required to fully secure the implant within the nerve (see fig. 6.1). By observing retraction of the nerve following transection and manipulation during suturing it was decided that the nerve should be divided more proximally, and the junction between the proximal and middle third of the thigh was chosen. During the cadaveric implantation the primary incision was widened to increase the view of the operative site, it was decided

that the primary incision should run from the hip joint to the knee joint in order to fully expose the operative site.

Following the dummy implantation the entire left hind-leg was shaved and exposed from the midline to the ankle by blunt dissection beneath the skin. The muscles of the leg were exposed and alternative surgical approaches were discussed. The animal was placed in a dorsal position and a ventral approach was considered, however this would require dividing through a muscle to expose the sciatic nerve and risk damaging a neurovascular bundle present on the muscle surface. The lateral approach was considered less invasive.

Figure 6.1: Cadaveric assessment of neural interface implantation. Adult male Wistar rat in right lateral position with left thigh and sciatic nerve exposed.

6.2.2 An *In Vivo* Comparison of Tissue Glue and Suture for Microchannel Neural Interface Implantation

Adult male Wistar rats (12 weeks, N=4) were acclimatised in paired housing for 7 days prior to surgery.

Animals were randomly assigned to two groups. Both groups underwent the following procedures. General Anesthesia was induced and maintained with 2% isoflurane (Isoflo, B506, Abbott) in oxygen (2 l/min). Animals were placed in the right lateral position. The operation site was shaved and prepared with Hydrex Clear (0.5% w/v Chlorhexidine Gluconated in 70% v/v Denatured Ethanol B, Ecolab Ltd.) and the operative field draped.

An incision was made over the left thigh between the knee and the hip joints approximately 5 mm posterior to the femur. The subdermal fascia was incised and the underlying Gluteus superficialis and Biceps femoris muscles were identified. Blunt dissection was performed between these 2 muscles to

reveal the sciatic nerve. The sciatic nerve was exposed and freed from surrounding tissue and divided at a the junction between the proximal and middle third of the thigh. Throughout the procedure care was taken to keep the operative field moist with regular irrigation using isotonic saline (Vetivex 1).

The sterile implant was washed with isotonic saline (Vetivex 1) immediately prior to implantation.

Implantation was carried out as described in sections sections 6.2.2.1 and 6.2.2.2.

Incisions of both groups were washed with isotonic saline and closed with a continuous buried subcuticular suture using 4-0 and 2-0 polyglactin 910 sutures (Vicryl, W9106). Final sutures were subcutaneous and knots were run subcutaneously.

The wound was treated with moisture permeable spray dressing (Opsite, Smith and Nephew). Analgesia was performed postoperatively using 2.5 mg/kg Flunixin (50 mg/mL in saline, Noorbrook) subcutaneously. Animals were returned to darkened individual housing and monitored until recovery from anasthesia was confirmed.

Animals were housed individually for 7 days after surgery and thereafter in pairs. The cage environment was enriched with extra bedding and other objects to reduce the likelihood of automutilation. Water and food were provided *ad libitum*.

6.2.2.1 Suture

For group 1 the nerve ends were sutured into the implant. The proximal nerve end was placed in the lumen of the implant abutted to the microchannels. The nerve was sutured to the implant using 9-0 polyamide monofilament suture (Ethicon, W2829). 3 epineurial sutures were used equidistant around the nerve. Sutures were passed through the perineurium proximally to distally and through the wall of the silastic tubing before being secured. The implant was manipulated to access the reverse side for suturing.

The distal end was sutured in the same manner with sutures passing through the perineurium distally to proximally and through the wall of the silastic tubing.

6.2.2.2 Tissue Glue

For group 2 the nerve ends were held in place using tissue glue. The proximal and distal ends of the nerve were places in the lumen of the implant abutted to either end of the microchannels. Tisseel Tissue Glue (Baxter, 2 mL, 1501764) was prepared according to manufacturer's instructions and kept at 37°C using Fibrinotherm equipment (Baxter). Tisseel was mounted into a mixer/applicator. The first 0.5 mL was expelled onto a sterile gauze. Approximately 0.5 mL Tisseel was applied to the nerves and implant encapsulating the entire area. The Tisseel was allowed to set for 3 minutes *in situ*.

6.2.3 An *In Vivo* Comparison of Internal Surface Coatings for Microchannel Neural Interface Implantation

Adult male Lewis rats (12 weeks, N=24) were acclimatised in group housing for 7 days prior to surgery.

Animals were randomly assigned to 4 groups. All groups underwent the following procedures. General anaesthesia was induced and maintained with 2% isoflurane (Isoflo, B506, Abbott) in oxygen (1 to 2 l/min). Animals were placed in the right lateral position. The operation site was shaved and prepared with Hydrex Clear (0.5% w/v Chlorhexidine Gluconated in 70% v/v Denatured Ethanol B, Ecolab Ltd.) and the operative field draped.

An incision was made over the left thigh between the knee and the hip joints approximately 5 mm posterior to the femur. The subdermal fascia was incised and the underlying Gluteus superficialis and Biceps femoris muscles were identified. Blunt dissection was performed between these 2 muscles to reveal the sciatic nerve. The sciatic nerve was exposed and freed from surrounding tissue and divided at the junction between the proximal and middle third of the thigh. Throughout the procedure care was taken to keep the operative field moist with regular irrigation using isotonic saline (Vetivex 1).

For all groups nerve ends were sutured to the implant. For two groups protein coated implants were used, and for two groups uncoated control implants were used. Sterile interfaces were coated with and all-in-one 10 μg/cm^2 Collagen-IV + 1 μg/cm^2 Laminin-2,-4 + 0.175 μg/cm^2 Nidogen-1 multi-protein coating previously described in Chapter 3. To coat the sample, sufficient mixed protein solution in the ratio 10:1:0.175 (Collagen:Laminin:Nidogen) was placed within the lumen of the interface. The interface was placed under vacuum for 5 minutes to remove and air and ensure the protein solution had sufficiently penetrated the microchannels. The interfaces were placed in an incubator at 37°C for 2 hours for protein adsorption, interfaces were turned once after 1 hour. Coated interfaces were washed by immersion into sterile phosphate buffered saline for 5 minutes 3 times. Coated and uncoated sterile implants were stored in sterile isotonic saline prior to implantation.

The proximal nerve end was placed in the lumen of the implant abutted to the microchannels. The nerve was sutured to the implant using 9-0 polyamide monofilament suture (S&T, 03180, Interfocus Ltd, UK). 3 epineurial sutures were used equidistant around the nerve. Sutures were passed through the perineurium proximally to distally and through the wall of the silastic tubing before being secured. The implant was manipulated to access the reverse side for suturing.

The distal end was sutured in the same manner with sutures passing through the perineurium distally to proximally and through the wall of the silastic tubing.

Incisions of both groups were washed with isotonic saline and closed with a continuous buried subcuticular suture using 4-0 polyglactin 910 sutures (Vicryl, W9106, Johnson & Johnson International, UK). Final sutures were subcutaneous and knots were run subcutaneously.

The wound was treated with moisture permeable spray dressing (Opsite, Smith and Nephew). Analgesia was performed immediately postoperatively using 3 μg buprenorphine subcutaneously (as buprenorphine hydrochloride, 3.24 μg in 1 ml, Vetergesic, Sogeval UK Ltd.). Animals were returned to darkened group housing and monitored until recovery from anaesthesia was confirmed. One animal was

lost during anaesthesia (Control, 4 week group), in all other cases recovery was uneventful.

Animals were housed in groups of 4. The cage environment was enriched with extra bedding and other objects to reduce the likelihood of automutilation. Water and food were provided *ad libitum*.

6.2.4 Electroneurography using Microchannel Electrodes

For the N=24 tests electrophysiological assessment was carried out using the electrode containing microchannel neural interfaces. After 1 month (4 weeks) following surgery and 2 months (8 weeks) following surgery two groups each of 12 animals were anaesthetised and prepared using the techniques described for implantation. The interface was exposed by dissection and the interface and nerve freed of connective tissue.

First, stimulation was applied to the proximal nerve and signals were recorded from the microchannel interface. A pair of stainless steel hook electrodes were used to lift the proximal nerve. The pads of the microchannel interface were laid over a stiff metal bar, a spring loaded connector described in Chapter 5 was used to form an electrical connection with the microchannel's electrodes in a tripolar configuration. Neural signals were recorded using a neural signal amplifier (Iso-DAMA8A, World Precision Instruments, Sarasota, USA) connected to BIOPAC recording equipment (MP150 and AcqKnowledge software, BIOPAC Systems, Inc., CA, USA). Hook electrode stimulation was carried out using the BIOPAC equipment: a balanced square 1ms $\pm$0.1V pulse train of 10 Hz was used. Recordings were made at 10 kiloSamples per second (kSps), amplified 1000x, with a high pass filter of 100 Hz and a low pass filter of 10 kHz. In addition, the proximal nerve was stimulated using a Medtronic Vari-Stim III Surgical Nerve Stimulator (Medtronic Inc., MN, USA) set to a 1 mA pulse.

Second, stimulation was applied to the nerve within the microchannel and signals were recorded from the tibialis anterior muscle. Stainless steel epimysial electrodes were placed on the muscle belly of the exposed muscle. The pads of the microchannel were connected as above. Muscle signals were recorded using BIOPAC amplifers and recording equipment (MP150, EMG100 and AcqKnowledge software). Microchannel interface stimulation was carried out using the BIOPAC equipment: a balanced square 1ms pulse train of 10 Hz between $\pm$0.01V and $\pm$0.1V was used. Recordings were made at 10 kSps, amplified 500x, with a high pass filter of 100 Hz and a low pass filter of 5 kHz. In addition, the proximal nerve was stimulated using a Medtronic Vari-Stim III Surgical Nerve Stimulator (Medtronic Inc., MN, USA) set to a 1 mA pulse.

The signal-to-noise ratio of outputs was calculated as the ratio of the peak-to-peak signal (μ) to the noise standard deviation (σ), see eq. (6.1).

$$SNR = \frac{\mu}{\sigma} \tag{6.1}$$

6.2.5 Histological Procedures

For the comparison of tissue glue and suture all animals were sacrificed 4 weeks following surgery.

For the comparison of internal surface coatings one uncoated group and one coated group were sacrificed 4 weeks following surgery. The second control group and the second coated group were sacrificed 8 weeks following surgery.

Animals were sacrificed by cervical fracture. For the N=4 tests the animal was laid in a left lateral position and the implant was exposed by dissection. For the N=24 tests the implant site was already exposed for electroneurography.

The neural interface and 1 cm of distal and proximal nerve were excised and immediately placed in 4% paraformaldehyde in phosphate buffered saline (PBS). After 2 to 6 hours in fixative the nerves were washed and stored in 0.2 wt% glycine in PBS. Nerve samples were stored at 4°C prior to histological processing. Prior to histological processing the nerve was freed of any remaining connective tissue by dissection and the sutures holding the nerve to the neural interface were cut. A single transverse cut was made through the silicone tubing adjacent to the neural interface on the distal side. The distal and proximal nerve sections were identified and removed carefully to preserve any microfascicles connected to the distal end.

The tibialis anterior and biceps femoris muscles were excised from the right and left legs. The muscles were stored in 4% paraformaldehyde at room temperature and weighed within 1 week.

The nerve fixation method described below is modified from Di Scipio *et. al.* [504]. Nerves for the N=24 test were post-fixed to make myelin visible. Samples were post-fixed for 2 hours in 1% osmium tetroxide (Agar Scientific) in 0.1M sodium cacodylate buffer. Samples were then washed 3 times in 0.1M sodium cacodylate buffer. Samples from both tests were dehydrated in ascending alcohol series with 3 washes for 5 minutes at each concentration: 20% industrial methylated spirits (IMS); 30% IMS; 40% IMS; 50% IMS; 60% IMS; 90% ethanol; 96% ethanol. Samples were washed twice in 100% ethanol for 30 minutes each and stored in ethanol prior to embedding. Samples were infiltrated by paraffin wax at 60°C for at least 24 hours. Samples were then embedded in paraffin wax and a series of 5 μm transverse sections were taken using a rotary microtome. Sections were stored for at least 24 hours at 60°C to partially deparaffinate.

All sections from the N=24 test and 50% of the sections from the N=4 test were then stained with haemotoxylin and eosin by the following method. Samples were deparaffinated in a series of 3 xylene baths for 4 minutes each. Samples were then taken to water in an ethanol series for 2 minutes each: 100% ethanol; 90% ethanol; 70% ethanol; tap water. Samples were immersed in Harris Haemotoxylin (Sigma HHS32) for 8 minutes. Samples were washed by dipping in tap water and transferred to acid alcohol for 20 seconds (70% industrial methylated spirits, 1% 18M HCl in distilled water). Samples were immersed in eosin (eosin Y-solution, 0.5% aqueous, Merck KGaA, 1.09844.1000) for 8 minutes.

Sections were washed under slowly running tap water and dehydrated in ascending ethanol series for 2 minutes each: 70% ethanol; 90% ethanol; 100% ethanol. Samples were cleared in 3 xylene baths for 4 minutes each.

50% of the sections from the N=4 test were stained using toluidine blue. Sections were de-paraffinated and taken to water as described in the methods for haemotoxylin and eosin staining. Sections were immersed in toluidine blue solution for 30 minutes at 37°C (1 wt% toluidine blue, Agar Scientific, in 50% propan-2-ol 50% distilled water). Sections were transferred to propan-2-ol for 1 minute. Sections were dehydrated and cleared in xylene as described in the methods for haemotoxylin and eosin staining.

All samples were air dried for approximately 5 minutes following clearing then mounted using a glass coverslip and DPX (VWR, 360294H). Slides were left flat for 1 hour to allow the mounting media to set and then stored vertically.

6.2.5.1 Imaging and Analysis

Sections were imaged at 10x, 20x and 40x using an Olympus slide microscope. Images were assessed using ImageJ, graticules were used to set image scales. Up to 50 axon cross sections per microchannel were counted [156]. Axon density (axons per μm^2) and axon diameter (μm) were determined [135]. Diameters were calculated using the axis parallel to the horizontal in the image and assuming a circular axonal morphology. Axon densities (axons per area) were calculated for each section using the Cell Counter ImageJ plugin. Statistical analysis was carried out using data from one proximal and one distal section of each explanted interface.

6.2.6 Gait Analysis by the Sciatic Functional Index

Animals were monitored for autotomy during SFI walking assessments [518].

A walking track was created consisting of an 82 mm by 420 mm track section (lined with paper for footpad recordings) with a large darkened box at one end. A similar design is shown by Brown *et. al.* [507].

For the N=4 tests of tissue glue compared with suture carbon-black in oil was used [509]. Approximately 1 g carbon black powder (Cornelissen and Son, UK) was mixed with approximately 5 ml clear cooking oil to form a thick, non-toxic paint. Plain white paper was used for lining the track section.

Animals were identified prior to walking using tail tattoos. Animals' hind feet were placed in a petri dish containing the carbon-black in oil. Animals were placed at the end of the track section facing towards the darkened box. Once animals had entered the darkened box the paper with footpads was immediately removed and recorded photographically. Animals' feet were cleaned with warm water prior to returning to housing.

To reduce mess and potential toxicity a cleaner method was sought for the N=24 tests. Bromophenol blue paper was chosen, this method uses water rather than carbon-black in oil [519], and has been used

clinical with humans [520]. Bromophenol blue is prepared as a 0.5 wt% solution (Bromophenol Blue, Sigma Aldrich, UK) in acetone. Paper is dipped into this solution, drip dried for 10 seconds and placed in a dry oven at 37°C for at least 1 hour to dry. This creates a yellow-blue paper which becomes brilliant blue on contact with liquid water. The colour fades to blue upon contact with moist air therefore the paper is sealed in a air tight bag until use. This paper is used for lining the track section.

Animals were identified prior to walking using tail tattoos. Animals' hind feet were placed in a petri dish containing warm tap water and excess water was removed using an absorbent tissue. Animals were placed at the end of the track section facing towards the darkened box. Once animals had entered the darkened box the bromophenol blue paper with footpads was immediately removed and recorded photographically. Animals' feet did not require cleaning and animals were returned to housing.

6.2.6.1 Calculating the Sciatic Function Index

Once a suitable set of prints from the normal and experimental hind paws have been recorded the SFI can be calculated. All measurements were made using ImageJ. Because only relative measures were used distances were recorded in pixels.

The formula derived by Bain *et. al.* was used [506]. The following measurement were taken (see fig. 6.2): print length (PL); the distance between the first and fifth toes or toe spread (TS); the distance between the second and fourth toes or intermediate toe spread (IT). These measurements were taken for two sequential hind-limb prints, one from the operated or experimental side (E), and one from the unoperated or normal side (N). This gave the following 6 measures: NPL, NTS, NIT, EPL, ETS, and EIT.

A difference factor for each measurement is calculated using eqs. (6.2) to (6.4). The sciatic function index (SFI) is calculated using eq. (6.5) from Bain *et. al.*, 1989, [506].

$$\text{Print Length Factor (PLF)} = \frac{\text{EPL} - \text{NPL}}{\text{NPL}} \tag{6.2}$$

$$\text{Toe Spread Factor (TSF)} = \frac{\text{ETS} - \text{NTS}}{\text{NTS}} \tag{6.3}$$

$$\text{Intermediate Toe Spread Factor (ITF)} = \frac{\text{EIT} - \text{NIT}}{\text{NIT}} \tag{6.4}$$

$$\text{Sciatic Function Index (SFI)} = -38.3 \times \text{PLF} + 109.5 \times \text{TSF} + 13.3 \times \text{ITF} - 8.8 \tag{6.5}$$

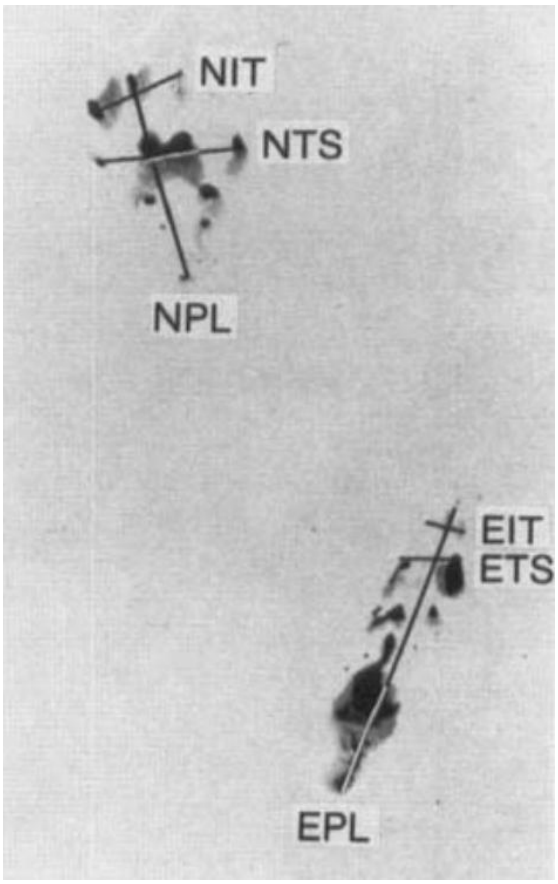

Figure 6.2: Rat footpad traces with the following measurements marked: print length (PL); toe spread (TS); intermediate toe spread (IT). These measurements are taken for the operated or experimental side (E) and unoperated or normal side (N). Figure from Brown *et. al.* [507], permission received. Copyright ©1989 Wiley-Liss, Inc., A Wiley Company.

6.2.7 Data Analysis

Unless otherwise stated data were analysed using SPSS version 21.0 (IBM, Windows and Linux versions). The data were not assumed to be normally distributed, and the conditions for parametric testing were not met, therefore non-parametric tests were used. Where unpaired samples were present statistical comparisons were made using the Mann Whitney U test. These cases are: muscle mass loss ratios; comparisons of histological morphometry between different treatment groups, and different time points; rates of SFI increase per day; signal to noise ratios; comparisons of impedance between different treatment groups. Where paired or related samples were present statistical comparisons were made using the Wilcoxon signed-rank test. These cases are: comparisons of histological morphometry between proximal and distal sections; comparisons of impedance between different time points. SFI was recorded as continual bivariate data (SFI and days since implantation) and correlations were evaluated using Spearman's rank correlation coefficient.

6.3 Results

6.3.1 Cadaveric Implantation of a Microchannel Neural Interface

The single animal cadaveric study demonstrated that a lateral approach to the sciatic nerve was suitable and that the nerve could be exposed by blunt dissection following the skin incision. In addition it was observed that the neural interface was of the correct diameter to suture within the nerve trunk.

6.3.2 An *In Vivo* Comparison of Tissue Glue and Suture for Microchannel Neural Interface Implantation

6.3.2.1 Gross Anatomy

On explantation the nerve was in continuity with the neural interface in all animals (see figs. 6.3a and 6.3b). A superficial infection associated with a skin suture was observed in one animal (fibrin glue group), this had not penetrated the tissues to the nerve transection site. A gross difference was observed between the groups. Where fibrin glue was used a thick transuclent capsule was present around the nerve (see fig. 6.3b), in one animal this had partially bound the nerve to the soft tissues, making blunt dissection for removal difficult.

6.3.2.2 Histology

When the implant was treated with tissue glue the nerve appeared to follow the glue rather than remain within the lumen of the implant figs. 6.4a to 6.4f. In contrast when the implant was sutured in place the nerve grew through the microchannels forming microfascicles or mini-nerves in a spiral formation (see figs. 6.5a and 6.5b).

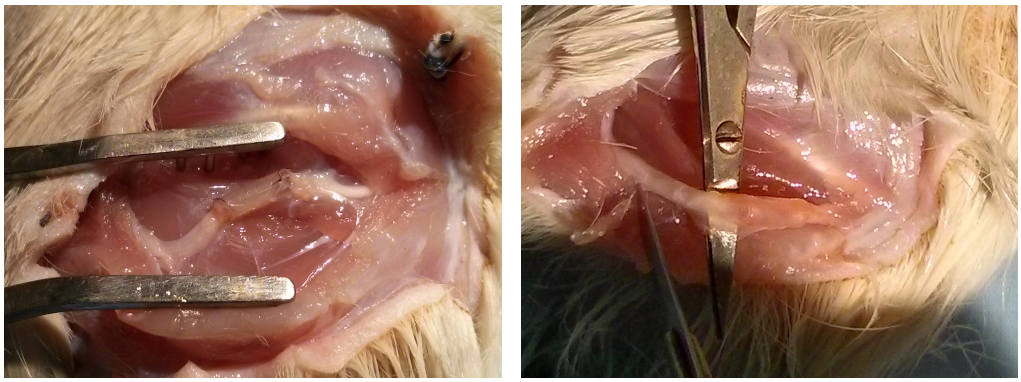

(a) Interface implanted using microsutures.

(b) Interface implanted using Tisseal (fibrin) tissue glue.

Figure 6.3: Passive microchannel neural interfaces *in situ* 1 month following implantation, demonstrating the sciatic nerve in continuity with the interface.

6.3.2.3 Sciatic Function Index

Three weeks and four weeks after surgery the sciatic function was greater in the tissue glue group compared with the sutured group (see fig. 6.6). After 3 weeks regeneration SFI in the tissue glue group was -66.6±21.3 (median ± I.Q. range) and was -77.9±19.3 in the sutured group. One week later sciatic function had improved in both groups: -64.1±30.7 in the tissue glue group; and -74.6±36.0 in the sutured group. Due to the nature of the study (pilot study with n = 2) no statistical comparison was made.

6.3.3 An *In Vivo* Comparison of Internal Surface Coatings for Microchannel Neural Interface Implantation

6.3.3.1 Gross Anatomy

In one case after 30 days, a control sample, the neural interface was found not in continuity with the nerve, following examination it was found that the sutures had pulled away from the epineurium at the proximal end. The proximal nerve stump had remained within the lumen of the silicone guide, but no regeneration into the microchannels was observed. In all other cases the MNI was in continuity with the nerve and tissue had filled the silicone guides both proximally and distally (see figs. 6.7, 6.8a and 6.8b).

During removal of the nerve when the first nerve transection was made (proximal to the implant) twitching of the hind-limb could be observed in some cases. After 4 weeks implantation, in the control group twitching was observed in 1 of 6 cases, and in the sECM coated group twitching was observed in 2 of 5 cases. After 8 weeks post implantation, in the control group twitching was observed in 4 of 6 cases, and in the sECM coated group twitching was observed in 4 of 6 cases. Twitching indicates that the muscles of the distal limb have reinnervated, and that therefore the nerve has regenerated beyond the MNI.

Following fixing with paraformaldehyde the interfaces were manually dissected. In some cases

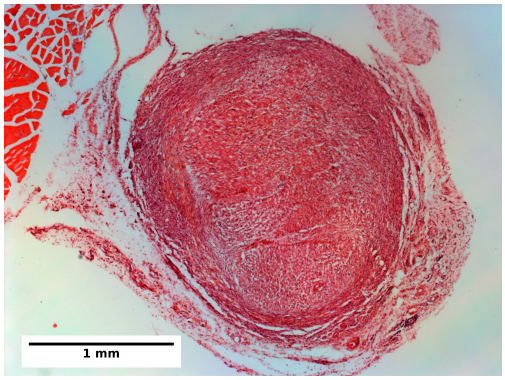

(a) Transverse distal sciatic nerve section 1.

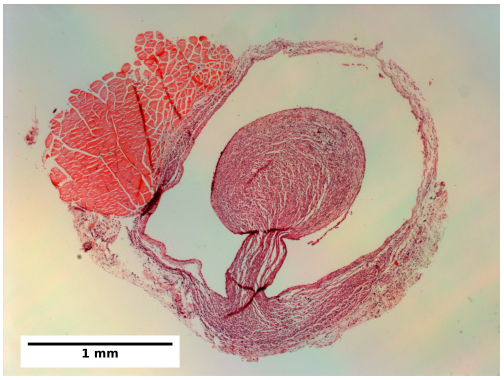

(b) Transverse distal sciatic nerve section 2.

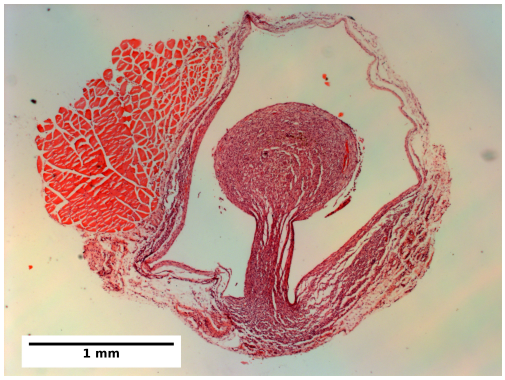

(c) Transverse distal sciatic nerve section 3.

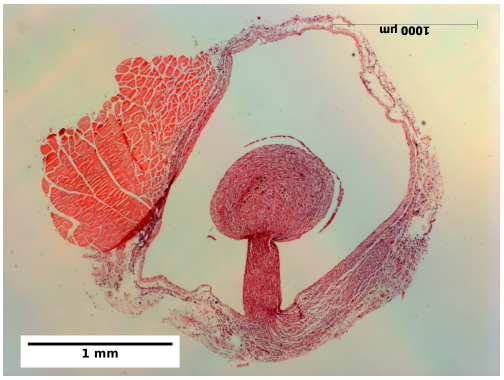

(d) Transverse distal sciatic nerve section 4.

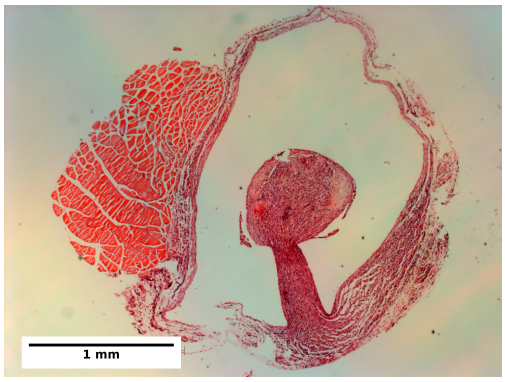

(e) Transverse distal sciatic nerve section 5.

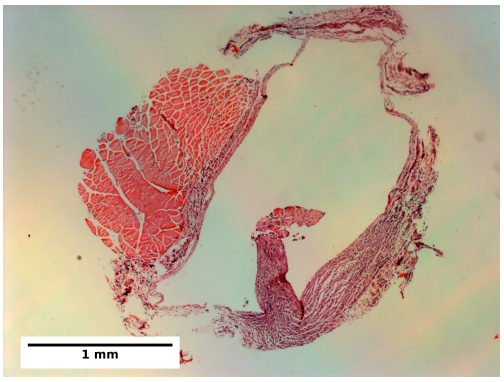

(f) Transverse distal sciatic nerve section 6.

Figure 6.4: Sequential transverse histology of sciatic nerve following tissue glue implanted interface. 5 μm sections from the proximal nerve portion, from proximal to distal, stained with haemotoxylin and eosin. N.B. the sections are not immediately consecutive, there is approximately 50 μm of nerve between each section not shown.

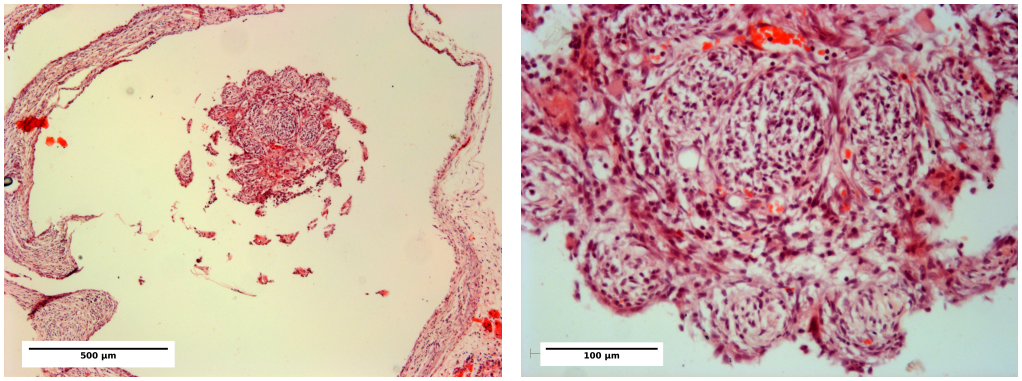

(a) Interface implanted using microsutures, at 5x magnification..

(b) Microfascicles, detail at 20x magnification.

Figure 6.5: Transverse histology of sciatic nerve following suture implanted interface. 5 μm sections from the proximal nerve portion, stained with haemotoxylin and eosin. Microfasciles are present in a spiral formation aligning with the spiral passive microchannel array design.

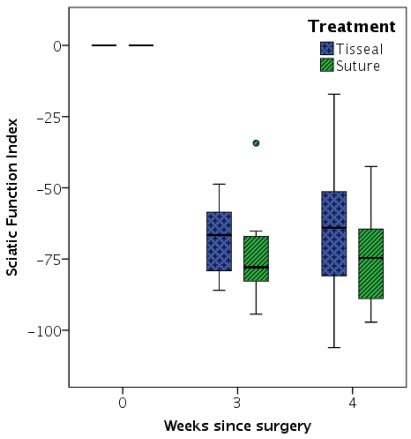

Figure 6.6: Sciatic Function Index following regeneration through Tisseal tissue glued and sutured microchannel conduits. n = 2 (N = 4) with 3 measurements per timepoint. A theoretical zero is included for comparison.

mini-nerves were observed growing into the microchannels and could be removed with careful dissection (see fig. 6.8c). Tissue remained within some microchannels, this could be seen under scanning electron microscopy (see figs. 6.9a and 6.9b).

Following MNI removal and dissection from the nerve some tissue was still present in the microchannels, when the plasma bonded layers were split using forceps mini-nerves could be seen within the channels under light microscopy (see figs. 5.12b and 6.10).

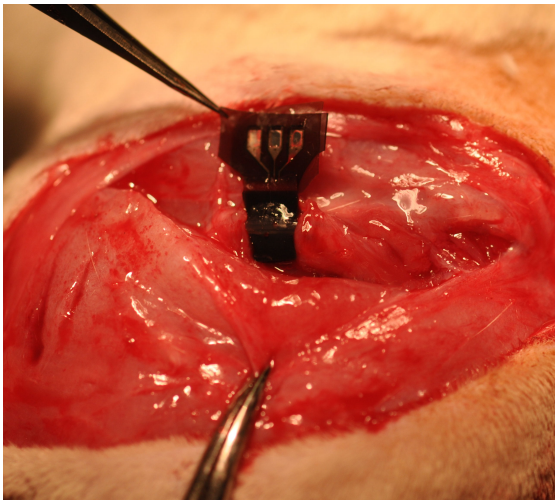

Figure 6.7: Stacked microchannel neural interface in situ after 60 days (8 weeks) implantation. Nerve, in continuity with the microchannel device, can be observed proximally (right) and distally (left).

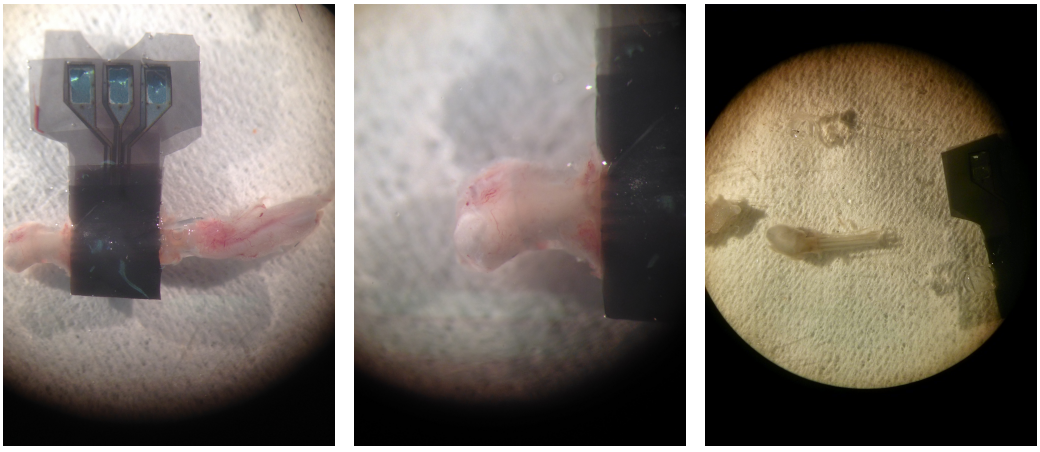

(a) Microchannel neural interface with nerves in continuity. Proximal nerve on right.

(b) Microchannel neural interface with distal nerve in continuity.

(c) Mini-nerves following removal dissection from a microchannel neural interface.

Figure 6.8: Light micrographs of microchannel neural interface dissection following 2 months *in vivo*.

6.3.3.2 Muscle Mass Changes

The relative changes in biceps femoris (BF) muscle mass and tibialis anterior (TA) muscle mass are presented in figs. 6.11a and 6.11b. Relative loss is greater for the TA than for the BF at 8 weeks, with a

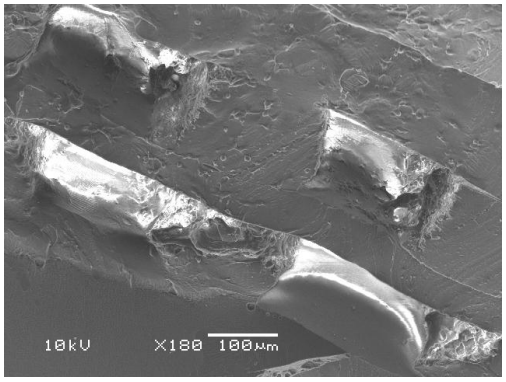

(a) Microchannels with some adherent tissue. 180x magnification.

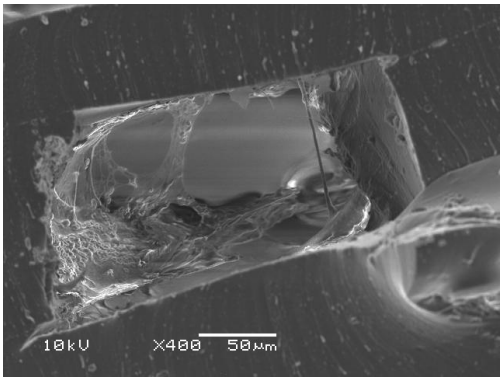

(b) Microchannel with some adherent tissue. 400x magnification.

Figure 6.9: Scanning electron Micrographs of microchannels following 2 months *in vivo*. Adherent tissue and space where tissue has been removed by dissection can be seen.

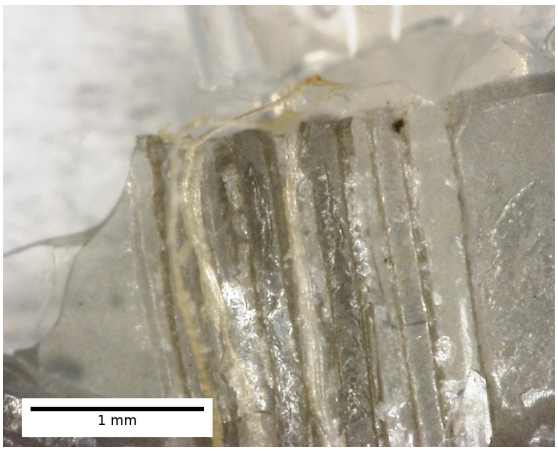

Figure 6.10: Light micrograph of a microchannel neural interface split between two plasma bonded layers. Images taken after *in vivo* study showing some adherent mini-nerve tissue (white/brown).

0.660±0.142 TA loss in the sECM treated group and a 0.671±0.139 TA loss in the control group (median ± interquartile range), meaning that the deinnervated TA muscles were over 50% smaller relative to the same muscle on the unimplanted (right) side. In contrast the BF muscles were approximately 20% smaller after 4 weeks, and less than 10% smaller after 8 weeks. There was no significant difference in muscle mass loss between the treatment groups for either the BF or TA at 4 and 8 weeks ($p > 0.794$).

Within treatment groups a trend in decreasing muscle mass loss from 4 weeks to 8 weeks was observed; however, this change was not significant. In the sECM treated group loss was greater at 4 weeks (0.195±0.260 median relative loss ± interquartile range) than at 8 weeks (0.028±0.145), this difference was not significant ($p = 0.434$). There was no significant difference in BF mass loss from in the control group between 4 weeks (0.127±0.549) and 8 weeks (0.032±0.146) ($p = 0.395$).

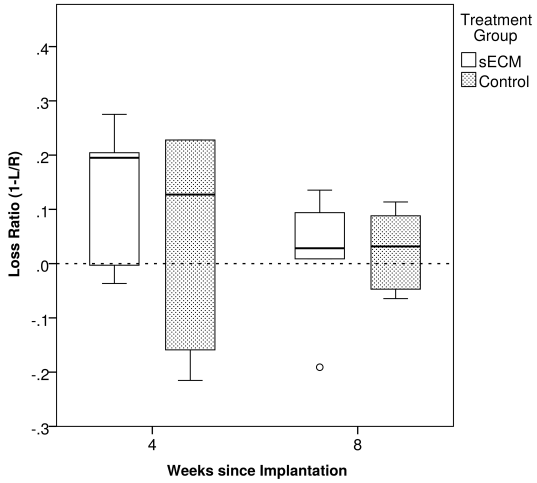

(a) Biceps Femoris muscle mass loss ratios. Differences are not significant $p \geq 0.395$.

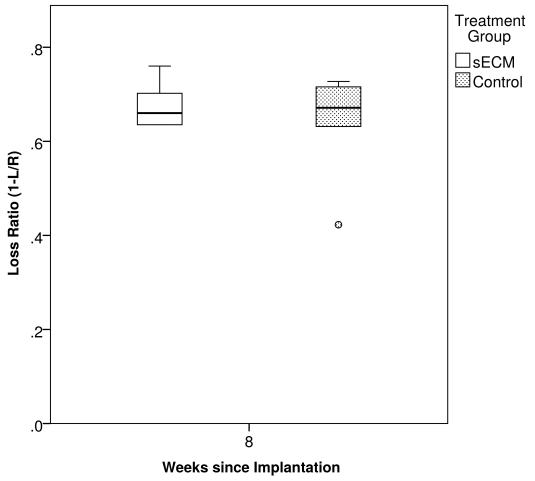

(b) Tibialis Anterior muscle mass loss ratios. Differences are not significant, $p = 1.000$.

Figure 6.11: Muscle mass loss ratios for biceps femoris and tibialis anterior. 0 is no change, >0 is relative muscle atrophy on implanted side, <0 is relative muscle hypertrophy on implanted side.

6.3.3.3 Histology

Axons were visible in transverse histological sections in the majority of samples. Example images of nerve proximal and distal to the implants are shown after 4 weeks implantation (figs. 6.12a to 6.12h) and 8 weeks implantation (figs. 6.13a to 6.13h).

At 4 weeks, little difference between the two treatment groups can be observed. The proximal nerve has regularly spaced axons and blood vessels throughout a nerve, fascicles are not visible in these sections indicating structural remodelling (figs. 6.12a to 6.12d). The distal nerves have axons and blood vessels present in a disordered structure (figs. 6.12e to 6.12h).

After 8 weeks the proximal nerve is more disordered in both groups. Fascicles are visible in the control group sections, with axons and blood vessels bundled within concentric connective tissue (figs. 6.13a

and 6.13b). The sECM treated group has formed a dense tissue with some axons present, the appearance is in part due to an oblique section and the high level of osmium tetroxide fixation present (figs. 6.13c and 6.13d). Distal to the implant at 8 weeks the control group has formed fasciles, with axons and blood vessels surrounded by vascularised connective tissue (figs. 6.13e and 6.13f). The sECM treated groups has formed a nerve without fascicles, but with regularly spaced axons and blood vessels (figs. 6.13g and 6.13h).

Microfascicles were observed in a few cases. An oblique microfascile section is shown in fig. 6.14b and transverse microfascicle sections are shown in fig. 6.14b. Staining quality appears poor; however, a layer of connective tissue can be seen surrounding a stained linearly aligned tissue, indicating the presence of myelinated axons.

Axon diameters and axon densities were calculated from transverse histological sections. Axon diameter distributions are presented in figs. 6.15a and 6.15b and are summarised in box plot form fig. 6.16a. Axon density is plotted in fig. 6.16b.

Axon diameters were analysed by comparing the different treatment groups (sECM coated or control) in the same location (proximal or distal) and time point (4 weeks or 8 weeks). 4 weeks after implantation there is no significant difference between proximal axon diameters for the sECM coated (3.81 ± 2.41 μm, median $\pm$ interquartile range) and control interfaces (4.24 ± 2.26 μm), $p = 0.274$. Distally the control group axon diameters are significantly larger at 4 weeks ($p = 0.0006$): sECM coated group diameters are 3.29 ± 2.22 μm; and control group diameters are 4.05 ± 2.28 μm. After 8 weeks implantation proximal axon diameters are not significantly different between treatment groups ($p = 0.345$): the sECM treated group has slightly larger diameters (3.51 ± 2.61 μm) compared with the treatment group (3.39 ± 2.19 μm). The distal axon diameters at 8 weeks are significantly larger in the sECM treated group (4.16 ± 3.09 μm) compared with the control group (3.12 ± 2.00 μm, $p < 0.001$).

Axon diameters were also analysed by comparing the different time points (4 weeks or 8 weeks) in the same location (proximal or distal) and treatment group (sECM coated or control). There was no significant difference in proximal diameter for sECM coated samples between 4 and 8 weeks post implantation ($p = 0.211$). Distally sECM coated group axon diameters were significantly larger at 8 weeks compared with 4 weeks ($p = 0.0012$). In the control group axon diameters were significantly smaller at 8 weeks compared with 4 weeks in both the proximal ($p = 0.0023$) and distal ($p < 0.001$) locations.

Finally, axon diameters were analysed by comparing the different locations (proximal or distal) at the same time point (4 weeks or 8 weeks) and treatment group (sECM coated or control). For the control group there was no significant difference between proximal and distal axon diameters at 4 weeks ($p = 0.724$) and 8 weeks ($p = 0.363$) post implantation. In the sECM coated group there was no significant difference between proximal and distal axon diameters at 4 weeks post implantation ($p = 0.0575$); how-

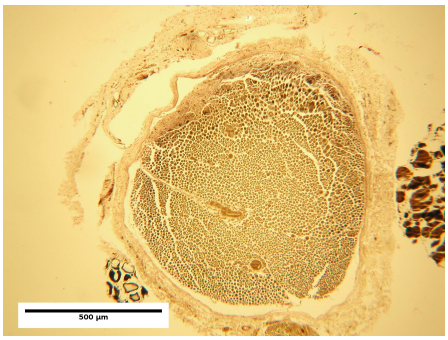

(a) 4 Weeks, Control, Proximal, 10x magnification.

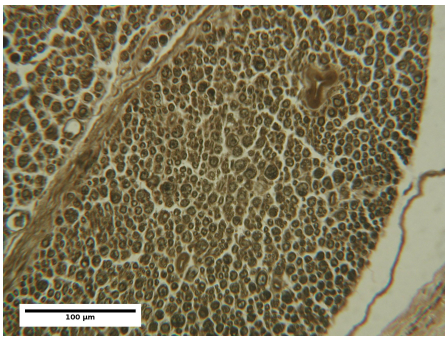

(b) 4 Weeks, Control, Proximal, 40x magnification.

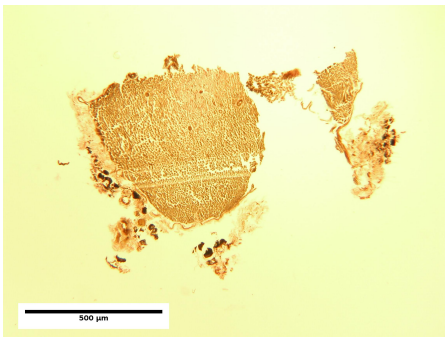

(c) 4 weeks, sECM treated, Proximal, 10x magnification.

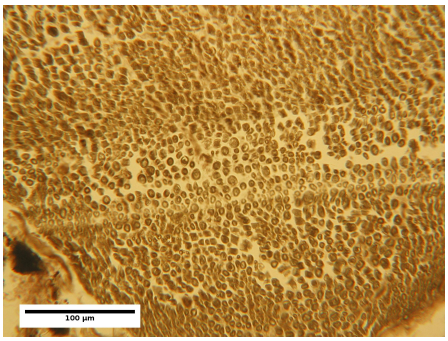

(d) 4 weeks, sECM treated, Proximal, 40x magnification.

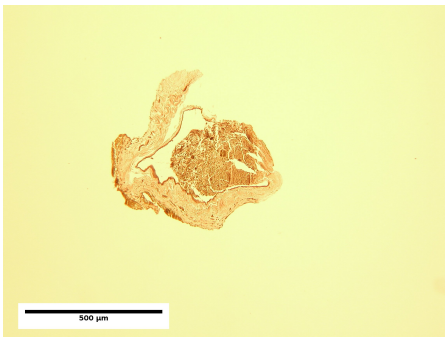

(e) 4 weeks, Control, Distal, 10x magnification.

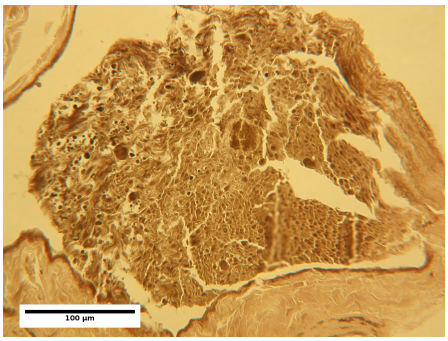

(f) 4 weeks, Control, Distal, 40x magnification.

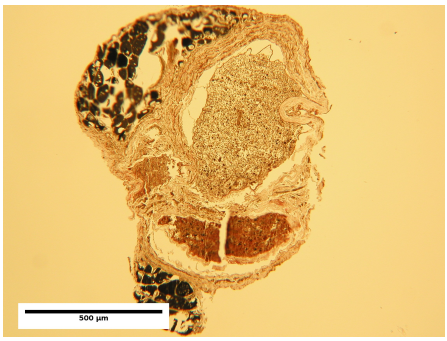

(g) 4 weeks, sECM treated, Distal, 10x magnification.

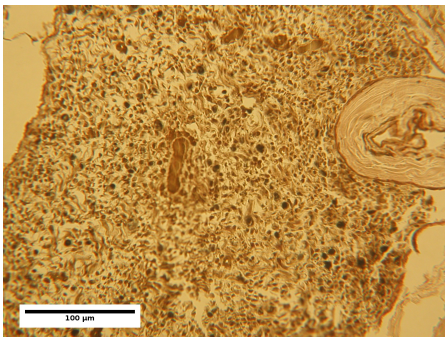

(h) 4 weeks, sECM treated, Distal, 40x magnification.

Figure 6.12: Transverse histology of regenerated nerves 4 weeks after microchannel neural interface implantation. Proximal and distal sections are shown, at 10x and 40x magnification for sECM treated and control interfaces.

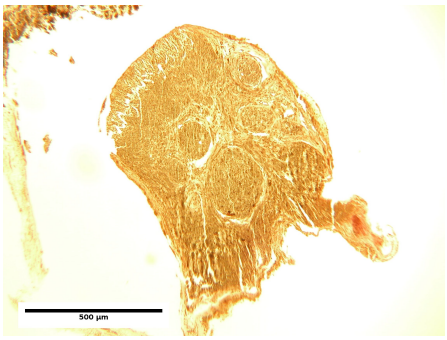

(a) 8 weeks, Control, Proximal, 10x magnification.

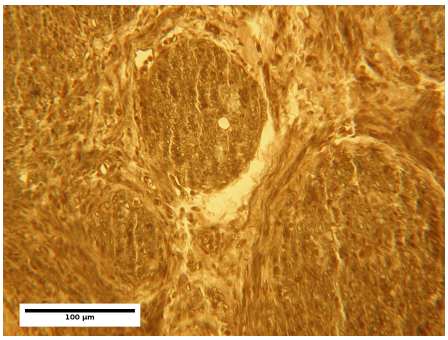

(b) 8 weeks, Control, Proximal, 40x magnification.

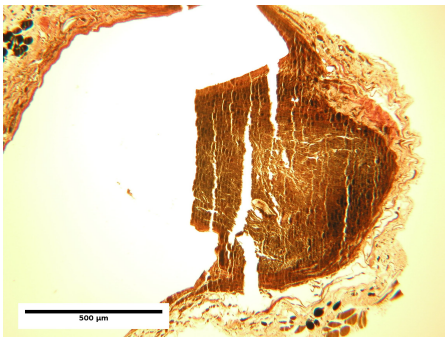

(c) 8 weeks, sECM treated, Proximal, 10x magnification.

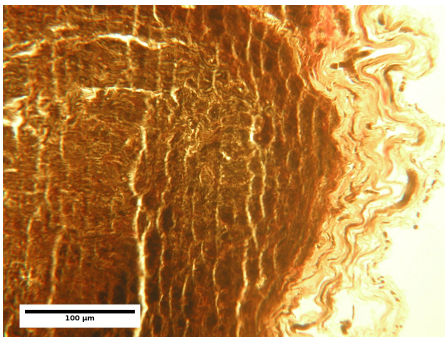

(d) 8 weeks, sECM treated, Proximal, 40x magnification.

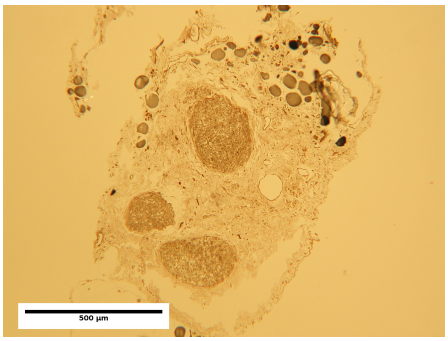

(e) 8 weeks, Control, Distal, 10x magnification.

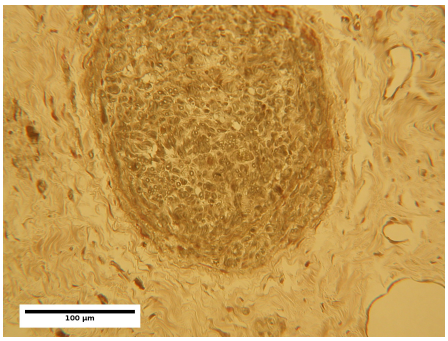

(f) 8 weeks, Control, Distal, 40x magnification.

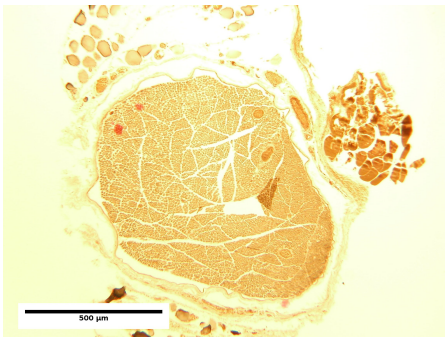

(g) 8 weeks, sECM treated, Distal, 10x magnification.

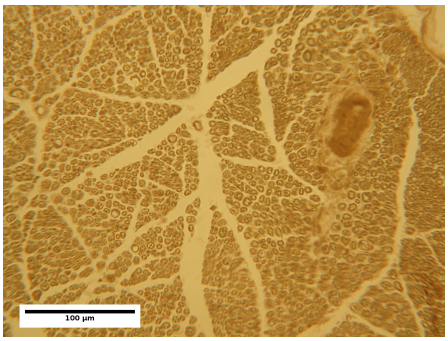

(h) 8 weeks, sECM treated, Distal, 40x magnification.

Figure 6.13: Transverse histology of regenerated nerves 8 weeks after microchannel neural interface implantation. Proximal and distal sections are shown, at 10x and 40x magnification for sECM treated and control interfaces.

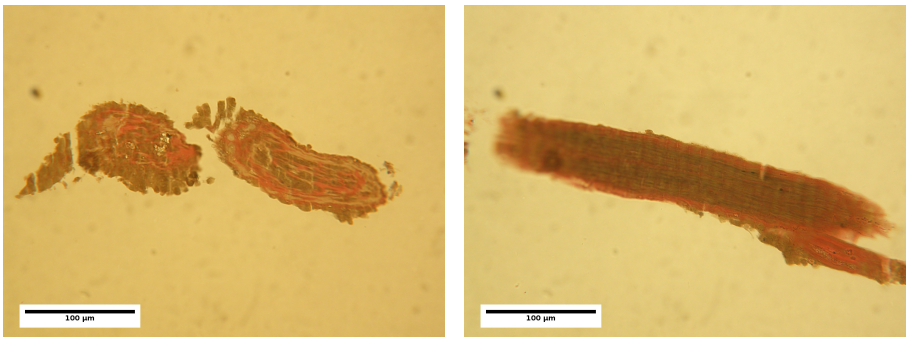

(a) Oblique microfascicle section. (b) Transverse microfascicle section.

Figure 6.14: Transverse and oblique histology of regenerated nerves 8 weeks after microchannel neural interface implantation. Microfascicle sections are shown, at 40x magnification for an sECM interface.

ever distal axon diameters were significantly larger compared with proximal diameters at 8 weeks post implantation ($p = 0.0113$).

Axon densities were compared with respect to location (proximal or distal), time point (4 weeks or 8 weeks), and treatment group (sECM coated or control), while keeping the other dependent variables constant. No significant differences in axon density were observed across all tests ($p \geq 0.188$). Axon density data is tabulated in table 6.1.

Group	**Weeks**	**Location**	**Median Axon Density (axons/μm^2)**	**Interquartile Range**
Control	4	Proximal	0.0135	0.0201
Control	4	Distal	0.00783	0.00902
Control	8	Proximal	0.0155	0.0131
Control	8	Distal	0.00694	0.0143
sECM Treated	4	Proximal	0.00957	0.00950
sECM Treated	4	Distal	0.00999	0.00558
sECM Treated	8	Proximal	0.00734	0.00880
sECM Treated	8	Distal	0.00939	0.0126

Table 6.1: Axon densities following microchannel neural interface implantation after 4 weeks and 8 weeks. Sections taken proximal to and distal from the site of microchannel neural interface implantation. Treated (sECM) and Untreated (Control) interfaces. All values to 3 significant figures.

6.3.3.4 Sciatic Function Index

An increasing trend in SFI was observed for both treatment groups (see fig. 6.17 and table 6.2). Linear trends were calculated for each group in the form $y = mx + b$, the details are given in table 6.3. In both groups the trend is weak but significant by Spearman's rank correlation. The increase per day is larger in the treated group (0.69 SFI units) than in the control group (0.48 SFI units). The rate of SFI increase per day was calculated for each animal as the slope from a linear regression. There was no significant

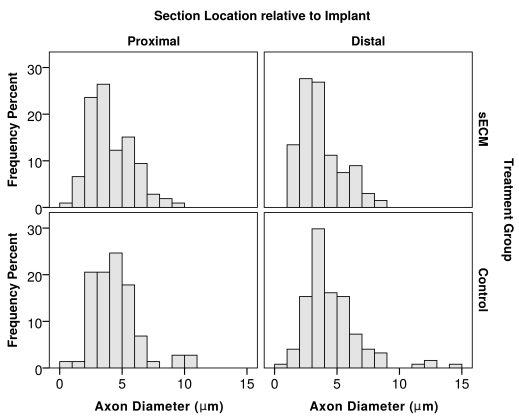

(a) Histogram of axon diameters after 4 weeks implantation.

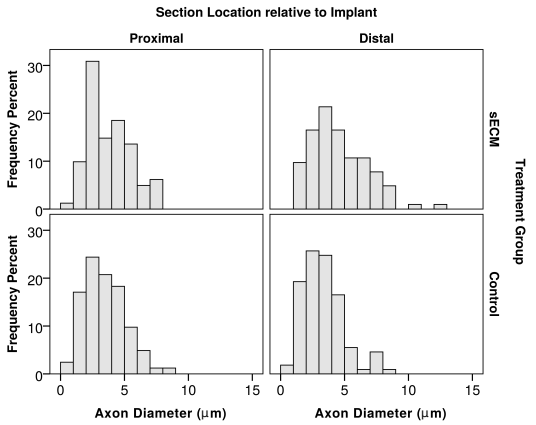

(b) Histogram of axon diameters after 8 weeks implantation.

Figure 6.15: Histograms of axon diameter following implantation after 4 weeks and 8 weeks. Sections taken proximal to and distal from the site of microchannel neural interface implantation. Treated (sECM) and Untreated (Control) interfaces. 1 μm bins. This data is also presented in fig. 6.16a.

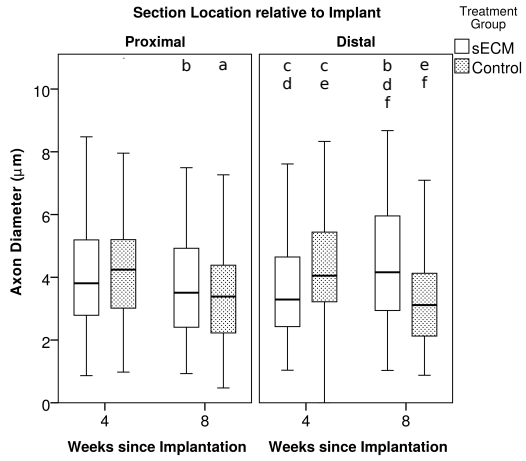

(a) Boxplot of Axon Diameter. Significant differences are indicated by paired letters: a, p = 0.002; b, p = 0.011; c,d,e,f, p = 0.001. This data is also presented in figs. 6.15a and 6.15b.

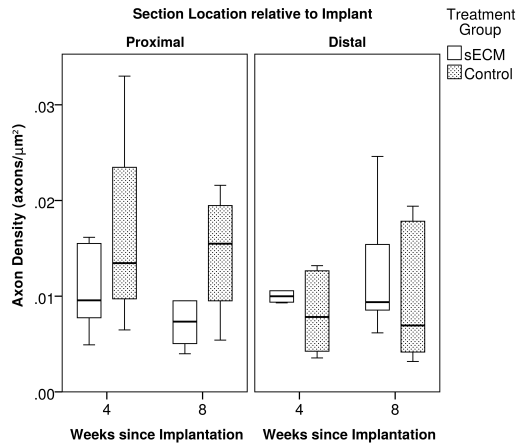

(b) Boxplot of Axon Density. Differences are not significant, p $\geq$ 0.188.

Figure 6.16: Boxplots of Axon Diameter and Axon Density following microchannel neural interface implantation after 4 weeks and 8 weeks. Sections taken proximal to and distal from the site of microchannel neural interface implantation. Treated (sECM) and Untreated (Control) interfaces.

difference in SFI trend between the treatment groups (p = 0.9286, fig. 6.18). Median gradient of the linear trend was 0.562±0.682 for the group with protein coated microchannels and 0.581±0.783 for the untreated group (median ± I.Q. range, in SFI units per day).

Weeks following surgery	Untreated Control SFI	sECM Treated SFI
1	-85.2 ± 15.4	-83.7 ± 12.8
2	-77.4 ± 21.2	-78.4 ± 17.9
3	-83.8 ± 23.4	-76.6 ± 16.8
4	-74.5 ± 22.2	-72.0 ± 17.0
5	-81.9 ± 21.2	-69.5 ± 5.13
6	-74.4 ± 16.1	-61.8 ± 25.9
7	-68.4 ± 12.2	-55.5 ± 10.9
8	-49.4 ± 38.2	-51.7 ± 12.4

Table 6.2: Medians ± interquartile range of sciatic function index (SFI)for 8 weeks following microchannel neural interface implantation.

Group	Slope (m)	Intercept (b)	R^2 value	Spearman's ρ	Significance
Control	0.48	-87.85	0.231	0.443243	<0.001
Treated	0.69	-91.31	0.394	0.665011	<0.001

Table 6.3: Correlation details for change in Sciatic Function Index by days following surgery. Significance for Spearman's ρ calculated with respect to a null hypothesis of $\rho = 0$, not between groups. In both cases the null hypothesis can be rejected.

6.3.3.5 Electrophysiology

Extracellular neural potentials were observed by recording from the microchannels following stimulation of the proximal nerve (see fig. 6.19). Following stimulation using the microchannel neural interface tibialis anterior compound motor action potentials were observed (see fig. 6.20).

Where spikes could be identified signal-to-noise ratios for the muscle and nerve signals were calculated. SNRs are shown in fig. 6.21. No significant differences in SNR either between treatment groups or between time points were observed for either muscle recordings (p >0.201) or nerve recordings (p >0.265).

Nerve recordings had consistently larger SNR in the treatment group compared with the control group, at 4 weeks (sECM treatment SNR = 7.29±2.31, control group SNR = 5.96±1.53, median ± I.Q. range) and at 8 weeks (sECM treatment SNR = 8.93±3.73, control group SNR = 5.51±0.480). In addition an increasing trend in SNR was observed in the treatment group while a decreasing trend was observed in the control group, neither difference was significant (p >0.533).

Muscle recording SNR was greater for the control group at 4 weeks (7.78±2.43) compared with the sECM treated group at the same time point (6.05±1.60). While at 8 weeks the sECM treated group

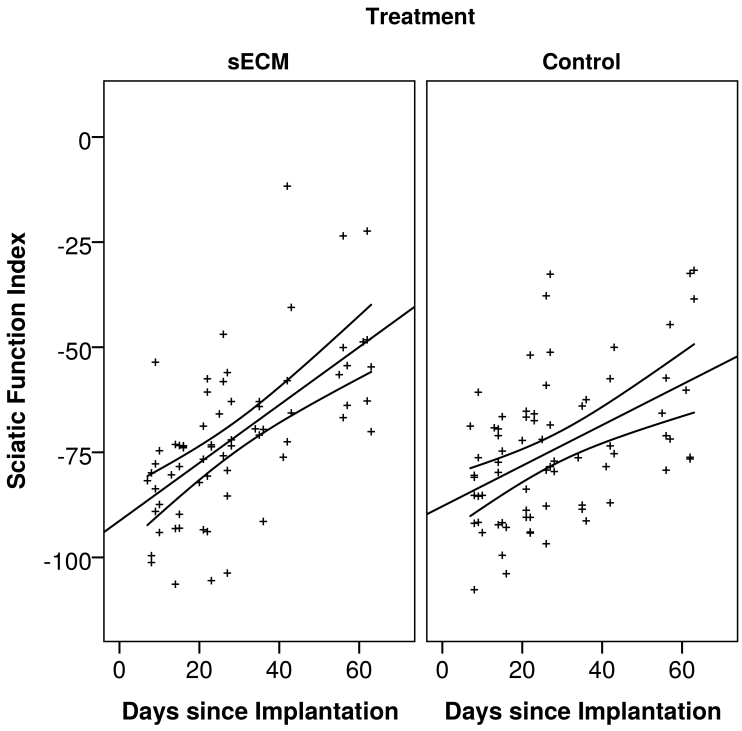

Figure 6.17: Sciatic Function Index following 2 months neural interface implantation. Linear trend lines with 95% confidence intervals of the mean. Both trends are significant: sECM, $R^2 = 0.394$, $\rho = 0.665$, $p < 0.001$; Control, $R^2 = 0.231$, $\rho = 0.443$, $p < 0.001$.

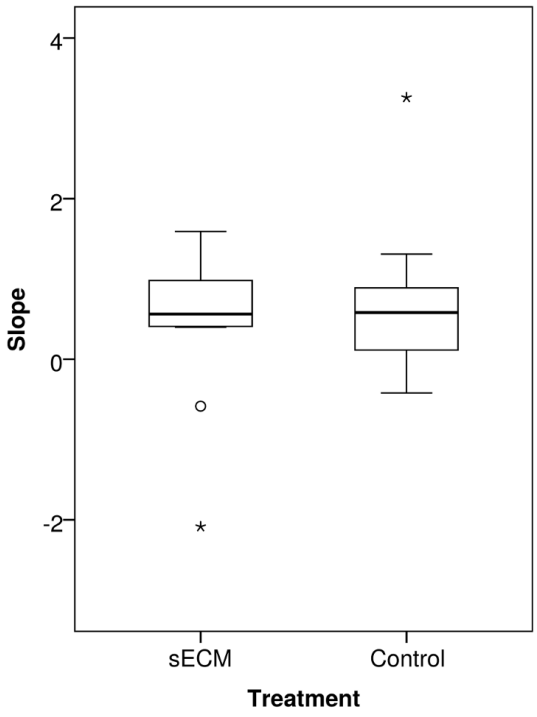

Figure 6.18: Rates of Sciatic Function Index increase per day following 2 months neural interface implantation. Per animal linear trend slopes. The difference is not significant, p = 0.929.

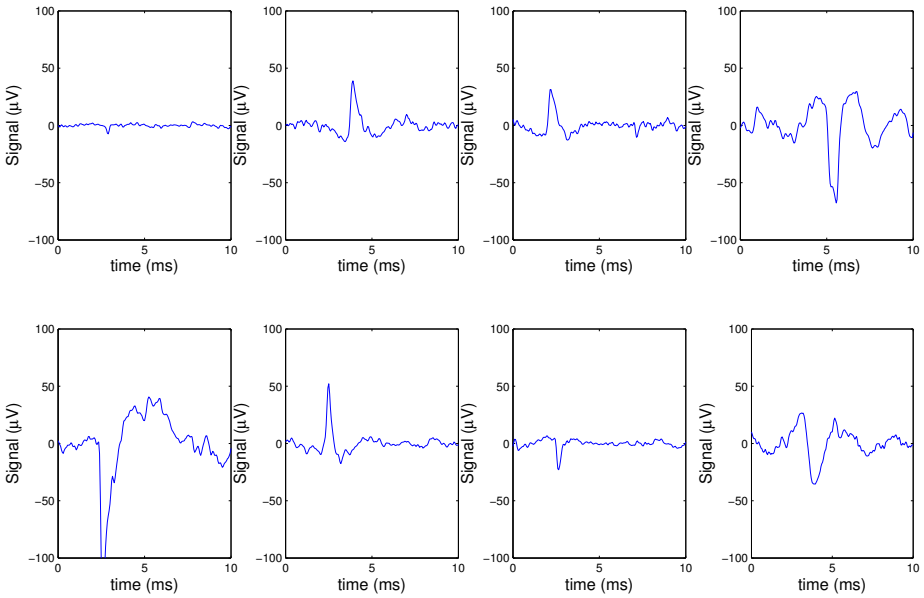

Figure 6.19: Evoked nerve signals recorded from microchannel neural interfaces.

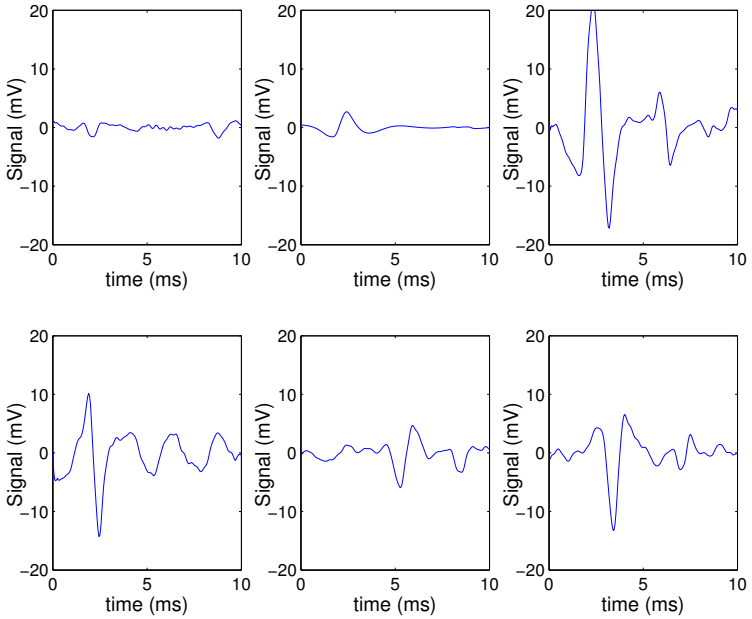

Figure 6.20: Evoked muscle signals recorded from tibialis anterior following stimulation through microchannel neural interface.

SNR was greater (6.69±1.27) compared with the control group (5.76±2.45). Both difference were not significant (p >0.201). The trends changes in SNR from 4 weeks to 8 weeks were also not significant: increasing SNR in the treated group (p = 0.856); and decreasing SNR in the control group (p = 0.629).

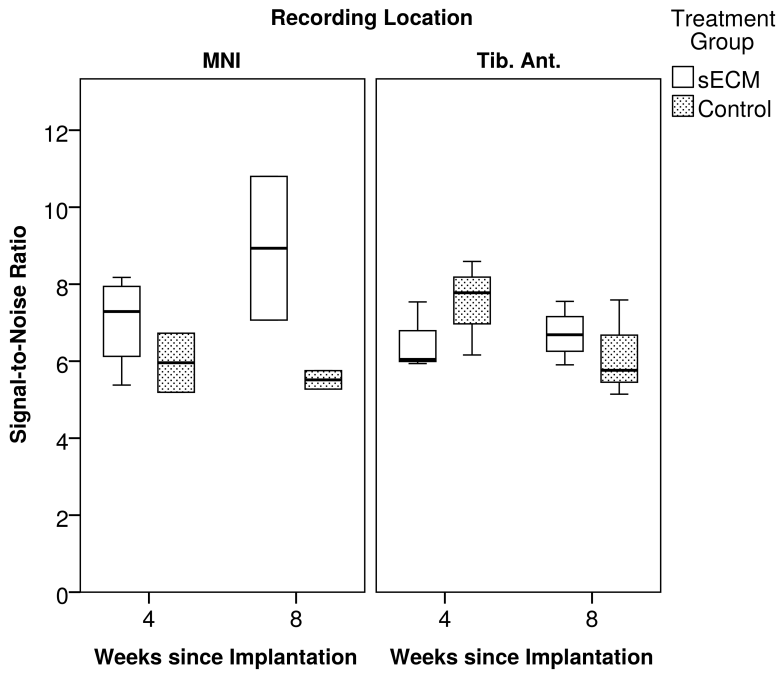

Figure 6.21: Signal-to-noise ratios for stimulation and recording with microchannel neural interfaces (MNI). 4 weeks and 8 weeks following interface implantation. Treated (sECM) and Untreated (Control) interfaces. MNI recordings are made from within the microchannel following nerve stimulation with a proximal hook electrode. Tibialis Anterior (Tib. Ant.) recordings are made using epimysial electrodes following stimulation of the nerve through the MNI. The differences are not significant, p >0.201.

6.3.3.6 Impedance Spectroscopy

Impedance reduced over time in both groups. 1kHz impedance (see fig. 6.22a) was not significantly different between electrodes randomly assigned to each group before surgery (p = 0.847). There was no significant difference in 1 kHz impedance between the treated and untreated groups after 1 month (p = 0.652), or after 2 months (p = 0.089). For the control group impedance was significantly lower after 2 months implantation compared with before implantation (p = 0.01), no other significant differences between time points were observed (p $\geq$ 0.133). Complete impedance spectrographs are given in fig. 6.22b.

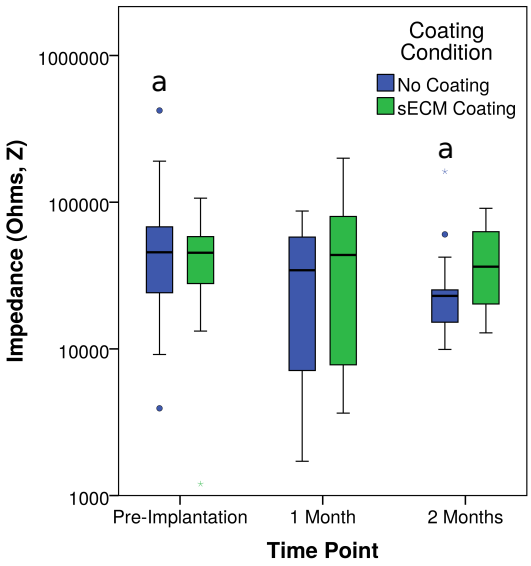

(a) 1kHz impedance plotted on a log scale. Significant differences are indicated by paired letters: a, p = 0.01.

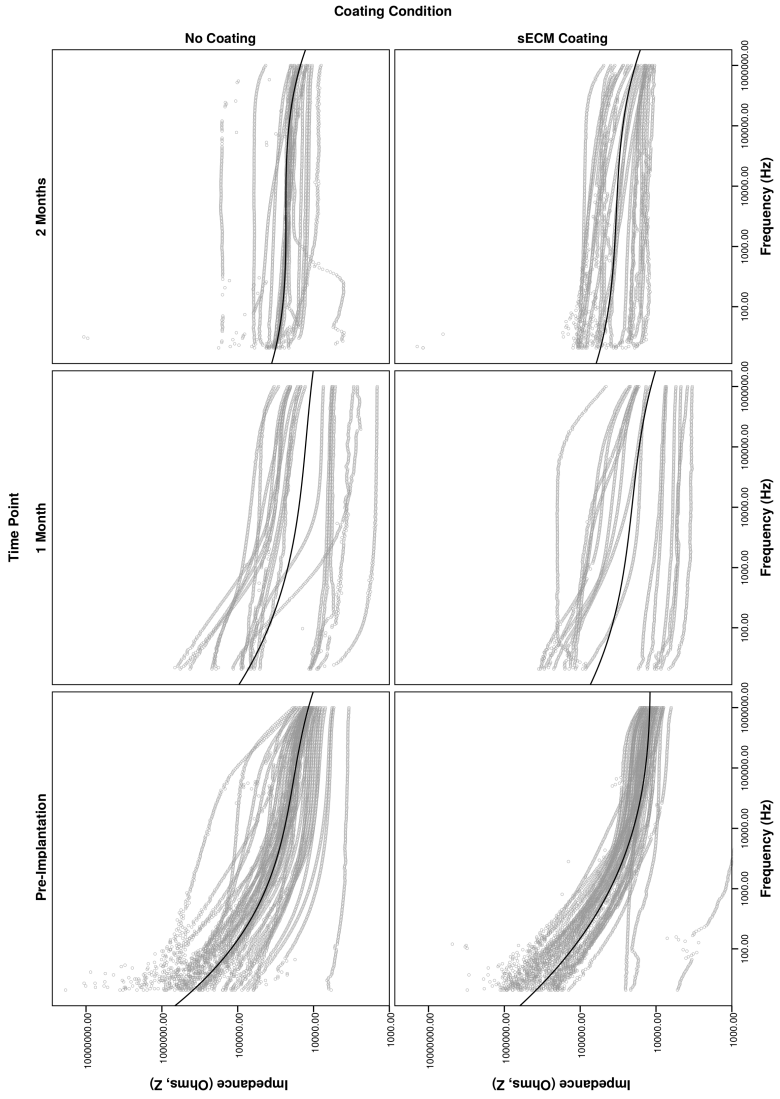

(b) Impedance plotted on a log-log scale.

Figure 6.22: Change in impedance following implantation.

6.4 Discussion

Regeneration of rat sciatic nerve was observed through passive, coiled, microchannel neural interfaces and electrode containing, stacked, microchannel neural interfaces. The regeneration was monitored through histological, functional and electrophysiological assessment.

6.4.1 Cadaveric implantation of a regenerative neural electrode

The cadaveric study was important to determine: that the surgical approach was suitable; the appropriate size of the neural interface; the suturing procedure was reliable; that the surgeon was sufficiently knowledgeable of the anatomy to keep surgical times to a minimum. Anatomical variations were slight, but were present during the course of the studies, with the nerve occasionally branching within the surgical window [497]. Variations were overcome by ensuring that the nerve was sutured proximal to any branch, and that, where possible fascicles were placed in the same orientation at either end of the MNI lumen.

6.4.2 An *In Vivo* Comparison of Tissue Glue and Suture for Microchannel Neural Interface Implantation

The results of this study do not support the hypothesis that fibrin glue is a suitable method for *in vivo* fixation of MNIs compared with standard microsurgical suture repair. This is in part due to method of fibrin application, on the outside of the MNI. In the fibrin glue group the nerve followed the glue rather than remaining within the lumen of the implant, this indicated two hypotheses. 1) fibrin glue is conducive to nerve growth, 2) To ensure regrowth down the microchannels the interface lumen must be fully sealed. In this case there was a small slit in the lumen of the silicone tubing used as a nerve guide proximal and distal to the interface, this was avoided in future applications by designing an alternative nerve guide and by sealing the nerve guide using silicone.

Microfascicles were observed in the sutured nerves, indicating that axons had regenerated along the microchannels. This supported the use of sutures for MNI implantation.

The benefits of both implantation methods could be exploited by filling the MNI lumen with fibrin glue, either alone or as a carrier for biomolecules or cells, and then suturing the fibrin-MNI in place. A number of challenges are expected in this design: fibrin is viscous and sets rapidly, a vacuum chamber should be used to ensure the lumen is filled; fibrin will attach to the outside of the MNI, this should be removed after it is set; Tisseal is expensive ($\sim$ £50 per ml [5]); fibin filling must be carried out under sterile conditions either during or shortly before surgery. A further hypothesis is proposed: fibrin glue filling will improve functional, histological and electrophysiological outcomes compared with untreated controls following MNI implantation in a rat sciatic nerve model

Fibrin glue may benefit the electrophysiological function in addition to histological measures [513, 514]. This study only continued for 3 weeks, and observed no significant differences in SFI (due to a

[5] 2014 figure.

low sample number). In a 12 week regeneration study no significant difference in sciatic function was observed between fibrin glue and suture repair, however, SFI was more normal[6], with mean values in the range -35 to -55 (compared with -65 to -75 after 4 weeks in this study) [514].

6.4.3 An *In Vivo* Comparison of Internal Surface Coatings for Microchannel Neural Interface Implantation

The results of this study support the hypothesis that rat sciatic nerve axons regenerate through stacked microchannel neural interfaces *in vivo*. However, there is some inconclusive, evidence to support the hypothesis that multi-protein coatings improve functional, histological and electrophysiological outcomes compared with uncoated controls following MNI implantation in a rat sciatic nerve model.

In line with previous studies of MNIs tissue was seen within the microchannels and could be removed, in part, during dissection [51, 113, 156]. However, these microfascicles ('mini-nerves') could not readily be observed following histological processing since they become brittle following osmium treatment. In a few cases transverse sections could be observed, however staining quality was poor. Myelinated and unmyelinated axon structures were observed proximal to and distal from the interfaces. Difficulty with sectioning nerves following regeneration through an MNI has been noted by other research groups, leading to quantitative analysis being abandoned in one case [148].

Distal axon diameters demonstrate significant differences between groups, the control group has larger axons after 4 weeks and the treated group has larger axons after 8 weeks. This is further confirmed by the findings that axon diameters were significantly smaller in the control group after 8 weeks compared with after 4 weeks, and that the opposite was found for distal axon diameters in the treatment group (increase from 4 weeks to 8 weeks). The increase in, and significantly larger, distal axon diameters supports the hypothesis that nerve regeneration is improved by sECM coatings. The differences are not large compared with the data variability, after 8 weeks median distal axon diameters are approximately 30% larger in the treatment group compared with the control group.

Axon densities were not significantly different between the treatment groups. However, the greatest axon densities were observed proximally in the control group, while the median densities were over 70% lower distally at both 4 weeks and 8 weeks. In contrast axon densities were more consistent in the sECM treated group. This may be due to frustrated regeneration in the control group causing a backup of sprouting axons proxmally, whereas the sECM coating encourages axon growth within the microchannels. Where axons are encouraged to follow the microchannel they will be directed distally, reducing axon number proximally and increasing the number of axons regenerating the correct direction distally.

Axon diameter distributions are similar to previous studies [51] and axon densities reported here

[6]Less negative, i.e. closer to zero.

fall close to the range of previous MNI results (0.000170 axons/μm^2 to 0.0163 axons/μm^2 in [51]). Other studies of MNI regeneration have not reported detailed axon density and diameter data [148, 156]. When compared with a study of an interface, which does not require complete nerve transection, the MNI studies have a reduced axon diameter (mean diameters between 5.11 μm and 5.75 μm following Utah array implantation [135]). MNI studies also show increased fibre density compared with a study of Utah array implantation in rat sciatic nerve (example mean densities of 0.000723 axons/μm^2 proximally and 0.00136 axons/μm^2 distally), fibre densities for MNI implantation are more similar to the proximal density values. Axon morphometry in healthy rat sciatic nerve shows some differences: diameter is greater than observed in this study (5.52$\pm$0.37 μm, mean $\pm$ S.D.); axon densities are in the range of the greatest densities observed in this study (0.011718$\pm$0.003287 axons/μm^2, mean $\pm$ S.D.). Different tissue processing methods used in this study compared with some previous work may have resulted in a slight underestimate of fibre diameter; however this may only result in the mean axon diameters being 0.1 μm smaller than expected [501].

At much longer time points than those used in this study axon diameter distribution shifts right (towards larger diameters); however, even after 200 days with immediate direct repair without a nerve gap the normal bimodal axon diameter distribution does not return [521], and after 2 years axon diameters are only 70% of the normal value [503]. In contrast, following nerve injury, axon counts are expected to increase up to 3 or 6 months after injury due to axon sprouting and frustrated regeneration causing retrograde (distal to proximal) axon growth [503]. Frustrated growth is expected in MNI implantation because the interface creates a partial physical block to further axon growth.

The processing method, using osmium tetroxide, caused hardening of tissues with high lipid concentrations, and some samples did not section cleanly, causing smearing or breaking of the section. By regularly changing the microtome blade this could be overcome, and high definition sections similar to those reported by Di Scipio *et. al.* were obtained [504].

Muscle mass changes showed atrophy in both the tibialis anterior and the biceps femoris. This occurred to a much greater extent in the more distal muscle, the tibialis anterior, due to the location of the sciatic nerve transection. After 3 months a previous MNI study showed less extensive tibialis anterior atrophy than observed here, this may be due to the one month difference in end-point, and to interface and surgical variation [51]. The use of the contralateral muscles as a control may misrepresent the changes in muscle mass: due to compensation by the non-operated limb hypertrophy may be present.

The sciatic function index and observation did not show a return to full function in either treatment group, with median SFIs of approximately -50 observed after 8 weeks. There was no statistical difference observed in recovery rate between the two groups; however, the untreated control group values consistently lagged the treated group in weeks 1 to 7. Assuming the linear trends observed continue full function could be expected to return after 183 days for the control group and 132 days for the treatment

group. However, this might not be true in practice because not all axons will regenerate and innervation patterns will be different. In addition, delayed reinnervation will cause loss of muscle mass and function, leaving some more permanent loss of function. Functionally the implantation of MNIs causes severe changes, in contrast implants which do not require nerve transection allow for rapid recovery of function, within 4 weeks post operatively for Utah Array implantation. When compared with a previous study of long nerve defects (12 mm gap, SFI <-80 after 12 weeks), the SFI values and rate of recovery indicate good nerve function following regeneration through the MNI [368]. However, short defects which do not disrupt nerve continuity (e.g. 5 mm nerve crush), recover much more quickly and more completely than MNI implantation: recovery to approximately SFI = -10 have been observed within 4 to 8 weeks [503, 508].

Motor and neural spikes were observed in some cases following MNI implantation. Neural spike amplitudes were within the range of previous recordings from *in vivo* MNIs [51, 148, 156]. Similarly motor unit action potentials conformed with previous findings. Due to the limitations of the stimulation equipment stimulus ramps could not be used to look for stimulation thresholds. All recorded SNRs were greater than the commonly accepted standard, SNR $\geq$ 5 [52]. However, these SNRs were calculated from identifiable spikes, setting an arbitrary minimum due to spikes which were either below the noise level or not identified due to their similarity to noise. The use of automated spike sorting may overcome this difficulty and provide a more objective measure of the noise and signal levels in MNI recordings [54, 170, 171].

6.4.4 General Discussion

It is concluded that stacked microchannel neural interfaces are suitable for *in vivo* use, although modifications and improvements are required. The interface coatings tested do not provide sufficient improvements to support their use in future application; however, there is still a need for treatments to improve neural regeneration within MNIs. One such treatment, fibrin, has shown unexpected promise, and should be examined in future.

One case where MNIs may present an advantage is during targeted muscle reinnervation (TMR, see chapter 2). For TMR nerves are transected and coapted to new, fresh muscle, close to the innervation point. Because the nerve already undergoes a type 5 injury [64] a conduit or MNI can be interposed during the reinnervation surgery. This may reduce the number of axons with reinnervate the target muscle; however the MNI would allow direct sensory feedback, achieving targeted sensory reinnervation [232] without the need for coaption to cutaneous nerves and providing a direct route to stimulate the nerve rather than using the reinnervated skin.

Other alternative implantation methods have already been used with MNIs. Teased nerve rootlets have been placed in microchannels, avoiding the need to transect the nerve, enabling recordings from

day 1 following implantation and avoiding the injury and recovery time associated with transection [153, 154]. This should be investigated in peripheral nerves in *ex vivo*, cadaveric, and if feasible *in vivo* studies.

In comparison to previous studies the rate of survival (96%) in this experimental series was good. In this study one superficial perioperative infection was observed at the normal study end point and one loss during anaesthesia occurred during implantation in a total of 28 animals, no significant autotomy was noted beyond toenail trimming in a few animals. Previous MNI studies have reported excellent, 100%, levels of recovery: 14/14 in [51]; 23/23 reported in [154]); 7/7 reported in [470]; 1/1 reported in [147]. In contrast some studies state poor survival rates for rat sciatic nerve transection studies (35%, 30/86 in [514]): it is key that studies are carried out to minimise this loss, the choice of appropriate strains (Lewis or Wistar), housing, anaesthesia and experimental protocol (e.g. minimising gap length) will go some way to increasing survival rates [497].

Improvements to the study design should be considered in future. In particular the requirement to carry out terminal anaesthesia for electrophysiology in this study. Chapter 2 of this thesis and previous studies with MNIs have demonstrated the use of hard wired connections for muscle and nerve recordings [148]. Recovery could be monitored both through function (SFI, nightly walking distance), and through electrophysiology during normal behaviour, while reducing the number of animals. The combination of MNI technology with ITAP bone anchored devices will make this possible in large animal models, and modified bone anchored devices could be used to provide long-term head stages for small animal studies.

The *in vivo* experiments presented in this chapter are limited by the model chosen. Rats are known to regenerate more quickly than humans [498], and other differences, such as nerve diameter and time following amputation (nerve transection in this case) will alter the rate and ability of the nerve to regenerate [143, 277]. Longer and larger nerves are present in larger animal models [496]; however, this change to study design would be costly, and ethical concerns and reduced availability of suitable immunological probes may make large models less suited. Further work is required to refine and improve upon microchannel neural interfaces in order to ensure that, in future, they can provide the best possible upper limb function for human amputees.

Chapter 7

General Discussion, Contribution to Scientific Research and Proposals for Future Work

This chapter summarises the key findings and conclusions of this thesis. The work is placed in the context of current clinical and experimental solutions to amputee prosthetic control. Future work is proposed including improvements required in engineering, experimental and clinical knowledge for the implementation of epimysial electodes, hard-wired interfaces and microchannel neural interfaces (MNIs).

The main aim this thesis was to investigate and improve implantable devices for prosthetic control.

Chapter 1 presented an overview of upper limb amputation and currently available prostheses. The limitations of current methods were identified, a central issue is the lack of intuitive, responsive systems. To achieve a more intuitive system it was proposed that an increased number of control signals are required. Methods for recording these signals from muscle and nerve were described, along with the relevant biology and electrophysiology. Interface designs follow a trade-off between invasivity and selectivity, this thesis considered two implantable interfaces from low invasivity (epimysial electrodes) to high invasivity (MNIs). The challenge of biocompatibility for muscle and neural interfaces was considered, in particular the challenge of encouraging nerve growth within small, long microchannels. Finally, surgical interventions for upper limb amputees were considered, targeted muscle reinnervation (TMR) for control, and intraosseous transcutaneous amputation prostheses (ITAP) for prosthetic attachment.

Chapter 2 presented the development and testing of a device to record epimysial EMG signals in cognisant, moving animals and transfer these signals transcutaneously. The design was shown to function for 19 weeks *in vivo* with recordable EMG signals in the majority of cases. The flange design was found to cause skin failure at sharp edges, and a domed implant design was proposed. Further, TMR was examined in a sheep model and recovery in gait and muscle activity was observed in tandem. This model is proposed for further investigation including active electrode designs and RPNI-like free muscle-flap implantations [230, 231].

This thesis has contributed to the literature surrounding the use of bone-anchored devices for bi-

osignal transmission. This work improved upon research by Pitkin et al [241] and similar ideas have led to the implementation of signal transmission in two-part osseointegrated prostheses [233, 281]. The initial pilot study was published [1], leading to discussion of the use of our ovine lower limb model for evaluating alternative muscle interface designs and signal transmission methods. Tripolar electrode configurations are of particular interest, and the manufacturing methods described in Chapter 5 of this thesis could be implemented to design a single interface with both tripolar and bipolar interfaces for a direct comparison. The research group which undertook this study of implanted muscle electrodes are undertaking further research to apply this design for human upper limb amputees, and funding for this has been has been granted from a charitable organisation (RAFT).

Targeted muscle reinnervation is in clinical use at a small number of centres. However, there is limited evidence surrounding the biological limits of TMR. Research into regenerative peripheral nerve interfaces has led to the use of smaller and smaller free muscle flaps [230, 231, 522]; however it is not known how multi-flap systems will survive or degrade over timescales required for clinical use (years). The extent of crosstalk in TMR is not widely discussed and should be examined in a multi-muscle system, the model presented in this work would be suitable for evaluating crosstalk by using up to the 6 muscles identified [1]. Clinical observations have shown that during reinnervation and training motor nerves coapted to a single muscle become coordinated [personal correspondence], the ability to monitor biosignals during recovery provided by our model will allow this to be examined in detail. By recording with a neural cuff interface on a coapted nerve and an epimysial interface on the reinnervated muscle, correlation between the recorded ENG and EMG signals could be calculated to assess the extent of coordination.

The implantable EMG based control system proposed overcomes some issues with current prosthesis control: electrode lift-off; repeatable placing of electrodes; *etc.*. However, standard muscle based control will not provide intuitive control over hand movement in cases of transhumeral amputation or shoulder disarticulation. TMR may provide more intuitive control by re-routing nerves previously responsible for hand and limb movement to surrogate muscles; however, there are limits on the number of control signals due to muscle and nerve availability. Nerves cannot be dissected sufficiently to map the nerve fibres responsible for a single muscle in the amputated limb to a single surrogate muscle. Therefore, a more intuitive control system is needed, this may be achieved using neural control. Neural control systems could increase the number of control signals, and provide sensory feedback by stimulating the nerve. Recording neural signals is challenging: extracellular nerve voltages are small; and fibrosis at the implant–nerve interface can hinder recordings. Following investigation into epimysial interfaces the use of MNIs was considered because these interfaces confine regenerating axons within small diameter, insulating, channels in theory increasing the signal voltage and avoid problems associated with

[1] All 6 muscles could not be used in a TMR model, however muscle proximity will allow crosstalk to be determined.

Node of Ranvier position. However, MNIs require that the nerve is resected, and regenerates within the interface. Although the greatest improvement in signal voltage should be achieved with long, narrow microchannels, nerves do not regenerate well through small structures and the channels become occluded by fibrosis. To improve MNI function the neurocompatibility of the interfaces must be improved.

The neurocompatibility of a range of surface modifications and topographies was assessed in this thesis. Chapter 3 investigated the effect of basement membrane proteins on neurocompatibility of silicone surfaces using a neural-like cell where neurite outgrowth was quantified. It was hypothesised that basement membrane proteins would improve neurite outgrowth, and that combining BM proteins would further improve neurocompatibility. This chapter demonstrated that BM proteins improve neurocompatibility *in vitro* with some noted exceptions. It was found that altering the order of application when combining BM proteins significantly affects neurite outgrowth, with pre-mixed coatings performing as well as the best layer-by-layer coatings. It was also found that coatings without Nidogen-1 performed significantly worse than the best coatings *in vitro*. This was found to be as good as commercial standard coatings and indicates coatings or gel fillers formed of BM proteins will improve neural regeneration *in vivo*.

Previous research has suggested that the natural regeneration pathway should be mimicked to encourage axon regeneration, and that protein specificity may be important in the mechanisms of neural growth [179]. In this study neural specific protein isoforms (laminin-2) were compared with generic, commonly used isoforms (laminin-1), this test demonstrated no significant differences; however, the concept that specific protein isoforms are more suited has not been disproven [179]. Therefore, this study should be carried out again with a larger sample and a more suitable cell type (e.g. dorsal root ganglion neurons). It has been demonstrated that neural specific protein mixes can be formed, avoiding the problems with Matrigel™-like ECM gels (poorly characterised, containing high levels of growth factors, and with batch-to-batch variability) [294–296]. The protein concentrations achieved were measured, but the change in concentration with time was not investigated, it can be expected that the protein coating will partially desorb and be remodelled and replaced *in vivo* as the nerve regenerates over the few mm of the MNI; however this needs to be investigated. A move to standardised protein mixes, with known protein concentrations at the material surface, could improve the understanding of how the protein interface effects neurite extention and neurocompatibility.

Chapter 4 investigated the effect of multiscale grooved and roughened topographies on neural-like cell neurite outgrowth. It was hypothesised that combining grooves and nanoscale roughening would have a synergistic effect on neural-like cell number and neurite outgrowth *in vitro*. Roughening was found to increase the number of neurites, while grooves increased the length of neurites, reduced neurite number and caused neurites to align through contact guidance. A synergistic effect was observed where roughening increased the number of neurites on grooved samples. Where protein mixtures investigated

in Chapter 3 were used to coat multiscale surfaces the coatings altered the extent of cell polarisation dependent upon on the underlying surface. These results indicate that grooved and roughened multiscale topographies could be used within microchannel neural interfaces *in vivo* to improve nerve regeneration within microchannels.

Multiscale or hierarchical topographies have been considered *in vitro* recently [376,378,379]; however, prior to this thesis this multiscale topographical biomimicry had not been applied to a neurocompatibility system. While similar to the artificial and natural Schwann-cell like topographies which have shown promise *in vitro* [341, 365], introducing a roughening stage allows mimicry of sub-cell (ECM) scale structures and could be used to tailor or enhance protein and cell adhesion.

The aim of both the *in vitro* studies of neurocompatibility was to develop a surface treatment which could be applied to a microchannel lumen for *in vivo* implantation. Of these only the BM protein coating was tested *in vivo* (chapter 6). Multiscale topographies could be applied to the MNIs developed in chapter 5; however, this would require precise patterning within areas of the electrode layers, while leaving unmodified flat surfaces for plasma bonding. Alternative methods include using removable or dissolvable formers, or post-processing the silicone surface to leave a microstructure. These surface topographies should be tested *in vivo*, and could be applied in a simpler *in vivo* test as the surface of a nerve guidance conduit, where the topography could be applied to a flat silicone surface using the negative template method described in this thesis, and where the flat surface is rolled to form the conduit.

To bring either of these surface modifications to clinical practice will require regulatory approval. The regulatory approval for the inclusion of a modified topography within a MNI can expected to be not substantially different from the requirements for approval of the MNI itself. However, the addition of a protein or protein mixture within the MNI can be expected to increase the regulatory burden. Xenogenic proteins have been given approval for use in nerve repair (e.g. NeuraGen® nerve guidance conduits, formed from bovine type I collagen) [76], and allogenic and recombinant proteins have been approved for use as drugs. In this work a combination of human (collagen-IV, laminin-2,-4, fibonectin), xenogenic (laminin-1, ECM Gel), and recombinant human (nidogen-1) proteins have been used, it may be costly to use all human or all recombinant human origin proteins; however this may be required for the coating to be approved for clinical use.

Both studies of neurocompatibility presented in this thesis focussed upon PC-12 cells, an immortalised cell line. This work should be expanded to consider the non-neuronal cells present in the peripheral nerves, for example Schwann cells, and to assess the surfaces with a primary neural cell culture, for example dorsal root ganglion (DRG) neurons. This would allow *in vitro* assessment of the glial and neuronal response likely *in vivo*, but in a simplified system. The effects of basement membrane protein combinations and multiscale topographies on gene expression in both Schwann cells and DRG neurons could be examined using quantitative real-time PCR. In addition, an *in vitro* study of competitive adhe-

sion could be used to determine the extent to which fibroblasts (in part responsible for fibrosis) adhere to the surfaces compared with Schwann cells or neural cells.

Chapter 5 presented the manufacture and preliminary bench-testing of MNIs using 4 different methods. Equipment and budget limitations determined the manufacturing processes chosen. It was concluded that stacking of single microchannel layers was most suited to the manufacture of MNIs. Working in thin film processes followed by plasma bonding enabled the formation of structures in 2- and 3-dimensions. In addition, electroetching was used to increase electrode surface area and reduce electrode impedance.

Improvements to MNI manufacture were achieved in this thesis. Stacking thin microchannel layers allows an increased number of instrumented channels; however, this advantage was not exploited *in vivo* in this thesis, due to the small size of the rat sciatic nerve, and thickness of the stacked layers. One immediate improvement would be to reduce the silicone thickness in the electrode layer, allowing more layers per stack. This could be accomplished using the laser patterning technology used in this thesis, or alternatively photosensitive polyimide or silicone thin films and evaporated gold could be used allowing further minaturisation of both the tracks and the microchannels [146, 149–152].

The mechanical properties of the interfaces manufactured in this project have not been assessed. Experience while handling indicated that, although slightly flexible, the implants were robust and much stiffer than the neural tissue. Accelerated tests should be used to determine whether plasma bonding is suitable to hold layers for long-term implantation: the adhesion strength of plasma bonded samples could be tested following a time course in heated saline with the Arrhenius equation used to determine bond lifetime [523, 524]. In addition, bending tests should be carried out on the electrode layers, to determine the modulus of elasticity, and fatigue testing should be used to determine whether the interface will survive movements associated with upper limb implantation. Cyclic 4-point bend testing could be used to mimic forces experienced by the MNI during implantation and caused by muscle movement around the interface *in vivo*.

In this thesis MNI manufacture was carried out in a batch process, with substrates mounted on small glass slides. For larger scale production of a similar device the batch processing route may be suitable, but a larger substrate carrier should be considered. For spiral MNI designs a $4''$ diameter silicon wafer is used, allowing multiple interfaces to be manufactured on one carrier [151]. To plasma bond larger areas in a controlled manner a flip-chip bonder could be used, to apply thermal-compression across the whole interface surface. In addition, the use of a flip-chip bonder would allow more precise alignment of the interface layers reducing the potential for wastage during manufacture.

Previous work on MNIs has proposed reducing the number of connections to and from the interface while increasing the number of instrumented channels by coupling the MNI to an amplifier and multiplexer at the implant site, creating an “active” array [151]. The ability to form MNIs by stacking

layers lends itself well to the introduction of application specific integrated circuits (ASICs). A thinned ASIC [525] could be used as a bus to connect multiple layers, amplify the signals and multiplex the channels, reducing the number of cores required for cable transfer and reducing the likelihood of cable artefact. Alternatively ASICs could be stacked in individual layers, either connected to the electrode tracks, or with electrodes formed directly on the ASIC surface.

The use of "active" implants may also be useful for epimysial electrodes. Where many electrodes are needed to record from multiple locations in an amputation stump a multiplexing system could be used to reduce the number of cores passing through the bone-anchored device. In addition, amplification and digitisation at the electrode site could be used to reduce susceptibility to cable artefact, cable impedance noise, and external noise.

Chapter 6 investigated the performance of stacked MNIs in a rat sciatic nerve model. First, suture and fibrin glue were compared as interface fixation methods, the nerve was seen to follow the fibrin glue outside the interface lumen, therefore sutures were used to attach the interfaces for the second experiment. In the second experiment the influence of all-in-one BM protein coatings on functional, histological and electrophysiological outcomes was investigated. Some weak evidence for the use of protein coatings was found, in particular improvements in distal axon diameters. Nerve regeneration within stacked MNIs was within the ranges of previous studies, and alternative implantation methods or improvements to the interface design may reduce frustrated axon sprouting and improve the regeneration across MNIs.

This thesis has not demonstrated that MNIs are suitable for clinical investigation. First, MNIs cannot be tested in short-term clinical studies, the implantation method tested in this thesis requires nerves to regenerate before signals can be recorded. This may take over one month and will depend upon the regenerative potential of nerves following long-term amputation. Second, this thesis has demonstrated no dramatic improvement to MNI function or regeneration over previous studies. There is still a need to test alternative solutions to improve the neurocompatibility of MNIs.

Alternative methods of MNI implantation have been used to avoid the long recovery times associated with nerve transection [153, 154]. The teased rootlet concept could be applied to peripheral nerves to separate either fascicles, or small axon bundles. By laying these within instrumented microchannels, then sealing the microchannels, recordings could be made immediately *in vivo*, and functional impairment could be reduced.

For clinical use MNIs must remain functional over the lifetime of the patient. For active amputees, the main target population for advanced prosthesis interfaces, lifetimes of more than 50 years may be required. Studies of MNIs from acute implantation up to 5 months *in vivo* have been carried out to date [51,148,153,154,156]. To better understand the chronic response to MNIs longer implantation times should be considered. Head-stages or bone-anchored devices will allow recording from the interfaces

throughout a study [148], by using regular or continual monitoring implantation times of one year or above could be considered. For longer implantations the rat model may not be suitable due to the expected mean lifetime[2], in this case a larger animal model must be considered.

In clinical practice TMR and MNI interventions have major differences when compared with the models used in this thesis. In particular, nerves of interest in upper limb amputees will have undergone long delays, of months to years [227,229,274], prior to the surgical intervention. The effect of prolonged axotomy on axon regeneration for TMR and MNI implantation should be examined [277]. For MNIs an additional complication is present: the absence of an end organ. In this thesis nerve regeneration through the MNI was presented with the natural reinnervation pathway (the sciatic nerve innervation), while in amputees a surrogate end organ may be required. The role of end organ in regeneration through MNIs should be assessed, and in addition, the potential to interpose MNIs during TMR could be investigated.

Implantable devices are promising interventions to provide improvements in hand control for upper-limb prosthesis users. This thesis has investigated two such devices and demonstrated incremental improvements in device design. However, to achieve "intuitive, closed-loop, adaptive, and robust real-time control" [14] further pre-clinical research and development is required.

7.1 Conclusions

Detailed conclusions to each study have been presented in the relevant experimental chapters of this thesis. Key conclusions for each experimental chapter are summarised below.

Chapter 2 A bone-anchored device is suitable for transcutaneous signal transmission from epimysial electrode(s) in cognisant moving animals and can be used to monitor recovery following targeted muscle reinnervation.

Chapter 3 Endoneurial basement membrane protein coatings increase neurite outgrowth on silicone surfaces; however, coating order and constituents can significantly affect neurite outgrowth.

Chapter 4 Multiscale surfaces with μm-scale grooves and nm-scale roughness can cause neurite alignment and synergistically enhance neurite outgrowth.

Chapter 5 Stacking microchannel layers by plasma bonding is a suitable method for manufacturing microchannel neural interfaces which can overcome some problems with channel sealing and electrode number.

Chapter 6 Peripheral nerve will regenerate through stacked microchannel neural interfaces; however, there is inconclusive evidence that endoneurial basement membrane microchannel coatings improve nerve regeneration.

[2]Mean laboratory rat lifetime is approximately 3 years [526]. Studies of more than 1 year can expect to run into problems associated with natural lifespan.

7.2 Future Work

In this thesis further hypotheses and extensions to the work have been proposed. Key proposed future work is listed briefly below.

- Develop an active, hard-wired, multichannel epimysial electrode system for use with a bone-anchored transcutaneous device.
- Develop a fail-safe mechanism and hermetic seal for the cable connection to the bone-anchored transcutaneous device.
- Use a domed rather than rectangular cross-section flange for future bone-anchors to reduce epidermal damage.
- Use the multichannel epimysial electrode system to investigate cross-talk from different electrode configurations (e.g. tripolar) with and without targeted muscle reinnervation.
- Investigate the effect of learning following targeted muscle reinnervation.
- Investigate the response of primary neural and Schwann cell cultures to endoneurial basement membrane proteins and multiscale topographies.
- Apply additional methods to the *in vitro* testing of neurite outgrowth including automated analysis and qPCR.
- Investigate the lifetime, conformation and desorption of endoneurial basement membrane proteins on silicone surfaces in a model *in vitro* environment.
- Investigate alternative laminin isoforms (e.g. laminins -8, -9 and -11).
- Carry out a multifactorial *in vitro* analysis of the effect of mixed endoneurial basement membrane proteins on neurite outgrowth.
- Develop an *in vitro* microchannel model (transwell microfluidics) to investigate neurite outgrowth through modified microchannels.
- Apply multiscale topographies to microchannels within a microchannel neural interface and investigate their effect *in vivo*.
- Increase the open cross sectional area of the microchannel neural interfaces by using thinner electrode layers or by using alternative manufacturing techniques.
- Apply the stacking technique to form microchannel neural interfaces with medical grade silicones (e.g. MED-1000) and metals more suited to long term implantation (e.g. Platinum).

- Develop an active microchannel neural interface with either: an active bus ASIC; or with stacked ASICs as electrode layers.
- Investigate the use of fibrin glue as a filler for the microchannel neural interface lumen.
- Investigate the effect of prolonged axotomy on neural regeneration for targeted muscle reinnervation and microchannel neural interfaces.
- Investigate the effect of an interposed microchannel neural interface on regeneration for targeted muscle reinnervation.
- Develop a head-stage or other system for continual microchannel neural interface signal monitoring from cognisant, behaving animals.

Appendices

A Few Notes on Methodology

Mead's Resource Equation was used to estimate sample sizes. A minimum size of n = 6 was set for all non-exploratory experiments. For *in vitro* exploratory experiments both qualititive and quantitive data were used, the β = 0.8 level of statistical power was not assumed, and a minimum sample size of n = 3 was set. For *in vivo* exploratory experiments both qualititive and quantitive data were used, statistical power was not assumed, and a minimum sample size of n = 1 was set.

Statistical significance for all tests was set at α=0.05. To correct for multiple comparisons, keeping the family-wise error rate less than α=0.05, the Holm-Bonferroni approximation was used, a refinement of the Bonferroni correction [319, 527]. Briefly, all the relevant 'm' pairwise comparisons are made and the p-values are ranked from lowest to highest (P_1 to P_m). The α for each for each ranked pairwise comparison (α_k) is modified such that $\alpha_k = \frac{\alpha}{m+1-k}$. An ordered series of α_k (or p_{cut}) are given: 0.05, 0.025, $0.01\dot{6}$, 0.0125, 0.01, $0.008\dot{3}$, $0.00714...$, 0.00625, $0.00\dot{5}$, 0.005, $0.004\dot{5}$, $0.004\dot{1}\dot{6}$, $0.0038...$, $0.0036...$, $0.00\dot{3}$, 0.003125.

For example 3 p-values are recorded from a family of tests, p_a=0.57, p_b=0.04 and p_c=0.01. Without correcting for multiple comparisons b and c would be considered significant. The ranked values are as follows p_1=0.01, p_2=0.04 and p_3=0.57. $\alpha_1 = \frac{\alpha}{3+1-1}$ therefore $\alpha_1 = \frac{0.05}{3} = 0.1\dot{6}$, p_1=0.01$<\alpha_1$, therefore the null hypothesis c can be rejected. $\alpha_2 = \frac{\alpha}{3+1-2}$ therefore $\alpha_2 = \frac{0.05}{2} = 0.025$, p_2=0.04$>\alpha_2$, therefore the null hypothesis b cannot be rejected. Once a null hypothesis is rejected all tests with larger values of k are also not significant, therefore the null hypothesis a cannot be rejected.

For all tests Shapiro-Wilk tests of normality were carried out on each group. The presence of non-parametric data (not normally distributed), and / or n <25 for all tests, required the use of non-parametric statistical tests. These include:

Kruskal-Wallis Test A non-parametric one-way ANOVA test for k independent samples. p $<\alpha$ indicates that at least one group is significantly different from all the others.

Mann-Whitney U Test A non-parametric test for 2 independent samples. p $<\alpha$ indicates that there is a significant difference between the two groups.

Spearman's Rank Correlation Coefficient A non-parametric measure of bivariate statistical dependence. A +ve value indicates a positive correlation between x and y values. A value of 1 or -1 indicates that the data can be described using a monotonic function. Also known as Spearman's ρ.

Wilcoxon signed-rank test A non-parametric test for 2 related samples. p $<\alpha$ indicates that there is a significant difference between the two groups.

Statistical tests were carried out using SPSS versions 20, 21, and 22 for Linux and Windows (IBM).

In Vitro Neuron Adhesion Studies: Basement Membrane Proteins

Tables of p-values

Poly-D-Lysine Concentration

	Neurite Number	Neurite Length	Cell Number
p-Value	0.078	**0.000**	**0.001**

Table 1: Kruskal Wallis Test results for Poly-D-Lysine Concentration Series. 4, 10 and 20 μg/cm^2 at 96 hours. p_{cut} = 0.05, bold values are statistically significant.

		PDL Concentration μg/cm^2			
		20	10	4	2
PDL Concentration μg/cm^2	20	-	0.956 (0.05)	0.21 (0.017)	0.043 (0.01)
	10		-	0.174 (0.013)	0.023 (0.008)
	4			-	0.412 (0.025)
	2				-

Table 2: Mann-Whitney U test results for Neurite Number on Poly-D-Lysine Concentration Series. 4, 10 and 20 μg/cm^2 at 96 hours. p_{cut} in brackets, bold values are statistically significant.

		PDL Concentration μg/cm^2			
		20	10	4	2
PDL Concentration μg/cm^2	20	-	**0.000** (0.008)	**0.001** (0.01)	0.019 (0.017)
	10		-	0.093 (0.025)	**0.002** (0.0125)
	4			-	0.259 (0.05)
	2				-

Table 3: Mann-Whitney U test results for Neurite Length on Poly-D-Lysine Concentration Series. 4, 10 and 20 μg/cm^2 at 96 hours. p_{cut} in brackets, bold values are statistically significant.

		PDL Concentration μg/cm^2			
		20	10	4	2
PDL Concentration μg/cm^2	20	-	1.000 (0.05)	**0.004** (0.008)	**0.004** (0.01)
	10		-	**0.002** (0.017)	**0.002** (0.0125)
	4			-	0.485 (0.025)
	2				-

Table 4: Mann-Whitney U test results for Cell Number on Poly-D-Lysine Concentration Series. 4, 10 and 20 μg/cm^2 at 96 hours. p_{cut} in brackets, bold values are statistically significant.

Collagen IV Concentration

	Neurite Number	Neurite Length
p-Value	0.217	**0.000**

Table 5: Kruskal Wallis Test results for Collagen IV Concentration Series. 1, 5 and 10 μg/cm^2 at 96 hours. p_{cut} = 0.05, bold values are statistically significant.

		Collagen IV μg/cm^2		
		10	5	1
Collagen IV μg/cm^2	10	-	**0.000** (0.017)	**0.000** (0.025)
	5		-	**0.001** (0.05)
	1			-

Table 6: Mann-Whitney U test results for Neurite Length on Collagen IV Concentration Series. 1, 5 and 10 μg/cm^2 at 96 hours. p_{cut} in brackets, bold values are statistically significant.

		Collagen IV μg/cm^2		
		10	5	1
Collagen IV μg/cm^2	10	-	N/A	N/A
	5		-	N/A
	1			-

Table 7: Mann-Whitney U test results for Neurite Number on Collagen IV Concentration Series. 1, 5 and 10 μg/cm^2 at 96 hours. p_{cut} in brackets, bold values are statistically significant.

	Neurite Number	Neurite Length
p-Value	0.942	0.063

Table 8: Kruskal Wallis Test results for Collagen IV Concentration Series. 10, 20 and 40 μg/cm^2 at 96 hours. p_{cut} = 0.05, bold values are statistically significant.

		Collagen IV μg/cm^2		
		40	20	10
Collagen IV μg/cm^2	40	-	0.692 (0.05)	0.229 (0.017)
	20		-	0.43 (0.025)
	10			-

Table 9: Mann-Whitney U test results for Neurite Length on Collagen IV Concentration Series. 40, 20 and 10 μg/cm^2 at 96 hours. p_{cut} in brackets, bold values are statistically significant.

		Collagen IV μg/cm^2		
		40	20	10
Collagen IV μg/cm^2	40	-	0.114 (0.025)	0.02 (0.017)
	20		-	0.453 (0.05)
	10			-

Table 10: Mann-Whitney U test results for Neurite Number on Collagen IV Concentration Series. 40, 20 and 10 μg/cm^2 at 96 hours. p_{cut} in brackets, bold values are statistically significant.

Laminin-2 (-4) Concentration

	Neurite Number	Neurite Length
p-Value	0.388	**0.000**

Table 11: Kruskal Wallis Test results for Laminin Concentration Series. 1, 2 and 5 μg/cm^2 at 96 hours. p$_{cut}$ = 0.05, bold values are statistically significant.

		Laminin μg/cm^2		
		5	2	1
Laminin μg/cm^2	5	-	0.166 (0.05)	**0.000** (0.017)
	2		-	**0.006** (0.025)
	1			-

Table 12: Mann-Whitney U test results for Neurite Length on Laminin Concentration Series. 1, 2 and 5 μg/cm^2 at 96 hours. p$_{cut}$ in brackets, bold values are statistically significant.

		Laminin μg/cm^2		
		5	2	1
Laminin μg/cm^2	5	-	0.166 (0.017)	0.428 (0.025)
	2		-	0.597 (0.05)
	1			-

Table 13: Mann-Whitney U test results for Neurite Number on Laminin Concentration Series. 1, 2 and 5 μg/cm^2 at 96 hours. p$_{cut}$ in brackets, bold values are statistically significant.

	Neurite Number	Neurite Length
p-Value	N/A	N/A

Table 14: Kruskal Wallis Test results for the second Laminin Concentration Series. 0.1, 0.5 and 1 μg/cm^2 at 96 hours. p$_{cut}$ = 0.05, bold values are statistically significant.

		Laminin μg/cm^2		
		0.1	0.5	1
Laminin μg/cm^2	0.1	-	N/A	N/A
	0.5		-	0.0264 (0.05)
	1			-

Table 15: Mann-Whitney U test results for Neurite Length on the second Laminin Concentration Series. 0.1, 0.5 and 1 μg/cm^2 at 96 hours. p$_{cut}$ in brackets, bold values are statistically significant.

		Laminin μg/cm^2		
		0.1	0.5	1
Laminin μg/cm^2	0.1	-	N/A	N/A
	0.5		-	0.0037 (0.05)
	1			-

Table 16: Mann-Whitney U test results for Neurite Number on the second Laminin Concentration Series. 0.1, 0.5 and 1 μg/cm^2 at 96 hours. p_{cut} in brackets, bold values are statistically significant.

Fibronectin Concentration

	Neurite Number	Neurite Length	Cell Number	Alamar Blue Assay	Hoescht DNA Assay
p-Value	N/A	N/A		**0.001**	**0.001**

Table 17: Kruskal Wallis Test results for Fibronectin Concentration Series. 1, 2 and 5 μg/cm^2 at 96 hours. p_{cut} = 0.05, bold values are statistically significant.

		Fibronectin μg/cm^2		
		5	2	1
Fibronectin μg/cm^2	5	-	**0.000** (0.017)	**0.000** (0.025)
	2		-	**0.000** (0.05)
	1			-

Table 18: Mann-Whitney U test results for Alamar Blue flourescence on Fibronectin Concentration Series. 1, 2 and 5 μg/cm^2. p_{cut} in brackets, bold values are statistically significant.

Nidogen-1 Concentration

	Neurite Number	Neurite Length	Cell Number	Alamar Blue Assay	Hoescht DNA Assay
p-Value	N/A	N/A		**0.000**	0.487

Table 19: Kruskal Wallis Test results for Nidogen-1 Concentration Series. 0.5, 1 and 2 μg/cm^2 at 96 hours. p_{cut} = 0.05, bold values are statistically significant.

		Nidogen-1 μg/cm^2		
		2	1	0.5
Nidogen-1 μg/cm^2	2	-	**0.000** (0.017)	**0.000** (0.025)
	1		-	**0.000** (0.05)
	0.5			-

Table 20: Mann-Whitney U test results for Alamar Blue flourescence on Nidogen-1 Concentration Series. 0.5, 1 and 2 μg/cm^2 at 96 hours. p_{cut} in brackets, bold values are statistically significant.

Poly-L-Orthinine Concentration

	Neurite Number	Neurite Length	Cell Number	Alamar Blue Assay	Hoescht DNA Assay
p-Value	N/A	N/A		0.059	

Table 21: Kruskal Wallis Test results for Poly-L-Orthinine Concentration Series. 5, 10, 20 and 40 μg/cm^2 at 96 hours. p_{cut} = 0.05, bold values are statistically significant.

Laminin-2,(-4) and Laminin-1

	Neurite Number	Neurite Length	Cell Number
p-Value	0.0554	0.4396	0.635

Table 22: Mann-Whitney U test results for 1 μg/cm^2 Laminin-1 and 1 μg/cm^2 Laminin-2,-4 coatings at 96 hours. p_{cut} = 0.05, bold values are statistically significant.

Comparison of Optimal Concentrations

	Neurite Number	Neurite Length
p-Value	**0.000**	**0.000**

Table 23: Kruskal Wallis Test results for optimal coating concentrations. Untreated silicone, 10 μg/cm^2 Collagen IV, 1 μg/cm^2 Laminin-2,-4, 10 μg/cm^2 Poly-D-Lysine, and CNL layer-by-layer at 96 hours. p_{cut} = 0.05, bold values are statistically significant.

p-value (and Bonferroni-Holm cut-off)	PDL	C-IV	Ln-2,-4	CNL
PDL	-	**0.000** (0.008)	**0.004** (0.05)	**0.000** (0.010)
C-IV		-	**0.000** (0.013)	**0.003** (0.025)
Ln-2,-4			-	**0.001** (0.017)
CNL				-

Table 24: Mann-Whitney U test results for Neurite Length on the optimal coating concentrations. 10 μg/cm^2 Collagen IV, 1 μg/cm^2 Laminin-2,-4, 10 μg/cm^2 Poly-D-Lysine, and CNL layer-by-layer at 96 hours. p_{cut} in brackets, bold values are statistically significant.

p-value (and Bonferroni-Holm cut-off)	PDL	C-IV	Ln-2,-4	CNL
PDL	-	**0.000** (0.008)	**0.000** (0.010)	**0.000** (0.013)
C-IV		-	0.225 (0.05)	**0.002** (0.025)
Ln-2,-4			-	**0.000** (0.017)
CNL				-

Table 25: Mann-Whitney U test results for Neurite Number on the optimal coating concentrations. 10 μg/cm^2 Collagen IV, 1 μg/cm^2 Laminin-2,-4, 10 μg/cm^2 Poly-D-Lysine, and CNL layer-by-layer at 96 hours. p_{cut} in brackets, bold values are statistically significant.

Comparison of Multi-Protein Coatings: Experiment 1

	Neurite Number	Neurite Length
p-Value	**0.012**	**0.000**

Table 26: Kruskal Wallis Test results for multi-protein coating concentrations. Experiment 1. ECM Gel, CNL all-in-one, CNL layer-by-layer and LNC layer-by-layer at 96 hours. p_{cut} = 0.05, bold values are statistically significant.

p-value (and Bonferroni-Holm cut-off)	ECM Gel	All-in-one CNL	CNL Layer-by-layer	LNC Layer-by-Layer
ECM Gel	-	0.996 (0.05)	0.902 (0.025)	**0.010** (0.010)
All-in-one CNL		-	0.843 (0.017)	**0.006** (0.008)
CNL Layer-by-layer			-	0.018 (0.013)
LNC Layer-by-Layer				-

Table 27: Mann-Whitney U test results for Neurite Length on multi-protein coating concentrations. Experiment 1. ECM Gel, CNL all-in-one, CNL layer-by-layer and LNC layer-by-layer at 96 hours. p_{cut} in brackets, bold values are statistically significant.

p-value (and Bonferroni-Holm cut-off)	ECM Gel	All-in-one CNL	CNL Layer-by-layer	LNC Layer-by-Layer
ECM Gel	-	0.424 (0.05)	0.313 (0.025)	**0.000** (0.013)
All-in-one CNL		-	0.090 (0.017)	**0.000** (0.010)
CNL Layer-by-layer			-	**0.000** (0.008)
LNC Layer-by-Layer				-

Table 28: Mann-Whitney U test results for Neurite Number on multi-protein coating concentrations. Experiment 1. ECM Gel, CNL all-in-one, CNL layer-by-layer and LNC layer-by-layer at 96 hours. p_{cut} in brackets, bold values are statistically significant.

	Neurite Number	Neurite Length
p-Value	**0.001**	**0.003**

Table 29: Kruskal Wallis Test results for multi-protein coating concentrations. Experiment 2. ECM Gel, CNL all-in-one, LC layer-by-layer, CL layer-by-layer, CL all-in-one and 10 μg/cm^2 C-IV at 96 hours. p$_{cut}$ = 0.05, bold values are statistically significant.

p-value (and Bonferroni-Holm cut-off)	ECM Gel	All-in-one CNL	LC Layer-by-layer	CL Layer-by-Layer	CL all-in-one	C-IV
ECM Gel	-	0.206 (0.01)	0.019 (0.004)	0.026 (0.004)	0.366 (0.013)	0.431 (0.017)
All-in-one CNL		-	**0.0003** (0.003)	**0.0006** (0.004)	0.032 (0.005)	0.042 (0.005)
LC Layer-by-layer			-	0.9747 (0.05)	0.1449 (0.007)	0.1325 (0.006)
CL Layer-by-Layer				-	0.1612 (0.008)	0.143 (0.006)
CL All-in-one					-	0.9394 (0.025)
C-IV						-

Table 30: Mann-Whitney U test results for Neurite Length on multi-protein coating concentrations. Experiment 2. ECM Gel, CNL all-in-one, LC layer-by-layer, CL layer-by-layer, CL all-in-one and 10 μg/cm^2 C-IV at 96 hours. p$_{cut}$ in brackets, bold values are statistically significant.

p-value (and Bonferroni-Holm cut-off)	ECM Gel	All-in-one CNL	LC Layer-by-layer	CL Layer-by-Layer	CL all-in-one	C-IV
ECM Gel	-	0.632 (0.025)	**0.0001** (0.003)	0.192 (0.007)	0.011 (0.004)	0.081 (0.006)
All-in-one CNL		-	**0.0009** (0.004)	0.381 (0.013)	0.032 (0.005)	0.181 (0.006)
LC Layer-by-layer			-	0.0159 (0.004)	0.216 (0.008)	0.0492 (0.005)
CL Layer-by-Layer				-	0.2169 (0.01)	0.653 (0.05)
CL All-in-one					-	0.4169 (0.017)
C-IV						-

Table 31: Mann-Whitney U test results for Neurite Number on multi-protein coating concentrations. Experiment 2. ECM Gel, CNL all-in-one, LC layer-by-layer, CL layer-by-layer, CL all-in-one and 10 μg/cm^2 C-IV at 96 hours. p_{cut} in brackets, bold values are statistically significant.

In Vitro Neuron Adhesion Studies: Topography

An Overview of Contact Guidance Studies

Varied Dimensions	Constant Dimensions	Substrate	Cell Type	Outcome	Ref.
1 μm to 10 μm pitch	200 nm deep	Polystyrene	PC-12 neuron-like	Cells aligned with smaller 1 μm and 1.5 μm pitch substrates and became polarised, expressing fewer, longer neurites.	[343, 344]
5 μm to 95 μm grooves	5 μm ridges, 3.4 μm deep	PMMA	Rat radial glia and cortical neurons	Glia adhered and aligned on 5 μm to 35 μm grooves, neurons aligned on 5 μm to 8 μm grooves.	[345]
2 μm to 20 μm grooves, with 2 μm to 20 μm ridges	3 μm deep	PCL	NG108-15 neuroblastoma and primary Schwann cells	Both cell types aligned better on smaller 5 μm to 10 μm features. 5 μm to 10 μm features reduced fibroblast contamination in primary culture.	[346]
100 nm to 400 nm deep	266 nm pitch	Fused quartz	Chick embryonic neurons and kidney cells.	Kidney cells aligned better to deeper grooves, while neurons did not align on all topographies.	[347]
4 μm to 24 μm pitch, 0.2 μm to 2 μm deep		Perspex	Chick embryonic neurons and kidney cells.	Cells aligned best on 2 μm deep grooves, with alignment increasing with groove depth.	[348]
100 nm to 400 nm width, 200 nm to 2 μm pitch	300 nm deep	PMMA	Sympathetic and sensory ganglion neurons	Larger patterns are more effective, especially with large ($>$1 μm) diameter axons.	[349]
20 μm to 60 μm grooves	11 μm deep, 10 μm ridges	Polyimide	PC-12	Cells in 20 μm to 30 μm channels expressed fewer, more aligned neurites.	[350]
5 μm and 10 μm pitch	2.5 μm deep	PLGA	PC-12	Alignment, longer neurites and reduced neurite number was observed on 5 μm and 10 μm pitch.	[351]

Varied Dimensions	Constant Dimensions	Substrate	Cell Type	Outcome	Ref.
2 μm to 69 μm deep, 50 μm to 350 μm grooves		PDMS	Rat embryonic neurons	Axons crossed small edges ($<$10 μm high), while axons aligned at deeper edges ($>$22 μm high). An optimal aspect ratio ($>$0.1) is implied.	[352]
100 μm to 250 μm grooves	150 μm deep, 250 μm ridges	PLGA	Transfected HEK293T cells	Neurites aligned and extended more in 100 μm grooves.	[353]
1 μm to 4 μm grooves, 14 nm to 1100 nm deep		Fused quartz	*Xenopus* spinal neurons and rat hippocampal neurons	*Xenopus* neurons aligned parallel to smaller deeper grooves, while rat neurites aligned perpendicular to small ($<$2 μm) grooves and parallel to larger (4 μm) and deeper ($>$130 nm) grooves.	[354]
1 μm to 2 μm grooves, 400 nm and 800 nm deep		PDMS	Rat hippocampal cells	Neurites extended parallel to wider (2 μm), deeper (800 nm) grooves, and perpendicular to narrower (1 μm), shallower (400 nm) grooves. The grooves initiated neurite extension, and could be enhance with growth factor addition.	[355]
1 μm to 8 μm grooves, 50 nm and 800 nm deep		Quartz	Various CNS, peripheral and olfactory neurons.	CNS neurons had the ability to extend perpendicularly on 1 μm grooves, while wider grooves tended to suppress perpendicular alignment. Peripheral nerve cells were not guided on small grooves.	[356]
30 μm to 1000 μm grooves, 30 μm to 1000 μm ridges	50 μm	PDMS	DRG, hippocampal neurons, B104 neuroblastoma.	Cells bridged wide grooves. Narrow ridges reduced bridging and increase alignment.	[357]

Varied Dimensions	Constant Dimensions	Substrate	Cell Type	Outcome	Ref.
4 μm to 20 μm pitch, 100 nm to 1.2 μm deep		Polystyrene	Human fibroblasts	Alignment was best on 10 μm pitch substrates with deep (800 nm) grooves. Increasing aspect ratio (depth / width) increases alignment.	[359]
200 nm to 20 μm pitch, 200 nm to 900 nm deep		Polystyrene	Smooth muscle cells	Increased depth and reduced width (ie. increased aspect ratio) improved alignment.	[362]
200 nm to 5 μm deep	8 μm pitch	PDMS	Aortic endothelial cells	Cells aligned better to deeper (>500 nm) grooves,	[360]
400 nm to 4 μm pitch, 75 to 880 nm deep		Silicon	Stromal fibroblasts	Alignment was better with increasing depth. Optimal pitch was around 1 μm.	[361]
	800 nm ridge, 100 nm groove, 1200 nm deep.	Silicon	PC-12	Grooves enhanced neuritogenesis and cell differentiation.	[358]
750 nm to 20 μm pitch	350 nm deep	PDMS	Mesenchymal stem cells	Cells aligned and upregulated neuronal markers, especially on narrower structures.	[363]
	10 μm pitch, 1 μm deep	PDMS	Primary embryonic fibroblasts	Grooves induced neuronal phenotype with greater efficiency than other substrates.	[364]

Table 32: An overview of groove/ridge dimensions used in contact guidance studies with neural and other cell types. Typically pitch refers to total periodicity. Where not explicitly mentioned groove and ridge widths are assumed to be equal (half the pitch value). Where stated the groove is the concave section and ridges are the convex section of the periodical structure.

NCP Periodogram MATLAB Code

```
% The basis for this script was originally written by Prof. Edith Seier ...
    (http://faculty.etsu.edu/seier/) based upon work by P.C.Hansen et.al., It was ...
    included as part of 'Introduction to Spectral Analysis' which is avalilable ...
    online (https://webcache.googleusercontent.com/search?q= ...
    cache:QVmA9zI6crkJ:read.pudn.com/downloads164/doc/comm/750295/day3.doc+&cd= ...
    7&hl=en&ct=clnk). This Script has been modified to allow the user to print the ...
    values of the Kolmogorov-Smirnov test, and to repeat the test for k neurites ...
    (k=1:length(series)) in order to determine at which neurite the index can be ...
    considered to deviate significantly from white noise. I would also like to ...
    thank Marcello DiStasio for his KS test code, although this hasn't directly ...
    been included here it inspired me to implement mine in this fashion ...
    (http://chelly.us/lab/ks_test). This script is intended to replicate the ...
    methods used by Nectow et. al. in their 2012 paper (PMID: 23008168). I would ...
    like to thank Alex Nectow and Prof. Kaplan for their help with this and for ...
    sending some raw data to get me started. This script correctly replicated the ...
    above paper with some slight changes in the way graphs are produced. Users ...
    should check the optional "for" statements around lines 265-315 for agreement ...
    with the techniques in the above paper.
%
% Henry Lancashire, 2013

% Originally this script was designed to load an input file, this has been
% removed because it was a regular source of warnings.

% load a:datafile.dat;

YN = input('This process will now delete all the variables it needs to continue. ...
    \nAre you happy to continue? [Y/N]\n\n','s');

    if YN == 'Y';

        clearvars Angles Diff_Vector LCDF Vector Vector_mean Vector_median Ytot ...
            Ytotl ;
        clearvars acut angles crit critl cuper cupera cuperal cuperl cut cv freq ...
            freql ;
        clearvars h indextot indextotl indfreq indfreql indtext indtextl iperiod ...
            iperiodl ;
        clearvars itime jtime k ksstat ktime largofre largofrel linea lineal maxav ;
        clearvars maxmedian maxmean maxser maxpow maxpowl n n2 nobs nobsl ;
        clearvars nyquist nyquistl p pfreq pfreql pmax pmaxl power powerl q ql ;
        clearvars series seriesl sugarm sugarml sumtruth truth uniform ;
```

```
21
22          elseif YN == 'N';
23
24              disp('Save any variables you need and try again.');
25
26          return
27
28          else
29
30              disp('Unknown answer, please use Y or N.');
31
32          return
33
34          end
35
36  % Data is included in a vector known as 'Angles'. This is the complete list of ...
        angles to be sorted.
37
38  Angles = input('Choose vector of neurite angles to be used for NCP calculation.\n\n');
39
40  % Angles are forced to values between 0 and 90, this assumes a range of -180 to ...
        180 degrees (extra terms have been added to expand this to -360, 360) , where ...
        -180, 0, 180 are perfectly aligned and -90, 90 are perfectly perpendicular to ...
        the surface.
41
42  angles = abs(Angles);
43
44  for k=1:(length(Angles))
45
46      if angles(k) <= 90
47          angles(k,1) = angles(k);
48
49      elseif 90 < angles(k) <= 180
50          angles(k,1) = 180 - angles(k);
51
52      elseif 180 < angles(k) <= 270
53          angles(k,1) = angles(k) - 180;
54
55      elseif 270 < angles(k) <= 360
56          angles(k,1) = 360 - angles(k);
57
58      else
59
```

```
60          warning('Warn:Angles','Angle greater than 360 or less than -360 given. ...
                \nCalculations will fail because this angle is unaccounted for in ...
                for,if condition at approximately line 50. \nCheck your input vector.\n')
61
62          return
63
64      end
65
66  end
67
68
69  % Angles are sorted in ascending order.
70  Vector = sort(angles);
71
72  Diff_Vector = zeros((length(Vector)-1),1);
73
74  % The 'difference vector' is calculated, this calculated the period between a ...
        given angle and the next angle.
75  for k=1:(length(Vector)-1),
76  Diff_Vector(k,1)=Vector(k+1)-Vector(k);
77  end;
78
79  % Diff_Vector = Diff_Vector';
80
81  series=Diff_Vector(:,1);
82
83
84  % IMPORTANT: NO MORE INPUT IS NEEDED - 'series' is sufficient
85
86  nobs=length(series); % identifies  number of observations in series
87
88  % calculates the periodogram
89  sugarm=series-mean(series);  % substracts the mean of the series
90  Ytot=fft(sugarm) ;   % finds the Fast Fourier Transform
91  n=length(Ytot) ;
92  n2=floor(n/2)+1; % Floor added to prevent warnings when n2 is index
93  power=(abs(Ytot(1:n2)).^2)/n; % calculates intensities
94  nyquist=1/2;
95  pfreq=(0:1:n/2);
96  largofre=length(pfreq)-1;
97  freq=pfreq/(largofre)*nyquist;
98  mpow=max(power); % finds the maximum intensity
99  pmax=1.1*mpow ;
```

```
indextot=find(power==max(power));  % identifies the frequency with the maximum ...
    intensity
indfreq=freq(indextot);
iperiod=1/indfreq;

indtext=indfreq+0.01 ;

% calculates cumulative periodogram
q=(nobs/2)+1;
% Critical values of the Komogorov-Smirnov Test
crit=1.36/(sqrt(q));
linea=freq*2;  % to create the diagonal from 0,0 to 0.5,1
cuper=cumsum(power);  % accumulates the intensities
cupera=cuper./max(cuper) ; % divides the intensities by  total sum so that curve ...
    goes up to 1

% cupera = cupera(2:q,1);
% linea = linea(2:q,1);
% freq = freq(2:q,1);

% It should be noted that this is a slightly incorrect implementation of the ...
    calculation described by Nectow et. al. because it includes a point (0,0), or ...
    (0,0+delta), as the DC portion of the signal. This is not required in the NCP ...
    criterion and may propagate errors when using the Kolmogorov Smirnov test, ...
    this point should therefore be removed by post processing.

% Calculated the linear cumulative distribution function for kstest
LCDF = cat(2,linea',freq');

% The Komogorov Smirnov test, this returns a p-value, however this isn't useful, ...
    the critical-value, cv is (this should be ~=crit).
[h,p,ksstat,cv] = kstest(cupera,LCDF,0.05);

disp(' ')
disp(' ')
disp('Results')
disp('    h         p         ksstat    cv')
disp([h,p,ksstat,cv])

if any(or(cupera > linea' + crit' , cupera < linea' - crit'))

    uniform = 'NCP diverges from uniform (95%CI).';
    disp(uniform);
```

```
136
137 else
138
139     uniform = 'NCP does not diverge from uniform (95%CI).';
140     disp(uniform);
141
142 end
143
144 % Calculating Mean-Median divergence.
145 for k=1:length(Vector),
146 Vector_mean(k)=mean(Vector(1:k));
147 end;
148
149 for k=1:length(Vector),
150     Vector_median(k)=median(Vector(1:k));
151 end;
152
153 % This test is intended to be a cycle from k=1:k=length(Diff_Vector) to determine ...
      the point at which the index flips from within 95%CIs to outside 95%CIs. This ...
      script requires that perio.m is run on all the data first. Alternatively, this ...
      script can be copied into the end of perio.m (perio.m is obsolete in this ...
      version) to run simultaneous, in this case cut and acut could be output ...
      alongside h, p, kstat & cv.
154
155     sumtruth = zeros(size(Diff_Vector));
156
157     for k=1:(length(Diff_Vector))
158
159         % Diff_Vector = Diff_Vector';
160
161         seriesl=Diff_Vector(1:k,1);
162
163         % IMPORTANT: NO MORE INPUT IS NEEDED - 'series' is sufficient
164
165         nobsl=length(seriesl); % identifies  number of observations in series
166
167         % calculates the periodogram
168         sugarml=seriesl-mean(seriesl);  % substracts the mean of the series
169         Ytotl=fft(sugarml) ;   % finds the Fast Fourier Transform
170         n=length(Ytotl) ;
171         n2=floor(n/2)+1; % Floor added to prevent warnings when n2 is index
172         powerl=(abs(Ytotl(1:n2)).^2)/n; % calculates intensities
173         nyquistl=1/2;
```

```
174         pfreql=(0:1:n/2);
175         largofrel=length(pfreql)-1;
176         freql=pfreql/(largofrel)*nyquistl;
177         mpowl=max(powerl); % finds the maximum intensity
178         pmaxl=1.1*mpowl ;
179         indextotl=find(powerl==max(powerl));  % identifies the frequency with the ...
                maximum intensity
180         indfreql = freql(indextotl);
181         iperiodl = ones(size(indfreql))/indfreql;
182
183         indtextl=indfreql+0.01 ;
184
185         % calculates cumulative periodogram
186         ql=(nobsl/2)+1;
187         % Critical values of the Komogorov-Smirnov Test
188         critl=1.36/(sqrt(ql));
189         lineal=freql*2;  % to create the diagonal from 0,0 to 0.5,1
190         cuperl=cumsum(powerl);  % accumulates the intensities
191         cuperal=cuperl./max(cuperl) ; % divides the intensities by  total sum so ...
                that curve goes up to 1
192
193         % cupera = cupera(2:q,1);
194         % linea = linea(2:q,1);
195         % freq = freq(2:q,1);
196
197         % It should be noted that this is a slightly incorrect implementation ...
                because it includes a point (0,0), or (0,0+delta), as the DC portion ...
                of the signal. This is not required in the NCP criterion and may ...
                propagate errors when using the Kolmogorov Smirnov test, this point is ...
                therefore be ignored in post processing.
198
199         % Determine whether the NCP for (1:k) has fallen within the critical ...
                values. A value of 1 (TRUE) means the NCP has fallen outside the ...
                critical values at a given point along its length.
200         truth = any(or(cuperal > lineal' + critl' , cuperal < lineal' - critl'));
201
202         sumtruth(k) = truth;
203
204     end
205
206
207
208 % Optional for statement: Knock out all but the multiples of ...
```

```
    (length(sumtruth))/100). This reduces the sensitivity of the test, but reduces ...
    suprious errors according to Nectow when used with small numbers of angles and ...
    a cut off of ~5. This is similar to the next optional statment, but is a more ...
    generic implementation.
%
% for k=1:(length(sumtruth))
%
%   if mod(k,floor((length(sumtruth))/100)) == 0 ;
%
%       sumtruth(k) = sumtruth(k) ;
%
%   else
%
%       sumtruth(k) = 0 ;
%
%   end
%
% end
%

% Optional for statement: Knock out all but the multiples of 5. This reduces the ...
    sensitivity of the test, but reduces suprious errors according to Nectow when ...
    used with small numbers of angles and a cut off of ~5.

% for k=1:(length(sumtruth))
%
%   if mod(k,5) == 0 ;
%
%       sumtruth(k) = sumtruth(k) ;
%
%   else
%
%       sumtruth(k) = 0 ;
%
%   end
%
%end
%

% Determine the point (k) at which the NCP has fallen outside the critical values. ...
    The -5 is to account for the 5 angle steps introduced above, omitting it and ...
    the previous "for" statement will give a more sensitive, but less specific answer.

```

```
cut = (find(sumtruth > 0.5, 1, 'first')) - 5;

% Report the angle at which the NCP falls outside the critical values.
acut = Vector((cut),1);

disp(' ')
disp('Results')
disp('    cut       angle')
disp([cut,acut])
% end

% Graphing the ranked angle data.
jtime = 1:1:(nobs+1);
subplot(2,2,1)
plot(jtime,Vector','b')
axis([0,nobs,0,90])
xlabel('Neuronal Index','Fontsize',8)
ylabel('Angle (degrees)','Fontsize',8)
title('A. Ranked Angles','Fontsize',10)

% Graphing the series - ie. the Difference Vector
maxser=max(series); % identifies maximum value to determine max value of y axis
itime=1:1:nobs ; % creates the sequence 1,2,  .
figure(1)
subplot(2,2,2)  % partitions the figure to have sub plots (4 plots arrayed in a ...
    2x2 pattern)
plot(itime,series,'b')  % plots the time series
axis([0,nobs,0,maxser])
% (labels for graph and axes are specified in next 3 lines)
xlabel('Neuronal Index','Fontsize',8)
ylabel('Angle Difference (degrees)','Fontsize',8)
title('\it{B. Time Series}','Fontsize',10)

% Graphing the mean-median divergence
maxmean = max(Vector_mean);
maxmedian = max(Vector_median);
maxav = max([maxmean,maxmedian]);
maxav = ceil(maxav);
subplot(2,2,3)
plot(jtime,Vector_mean,'--r')
axis([0,nobs,0,maxav+5])
xlabel('Neuronal Index','Fontsize',8)
ylabel('Mean or Median (degrees)','Fontsize',8)
```

```
hold on
plot(jtime,Vector_median,'g')
hold off
title('\it{C. Mean-Median Divergence}','Fontsize',10)

% Graphing the Cumulative Periodogram
ktime=1:1:q ;
subplot(2,2,4) ;
plot(ktime,cupera,'g')
axis([0 q 0 1])
xlabel('Neuronal Index','Fontsize',8)
hold on
plot(ktime,linea,'--r')
plot(ktime,linea+crit,':r') % plots the bands
plot(ktime,linea-crit,':r')
% text(0.01,0.9,['p-value=', num2str(p)],'Fontsize',8);
text(1,0.9,['Critical value= ', num2str(cv) ],'Fontsize',8);
text(1,0.8,[uniform],'Fontsize',8);
text(1,0.7,['Critical angle (degrees)= ', num2str(acut) ],'Fontsize',8);
text(1,0.6,['Critical neurite= ', num2str(cut) ],'Fontsize',8);
hold off
title('\it{D. Cumulative Periodogram}','Fontsize',10)

% The following graph is optional and adds nothing of use in this case, it
% is given below, unquote if needed.

% % Graphing the intensity / frequency curve.
% subplot(2,2,3)
% plot(freq,power,'g') % plots the intensities vs. the frequencies
% axis([0,0.5,0,pmax])
% xlabel('frequency','Fontsize',8)
% title('\it{C. Periodogram}')
% text(indtext,mpow,['maximum at freq=', num2str(indfreq)],'Fontsize',8);
% text(indtext+0.01,0.9*mpow,['period=', num2str(iperiod) ],'Fontsize',8);
%
% end;
```

Tables of p-values

HF Etched Surfaces

p-value (and Bonferroni-Holm cut-off)	Control	1 minute HF etched	4 minute HF etched
Control	-	**0.017** (0.025)	**0.011** (0.017)
1 minute HF etched		-	0.977 (0.05)
4 minute HF etched			-

Table 33: Mann-Whitney U test results for number of cells on roughened surfaces. Polished control surfaces, 1 minute HF etched surfaces, and 4 minute HF etched surfaces at 96 hours. p_{cut} in brackets, bold values are statistically significant.

p-value (and Bonferroni-Holm cut-off)	Control	1 minute HF etched	4 minute HF etched
Control	-	0.558 (0.05)	**0.001** (0.017)
1 minute HF etched		-	**0.001** (0.025)
4 minute HF etched			-

Table 34: Mann-Whitney U test results for Neurite Number on roughened surfaces. Polished control surfaces, 1 minute HF etched surfaces, and 4 minute HF etched surfaces at 96 hours. p_{cut} in brackets, bold values are statistically significant.

p-value (and Bonferroni-Holm cut-off)	Control	1 minute HF etched	4 minute HF etched
Control	-	**0.001** (0.017)	**0.001** (0.025)
1 minute HF etched		-	**0.001** (0.05)
4 minute HF etched			-

Table 35: Mann-Whitney U test results for Neurite Length on roughened surfaces. Polished control surfaces, 1 minute HF etched surfaces, and 4 minute HF etched surfaces at 96 hours. p_{cut} in brackets, bold values are statistically significant.

Grooved Surfaces

p-value (and Bonferroni-Holm cut-off)	Control	30/30/10	30/30/5	15/30/10
Control	-	**0.007** (0.01)	0.045 (0.0125)	**0.001** (0.008)
30/30/10		-	0.671 (0.05)	0.143 (0.017)
30/30/5			-	0.198 (0.025)
15/30/10				-

Table 36: Mann-Whitney U test results for number of cells on grooved surfaces. Polished control surfaces, 30/30/10, 30/30/5, and 15/30/10 grooved surfaces at 96 hours. p_{cut} in brackets, bold values are statistically significant.

p-value (and Bonferroni-Holm cut-off)	Control	30/30/10	30/30/5	15/30/10
Control	-	0.021 (0.0125)	0.107 (0.025)	**0.001** (0.017)
30/30/10		-	0.619 (0.05)	**0.001** (0.01)
30/30/5			-	**0.001** (0.008)
15/30/10				-

Table 37: Mann-Whitney U test results for neurite number on grooved surfaces. Polished control surfaces, 30/30/10, 30/30/5, and 15/30/10 grooved surfaces at 96 hours. p_{cut} in brackets, bold values are statistically significant.

p-value (and Bonferroni-Holm cut-off)	Control	30/30/10	30/30/5	15/30/10
Control	-	**0.001** (0.0125)	0.168 (0.05)	**0.001** (0.017)
30/30/10		-	**0.001** (0.025)	**0.001** (0.01)
30/30/5			-	**0.001** (0.008)
15/30/10				-

Table 38: Mann-Whitney U test results for neurite alignment on grooved surfaces. Polished control surfaces, 30/30/10, 30/30/5, and 15/30/10 grooved surfaces at 96 hours. p_{cut} in brackets, bold values are statistically significant.

p-value (and Bonferroni-Holm cut-off)	Control	30/30/10	30/30/5	15/30/10
Control	-	0.947 (0.05)	**0.001** (0.008)	0.041 (0.017)
30/30/10		-	**0.001** (0.01)	0.038 (0.0125)
30/30/5			-	0.296 (0.025)
15/30/10				-

Table 39: Mann-Whitney U test results for neurite length on grooved surfaces. Polished control surfaces, 30/30/10, 30/30/5, and 15/30/10 grooved surfaces at 96 hours. p_{cut} in brackets, bold values are statistically significant.

Multiscale Surfaces: Experiment 1

p-value (and Bonferroni-Holm cut-off)	Control	30/30/5 + 1 minute etch	30/30/5	1 minute etch
Control	-	**0.002** (0.017)	**0.001** (0.01)	**0.011** (0.025)
30/30/5 + 1 minute etch		-	0.548 (0.05)	**0.001** (0.0125)
30/30/5			-	**0.001** (0.008)
1 minute etch				-

Table 40: Mann-Whitney U test results for neurite number on grooved surfaces. Polished control surfaces, 30/30/5 grooved surfaces, 1 minute HF etched surfaces and multiscale 30/30/5 grooved + 1 minute HF etched surfaces at 96 hours. p_{cut} in brackets, bold values are statistically significant.

p-value (and Bonferroni-Holm cut-off)	Control	30/30/5 + 1 minute etch	30/30/5	1 minute etch
Control	-	**0.001** (0.0125)	**0.001** (0.01)	0.742 (0.05)
30/30/5 + 1 minute etch		-	**0.014** (0.025)	**0.003** (0.017)
30/30/5			-	**0.001** (0.008)
1 minute etch				-

Table 41: Mann-Whitney U test results for neurite length on grooved surfaces. Polished control surfaces, 30/30/5 grooved surfaces, 1 minute HF etched surfaces and multiscale 30/30/5 grooved + 1 minute HF etched surfaces at 96 hours. p_{cut} in brackets, bold values are statistically significant.

p-value (and Bonferroni-Holm cut-off)	Control	15/30/10 + 4 minute etch	15/30/10	4 minute etch
Control	-	0.061 (0.025)	**0.006** (0.017)	0.055 (0.0125)
15/30/10 + 4 minute etch		-	0.729 (0.05)	**0.008** (0.01)
15/30/10			-	**0.005** (0.008)
4 minute etch				-

Table 42: Mann-Whitney U test results for number of cells on grooved surfaces. Polished control surfaces, 30/15/10 grooved surfaces, 4 minute HF etched surfaces and multiscale 30/15/10 grooved + 4 minute HF etched surfaces at 96 hours. p_{cut} in brackets, bold values are statistically significant.

p-value (and Bonferroni-Holm cut-off)	Control	15/30/10 + 4 minute etch	15/30/10	4 minute etch
Control	-	**0.001** (0.0125)	**0.001** (0.01)	0.192 (0.05)
15/30/10 + 4 minute etch		-	**0.006** (0.025)	**0.001** (0.017)
15/30/10			-	**0.001** (0.008)
4 minute etch				-

Table 43: Mann-Whitney U test results for neurite number on grooved surfaces. Polished control surfaces, 30/15/10 grooved surfaces, 4 minute HF etched surfaces and multiscale 30/15/10 grooved + 4 minute HF etched surfaces at 96 hours. p_{cut} in brackets, bold values are statistically significant.

p-value (and Bonferroni-Holm cut-off)	Control	15/30/10 + 4 minute etch	15/30/10	4 minute etch
Control	-	**0.001** (0.0125)	**0.001** (0.01)	**0.001** (0.008)
15/30/10 + 4 minute etch		-	0.231 (0.05)	**0.001** (0.017)
15/30/10			-	0.044 (0.025)
4 minute etch				-

Table 44: Mann-Whitney U test results for neurite length on grooved surfaces. Polished control surfaces, 30/15/10 grooved surfaces, 4 minute HF etched surfaces and multiscale 30/15/10 grooved + 4 minute HF etched surfaces at 96 hours. p_{cut} in brackets, bold values are statistically significant.

p-value (and Bonferroni-Holm cut-off)	Control	15/30/10 + 4 minute etch	15/30/10	4 minute etch
Control	-	**0.005** (0.0125)	**0.001** (0.01)	0.917 (0.05)
15/30/10 + 4 minute etch		-	0.05 (0.025)	**0.01** (0.017)
15/30/10			-	**0.001** (0.008)
4 minute etch				-

Table 45: Mann-Whitney U test results for neurite alignment on grooved surfaces. Polished control surfaces, 30/15/10 grooved surfaces, 4 minute HF etched surfaces and multiscale 30/15/10 grooved + 4 minute HF etched surfaces at 96 hours. p_{cut} in brackets, bold values are statistically significant.

Protein Mixes on Multiscale Surfaces

	Neurite Number	Neurite Length	Cell Number	Neurite Alignment
p-Value	**0.000**	**0.000**	**0.000**	**0.000**

Table 46: Kruskal Wallis Test results for protein coated multiscale surfaces. Polished control surfaces, 30/15/10 grooved surfaces, 4 minute HF etched surfaces and multiscale 30/15/10 grooved + 4 minute HF etched surfaces coated with either 10 μg/cm^2 Collagen-IV or CNL all-in-one at 96 hours. p_{cut} = 0.05, bold values are statistically significant.

p-value (and Bonferroni-Holm cut-off)	Polished C-IV	Polished All-in-one	4 minute HF C-IV	4 minute HF All-in-one	15/30/10 C-IV	15/30/10 All-in-one	Multiscale C-IV	Multiscale All-in-one
Polished C-IV	-	0.792 (0.017)	0.799 (0.025)	*0.245*	**0.000** (0.003)	*0.000*	0.108 (0.006)	*0.043*
Polished All-in-one		-	*0.509*	0.229 (0.007)	*0.000*	**0.000** (0.003)	*0.024*	0.005 (0.004)
4 minute HF C-IV			-	0.315 (0.008)	**0.000** (0.004)	*0.000*	0.102 (0.006)	*0.051*
4 minute HF All-in-one				-	*0.356*	0.349 (0.010)	*0.957*	0.982 (0.050)
15/30/10 C-IV					-	0.019 (0.005)	**0.000** (0.004))	*0.001*
15/30/10 All-in-one						-	*0.000*	0.045 (0.005)
Multiscale C-IV							-	0.372 (0.013)
Multiscale All-in-one								-

Table 47: Mann-Whitney U test results for number of cells on protein coated multiscale surfaces. Polished control surfaces, 30/15/10 grooved surfaces, 4 minute HF etched surfaces and multiscale 30/15/10 grooved + 4 minute HF etched surfaces coated with either 10 μg/cm^2 Collagen-IV or CNL all-in-one at 96 hours. p_{cut} in brackets, bold values are statistically significant. Some comparisons are not applicable due to a change in two variables, these are noted by *grey italicised* values.

p-value (and Bonferroni-Holm cut-off)	Polished C-IV	Polished All-in-one	4 minute HF C-IV	4 minute HF All-in-one	15/30/10 C-IV	15/30/10 All-in-one	Multiscale C-IV	Multiscale All-in-one
Polished C-IV	-	0.216 (0.013)	0.04 (0.006)	*0.144*	**0.000** (0.004)	*0.000*	**0.000** (0.004)	*0.059*
Polished All-in-one		-	*0.003*	0.758 (0.050)	*0.000*	**0.004** (0.005)	*0.003*	0.481 (0.017)
4 minute HF C-IV			-	**0.000** (0.004)	**0.000** (0.003)	*0.000*	**0.000** (0.003)	*0.000*
4 minute HF All-in-one				-	*0.000*	0.020 (0.005)	*0.16*	0.706 (0.025)
15/30/10 C-IV					-	0.09 (0.008)	0.026 (0.005)	*0.000*
15/30/10 All-in-one						-	*0.78*	0.05 (0.010)
Multiscale C-IV							-	0.044 (0.007)
Multiscale All-in-one								-

Table 48: Mann-Whitney U test results for neurite number on protein coated multiscale surfaces. Polished control surfaces, 30/15/10 grooved surfaces, 4 minute HF etched surfaces and multiscale 30/15/10 grooved + 4 minute HF etched surfaces coated with either 10 μg/cm^2 Collagen-IV or CNL all-in-one at 96 hours. p_{cut} in brackets, bold values are statistically significant. Some comparisons are not applicable due to a change in two variables, these are noted by *grey italicised* values.

p-value (and Bonferroni-Holm cut-off)	Polished C-IV	Polished All-in-one	4 minute HF C-IV	4 minute HF All-in-one	15/30/10 C-IV	15/30/10 All-in-one	Multiscale C-IV	Multiscale All-in-one
Polished C-IV	-	0.194 (0.017)	**0.000** (0.006)	*0.000*	**0.001** (0.007)	*0.634*	**0.000** (0.006)	*0.000*
Polished All-in-one		-	*0.008*	**0.000** (0.005)	*0.000*	0.539 (0.025)	*0.000*	0.000 (0.005)
4 minute HF C-IV			-	0.051 (0.010)	**0.000** (0.004)	*0.004*	**0.000** (0.004)	*0.000*
4 minute HF All-in-one				-	*0.000*	**0.000** (0.004)	*0.000*	**0.000** (0.003)
15/30/10 C-IV					-	**0.001** (0.008)	0.752 (0.050)	*0.548*
15/30/10 All-in-one						-	*0.001*	**0.000** (0.003)
Multiscale C-IV							-	0.142 (0.013)
Multiscale All-in-one								-

Table 49: Mann-Whitney U test results for neurite length on protein coated multiscale surfaces. Polished control surfaces, 30/15/10 grooved surfaces, 4 minute HF etched surfaces and multiscale 30/15/10 grooved + 4 minute HF etched surfaces coated with either 10 μg/cm^2 Collagen-IV or CNL all-in-one at 96 hours. p_{cut} in brackets, bold values are statistically significant. Some comparisons are not applicable due to a change in two variables, these are noted by *grey italicised* values.

p-value (and Bonferroni-Holm cut-off)	Polished C-IV	Polished All-in-one	4 minute HF C-IV	4 minute HF All-in-one	15/30/10 C-IV	15/30/10 All-in-one	Multiscale C-IV	Multiscale All-in-one
Polished C-IV	-	0.121 (0.017)	0.48 (0.010)	*0.170*	**0.000** (0.006)	*0.000*	**0.000** (0.005)	*0.000*
Polished All-in-one		-	*0.048*	0.008 (0.007)	*0.000*	**0.000** (0.005)	*0.000*	**0.000** (0.004)
4 minute HF C-IV			-	0.557 (0.050)	**0.000** (0.004)	*0.000*	**0.000** (0.004)	*0.001*
4 minute HF All-in-one				-	*0.000*	**0.000** (0.003)	*0.000*	**0.000** (0.003)
15/30/10 C-IV					-	0.457 (0.025)	0.017 (0.008)	*0.000*
15/30/10 All-in-one						-	*0.098*	**0.002** (0.006)
Multiscale C-IV							-	0.105 (0.013)
Multiscale All-in-one								-

Table 50: Mann-Whitney U test results for neurite angle on protein coated multiscale surfaces. Polished control surfaces, 30/15/10 grooved surfaces, 4 minute HF etched surfaces and multiscale 30/15/10 grooved + 4 minute HF etched surfaces coated with either 10 μg/cm^2 Collagen-IV or CNL all-in-one at 96 hours. p_{cut} in brackets, bold values are statistically significant. Some comparisons are not applicable due to a change in two variables, these are noted by *grey italicised* values.

Bibliography

[1] Y Al-Ajam, H Lancashire, C Pendegrass, N Kang, and G Blunn. The use of skeletal muscle to amplify action potentials in transected peripheral nerves. In *Plastic & Reconstructive Surgery*, volume 130 (1S), page 44, 2012.

[2] Y Al-Ajam, H Lancashire, C Pendegrass, N Kang, R P Dowling, S J G Taylor, and G Blunn. The use of a bone-anchored device as a hard-wired conduit for transmitting EMG signals from implanted muscle electrodes. *IEEE transactions on bio-medical engineering*, 60(6):1654–1659, 2013.

[3] National Amutee Statistical Database. The amputee statistical database for the united kingdom 2006/07 annual report. Technical Report 10, Information Services Division NHS Scotland, Edinburgh, UK, 2009.

[4] Kengo Ohnishi, Richard F Weir, and Todd A Kuiken. Neural machine interfaces for controlling multifunctional powered upper-limb prostheses. *Expert Review of Medical Devices*, 4(1):43–53, 2007.

[5] K. Ziegler-Graham, E.J. MacKenzie, P.L. Ephraim, T.G. Travison, and R. Brookmeyer. Estimating the prevalence of limb loss in the united states: 2005 to 2050. *Archives of Physical Medicine and Rehabilitation*, 89(3):422–429, 2008.

[6] A. S. Jain, D. P. H. Robinson, and A. H. Davies. Synopsis of causation: amputation of the upper limb. Technical report, Veterans UK / Ministry of Defence (UK), 2008.

[7] N. F. Jones and S. Schneeberger. Arm transplantation: Prospects and visions. *Transplantation Proceedings*, 41(2):476–480, 2009.

[8] Janet H. Yueh, Eran D. Bar-Meir, Eric C. Liao, and Bernard T. Lee. Major limb replantation. *Eplasty*, 11, 2011.

[9] Harry J. Buncke Jr. Microvascular hand surgery—transplants and replants—over the past 25 years. *The Journal of Hand Surgery*, 25(3):415–428, 2000.

[10] Elaine Biddiss, Dorcas Beaton, and Tom Chau. Consumer design priorities for upper limb prosthetics. *Disability and Rehabilitation: Assistive Technology*, 2(6):346–357, 2007.

[11] I. Dudkiewicz, R. Gabrielov, I. Seiv-Ner, G. Zelig, and M. Heim. Evaluation of prosthetic usage in upper limb amputees. *Disability & Rehabilitation*, 26(1):60–63, 2004.

[12] David J. Beard Peter J. Kyberd. A survey of upper-limb prosthesis users in oxfordshire. *Jpo Journal of Prosthetics and Orthotics*, 10(4):84–91, 1998.

[13] Aidan D. Roche, Hubertus Rehbaum, Dario Farina, and Oskar C. Aszmann. Prosthetic myoelectric control strategies: A clinical perspective. *Current Surgery Reports*, 2(3):1–11, 2014.

[14] D. Farina, N. Jiang, H. Rehbaum, A Holobar, B. Graimann, H. Dietl, and O.C. Aszmann. The extraction of neural information from the surface EMG for the control of upper-limb prostheses: Emerging avenues and challenges. *IEEE Transactions on Neural Systems and Rehabilitation Engineering*, 22(4):797–809, 2014.

[15] Levi J Hargrove, Kevin Englehart, and Bernard Hudgins. A comparison of surface and intramuscular myoelectric signal classification. *IEEE Transactions on Bio-Medical Engineering*, 54(5):847–853, 2007. PMID: 17518281.

[16] M. Saliba and C.W. de Silva. An innovative robotic gripper for grasping and handling research. In *International Conference on Industrial Electronics, Control and Instrumentation.*, pages 975 –979 vol.2, 1991.

[17] W. J. Gaine, C. Smart, and M. Bransby-Zachary. Upper limb traumatic amputees: Review of prosthetic use. *The Journal of Hand Surgery: British & European Volume*, 22(1):73–76, 1997.

[18] Aimee E. Schultz and Todd A. Kuiken. Neural interfaces for control of upper limb prostheses: The state of the art and future possibilities. *PM&R*, 3(1):55–67, 2011.

[19] S.A. Dalley, H.A. Varol, and M. Goldfarb. A method for the control of multigrasp myoelectric prosthetic hands. *IEEE Transactions on Neural Systems and Rehabilitation Engineering*, 20(1):58 –67, 2012.

[20] J.I. Hubbard. *The Peripheral Nervous System*. Plenum Press, New York, 1974.

[21] H. deF Webster. Peripheral nerve structure. In *The Peripheral Nervous System*, pages 3–26. Plenum Press, New York, USA, 1974.

[22] Douglas W. Zochodne. *Neurobiology of Peripheral Nerve Regeneration*. Cambridge University Press, Cambridge UK, 1 edition, 2008.

[23] J.M. Barkmeier and E.S. Luschei. Quantitative analysis of the anatomy of the epineurium of the canine recurrent laryngeal nerve. *Journal of Anatomy*, 196(1):85–101, 2000.

[24] Valerie S. LeBleu, Brian MacDonald, and Raghu Kalluri. Structure and function of basement membranes. *Experimental Biology and Medicine*, 232(9):1121–1129, 2007.

[25] M B Bunge, P M Wood, L B Tynan, M L Bates, and J R Sanes. Perineurium originates from fibroblasts: demonstration in vitro with a retroviral marker. *Science*, 243(4888):229–231, 1989.

[26] Warren M. Grill, Sharon E. Norman, and Ravi V. Bellamkonda. Implanted neural interfaces: Biochallenges and engineered solutions. *Annual Review of Biomedical Engineering*, 11(1):1–24, 2009.

[27] S.K. Seidlits, J.Y. Lee, and C.E. Schmidt. Nanostructured scaffolds for neural applications. *Nanomedicine*, 3(2):183–199, 2008.

[28] Gerard J. Tortora and Bryan Derrickson. *Introduction to the human body: the essentials of anatomy and physiology*. J. Wiley & Sons, New York, 7th ed edition, 2007.

[29] B.A. Koeneman, K.-K. Lee, A. Singh, J. He, G.B. Raupp, A. Panitch, and D.G. Capco. An ex vivo method for evaluating the biocompatibility of neural electrodes in rat brain slice cultures. *Journal of Neuroscience Methods*, 137(2):257–263, 2004.

[30] G. Banker and K. Goslin. *Culturing Nerve Cells*. MIT Press, Cambridge, USA, 2nd edition, 1998.

[31] Vadim Polikov, Michelle Block, Cen Zhang, W. Monty Reichert, and J. S. Hong. In vitro models for neuroelectrodes: A paradigm for studying Tissue–Materials interactions in the brain. In William M. Reichert, editor, *Indwelling Neural Implants: Strategies for Contending with the In Vivo Environment*, Frontiers in Neuroengineering, chapter 4. CRC Press, Boca Raton, 2008.

[32] L.A. Greene, S.E. Farinelli, M.E. Cunningham, and D.S. Park. Culture and experimental use of the pc12 rat pheochromocytoma cell line. In G. Banker and K. Goslin, editors, *Culturing Nerve Cells*, pages 161–188. MIT Press, Cambridge, USA, 2nd edition, 1998.

[33] Joseph A. Chromiak and Jose Antonio. Skeletal muscle plasticity. In Jose Antonio, Douglas Kalman RD, Jeffrey R. Stout, Mike Greenwood, Darryn S. Willoughby, and G. Gregory Haff, editors, *Essentials of Sports Nutrition and Supplements*, pages 21–52. Humana Press, 2008.

[34] William D. McArdle, Frank I. Katch, and Victor L. Katch. *Exercise physiology: nutrition, energy, and human performance*. Wolters Kluwer Health/Lippincott Williams & Wilkins, Philadelphia, eighth edition edition, 2015.

[35] J.S. Uglow. *The lunar men: the friends who made the future, 1730-1810*. Faber and Faber, London, UK, 2003.

[36] Aloysii Galvani. *De viribus electricitatis in motu musculari commentarius (The Effects of Artificial Electricity on Muscular Motion)*. Apud Societatem Typographicam, Modena, Italy, 1792.

[37] L.A. Geddes and H.E. Hoff. The discovery of bioelectricity and current electricity the Galvani-Volta controversy. *Spectrum, IEEE*, 8(12):38–46, 1971.

[38] C.D. McCaig, A.M. Rajnicek, B. Song, and M. Zhao. Controlling cell behavior electrically: Current views and future potential. *Physiological Reviews*, 85(3):943–978, 2005.

[39] S. Finger. Benjamin Franklin, electricity, and the palsies. *Neurology*, 66(10):1559–1563, 2006.

[40] P.J. Koehler, S. Finger, and M. Piccolino. The "eels" of south america: Mid-18th-Century Dutch contributions to the theory of animal electricity. *Journal of the History of Biology*, 42(4):715–763, 2009.

[41] J.E. Jensen, R.R. Conn, G. Hazelrigg, and J.E. Hewett. The use of transcutaneous neural stimulation and isokinetic testing in arthroscopic knee surgery. *The American Journal of Sports Medicine*, 13(1):27–33, 1985.

[42] Nicholas A. Kotov, Jessica O. Winter, Isaac P. Clements, Edward Jan, Brian P. Timko, Stéphane Campidelli, Smita Pathak, Andrea Mazzatenta, Charles M. Lieber, Maurizio Prato, Ravi V. Bellamkonda, Gabriel A. Silva, Nadine Wong Shi Kam, Fernando Patolsky, and Laura Ballerini. Nanomaterials for neural interfaces. *Advanced Materials*, 21(40):3970–4004, 2009.

[43] M. Bragg, C. Blakemore, V. Nutton, T. Tansey, and T. Morris. The nervous system. *In Our Time*, 2011. First broadcast at 0900GMT on 10th February 2011. Available from http://www.bbc.co.uk/programmes/b00y9283.

[44] J.M.S. Pearce. Emil Heinrich Du Bois-Reymond (1818-96). *Journal of Neurology, Neurosurgery & Psychiatry*, 71(5):620–620, 2001.

[45] John Enderle. Bioelectric phenomena. In John Enderle, Blanchard, and Joseph Bronzino, editors, *Introduction to Biomedical Engineering (Second Edition)*, Biomedical Engineering, pages 627–691. Academic Press, Boston, 2005.

[46] David A McCormick. Membrane potential and action potential. In Larry L Squire, Darwin Berg, Floyd E Bloom, Sascha du Lac, Anirvan Ghosh, and Nicholas C Spitzer, editors, *Fundamental Neuroscience*, pages 93–116. Academic Press, Oxford, 4 edition, 2013.

[47] Charles R Noback, Norman L Strominger, Robert J Demarest, and David A Ruggiero. Basic neurophysiology. In *The Human Nervous System: Structure and Function*, pages 41–75. Humana Press, Totowa, NJ, 6 edition, 2005.

[48] Gary G. Matthews. *Cellular physiology of nerve and muscle*. Blackwell Publishing, Osney Mead, Oxford ; Malden, MA, 4th ed edition, 2003.

[49] George Z Mentis. The spinal and peripheral motor system. In Larry L Squire, Darwin Berg, Floyd E Bloom, Sascha du Lac, Anirvan Ghosh, and Nicholas C Spitzer, editors, *Fundamental Neuroscience*, pages 613–630. Academic Press, Oxford, 4 edition, 2013.

[50] Harvey Lodish, Arnold Berk, S. Lawrence Zipursky, Paul Matsudaira, David Baltimore, and James Darnell. *Molecular Cell Biology*. W. H. Freeman, 4th edition, 2000.

[51] James J FitzGerald, Natalia Lago, Samia Benmerah, Jordi Serra, Christopher P Watling, Ruth E Cameron, Edward Tarte, Stéphanie P Lacour, Stephen B McMahon, and James W Fawcett. A regenerative microchannel neural interface for recording from and stimulating peripheral axons in vivo. *Journal of Neural Engineering*, 9(1):016010, 2012. PMID: 22258138.

[52] Stuart F. Cogan. Neural stimulation and recording electrodes. *Annual Review of Biomedical Engineering*, 10(1):275–309, 2008.

[53] Wim L. C Rutten. Selective electrical interfaces with the nervous system. *Annual Review of Biomedical Engineering*, 4(1):407–452, 2002.

[54] Sonia Todorova, Patrick Sadtler, Aaron Batista, Steven Chase, and Valérie Ventura. To sort or not to sort: the impact of spike-sorting on neural decoding performance. *Journal of Neural Engineering*, 11(5):056005, 2014.

[55] X. Navarro, T.B. Krueger, N. Lago, S. Micera, T. Stieglitz, and P. Dario. A critical review of interfaces with the peripheral nervous system for the control of neuroprostheses and hybrid bionic systems. *Journal of the Peripheral Nervous System*, 10(3):229–258, 2005.

[56] Gerald E. Loeb. *Electromyography for experimentalists*. University of Chicago Press, Chicago, 1986.

[57] Vadim S. Polikov, Patrick A. Tresco, and William M. Reichert. Response of brain tissue to chronically implanted neural electrodes. *Journal of Neuroscience Methods*, 148(1):1–18, 2005.

[58] S. Micera, J. Carpaneto, and S. Raspopovic. Control of hand prostheses using peripheral information. *IEEE Reviews in Biomedical Engineering*, 3:48–68, 2010.

[59] James J. Fitzgerald, Stéphanie P. Lacour, Stephen B. McMahon, and James W. Fawcett. Microchannels as axonal amplifiers. *IEEE transactions on bio-medical engineering*, 55(3):1136–1146, 2008.

[60] Rylie A. Green, Nigel H. Lovell, Gordon G. Wallace, and Laura A. Poole-Warren. Conducting polymers for neural interfaces: Challenges in developing an effective long-term implant. *Biomaterials*, 29(24–25):3393–3399, 2008.

[61] X. Cui, J. Wiler, M. Dzaman, R.A. Altschuler, and D.C. Martin. In vivo studies of polypyrrole/peptide coated neural probes. *Biomaterials*, 24(5):777–787, 2003.

[62] K.C. Cheung. Thin-Film microelectrode arrays for biomedical applications. In D.D. Zhou and E.S. Greenbaum, editors, *Implantable Neural Prostheses 2*, Biological and Medical Physics, Biomedical Engineering, pages 157–190. Springer, New York, USA, 2010.

[63] Joseph D. Bronzino. *Biomedical Engineering Handbook, Volume I*. CRC Press, 2 sub edition, 1999.

[64] S Sunderland. The anatomy and physiology of nerve injury. *Muscle & nerve*, 13(9):771–784, 1990. PMID: 2233864.

[65] Sydney Sunderland. A classification of peripheral nerve injuries producing loss of function. *Brain*, 74(4):491–516, 1951.

[66] Amer Al-Shekhlee, Barbara E. Shapiro, and David C. Preston. Iatrogenic complications and risks of nerve conduction studies and needle electromyography. *Muscle & Nerve*, 27(5):517–526, 2003.

[67] M E Watson. Median nerve damage from brachial artery puncture: a case report. *Respiratory care*, 40(11):1141–1143, 1995. PMID: 10152854.

[68] David Preston and Eric Logigian. Iatrogenic needle-induced peroneal neuropathy in the foot. *Annals of Internal Medicine*, 109(11):921–922, 1988.

[69] Augustus Waller. Experiments on the section of the glossopharyngeal and hypoglossal nerves of the frog, and observations of the alterations produced thereby in the structure of their primitive fibres. *Philosophical Transactions of the Royal Society of London*, 140:423–429, 1850.

[70] Andrew D Gaudet, Phillip G Popovich, and Matt S Ramer. Wallerian degeneration: gaining perspective on inflammatory events after peripheral nerve injury. *Journal of Neuroinflammation*, 8(1):110, 2011.

[71] Elizabeth O. Johnson, Aristides B. Zoubos, and Panayotis N. Soucacos. Regeneration and repair of peripheral nerves. *Injury*, 36(4, Supplement):S24–S29, 2005.

[72] Wei Cheong Ngeow. Scar less: a review of methods of scar reduction at sites of peripheral nerve repair. *Oral surgery, oral medicine, oral pathology, oral radiology, and endodontics*, 109(3):357–366, 2010.

[73] A B Dagum. Peripheral nerve regeneration, repair, and grafting. *Journal of hand therapy*, 11(2):111–117, 1998. PMID: 9602967.

[74] Eric G. Fine, Robert F. Valentini, and Patrick Aebischer. Nerve regeneration. In Robert P. Lanza, Robert Langer, and Joseph Vacanti, editors, *Principles of Tissue Engineering*, pages 785 – 798. Academic Press, San Diego, CA, USA, 2nd edition, 2007.

[75] Amit Pabari, Shi Yu Yang, Alexander M. Seifalian, and Ash Mosahebi. Modern surgical management of peripheral nerve gap. *Journal of Plastic, Reconstructive & Aesthetic Surgery*, 63(12):1941–1948, 2010.

[76] W. Daly, L. Yao, D. Zeugolis, A. Windebank, and A. Pandit. A biomaterials approach to peripheral nerve regeneration: bridging the peripheral nerve gap and enhancing functional recovery. *Journal of The Royal Society Interface*, 2011.

[77] Jason S Belkas, Molly S Shoichet, and Rajiv Midha. Peripheral nerve regeneration through guidance tubes. *Neurological research*, 26(2):151–160, 2004. PMID: 15072634.

[78] Pei-Hwa Wang, I-Ling Tseng, and Shan-Hui Hsu. Bioengineering approaches for guided peripheral nerve regeneration. *Journal of Medical and Biological Engineering*, 31(3):151–160, 2011.

[79] Max Ortiz-Catalan, Rickard Brånemark, Bo Håkansson, and Jean Delbeke. On the viability of implantable electrodes for the natural control of artificial limbs: Review and discussion. *BioMedical Engineering OnLine*, 11:33, 2012.

[80] Cristina Marin and Eduardo Fernandez. Biocompatibility of intracortical microelectrodes: current status and future prospects. *Frontiers in Neuroengineering*, 3:8, 2010.

[81] R.F. Weir, P.R. Troyk, G.A. DeMichele, D.A. Kerns, J.F. Schorsch, and H. Maas. Implantable myoelectric sensors (IMESs) for intramuscular electromyogram recording. *IEEE Transactions on Bio-Medical Engineering*, 56(1):159–171, 2009.

[82] Peter Konrad. The ABC of EMG: a practical introduction to kinesiological electromyography, 2005.

[83] K. Yoshida, D. Farina, M. Akay, and W. Jensen. Multichannel intraneural and intramuscular techniques for multiunit recording and use in active prostheses. *Proceedings of the IEEE*, 98(3):432–449, 2010.

[84] Todd R. Farrell and Richard F. ff. Weir. A comparison of the effects of electrode implantation and targeting on pattern classification accuracy for prosthesis control. *IEEE transactions on biomedical engineering*, 55(9):2198–2211, 2008.

[85] J.M. Akers, P.H. Peckham, M.W. Keith, and K. Merritt. Tissue response to chronically stimulated implanted epimysial and intramuscular electrodes. *IEEE Transactions on Rehabilitation Engineering*, 5(2):207–220, 1997.

[86] Kevin L. Kilgore, P. Hunter Peckham, Michael W. Keith, Fred W. Montague, Ronald L. Hart, Martha M. Gazdik, Anne M. Bryden, Scott A. Snyder, and Thomas G. Stage. Durability of implanted electrodes and leads in an upper-limb neuroprosthesis. *Journal of Rehabilitation Research and Development*, 40(6):457–468, 2003.

[87] P. Hunter Peckham and Jayme S. Knutson. Functional electrical stimulation for neuromuscular applications. *Annual Review of Biomedical Engineering*, 7:327–360, 2005.

[88] D. N. Rushton. Functional electrical stimulation. *Physiological Measurement*, 18(4):241, 1997.

[89] European Commission, Directorate General for Research, Commission of the European Communities, and Biomedical and Health Research Programme. *SENIAM: European recommendations for surface electromyography*. Roessingh Research and Development, Netherlands, 1999.

[90] Michael J. Kane, Paul P. Breen, Fabio Quondamatteo, and Gearóid ÓLaighin. BION microstimulators: a case study in the engineering of an electronic implantable medical device. *Medical Engineering & Physics*, 33(1):7–16, 2011.

[91] P.R. Troyk, G.A DeMichele, D.A Kerns, and R.F. Weir. IMES: An implantable myoelectric sensor. In *29th Annual International Conference of the IEEE Engineering in Medicine and Biology Society.*, pages 1730–1733, 2007.

[92] Daniel R. Merrill, Joseph Lockhart, Phil R. Troyk, Richard F. Weir, and David L. Hankin. Development of an implantable myoelectric sensor for advanced prosthesis control. *Artificial Organs*, 35(3):249–252, 2011.

[93] S. Lewis, M. Russold, H. Dietl, R. Ruff, J.M.C. Audi, K.-P. Hoffmann, L. Abu-Saleh, D. Schroeder, W.H. Krautschneider, S. Westendorff, A Gail, T. Meiners, and E. Kaniusas. Fully implantable multi-channel measurement system for acquisition of muscle activity. *IEEE Transactions on Instrumentation and Measurement*, 62(7):1972–1981, 2013.

[94] D. McDonnall, S. Hiatt, C. Smith, and K.S. Guillory. Implantable multichannel wireless electromyography for prosthesis control. In *Annual International Conference of the IEEE Engineering in Medicine and Biology Society*, pages 1350–1353, 2012.

[95] Dario Farina, Ken Yoshida, Thomas Stieglitz, and Klaus Peter Koch. Multichannel thin-film electrode for intramuscular electromyographic recordings. *Journal of Applied Physiology*, 104(3):821–827, 2008.

[96] R. Ruff, W. Poppendieck, A. Gail, S. Westendorff, M. Russold, S. Lewis, T. Meiners, and K. P Hoffmann. Acquisition of myoelectric signals to control a hand prosthesis with implantable epimysial electrodes. In *Annual International Conference of the IEEE Engineering in Medicine and Biology Society*, pages 5070–5073, 2010.

[97] M.M. Lowery, R.F. Weir, and T.A. Kuiken. Simulation of intramuscular EMG signals detected using implantable myoelectric sensors (IMES). *IEEE Transactions on Bio-Medical Engineering*, 53(10):1926–1933, 2006. PMID: 17019856.

[98] Mehdi Jorfi, John L. Skousen, Christoph Weder, and Jeffrey R. Capadona. Progress towards biocompatible intracortical microelectrodes for neural interfacing applications. *Journal of Neural Engineering*, 12(1):011001, 2015.

[99] W. M. Grill and J. T. Mortimer. Electrical properties of implant encapsulation tissue. *Annals of Biomedical Engineering*, 22(1):23–33, February 1994.

[100] G.S. Dhillon and K.W. Horch. Direct neural sensory feedback and control of a prosthetic arm. *Neural Systems and Rehabilitation Engineering, IEEE Transactions on*, 13(4):468–472, 2005.

[101] G.S. Dhillon and Sandford Meek. Challenges to developing a neurally controlled upper limb prosthesis. In Kenneth W Horch, Gurpreet S Dhillon, and John K-J Li, editors, *Neuroprosthetics: Theory and Practice*, volume 2 of *Series on Bioengineering and Biomedical Engineering*, pages 1005–1034. World Scientific, Singapore, 2004.

[102] Karen C Cheung. Implantable microscale neural interfaces. *Biomedical Microdevices*, 9(6):923–938, 2007. PMID: 17252207.

[103] Young-tae Kim and Mario I. Romero-Ortega. Material considerations for peripheral nerve interfacing. *MRS Bulletin*, 37(06):573–580, 2012.

[104] N Brill, K Polasek, E Oby, C Ethier, L Miller, and D Tyler. Nerve cuff stimulation and the effect of fascicular organization for hand grasp in nonhuman primates. *Annual International Conference of the IEEE Engineering in Medicine and Biology Society.*, 2009:1557–1560, 2009.

[105] Almut Branner and Richard Alan Normann. A multielectrode array for intrafascicular recording and stimulation in sciatic nerve of cats. *Brain Research Bulletin*, 51(4):293–306, 2000.

[106] A. Branner, R.B. Stein, E. Fernandez, Y. Aoyagi, and R.A. Normann. Long-term stimulation and recording with a penetrating microelectrode array in cat sciatic nerve. *Biomedical Engineering, IEEE Transactions on*, 51(1):146–157, 2004.

[107] S.M. Lawrence, J.O. Larsen, K.W. Horch, R.Riso, and T.Sinkjær. Long-term biocompatibility of implanted polymer-based intrafascicular electrodes. *Journal of Biomedical Materials Research*, 63(5):501–506, 2002.

[108] N. Lago, K. Yoshida, K.P. Koch, and X. Navarro. Assessment of biocompatibility of chronically implanted polyimide and platinum intrafascicular electrodes. *IEEE Transactions on Biomedical Engineering*, 54(2):281–290, 2007.

[109] Tim Boretius, Jordi Badia, Aran Pascual-Font, Martin Schuettler, Xavier Navarro, Ken Yoshida, and Thomas Stieglitz. A transverse intrafascicular multichannel electrode (TIME) to interface with the peripheral nerve. *Biosensors and Bioelectronics*, 26:62–69, 2010.

[110] A. Kundu, K.R. Harreby, K. Yoshida, T. Boretius, T. Stieglitz, and W. Jensen. Stimulation selectivity of the thin-film longitudinal intrafascicular electrode (tfLIFE) and the transverse intrafascicular multi-channel electrode (TIME) in the large nerve animal model. *IEEE Transactions on Neural Systems and Rehabilitation Engineering*, 22(2):400–410, 2014.

[111] Natalia Lago, Esther Udina, Anup Ramachandran, and Xavier Navarro. Neurobiological assessment of regenerative electrodes for bidirectional interfacing injured peripheral nerves. *IEEE Transactions on Bio-Medical Engineering*, 54(6 Pt 1):1129–1137, 2007.

[112] Natalia Lago, Dolores Ceballos, Francisco J Rodriguez, Thomas Stieglitz, and Xavier Navarro. Long term assessment of axonal regeneration through polyimide regenerative electrodes to interface the peripheral nerve. *Biomaterials*, 26(14):2021–2031, May 2005.

[113] Stéphanie P Lacour, James J Fitzgerald, Natalia Lago, Edward Tarte, Stephen McMahon, and James Fawcett. Long micro-channel electrode arrays: a novel type of regenerative peripheral nerve interface. *IEEE Transactions on Neural Systems and Rehabilitation Engineering*, 17(5):454–460, 2009. PMID: 19744916.

[114] IP. Clements, V.J. Mukhatyar, A Srinivasan, J.T. Bentley, D.S. Andreasen, and R.V. Bellamkonda. Regenerative scaffold electrodes for peripheral nerve interfacing. *IEEE Transactions on Neural Systems and Rehabilitation Engineering*, 21(4):554–566, 2013.

[115] A Srinivasan, Liang Guo, and R.V. Bellamkonda. Regenerative microchannel electrode array for peripheral nerve interfacing. In *5th International IEEE/EMBS Conference on Neural Engineering*, pages 253–256, 2011.

[116] Daniel K Leventhal, Mark Cohen, and Dominique M Durand. Chronic histological effects of the flat interface nerve electrode. *Journal of Neural Engineering*, 3(2):102–113, 2006.

[117] Daniel W. Tan, Matthew A. Schiefer, Michael W. Keith, James Robert Anderson, Joyce Tyler, and Dustin J. Tyler. A neural interface provides long-term stable natural touch perception. *Science Translational Medicine*, 6(257):257ra138–257ra138, 2014.

[118] D. J. Tyler and D. M. Durand. A slowly penetrating interfascicular nerve electrode for selective activation of peripheral nerves. *IEEE transactions on rehabilitation engineering*, 5(1):51–61, 1997.

[119] Felix Strumwasser. Long-term recording from single neurons in brain of unrestrained mammals. *Science*, 127(3296):469–470, 1958.

[120] Yuan Yao, Gang Li, Qinghui Jin, and Jianglong Zhao. A micromachine-based assembly of tungsten multichannel electrodes for neural recording. In *3rd IEEE International Conference on Nano/Micro Engineered and Molecular Systems*, pages 410–413, 2008.

[121] Miguel A. L. Nicolelis, Dragan Dimitrov, Jose M. Carmena, Roy Crist, Gary Lehew, Jerald D. Kralik, and Steven P. Wise. Chronic, multisite, multielectrode recordings in macaque monkeys. *Proceedings of the National Academy of Sciences*, 100(19):11041–11046, 2003.

[122] Miguel A. L Nicolelis, Asif A Ghazanfar, Barbara M Faggin, Scott Votaw, and Laura M. O Oliveira. Reconstructing the engram: Simultaneous, multisite, many single neuron recordings. *Neuron*, 18(4):529–537, 1997.

[123] Anil K. Thota, Sathyakumar Kuntaegowdanahalli, Amy K. Starosciak, James J. Abbas, Jorge Orbay, Kenneth W. Horch, and Ranu Jung. A system and method to interface with multiple groups of axons in several fascicles of peripheral nerves. *Journal of Neuroscience Methods*, 244:78–84, 2015.

[124] Stanisa Raspopovic, Marco Capogrosso, Francesco Maria Petrini, Marco Bonizzato, Jacopo Rigosa, Giovanni Di Pino, Jacopo Carpaneto, Marco Controzzi, Tim Boretius, Eduardo Fernandez, Giuseppe Granata, Calogero Maria Oddo, Luca Citi, Anna Lisa Ciancio, Christian Cipriani, Maria Chiara Carrozza, Winnie Jensen, Eugenio Guglielmelli, Thomas Stieglitz, Paolo Maria Rossini, and Silvestro Micera. Restoring natural sensory feedback in real-time bidirectional hand prostheses. *Science Translational Medicine*, 6(222):222ra19–222ra19, 2014.

[125] Jordi Badia, Tim Boretius, Arán Pascual-Font, Esther Udina, Thomas Stieglitz, and Xavier Navarro. Biocompatibility of chronically implanted transverse intrafascicular multichannel electrode (TIME) in the rat sciatic nerve. *IEEE transactions on bio-medical engineering*, 58(8), 2011.

[126] Ivan R. Minev, Pavel Musienko, Arthur Hirsch, Quentin Barraud, Nikolaus Wenger, Eduardo Martin Moraud, Jérôme Gandar, Marco Capogrosso, Tomislav Milekovic, Léonie Asboth, Rafael Fajardo Torres, Nicolas Vachicouras, Qihan Liu, Natalia Pavlova, Simone Duis, Alexandre Larmagnac, Janos Vörös, Silvestro Micera, Zhigang Suo, Grégoire Courtine, and Stéphanie P. Lacour. Electronic dura mater for long-term multimodal neural interfaces. *Science*, 347(6218):159–163, September 2015.

[127] Takashi D. Yoshida Kozai, Nicholas B. Langhals, Paras R. Patel, Xiaopei Deng, Huanan Zhang, Karen L. Smith, Joerg Lahann, Nicholas A. Kotov, and Daryl R. Kipke. Ultrasmall implantable composite microelectrodes with bioactive surfaces for chronic neural interfaces. *Nature Materials*, 11(12):1065–1073, 2012.

[128] Grigori Guitchounts, Jeffrey E. Markowitz, William A. Liberti, and Timothy J. Gardner. A carbon-fiber electrode array for long-term neural recording. *Journal of Neural Engineering*, 10(4):046016, 2013.

[129] Dominique M. Durand, Maysam Ghovanloo, and Elliot Krames. Time to address the problems at the neural interface. *Journal of Neural Engineering*, 11(2):020201, 2014.

[130] H. a. C. Wark, R. Sharma, K. S. Mathews, E. Fernandez, J. Yoo, B. Christensen, P. Tresco, L. Rieth, F. Solzbacher, R. A. Normann, and P. Tathireddy. A new high-density (25 electrodes/mm2) penetrating microelectrode array for recording and stimulating sub-millimeter neuroanatomical structures. *Journal of Neural Engineering*, 10(4):045003, 2013.

[131] Kevin Warwick, Mark Gasson, Benjamin Hutt, Iain Goodhew, Peter Kyberd, Brian Andrews, Peter Teddy, and Amjad Shad. The application of implant technology for cybernetic systems. *Arch Neurol*, 60(10):1369–1373, 2003.

[132] M Gasson, Benjamin Hutt, Iain Goodhew, Peter Kyberd, and Kevin Warwick. Invasive neural prosthesis for neural signal detection and nerve stimulation. *International journal of adaptive control and signal processing*, 19(5):365–375, 2004.

[133] Leigh R. Hochberg, Daniel Bacher, Beata Jarosiewicz, Nicolas Y. Masse, John D. Simeral, Joern Vogel, Sami Haddadin, Jie Liu, Sydney S. Cash, Patrick van der Smagt, and John P. Donoghue. Reach and grasp by people with tetraplegia using a neurally controlled robotic arm. *Nature*, 485(7398):372–375, 2012.

[134] J. D. Simeral, S.-P. Kim, M. J. Black, J. P. Donoghue, and L. R. Hochberg. Neural control of cursor trajectory and click by a human with tetraplegia 1000 days after implant of an intracortical microelectrode array. *Journal of Neural Engineering*, 8(2):025027, 2011.

[135] H. a. C. Wark, K. S. Mathews, R. A. Normann, and E. Fernandez. Behavioral and cellular consequences of high-electrode count Utah Arrays chronically implanted in rat sciatic nerve. *Journal of Neural Engineering*, 11(4):046027, 2014.

[136] Kiran S. Mathews, Heather A. C. Wark, and Richard A. Normann. Assessment of rat sciatic nerve function following acute implantation of high density utah slanted electrode array (25 electrodes/mm(2)) based on neural recordings and evoked muscle activity. *Muscle & Nerve*, 50(3):417–424, 2014.

[137] M. B. Christensen, S. M. Pearce, N. M. Ledbetter, D. J. Warren, G. A. Clark, and P. A. Tresco. The foreign body response to the utah slant electrode array in the cat sciatic nerve. *Acta Biomaterialia*, 10(11):4650–4660, 2014.

[138] Braingate. Braingate. http://www.braingate.com/, 2009. Accessed 2011.01.27.

[139] K. Wise and J. Angell. A microprobe with integrated amplifiers for neurophysiology. In *IEEE International Solid-State Circuits Conference.*, volume XIV, pages 100–101, 1971.

[140] Matthew P. Ward, Pooja Rajdev, Casey Ellison, and Pedro P. Irazoqui. Toward a comparison of microelectrodes for acute and chronic recordings. *Brain Research*, 1282:183–200, 2009.

[141] X. Navarro, S. Calvet, M. Butí, N. Gómez, E. Cabruja, P. Garrido, R. Villa, and E. Valderrama. Peripheral nerve regeneration through microelectrode arrays based on silicon technology. *Restorative Neurology and Neuroscience*, 9(3):151–160, 1996.

[142] Sung-Hoon Cho, Hong Meng Lu, L. Cauller, M.I Romero-Ortega, Jeong-Bong Lee, and G.A Hughes. Biocompatible SU-8-based microprobes for recording neural spike signals from regenerated peripheral nerve fibers. *IEEE Sensors Journal*, 8(11):1830–1836, 2008.

[143] Tessa Gordon, Neil Tyreman, and Mukaila A. Raji. The basis for diminished functional recovery after delayed peripheral nerve repair. *The Journal of Neuroscience*, 31(14):5325–5334, 2011.

[144] John Clark and Robert Plonsey. The extracellular potential field of the single active nerve fiber in a volume conductor. *Biophysical Journal*, 8(7):842–864, 1968.

[145] L. Pan, S. Alagapan, E. Franca, T. DeMarse, G.J. Brewer, and B.C. Wheeler. Large extracellular spikes recordable from axons in microtunnels. *IEEE Transactions on Neural Systems and Rehabilitation Engineering*, Early Access Online, 2014.

[146] James J. FitzGerald, Stéphanie P. Lacour, Stephen B. McMahon, and James W. Fawcett. Microchannel electrodes for recording and stimulation: in vitro evaluation. *IEEE transactions on bio-medical engineering*, 56(5):1524–1534, 2009.

[147] Bongkyun Kim, Alejandro Reyes, Bernardo Garza, and Yoonsu Choi. A microchannel neural interface with embedded microwires targeting the peripheral nervous system. *Microsystem Technologies*, pages 1–7, October 2014.

[148] Russell K. Gore, Yoonsu Choi, Ravi Bellamkonda, and Arthur English. Functional recordings from awake, behaving rodents through a microchannel based regenerative neural interface. *Journal of Neural Engineering*, 12(1):016017, 2015.

[149] Stéphanie P. Lacour, Raghied Atta, James J. FitzGerald, Mark Blamire, Edward Tarte, and James Fawcett. Polyimide micro-channel arrays for peripheral nerve regenerative implants. *Sensors and Actuators A: Physical*, 147(2):456–463, 2008.

[150] R. Barrett, S. Benmerah, A. Frommhold, and E. Tarte. Spiral peripheral nerve interface; updated fabrication process of the regenerative implant. In *35th Annual International Conference of the IEEE Engineering in Medicine and Biology Society*, pages 771–774, 2013.

[151] Richard Barrett. *Novel processing routes for neural interfaces*. d_ph, University of Birmingham, 2014.

[152] E. Delivopoulos, IR. Minev, and S.P. Lacour. Evaluation of negative photo-patternable PDMS for the encapsulation of neural electrodes. In *5th International IEEE/EMBS Conference on Neural Engineering*, pages 490–494, 2011.

[153] Evangelos Delivopoulos, Daniel J. Chew, Ivan R. Minev, James W. Fawcett, and Stéphanie P. Lacour. Concurrent recordings of bladder afferents from multiple nerves using a microfabricated PDMS microchannel electrode array. *Lab on a Chip*, 12(14):2540–2551, 2012.

[154] Daniel J. Chew, Lan Zhu, Evangelos Delivopoulos, Ivan R. Minev, Katherine M. Musick, Charles A. Mosse, Michael Craggs, Nicholas Donaldson, Stéphanie P. Lacour, Stephen B. McMahon, and James W. Fawcett. A microchannel neuroprosthesis for bladder control after spinal cord injury in rat. *Science Translational Medicine*, 5(210):210ra155–210ra155, June 2013.

[155] A Srinivasan, Adel Haque, Mayank Tahilramani, Garrett Stanley, and Ravi Bellamkonda. Microchannel scaffolds as regeenerative peripheral nerve interfaces. In *Biomaterials Revolution*, Boston, MA, 2013.

[156] Akhil Srinivasan, Mayank Tahilramani, John T. Bentley, Russell K. Gore, Daniel C. Millard, Vivek J. Mukhatyar, Anish Joseph, Adel S. Haque, Garrett B. Stanley, Arthur W. English, and Ravi V. Bellamkonda. Microchannel-based regenerative scaffold for chronic peripheral nerve interfacing in amputees. *Biomaterials*, 41:151–165, 2015.

[157] J.M Starobin, V. Varadarajan, and S. Aravamudhan. High-density peripheral nerve resonant stimulation system. In *Proceedings of BMES*, Hartford, Conneticut, USA, 2011.

[158] Joseph Starobin, Syed Gilani, and Shyam Aravamudhan. Application of micro-/nanotechnology in the design and control of neural interfaces. In *Nanoscience and Nanoengineering*, pages 51–66. CRC Press, 2014.

[159] J.P.P van Vugt and J.G van Dijk. A convenient method to reduce crosstalk in surface EMG. *Clinical Neurophysiology*, 112(4):583–592, 2001.

[160] T J Koh and M D Grabiner. Evaluation of methods to minimize cross talk in surface electromyography. *Journal of Biomechanics*, 26 Suppl 1:151–157, 1993. PMID: 8505349.

[161] A. Demosthenous, I. Pachnis, M. Rahal, Dai Jiang, and N. Donaldson. An ENG amplifier with passive EMG neutralization. In *14th IEEE International Conference on Electronics, Circuits and Systems.*, pages 66 –69, 2007.

[162] Madeleine M Lowery, Nikolay S Stoykov, and Todd A Kuiken. Independence of myoelectric control signals examined using a surface EMG model. *IEEE Transactions on Bio-Medical Engineering*, 50(6):789–793, 2003. PMID: 12814247.

[163] Jun-Uk Chu, Kang-Il Song, Sungmin Han, Soo Hyun Lee, Jinseok Kim, Ji Yoon Kang, Dosik Hwang, Jun-Kyo Francis Suh, Kuiwon Choi, and Inchan Youn. Improvement of signal-to-interference ratio and signal-to-noise ratio in nerve cuff electrode systems. *Physiological Measurement*, 33(6):943–967, 2012.

[164] J.N.Y. Aziz, Karim Abdelhalim, R. Shulyzki, R. Genov, B.L. Bardakjian, M. Derchansky, D. Serletis, and P.L. Carlen. 256-channel neural recording and delta compression microsystem with 3d electrodes. *IEEE Journal of Solid-State Circuits*, 44(3):995–1005, 2009.

[165] David A. Borton, Ming Yin, Juan Aceros, and Arto Nurmikko. An implantable wireless neural interface for recording cortical circuit dynamics in moving primates. *Journal of Neural Engineering*, 10(2):026010, 2013.

[166] Nick Donaldson, Tim Perkins, Ioannis Pachnis, Anne Vanhoest, and Andreas Demosthenous. Design of an implant for preventing incontinence after spinal cord injury. *Artificial Organs*, 32(8):586–591, 2008.

[167] Dr N. de N. Donaldson, L. Zhou, T. A. Perkins, M. Munih, M. Haugland, and T. Sinkjaer. Implantable telemeter for long-term electroneurographic recordings in animals and humans. *Medical and Biological Engineering and Computing*, 41(6):654–664, 2003.

[168] Anne Vanhoestenberghe. Implantable electronic devices technology challenges for long-term human implantation. *Sensor Review*, 29(4):345–348, 2009.

[169] Rylie A. Green, Thomas Guenther, Christoph Jeschke, Amandine Jaillon, Jin F. Yu, Wolfram F. Dueck, William W. Lim, William C. Henderson, Anne Vanhoestenberghe, Nigel H. Lovell, and Gregg J. Suaning. Integrated electrode and high density feedthrough system for chip-scale implantable devices. *Biomaterials*, 34(26):6109–6118, 2013.

[170] Rodrigo Quian Quiroga and Stefano Panzeri. Extracting information from neuronal populations: information theory and decoding approaches. *Nature Reviews Neuroscience*, 10(3):173–185, 2009.

[171] S. Gibson, J.W. Judy, and D. Markovic. Spike sorting: The first step in decoding the brain: The first step in decoding the brain. *IEEE Signal Processing Magazine*, 29(1):124–143, 2012.

[172] Carlos Pedreira, Juan Martinez, Matias J. Ison, and Rodrigo Quian Quiroga. How many neurons can we see with current spike sorting algorithms? *Journal of Neuroscience Methods*, 211(1):58–65, 2012.

[173] David Williams. The inert-bioactivity conundrum. In Jan Eirik Ellingsen and S Petter Lyngstadaas, editors, *Bio-Implant Interface*. CRC Press, April 2003.

[174] A. D. Bach, J. P. Beier, J. Stern-Staeter, and R. E. Horch. Skeletal muscle tissue engineering. *Journal of Cellular and Molecular Medicine*, 8(4):413–422, 2004.

[175] Shulamit Levenberg, Jeroen Rouwkema, Mara Macdonald, Evan S. Garfein, Daniel S. Kohane, Diane C. Darland, Robert Marini, Clemens A. van Blitterswijk, Richard C. Mulligan, Patricia A. D'Amore, and Robert Langer. Engineering vascularized skeletal muscle tissue. *Nature Biotechnology*, 23(7):879–884, 2005.

[176] Juliet H.A. Bell and John W. Haycock. Next generation nerve guides: Materials, fabrication, growth factors, and cell delivery. *Tissue Engineering Part B: Reviews*, 18(2):116–128, 2012.

[177] Ravi V. Bellamkonda. Peripheral nerve regeneration: an opinion on channels, scaffolds and anisotropy. *Biomaterials*, 27(19):3515–3518, 2006.

[178] S. Hall. The response to injury in the peripheral nervous system. *Journal of Bone & Joint Surgery, British Volume*, 87-B(10):1309–1319, 2005. PMID: 16189300.

[179] Aleesha McCormick and Nic Leipzig. Neural regenerative strategies incorporating biomolecular axon guidance signals. *Annals of Biomedical Engineering*, 40(3):578–597, 2012.

[180] Alexander R. Nectow, Kacey G. Marra, and David L. Kaplan. Biomaterials for the development of peripheral nerve guidance conduits. *Tissue Engineering Part B: Reviews*, 18(1):40–50, 2012.

[181] Gustav Lind, Cecilia Eriksson Linsmeier, and Jens Schouenborg. The density difference between tissue and neural probes is a key factor for glial scarring. *Scientific Reports*, 3, 2013.

[182] Jonathan Wolpaw and Elizabeth Winter Wolpaw. *Brain-Computer Interfaces: Principles and Practice*. Oxford University Press, 2012.

[183] William M. Reichert. *Indwelling Neural Implants: Strategies for Contending with the In Vivo Environment*. CRC Press, 2007.

[184] Dennis E. Discher, Paul Janmey, and Yu-li Wang. Tissue cells feel and respond to the stiffness of their substrate. *Science*, 310(5751):1139–1143, 2005.

[185] Bradley W. Tuft, Lichun Zhang, Linjing Xu, Austin Hangartner, Braden Leigh, Marlan R. Hansen, and C. Allan Guymon. Material stiffness effects on neurite alignment to photopolymerized micropatterns. *Biomacromolecules*, 15(10):3717–3727, 2014.

[186] Lisa A. Flanagan, Yo-El Ju, Beatrice Marg, Miriam Osterfield, and Paul A. Janmey. Neurite branching on deformable substrates. *Neuroreport*, 13(18):2411–2415, 2002.

[187] André Colas and Jim Curtis. Silicone biomaterials: History and chemistry. In Buddy D. Ratner, Allan Hoffman, Frederick J Schoen, and Jack E Lemons, editors, *Biomaterials Science*, pages 80–86. Elsevier, 2 edition, 2004.

[188] Andre Colas and Jim Curtis. Silicone biomaterials: History and chemistry. In Buddy D. Ratner, Allan S. Hoffmann, Fredrick J. Schoen, and Jack E. Lemons, editors, *Biomaterials Science: An introduction to materials in medicine*, pages 80–86. Elsevier Academic Press, 2 edition, 2004.

[189] Andre Colas and Jim Curtis. Medical applications of silicones. In Buddy D. Ratner, Allan S. Hoffmann, Fredrick J. Schoen, and Jack E. Lemons, editors, *Biomaterials Science: An introduction to materials in medicine*, pages 697–707. Elsevier Academic Press, 2 edition, 2004.

[190] Paul Weiss. In vitro experiments on the factors determining the course of the outgrowing nerve fiber. *Journal of Experimental Zoology*, 68(3):393–448, 1934.

[191] Paul Weiss. Experiments on cell and axon orientation in vitro: The role of colloidal exudates in tissue organization. *Journal of Experimental Zoology*, 100(3):353–386, 1945.

[192] P. Roach, T. Parker, N. Gadegaard, and M. R. Alexander. Surface strategies for control of neuronal cell adhesion: A review. *Surface Science Reports*, 65(6):145–173, 2010.

[193] Adam Curtis and Chris Wilkinson. Topographical control of cells. *Biomaterials*, 18(24):1573–1583, 1997.

[194] Deok-Ho Kim, Paolo P. Provenzano, Chris L. Smith, and Andre Levchenko. Matrix nanotopography as a regulator of cell function. *The Journal of Cell Biology*, 197(3):351–360, 2012. PMID: 22547406.

[195] Saida Khan and Golam Newaz. A comprehensive review of surface modification for neural cell adhesion and patterning. *Journal of Biomedical Materials Research Part A*, 93A(3):1209–1224, 2010.

[196] Diane Hoffman-Kim, Jennifer A Mitchel, and Ravi V Bellamkonda. Topography, cell response, and nerve regeneration. *Annual review of biomedical engineering*, 12:203–231, 2010.

[197] Y. W Fan, F. Z Cui, L. N Chen, Y Zhai, Q. Y Xu, and I-S Lee. Adhesion of neural cells on silicon wafer with nano-topographic surface. *Applied Surface Science*, 187(3–4):313–318, 2002.

[198] Vittoria Raffa, Virginia Pensabene, Arianna Menciassi, and Paolo Dario. Design criteria of neuron/electrode interface. the focused ion beam technology as an analytical method to investigate the effect of electrode surface morphology on neurocompatibility. *Biomedical Microdevices*, 9(3):371–383, 2007.

[199] K.A. Moxon, N.M. Kalkhoran, M. Markert, M.A. Sambito, J.L. McKenzie, and J.T. Webster. Nanostructured surface modification of ceramic-based microelectrodes to enhance biocompatibility for a direct brain-machine interface. *IEEE Transactions on Bio-Medical Engineering*, 51(6):881–889, 2004.

[200] Y. W. Fan, F. Z. Cui, L. N. Chen, Y. Zhai, and Q. Y. Xu. Improvement of neural cell adherence to silicon surface by hydroxyl ion implantation. *Surface and Coatings Technology*, 131(1-3):355–359, 2000.

[201] E.A. Blakely, K.A. Bjornstad, J.E. Galvin, O.R. Monteiro, and I.G. Brown. Selective neuron growth on ion implanted and plasma deposited surfaces. In *The 29th IEEE International Conference on Plasma Science*, pages 253–, 2002.

[202] Xinyan Cui, Valerie A. Lee, Yehoash Raphael, James A. Wiler, Jamille F. Hetke, David J. Anderson, and David C. Martin. Surface modification of neural recording electrodes with conducting polymer/biomolecule blends. *Journal of Biomedical Materials Research*, 56(2):261–272, 2001.

[203] Bo Zhu, Shyh-Chyang Luo, Haichao Zhao, Hsing-An Lin, Jun Sekine, Aiko Nakao, Chi Chen, Yoshiro Yamashita, and Hsiao-hua Yu. Large enhancement in neurite outgrowth on a cell membrane-mimicking conducting polymer. *Nature Communications*, 5, 2014.

[204] Natalia Gomez and Christine E. Schmidt. Nerve growth factor-immobilized polypyrrole: Bioactive electrically conducting polymer for enhanced neurite extension. *Journal of biomedical materials research. Part A*, 81(1):135–149, 2007.

[205] Pouria Fattahi, Guang Yang, Gloria Kim, and Mohammad Reza Abidian. A review of organic and inorganic biomaterials for neural interfaces. *Advanced Materials*, 26(12):1846–1885, 2014.

[206] Murali Naidu. The role of cells, neurotrophins, extracellular matrix and cell surface molecules in peripheral nerve regeneration. *The Malaysian Journal of Medical Sciences : MJMS*, 16(2):10–14, 2009.

[207] Raghu Kalluri. Basement membranes: structure, assembly and role in tumour angiogenesis. *Nature Reviews Cancer*, 3(6):422–433, 2003.

[208] Rudolf Martini. Expression and functional roles of neural cell surface molecules and extracellular matrix components during development and regeneration of peripheral nerves. *Journal of Neurocytology*, 23(1):1–28, 1994.

[209] Nicholas A. Kefalides and Jacques P. Borel. Structural macromolecules: Laminins, Entactin/Nidogen, and proteoglycans (Perlecan, agrin). In Nicholas A. Kefalides and Jacques P. Borel, editors, *Current Topics in Membranes*, volume Volume 56, pages 147–197. Academic Press, 2005.

[210] Shirley Ayad. *The Extracellular Matrix Factsbook*. Academic Press, 1998.

[211] Rupert Timpl. Nidogen. In Thomas Kreis and Ronald Vale, editors, *Guidebook to the Extracellular Matrix, Anchor, and Adhesion Proteins*, pages 455–457. Oxford University Press, Oxford, 2 edition, 1999.

[212] Kefalides Nicholas A. and Borel Jacques P. The early years of basement membrane research. In Nicholas A. Kefalides and Jacques P. Borel, editors, *Current Topics in Membranes*, volume Volume 56, pages 3–18. Academic Press, 2005.

[213] Monique Aumailley, Leena Bruckner-Tuderman, William G. Carter, Rainer Deutzmann, David Edgar, Peter Ekblom, Jürgen Engel, Eva Engvall, Erhard Hohenester, Jonathan C. R. Jones, Hynda K. Kleinman, M. Peter Marinkovich, George R. Martin, Ulrike Mayer, Guerrino Meneguzzi, Jeffrey H. Miner, Kaoru Miyazaki, Manuel Patarroyo, Mats Paulsson, Vito Quaranta, Joshua R. Sanes, Takako Sasaki, Kiyotoshi Sekiguchi, Lydia M. Sorokin, Jan F. Talts, Karl Tryggvason, Jouni Uitto, Ismo Virtanen, Klaus von der Mark, Ulla M. Wewer, Yoshihiko Yamada, and Peter D. Yurchenco. A simplified laminin nomenclature. *Matrix Biology*, 24(5):326–332, 2005.

[214] Wilhelm Wallquist, Stefan Plantman, Sebastian Thams, Jill Thyboll, Jarkko Kortesmaa, Jan Lännergren, Anna Domogatskaya, Sven Ove Ogren, Mårten Risling, Henrik Hammarberg, Karl Tryggvason, and Staffan Cullheim. Impeded interaction between schwann cells and axons in the absence of laminin alpha4. *The Journal of neuroscience*, 25(14):3692–3700, 2005.

[215] James B Phillips, Stephen C J Bunting, Susan M Hall, and Robert A Brown. Neural tissue engineering: a self-organizing collagen guidance conduit. *Tissue engineering*, 11(9-10):1611–1617, 2005.

[216] Marithea Smit, Jay Leng, and Richard L. Klemke. Assay for neurite outgrowth quantification. *BioTechniques*, 35(2):254–256, 2003.

[217] R. J. Geraghty, A. Capes-Davis, J. M. Davis, J. Downward, R. I. Freshney, I. Knezevic, R. Lovell-Badge, J. R. W. Masters, J. Meredith, G. N. Stacey, P. Thraves, and M. Vias. Guidelines for the use of cell lines in biomedical research. *British Journal of Cancer*, 111(6):1021–1046, 2014.

[218] Lucio G. Costa and Gennaro Giordano. Primary Neurons in Culture and Neuronal Cell Lines for In Vitro Neurotoxicological Studies. In Marina Guizzetti, Lucio G. Costa, and Gennaro Giordano, editors, *In Vitro Neurotoxicology*, number 758 in Methods in Molecular Biology, pages 13–27. Humana Press, 2011.

[219] Giorgia Melli and Ahmet Höke. Dorsal root ganglia sensory neuronal cultures: a tool for drug discovery for peripheral neuropathies. *Expert opinion on drug discovery*, 4(10):1035–1045, 2009.

[220] Shields Warren and Rosanna N. Chute. Pheochromocytoma. *Cancer*, 29(2):327–331, 1972.

[221] L. A. Greene and A. S. Tischler. Establishment of a noradrenergic clonal line of rat adrenal pheochromocytoma cells which respond to nerve growth factor. *Proceedings of the National Academy of Sciences*, 73(7):2424–2428, 1976.

[222] Rylie A. Green, Nigel H. Lovell, and Laura A. Poole-Warren. Cell attachment functionality of bioactive conducting polymers for neural interfaces. *Biomaterials*, 30(22):3637–3644, 2009.

[223] Gymama E Slaughter, Erhard Bieberich, Gary E Wnek, Kenneth J Wynne, and Anthony Guiseppi-Elie. Improving neuron-to-electrode surface attachment via alkanethiol self-assembly: an alternating current impedance study. *Langmuir*, 20(17):7189–7200, 2004. PMID: 15301505.

[224] K. A. Moxon, S. Hallman, A. Aslani, N. M. Kalkhoran, and P. I. Lelkes. Bioactive properties of nanostructured porous silicon for enhancing electrode to neuron interfaces. *Journal of Biomaterials Science, Polymer Edition*, 18(10):1263–1281, 2007.

[225] Aviad Hai, Ada Dormann, Joseph Shappir, Shlomo Yitzchaik, Carmen Bartic, Gustaaf Borghs, J. P. M. Langedijk, and Micha E. Spira. Spine-shaped gold protrusions improve the adherence and electrical coupling of neurons with the surface of micro-electronic devices. *Journal of The Royal Society Interface*, 6(41):1153 –1165, 2009.

[226] Uta Reich, Elena Fadeeva, Athanasia Warnecke, Gerrit Paasche, Peter Müller, Boris Chichkov, Timo Stöver, Thomas Lenarz, and Günter Reuter. Directing neuronal cell growth on implant material surfaces by microstructuring. *Journal of biomedical materials research. Part B, Applied biomaterials*, 100(4):940–947, 2012. PMID: 22287482.

[227] Todd A Kuiken, Guanglin Li, Blair A Lock, Robert D Lipschutz, Laura A Miller, Kathy A Stubblefield, and Kevin B Englehart. Targeted muscle reinnervation for real-time myoelectric control of multifunction artificial arms. *JAMA*, 301(6):619–628, 2009.

[228] John B. Hijjawi, Todd A. Kuiken, Robert D. Lipschutz, Laura A. Miller, Kathy A. Stubblefield, and Gregory A. Dumanian. Improved myoelectric prosthesis control accomplished using multiple nerve transfers. *Plastic and Reconstructive Surgery*, 118(7):1573–1578, 2006.

[229] Reuben A. Bueno, Brooke French, Damon Cooney, and Michael W. Neumeister. Targeted muscle reinnervation of a muscle-free flap for improved prosthetic control in a shoulder amputee: case report. *The Journal of Hand Surgery*, 36(5):890–893, 2011.

[230] Theodore A. Kung, Nicholas B. Langhals, David C. Martin, Philip J. Johnson, Paul S. Cederna, and Melanie G. Urbanchek. Regenerative peripheral nerve interface viability and signal transduction with an implanted electrode. *Plastic and Reconstructive Surgery*, 133(6):1380–1394, 2014.

[231] Nicholas Langerhals, John Larson, Theodore A. Kung, Kristoffer Sugg, Jana Moon, Paul S. Cederna, and Melanie G. Urbanchek. Biomaterials and electrode strategies in regenerative peripheral nerve interfaces. In *Society for Biomaterials Annual Meeting*, page 223, Boston, MA, 2013.

[232] J.S. Hebert, J.L. Olson, M.J. Morhart, M.R. Dawson, P.D. Marasco, T.A Kuiken, and K.M. Chan. Novel targeted sensory reinnervation technique to restore functional hand sensation after transhumeral amputation. *IEEE Transactions on Neural Systems and Rehabilitation Engineering*, 22(4):765–773, 2014.

[233] Max Ortiz-Catalan, Bo Håkansson, and Rickard Brånemark. An osseointegrated human-machine gateway for long-term sensory feedback and motor control of artificial limbs. *Science Translational Medicine*, 6(257):257re6–257re6, 2014.

[234] Moo Sung Chae, Zhi Yang, Mehmet R. Yuce, Linh Hoang, and Wentai Liu. A 128-channel 6 mW wireless neural recording IC with spike feature extraction and UWB transmitter. *IEEE transactions on neural systems and rehabilitation engineering*, 17(4):312–321, 2009.

[235] Henry Lancashire. *Implantable Electrodes for Prosthetic Control.* MRes thesis, University College London, London, 2011.

[236] Stewe Jönsson, Kerstin Caine-Winterberger, and Rickard Brånemark. Osseointegration amputation prostheses on the upper limbs: methods, prosthetics and rehabilitation. *Prosthetics and Orthotics International*, 35(2):190–200, 2011.

[237] Norbert V Kang, Catherine Pendegrass, Linda Marks, and Gordon Blunn. Osseocutaneous integration of an intraosseous transcutaneous amputation prosthesis implant used for reconstruction of a transhumeral amputee: case report. *The Journal of Hand Surgery*, 35(7):1130–1134, 2010. PMID: 20541327.

[238] M. Pitkin. Design features of implants for direct skeletal attachment of limb prostheses. *Journal of Biomedical Materials Research - Part A*, 101(11):3339–3348, 2013.

[239] Noel Fitzpatrick, Thomas J. Smith, Catherine J. Pendegrass, Russell Yeadon, Michael Ring, Allen E. Goodship, and Gordon W. Blunn. Intraosseous transcutaneous amputation prosthesis (ITAP) for limb salvage in 4 dogs. *Veterinary Surgery*, 40(8):909–925, 2011.

[240] Catherine J Pendegrass, Allen E Goodship, and Gordon W Blunn. Development of a soft tissue seal around bone-anchored transcutaneous amputation prostheses. *Biomaterials*, 27(23):4183–4191, August 2006.

[241] M Pitkin, C Cassidy, R Muppavarapu, and D Edell. Recording of electric signal passing through a pylon in direct skeletal attachment of leg prostheses with neuromuscular control. *IEEE Transactions on Bio-Medical Engineering*, 59(5):1349–1353, 2012. PMID: 22345523.

[242] Features - i-limb ultra, 2014.

[243] S.A. Dalley, H.A. Varol, and M. Goldfarb. Multigrasp myoelectric control for a transradial prosthesis. In *IEEE International Conference on Rehabilitation Robotics*, pages 1–6, 2011.

[244] M. B. I. Reaz, M. S. Hussain, and F. Mohd-Yasin. Techniques of EMG signal analysis: detection, processing, classification and applications. *Biological Procedures Online*, 8(1):11–35, 2006.

[245] J.M. Hahne, F. Biebmann, N. Jiang, H. Rehbaum, D. Farina, F.C. Meinecke, K.-R. Muller, and L.C. Parra. Linear and nonlinear regression techniques for simultaneous and proportional

myoelectric control. *IEEE Transactions on Neural Systems and Rehabilitation Engineering*, 22(2):269–279, 2014.

[246] N. Jiang, H. Rehbaum, I. Vujaklija, B. Graimann, and D. Farina. Intuitive, online, simultaneous and proportional myoelectric control over two degrees of freedom in upper limb amputees. *IEEE Transactions on Neural Systems and Rehabilitation Engineering*, Early Access Online, 2014.

[247] P Parker, K Englehart, and B Hudgins. Myoelectric signal processing for control of powered limb prostheses. *Journal of Electromyography and Kinesiology*, 16(6):541–548, 2006. PMID: 17045489.

[248] Aaron J. Young, Lauren H. Smith, Elliott J. Rouse, and Levi J. Hargrove. A comparison of the real-time controllability of pattern recognition to conventional myoelectric control for discrete and simultaneous movements. *Journal of NeuroEngineering and Rehabilitation*, 11(1):5, 2014.

[249] J.P. Uhlir, R.J. Triolo, J.A. Davis, and C. Bieri. Performance of epimysial stimulating electrodes in the lower extremities of individuals with spinal cord injury. *IEEE Transactions on Neural Systems and Rehabilitation Engineering*, 12(2):279–287, 2004.

[250] Isabel Arcos, R. Davis, K. Fey, D. Mishler, D. Sanderson, C. Tanacs, M.j. Vogel, R. Wolf, Y. Zilberman, and J. Schulman. Second-generation microstimulator. *Artificial Organs*, 26(3):228–231, 2002.

[251] Gianluca de Luca. Fundamental concepts in EMG signal acquisition. Technical Report Rev. 2.1, DelSys Inc, 2003.

[252] Jeffrey C. Ives and Janet K. Wigglesworth. Sampling rate effects on surface EMG timing and amplitude measures. *Clinical Biomechanics*, 18(6):543–552, 2003.

[253] Justin J. Baker, Erik Scheme, Kevin Englehart, Douglas T. Hutchinson, and Bradley Greger. Continuous detection and decoding of dexterous finger flexions with implantable myoelectric sensors. *IEEE transactions on neural systems and rehabilitation engineering*, 18(4):424–432, 2010.

[254] Theodore A. Kung, Reuben A. Bueno, Ghadah K. Alkhalefah, Nicholas B. Langhals, Melanie G. Urbanchek, and Paul S. Cederna. Innovations in prosthetic interfaces for the upper extremity. *Plastic and Reconstructive Surgery*, 132(6):1515–1523, 2013.

[255] Michael C Park, Abderraouf Belhaj-Saif, and Paul D Cheney. Chronic recording of EMG activity from large numbers of forelimb muscles in awake macaque monkeys. *Journal of Neuroscience Methods*, 96(2):153–160, 2000.

[256] Heather M. Hudson, Darcy M. Griffin, Abderraouf Belhaj-Saïf, Sang-Pil Lee, and Paul D. Cheney. Methods for chronic recording of EMG activity from large numbers of hindlimb muscles in awake rhesus macaques. *Journal of Neuroscience Methods*, 189(2):153–161, 2010.

[257] A.M. Sodagar, G.E. Perlin, Ying Yao, K. Najafi, and K.D. Wise. An implantable 64-channel wireless microsystem for single-unit neural recording. *IEEE Journal of Solid-State Circuits*, 44(9):2591–2604, 2009.

[258] D. Farina, Winnie Jensen, and Metin Akay, editors. *Introduction to Neural Engineering for Motor Rehabilitation*. IEEE Press, Hoboken, NJ, USA, 2013.

[259] Kerstin Hagberg, Eva Häggström, Stewe Jönsson, Björn Rydevik, and Rickard Brånemark. Osseoperception and osseointegrated prosthetic limbs. In Pamela Gallagher, Deirdre Desmond, and Malcolm MacLachlan, editors, *Psychoprosthetics*, pages 131–140. Springer London, 2008.

[260] Daniel Van Steenberghe. From osseointegration to osseoperception. *Journal of Dental Research*, 79(11):1833–1837, 2000.

[261] K. Hagberg, E. Häggström, M. Uden, and R. Brånemark. Socket versus bone-anchored transfemoral prostheses: Hip range of motion and sitting comfort. *Prosthetics and Orthotics International*, 29(2):153–163, 2005.

[262] Jonatan Tillander, Kerstin Hagberg, Lars Hagberg, and Rickard Brånemark. Osseointegrated titanium implants for limb prostheses attachments: Infectious complications. *Clinical Orthopaedics and Related Research®*, 468(10):2781–2788, 2010.

[263] Georgios Tsikandylakis, Örjan Berlin, and Rickard Brånemark. Implant survival, adverse events, and bone remodeling of osseointegrated percutaneous implants for transhumeral amputees. *Clinical Orthopaedics and Related Research®*, pages 1–10, 2014.

[264] M. J. Allen, J. E. F. Houlton, S. B. Adams, and N. Rushton. The surgical anatomy of the stifle joint in sheep. *Veterinary Surgery*, 27(6):596–605, 1998.

[265] Abhishek Prasad and Justin C Sanchez. Quantifying long-term microelectrode array functionality using chronic in vivo impedance testing. *Journal of Neural Engineering*, 9(2):026028, 2012.

[266] Johnes and other wasting diseases in sheep, 2014.

[267] R. Munoz, L. Leija, Ja. Alvarez, J. L. Reyes, J. Flores, Pablo-Ro. Hedz, A. Minor, and G. Sierra. Evaluation of electrical impedance of pt–ir epimysial electrodes under implantation in muscles. *Sensors and Actuators A: Physical*, 101(1–2):117–122, 2002.

[268] Lindsay Kathleen Newcombe and Michael Ernest Dewar. Prosthetic limb attachment. Patent, 2005. WO2005087145 A1.

[269] Madeleine M. Lowery, Nikolay S. Stoykov, Allen Taflove, and Todd A. Kuiken. A multiple-layer finite-element model of the surface EMG signal. *IEEE transactions on bio-medical engineering*, 49(5):446–454, 2002.

[270] J.P.P van Vugt and J.G van Dijk. A convenient method to reduce crosstalk in surface EMG. *Clinical Neurophysiology*, 112(4):583–592, 2001.

[271] F. Mandrile, D. Farina, M. Pozzo, and R. Merletti. Stimulation artifact in surface EMG signal: effect of the stimulation waveform, detection system, and current amplitude using hybrid stimulation technique. *IEEE Transactions on Neural Systems and Rehabilitation Engineering*, 11(4):407–415, 2003.

[272] L.H. Smith and L.J. Hargrove. Intramuscular EMG after targeted muscle reinnervation for pattern recognition control of myoelectric prostheses. In *6th International IEEE/EMBS Conference on Neural Engineering*, pages 1155–1158, 2013.

[273] Todd A. Kuiken, Aimee E. Schultz Feuser, and Ann K. Barlow. *Targeted Muscle Reinnervation: A Neural Interface for Artificial Limbs*. CRC Press, Boca Raton, 1 edition edition, 2013.

[274] Todd A Kuiken, Laura A Miller, Robert D Lipschutz, Blair A Lock, Kathy Stubblefield, Paul D Marasco, Ping Zhou, and Gregory A Dumanian. Targeted reinnervation for enhanced prosthetic arm function in a woman with a proximal amputation: a case study. *The Lancet*, 369(9559):371–380, 2007.

[275] Samuel C. Lien, Paul S. Cederna, and William M. Kuzon Jr. Optimizing skeletal muscle reinnervation with nerve transfer. *Hand Clinics*, 24(4):445–454, 2008.

[276] P. S. Cederna, M. K. Youssef, H. Asato, M. G. Urbanchek, and W. M. Kuzon. Skeletal muscle reinnervation by reduced axonal numbers results in whole muscle force deficits. *Plastic and Reconstructive Surgery*, 105(6):2003–2009; discussion 2010–2011, 2000.

[277] S. Y. Fu and T. Gordon. Contributing factors to poor functional recovery after delayed nerve repair: prolonged axotomy. *The Journal of Neuroscience*, 15(5):3876–3885, 1995.

[278] J. C. Baldi, R. D. Jackson, R. Moraille, and W. J. Mysiw. Muscle atrophy is prevented in patients with acute spinal cord injury using functional electrical stimulation. *Spinal Cord*, 36(7):463–469, 1998.

[279] Masaru Kawabuchi, Huibing Tan, and Songyan Wang. Age affects reciprocal cellular interactions in neuromuscular synapses following peripheral nerve injury. *Ageing Research Reviews*, 10(1):43–53, 2011.

[280] Hyuno Kang and Jeff W. Lichtman. Motor axon regeneration and muscle reinnervation in young adult and aged animals. *The Journal of Neuroscience*, 33(50):19480–19491, 2013.

[281] R. Branemark, O Berlin, K. Hagberg, P. Bergh, B. Gunterberg, and B. Rydevik. A novel osseointegrated percutaneous prosthetic system for the treatment of patients with transfemoral amputation a prospective study of 51 patients. *Bone & Joint Journal*, 96-B(1):106–113, 2014.

[282] N. Jiang, I. Vujaklija, H. Rehbaum, B. Graimann, and D. Farina. Is accurate mapping of EMG signals on kinematics needed for precise online myoelectric control? *IEEE Transactions on Neural Systems and Rehabilitation Engineering*, Early Access Online, 2014.

[283] S. Muceli, Ning Jiang, and D. Farina. Extracting signals robust to electrode number and shift for online simultaneous and proportional myoelectric control by factorization algorithms. *IEEE Transactions on Neural Systems and Rehabilitation Engineering*, 22(3):623–633, 2014.

[284] E.N. Kamavuako, J.C. Rosenvang, R. Horup, W. Jensen, D. Farina, and K.B. Englehart. Surface versus untargeted intramuscular EMG based classification of simultaneous and dynamically changing movements. *IEEE Transactions on Neural Systems and Rehabilitation Engineering*, 21(6):992–998, 2013.

[285] P. E. K. Donaldson. The craggs connector; a termination for cooper cable. *Medical and Biological Engineering and Computing*, 23(2):195–196, 1985.

[286] Maria Siemionow and Grzegorz Brzezicki. Chapter 8 current techniques and concepts in peripheral nerve repair. In Stefano Geuna, Pierluigi Tos, and Bruno Battiston, editors, *International Review of Neurobiology*, volume Volume 87, pages 141–172. Academic Press, 2009.

[287] Kshitija Garde, Edward Keefer, Barry Botterman, Pedro Galvan, and Mario I. Romero. Early interfaced neural activity from chronic amputated nerves. *Frontiers in Neuroengineering*, 2:5, 2009.

[288] Natalia Lago and Xavier Navarro. Evaluation of the long-term regenerative potential in an experimental nerve amputee model. *Journal of the Peripheral Nervous System*, 12(2):108–120, 2007. PMID: 17565536.

[289] David J Edell. Insulating biomaterials. In Kenneth W Horch, Gurpreet S Dhillon, and John K-J Li, editors, *Neuroprosthetics: Theory and Practice*, volume 2 of *Series on Bioengineering and Biomedical Engineering*, pages 517–579. World Scientific, Singapore, 2004.

[290] Hynda K. Kleinman and George R. Martin. Matrigel: Basement membrane matrix with biological activity. *Seminars in Cancer Biology*, 15(5):378–386, 2005.

[291] Renato Donzelli, Francesco Maiuri, Gennaro Andrea Piscopo, Matteo de Notaris, Andrea Colella, and Enricode Divitiis. Role of extracellular matrix components in facial nerve regeneration: an experimental study. *Neurological research*, 28(8):794–801, 2006. PMID: 17288733.

[292] D.A. Tonge, J.P. Golding, M. Edbladh, M. Kroon, P.E.R. Ekström, and A. Edström. Effects of extracellular matrix components on axonal outgrowth from peripheral nerves of adult animalsin vitro. *Experimental Neurology*, 146(1):81–90, 1997.

[293] Eve C. Tsai, Paul D. Dalton, Molly S. Shoichet, and Charles H. Tator. Matrix inclusion within synthetic hydrogel guidance channels improves specific supraspinal and local axonal regeneration after complete spinal cord transection. *Biomaterials*, 27(3):519–533, 2006.

[294] Slobodan Vukicevic, Hynda K. Kleinman, Frank P. Luyten, Anita B. Roberts, Nanette S. Roche, and A.H. Reddi. Identification of multiple active growth factors in basement membrane matrigel suggests caution in interpretation of cellular activity related to extracellular matrix components. *Experimental Cell Research*, 202(1):1–8, 1992.

[295] E. Polykandriotis, A. Arkudas, RE. Horch, and U. Kneser. To matrigel or not to matrigel. *The American Journal of Pathology*, 172(5):1441–1442, 2008.

[296] Chris S. Hughes, Lynne M. Postovit, and Gilles A. Lajoie. Matrigel: A complex protein mixture required for optimal growth of cell culture. *PROTEOMICS*, 10(9):1886–1890, 2010.

[297] Peter D. Yurchenco and Bruce L. Patton. Developmental and pathogenic mechanisms of basement membrane assembly. *Current pharmaceutical design*, 15(12):1277–1294, 2009.

[298] A Joester and A Faissner. The structure and function of tenascins in the nervous system. *Matrix biology: journal of the International Society for Matrix Biology*, 20(1):13–22, 2001. PMID: 11246000.

[299] Hynda K. Kleinman, Mary L. McGarvey, John R. Hassell, Vicki L. Star, Frances B. Cannon, Gordon W. Laurie, and George R. Martin. Basement membrane complexes with biological activity. *Biochemistry*, 25(2):312–318, 1986.

[300] W.V. Soussou, G.J. Yoon, R.D. Brinton, and T.W. Berger. Neuronal network morphology and electrophysiologyof hippocampal neurons cultured on surface-treated multielectrode arrays. *IEEE Transactions on Biomedical Engineering*, 54(7):1309–1320, 2007.

[301] B L Patton. Laminins of the neuromuscular system. *Microscopy research and technique*, 51(3):247–261, 2000.

[302] K. Ehrig, I. Leivo, W. S. Argraves, E. Ruoslahti, and E. Engvall. Merosin, a tissue-specific basement membrane protein, is a laminin-like protein. *Proceedings of the National Academy of Sciences*, 87(9):3264–3268, January 1990. PMID: 2185464.

[303] María-Carolina Paez, María-Julieta Gonzalez, Norma C Serrano, Yehuda Shoenfeld, and Juan-Manuel Anaya. Physiological and pathological implications of laminins: from the gene to the protein. *Autoimmunity*, 40(2):83–94, 2007. PMID: 17453709.

[304] S Y Seo, S-K Min, H K Bae, D Roh, H K Kang, S Roh, S Lee, G-S Chun, D-J Chung, and B-M Min. A laminin-2-derived peptide promotes early-stage peripheral nerve regeneration in a dual-component artificial nerve graft. *Journal of tissue engineering and regenerative medicine*, 2012. PMID: 22438104.

[305] Charles E. Dumont and Walter Born. Stimulation of neurite outgrowth in a human nerve scaffold designed for peripheral nerve reconstruction. *Journal of Biomedical Materials Research Part B: Applied Biomaterials*, 73B(1):194–202, 2005.

[306] Pejman Naghdi, Taki Tiraihi, Fariba Ganji, Shehram Darabi, Taher Taheri, and Hadi Kazemi. Survival, proliferation and differentiation enhancement of neural stem cells cultured in three-dimensional polyethylene glycol–RGD hydrogel with tenascin. *Journal of Tissue Engineering and Regenerative Medicine*, October 2014.

[307] E. Ruoslahti. RGD and other recognition sequences for integrins. *Annual Review of Cell and Developmental Biology*, 12:697–715, 1996.

[308] Fabio Quondamatteo. Assembly, stability and integrity of basement membranes in vivo. *The Histochemical Journal*, 34(8-9):369–381, 2002.

[309] Bjorn R Olsen and Yoshifumi Ninomiya. Basement membrane collagens. In Thomas Kreis and Ronald Vale, editors, *Guidebook to the Extracellular Matrix, Anchor, and Adhesion Proteins*, pages 395–398. Oxford University Press, Oxford, 2 edition, 1999.

[310] Takako Sasaki and Rupert Timpl. Laminins. In Thomas Kreis and Ronald Vale, editors, *Guidebook to the Extracellular Matrix, Anchor, and Adhesion Proteins*, pages 434–443. Oxford University Press, Oxford, 2 edition, 1999.

[311] Soon Eon Bae, Suk Ho Bhang, Byung-Soo Kim, and Kwideok Park. Self-assembled extracellular macromolecular matrices and their different osteogenic potential with preosteoblasts and rat bone marrow mesenchymal stromal cells. *Biomacromolecules*, 13(9):2811–2820, 2012.

[312] John M. Walker. The bicinchoninic acid (BCA) assay for protein quantitation. In John M. Walker, editor, *The Protein Protocols Handbook*, Springer Protocols Handbooks, pages 11–15. Humana Press, 2009.

[313] Christine V. Sapan, Roger L. Lundblad, and Nicholas C. Price. Colorimetric protein assay techniques. *Biotechnology and Applied Biochemistry*, 29(2):99–108, 1999.

[314] Sigma and ECACC. *Fundamental Techniques in Cell Culture Laboratory Handbook*. Sigma-Aldrich, St. Louis, MO, 2 edition, 2010.

[315] Furqan Haq, Charles Keith, and Guigen Zhang. Neurite development in PC12 cells on flexible micro-textured substrates under cyclic stretch. *Biotechnology Progress*, 22(1):133–140, 2006.

[316] David E. Burstein and Lloyd A. Greene. Evidence for RNA synthesis-dependent and -independent pathways in stimulation of neurite outgrowth by nerve growth factor. *Proceedings of the National Academy of Sciences*, 75(12):6059–6063, 1978.

[317] Caroline A. Schneider, Wayne S. Rasband, and Kevin W. Eliceiri. NIH image to ImageJ: 25 years of image analysis. *Nature Methods*, 9(7):671–675, 2012.

[318] Johannes Schindelin, Ignacio Arganda-Carreras, Erwin Frise, Verena Kaynig, Mark Longair, Tobias Pietzsch, Stephan Preibisch, Curtis Rueden, Stephan Saalfeld, Benjamin Schmid, Jean-Yves Tinevez, Daniel James White, Volker Hartenstein, Kevin Eliceiri, Pavel Tomancak, and Albert Cardona. Fiji: an open-source platform for biological-image analysis. *Nature Methods*, 9(7):676–682, 2012.

[319] Sture Holm. A simple sequentially rejective multiple test procedure. *Scandinavian Journal of Statistics*, 6(2):65–70, 1979.

[320] R. D. K. Misra and C. Nune. Biological response to self-assembly of preadsorbed proteins at biointerfaces: significance, cellular activity and perspective. *Materials Technology: Advanced Biomaterials*, 1(1):B41–B48, 2013.

[321] Tugba Akkas, Cansu Citak, Ahmet Sirkecioglu, and F Seniha Güner. Which is more effective for protein adsorption: surface roughness, surface wettability or swelling? case study of polyurethane films prepared from castor oil and poly(ethylene glycol). *Polymer International*, 62(8):1202–1209, 2013.

[322] C A Middleton, C J Pendegrass, D Gordon, J Jacob, and G W Blunn. Fibronectin silanized titanium alloy: a bioinductive and durable coating to enhance fibroblast attachment in vitro. *Journal of Biomedical Materials Research. Part A*, 83(4):1032–1038, 2007.

[323] D.W. Branch, B.C. Wheeler, G.J. Brewer, and D.E. Leckband. Long-term maintenance of patterns of hippocampal pyramidal cells on substrates of polyethylene glycol and microstamped polylysine. *IEEE Transactions on Biomedical Engineering*, 47(3):290–300, 2000.

[324] M. Chimutengwende-Gordon, C. Pendegrass, and G. Blunn. Enhancing the soft tissue seal around intraosseous transcutaneous amputation prostheses using silanized fibronectin titanium alloy. *Biomedical Materials*, 6(2):025008, 2011.

[325] Bradley J.S.C. Olson and John Markwell. Assays for determination of protein concentration. In *Current Protocols in Protein Science*. John Wiley & Sons, Inc., 2001.

[326] Krishnan K. Chittur. FTIR/ATR for protein adsorption to biomaterial surfaces. *Biomaterials*, 19(4–5):357–369, 1998.

[327] Tamar Shahal, Kathryn A. Melzak, Christopher R. Lowe, and Electra Gizeli. Poly(dimethylsiloxane)-coated sensor devices for the formation of supported lipid bilayers and the subsequent study of membrane interactions. *Langmuir*, 24(19):11268–11275, 2008.

[328] Esa Stenberg, Björn Persson, Håkan Roos, and Csaba Urbaniczky. Quantitative determination of surface concentration of protein with surface plasmon resonance using radiolabeled proteins. *Journal of Colloid and Interface Science*, 143(2):513–526, 1991.

[329] Hyun Kyoung Lee, In Ae Seo, Hye Kyung Park, Yoo Mi Park, Kyoung Jin Ahn, Young Hyun Yoo, and Hwan Tae Park. Nidogen is a prosurvival and promigratory factor for adult schwann cells. *Journal of Neurochemistry*, 102(3):686–698, 2007.

[330] K. J. Tomaselli, C. H. Damsky, and L. F. Reichardt. Interactions of a neuronal cell line (PC12) with laminin, collagen IV, and fibronectin: identification of integrin-related glycoproteins involved in attachment and process outgrowth. *The Journal of Cell Biology*, 105(5):2347–2358, 1987.

[331] Eric J. Berns, Shantanu Sur, Liuliu Pan, Joshua E. Goldberger, Sunitha Suresh, Shuming Zhang, John A. Kessler, and Samuel I. Stupp. Aligned neurite outgrowth and directed cell migration in self-assembled monodomain gels. *Biomaterials*, 35(1):185–195, 2014.

[332] Qiongjiao Yan, Yixia Yin, and Binbin Li. Use new PLGL-RGD-NGF nerve conduits for promoting peripheral nerve regeneration. *Biomedical engineering online*, 11:36, 2012.

[333] Ulrich Hersel, Claudia Dahmen, and Horst Kessler. RGD modified polymers: biomaterials for stimulated cell adhesion and beyond. *Biomaterials*, 24(24):4385–4415, 2003.

[334] Len Thomas. Retrospective power analysis. *Conservation Biology*, 11(1):276–280, 1997.

[335] John M Hoenig and Dennis M Heisey. The abuse of power: The pervasive fallacy of power calculations for data analysis. *The American Statistician*, 55(1):19–24, 2001.

[336] David Richard Schmidt, Heather Waldeck, and Weiyuan John Kao. Protein Adsorption to Biomaterials. In David A. Puleo and Rena Bizios, editors, *Biological Interactions on Materials Surfaces*, pages 1–18. Springer US, 2009.

[337] Stacey L Hirsh, David R McKenzie, Neil J Nosworthy, John A Denman, Osman U Sezerman, and Marcela M M Bilek. The vroman effect: competitive protein exchange with dynamic multilayer protein aggregates. *Colloids and surfaces. B, Biointerfaces*, 103:395–404, 2013. PMID: 23261559.

[338] Li Yao, Godard C.W. de Ruiter, Huan Wang, Andrew M. Knight, Robert J. Spinner, Michael J. Yaszemski, Anthony J. Windebank, and Abhay Pandit. Controlling dispersion of axonal regeneration using a multichannel collagen nerve conduit. *Biomaterials*, 31(22):5789–5797, 2010.

[339] C. Deister, S. Aljabari, and C.E. Schmidt. Effects of collagen 1, fibronectin, laminin and hyaluronic acid concentration in multi-component gels on neurite extension. *Journal of Biomaterials Science, Polymer Edition*, 18(8):983–997, 2007.

[340] Shreya Raghavan, Robert R. Gilmont, and Khalil N. Bitar. Neuroglial differentiation of adult enteric neuronal progenitor cells as a function of extracellular matrix composition. *Biomaterials*, 34(28):6649–6658, 2013.

[341] J A Richardson, C W Rementer, Jan M Bruder, and D Hoffman-Kim. Guidance of dorsal root ganglion neurites and schwann cells by isolated schwann cell topography on poly(dimethyl siloxane) conduits and films. *Journal of neural engineering*, 8(4):046015, 2011. PMID: 21673394.

[342] Yuanyuan Zhang, Yujiang He, Shantaram Bharadwaj, Nevin Hammam, Kristen Carnagey, Regina Myers, Anthony Atala, and Mark Van Dyke. Tissue-specific extracellular matrix coatings for the promotion of cell proliferation and maintenance of cell phenotype. *Biomaterials*, 30(23-24):4021–4028, 2009. PMID: 19410290.

[343] Marco Cecchini, Giorgia Bumma, Michela Serresi, and Fabio Beltram. PC12 differentiation on biopolymer nanostructures. *Nanotechnology*, 18(50):505103, 2007.

[344] M. Cecchini, A. Ferrari, and F. Beltram. PC12 polarity on biopolymer nanogratings. *Journal of Physics: Conference Series*, 100(1):012003, 2008.

[345] Paul Roach, Terrance Parker, Nikolaj Gadegaard, and Morgan R. Alexander. A bio-inspired neural environment to control neurons comprising radial glia, substrate chemistry and topography. *Biomaterials Science*, 1(1):83–93, 2012.

[346] Mingzhu Sun, Malachy McGowan, Paul J Kingham, Giorgio Terenghi, and Sandra Downes. Novel thin-walled nerve conduit with microgrooved surface patterns for enhanced peripheral nerve repair. *Journal of materials science. Materials in medicine*, 21(10):2765–2774, 2010. PMID: 20878209.

[347] P Clark, P Connolly, A S Curtis, J A Dow, and C D Wilkinson. Cell guidance by ultrafine topography in vitro. *Journal of cell science*, 99 (Pt 1):73–77, 1991. PMID: 1757503.

[348] P Clark, P Connolly, A S Curtis, J A Dow, and C D Wilkinson. Topographical control of cell behaviour: II. multiple grooved substrata. *Development (Cambridge, England)*, 108(4):635–644, 1990. PMID: 2387239.

[349] Fredrik Johansson, Patrick Carlberg, Nils Danielsen, Lars Montelius, and Martin Kanje. Axonal outgrowth on nano-imprinted patterns. *Biomaterials*, 27(8):1251–1258, 2006. PMID: 16143385.

[350] Melissa J Mahoney, Ruth R Chen, Jian Tan, and W Mark Saltzman. The influence of microchannels on neurite growth and architecture. *Biomaterials*, 26(7):771–778, 2005. PMID: 15350782.

[351] Li Yao, Shenguo Wang, Wenjin Cui, Richard Sherlock, Claire O'Connell, Gopinath Damodaran, Adrienne Gorman, Anthony Windebank, and Abhay Pandit. Effect of functionalized micropatterned PLGA on guided neurite growth. *Acta biomaterialia*, 5(2):580–588, 2009. PMID: 18835227.

[352] Nianzhen Li and Albert Folch. Integration of topographical and biochemical cues by axons during growth on microfabricated 3-d substrates. *Experimental cell research*, 311(2), 2005.

[353] Tiffany Houchin-Ray, Laura A Swift, Jae-Hyung Jang, and Lonnie D Shea. Patterned PLG substrates for localized DNA delivery and directed neurite extension. *Biomaterials*, 28(16):2603–2611, 2007.

[354] A. Rajnicek, S. Britland, and C. McCaig. Contact guidance of CNS neurites on grooved quartz: influence of groove dimensions, neuronal age and cell type. *Journal of Cell Science*, 110(23):2905–2913, 1997. PMID: 9359873.

[355] Natalia Gomez, Yi Lu, Shaochen Chen, and Christine E. Schmidt. Immobilized nerve growth factor and microtopography have distinct effects on polarization versus axon elongation in hippocampal cells in culture. *Biomaterials*, 28(2):271–284, 2007.

[356] I Nagata, A Kawana, and N Nakatsuji. Perpendicular contact guidance of CNS neuroblasts on artificial microstructures. *Development (Cambridge, England)*, 117(1):401–408, 1993. PMID: 8223260.

[357] Joshua S. Goldner, Jan M. Bruder, Grace Li, Daniele Gazzola, and Diane Hoffman-Kim. Neurite bridging across micropatterned grooves. *Biomaterials*, 27(3):460–472, 2006.

[358] Wen-Ta Su, Yung-Feng Liao, Tai-Wei Wu, Bo-Jeng Wang, and Yu-Yin Shih. Microgrooved patterns enhanced PC12 cell growth, orientation, neurite elongation, and neuritogenesis. *Journal of biomedical materials research. Part A*, 101(1):185–194, 2013. PMID: 22829561.

[359] Adam S. Crouch, D. Miller, Kevin J. Luebke, and W. Hu. Correlation of anisotropic cell behaviors with topographic aspect ratio. *Biomaterials*, 30(8):1560–1567, 2009.

[360] Pimpon Uttayarat, George K Toworfe, Franziska Dietrich, Peter I Lelkes, and Russell J Composto. Topographic guidance of endothelial cells on silicone surfaces with micro- to nanogrooves: orientation of actin filaments and focal adhesions. *Journal of biomedical materials research. Part A*, 75(3):668–680, 2005. PMID: 16110489.

[361] Sarah A Fraser, Yuk-Hong Ting, Kelly S Mallon, Amy E Wendt, Christopher J Murphy, and Paul F Nealey. Sub-micron and nanoscale feature depth modulates alignment of stromal fibroblasts and corneal epithelial cells in serum-rich and serum-free media. *Journal of biomedical materials research. Part A*, 86(3):725–735, 2008.

[362] W. Hu, E. K. F. Yim, R. M. Reano, K. W. Leong, and S. W. Pang. Effects of nanoimprinted patterns in tissue-culture polystyrene on cell behavior. *Journal of vacuum science & technology. A, Vacuum, surfaces, and films*, 23(6):2984–2989, 2005.

[363] Evelyn K F Yim, Stella W Pang, and Kam W Leong. Synthetic nanostructures inducing differentiation of human mesenchymal stem cells into neuronal lineage. *Experimental cell research*, 313(9):1820–1829, 2007.

[364] Karina Kulangara, Andrew F. Adler, Hong Wang, Malathi Chellappan, Ellen Hammett, Ryohei Yasuda, and Kam W. Leong. The effect of substrate topography on direct reprogramming of fibroblasts to induced neurons. *Biomaterials*, 35(20):5327–5336, 2014.

[365] Cristina López-Fagundo, Jennifer A Mitchel, Talisha D Ramchal, Yu-Ting L Dingle, and Diane Hoffman-Kim. Navigating neurites utilize cellular topography of schwann cell somas and processes for optimal guidance. *Acta biomaterialia*, 9(7):7158–7168, 2013. PMID: 23557939.

[366] Jin Woo Lee, Kyong Soo Lee, Nana Cho, Byeong Kwon Ju, Kyu Back Lee, and Sang Ho Lee. Topographical guidance of mouse neuronal cell on SiO2 microtracks. *Sensors and Actuators B: Chemical*, 128(1):252–257, 2007.

[367] Xu Jiang, Ruifa Mi, Ahmet Hoke, and Sing Yian Chew. Nanofibrous nerve conduit-enhanced peripheral nerve regeneration. *Journal of Tissue Engineering and Regenerative Medicine*, 8(5):377–385, 2014.

[368] Andrew Li, Akishige Hokugo, Anisa Yalom, Eric J. Berns, Nicholas Stephanopoulos, Mark T. McClendon, Luis A. Segovia, Igor Spigelman, Samuel I. Stupp, and Reza Jarrahy. A bioengineered peripheral nerve construct using aligned peptide amphiphile nanofibers. *Biomaterials*, 35(31):8780–8790, 2014.

[369] George A Abrams, Christopher J Murphy, Zun-Yi Wang, Paul F Nealey, and Dale E Bjorling. Ultrastructural basement membrane topography of the bladder epithelium. *Urological research*, 31(5):341–346, 2003.

[370] G A Abrams, S L Goodman, P F Nealey, M Franco, and C J Murphy. Nanoscale topography of the basement membrane underlying the corneal epithelium of the rhesus macaque. *Cell and tissue research*, 299(1):39–46, 2000.

[371] Jose Carlos Rodriguez Hernandez, Manuel Salmeron Sanchez, Jose Miguel Soria, Jose Luis Gomez Ribelles, and Manuel Monleon Pradas. Substrate chemistry-dependent conformations of single laminin molecules on polymer surfaces are revealed by the phase signal of atomic force microscopy. *Biophysical Journal*, 93(1):202–207, 2007. PMID: 17416620.

[372] Stephanie K Seidlits, Jae Y Lee, and Christine E Schmidt. Nanostructured scaffolds for neural applications. *Nanomedicine*, 3(2):183–199, 2008. PMID: 18373425.

[373] S L Goodman, P A Sims, and R M Albrecht. Three-dimensional extracellular matrix textured biomaterials. *Biomaterials*, 17(21):2087–2095, 1996.

[374] S. C. Bayliss, L. D. Buckberry, I. Fletcher, and M. J. Tobin. The culture of neurons on silicon. *Sensors and Actuators A: Physical*, 74(1-3):139–142, 1999.

[375] C P Pennisi, C Sevcencu, A Dolatshahi-Pirouz, M Foss, J Lundsgaard Hansen, A Nylandsted Larsen, V Zachar, F Besenbacher, and K Yoshida. Responses of fibroblasts and glial cells to nanostructured platinum surfaces. *Nanotechnology*, 20(38):385103, 2009. PMID: 19713588.

[376] Huaqiong Li, Yee Shan Wong, Feng Wen, Kee Woei Ng, Gary Ka Lai Ng, Subbu S. Venkatraman, Freddy Yin Chiang Boey, and Lay Poh Tan. Human mesenchymal stem-cell behaviour on direct laser micropatterned electrospun scaffolds with hierarchical structures. *Macromolecular Bioscience*, page n/a–n/a, 2012.

[377] Molly M. Stevens and Julian H. George. Exploring and engineering the cell surface interface. *Science*, 310(5751):1135–1138, 2005. PMID: 16293749.

[378] Anne Géraldine Guex, Dominique Lisa Birrer, Giuseppino Fortunato, Hendrik Tinorua Tevaearai, and Marie-Noëlle Giraud. Anisotropically oriented electrospun matrices with an imprinted periodic micropattern: a new scaffold for engineered muscle constructs. *Biomedical Materials*, 8(2):021001, April 2013.

[379] J.-Y. Li, Y.-C. Ho, Y.-C. Chung, F.-C. Lin, W.-L. Liao, and W.-B. Tsai. Preparation of micron/submicron hybrid patterns via a two-stage UV-imprint technique and their dimensional effects on cell adhesion and alignment. *Biofabrication*, 5(3):035003, 2013.

[380] Alexander R. Nectow, Eun Seok Gil, David L. Kaplan, and Misha E. Kilmer. A statistical algorithm for assessing cellular alignment. *Journal of Biomedical Materials Research Part A*, 101A(3):884–891, 2013.

[381] P. C. Hansen, M. E. Kilmer, and R. H. Kjeldsen. Exploiting residual information in the parameter choice for discrete ill-posed problems. *BIT Numerical Mathematics*, 46(1):41–59, 2006.

[382] Yuehua Yuan and T. Randall Lee. Contact angle and wetting properties. In Gianangelo Bracco and Bodil Holst, editors, *Surface Science Techniques*, number 51 in Springer Series in Surface Sciences, pages 3–34. Springer Berlin Heidelberg, 2013.

[383] Jan Kottner, Laurent Audigé, Stig Brorson, Allan Donner, Byron J Gajewski, Asbjørn Hróbjartsson, Chris Roberts, Mohamed Shoukri, and David L Streiner. Guidelines for reporting reliability and agreement studies (GRRAS) were proposed. *Journal of clinical epidemiology*, 64(1):96–106, 2011. PMID: 21130355.

[384] Qiaoling Huang, Longxiang Lin, Yun Yang, Ren Hu, Erwin A Vogler, and Changjian Lin. Role of trapped air in the formation of cell-and-protein micropatterns on superhydrophobic/superhydrophilic microtemplated surfaces. *Biomaterials*, 33(33):8213–8220, 2012. PMID: 22917736.

[385] K. Rechendorff, M. B. Hovgaard, M. Foss, V. P. Zhdanov, and F. Besenbacher. Enhancement of protein adsorption induced by surface roughness. *Langmuir*, 22(26):10885–10888, 2006.

[386] Satoru K. Nishimoto, Miyako Nishimoto, Sang-Won Park, Kwang-Min Lee, Hyun-Seung Kim, Jeong-Tae Koh, Joo L. Ong, Yongxing Liu, and Yunzhi Yang. The effect of titanium surface roughening on protein Absorption,Cell attachment, and cell spreading. *International Journal of Oral & Maxillofacial Implants*, 23(4):675–680, 2008.

[387] C. Nune, R. D. K. Misra, M. C. Somani, and L. P. Karjalainen. Dependence of cellular activity at protein adsorbed biointerfaces with nano- to microscale dimensionality. *Journal of Biomedical Materials Research Part A*, 102(6):1663–1676, 2014.

[388] Y. W. Fan, F. Z. Cui, S. P. Hou, Q. Y. Xu, L. N. Chen, and I. S. Lee. Culture of neural cells on silicon wafers with nano-scale surface topograph. *Journal of Neuroscience Methods*, 120(1):17–23, 2002.

[389] Stefan Hengsbach and Andrés Díaz Lantada. Rapid prototyping of multi-scale biomedical microdevices by combining additive manufacturing technologies. *Biomedical Microdevices*, 16(4):617–627, 2014.

[390] R. A. Green, P. B. Matteucci, C. W. D. Dodds, J. Palmer, W. F. Dueck, R. T. Hassarati, P. J. Byrnes-Preston, N. H. Lovell, and G. J. Suaning. Laser patterning of platinum electrodes for safe neurostimulation. *Journal of Neural Engineering*, 11(5):056017, 2014.

[391] Alejandro Carnicer Lombarte, H Lancashire, and A Vanhoestenberghe. *Biocompatibility of thick film platinum/gold electrodes printed on ceramic, and effect of current pulses through the culture medium*. Masters thesis, University College London, London, UK, 2014.

[392] Thomas Stieglitz. Manufacturing, assembling and packaging of miniaturized neural implants. *Microsystem Technologies*, 16(5):723–734, 2010.

[393] Lynne E. Bilston. *Neural Tissue Biomechanics*. Springer Science & Business Media, 2011.

[394] K. E. Jones, P. K. Campbell, and R. A. Normann. A glass/silicon composite intracortical electrode array. *Annals of Biomedical Engineering*, 20(4):423–437, 1992.

[395] K.D. Wise, D.J. Anderson, J.F. Hetke, D.R. Kipke, and K. Najafi. Wireless implantable microsystems: high-density electronic interfaces to the nervous system. *Proceedings of the IEEE*, 92(1):76–97, 2004.

[396] K. Cheung, Gun Lee, Kaj Djupsund, Yang Dan, and Luke P. Lee. A new neural probe using SOI wafers with topological interlocking mechanisms. In *1st Annual International Conference On Microtechnologies in Medicine and Biology*, pages 507–511, 2000.

[397] Maria Kindlundh, Peter Norlin, and Ulrich G. Hofmann. A neural probe process enabling variable electrode configurations. *Sensors and Actuators B: Chemical*, 102(1):51–58, 2004.

[398] M. Han, P.S. Manoonkitiwongsa, C.X. Wang, and D.B. McCreery. In vivo validation of custom-designed silicon-based microelectrode arrays for long-term neural recording and stimulation. *IEEE Transactions on Biomedical Engineering*, 59(2):346–354, 2012.

[399] P.S. Motta and J.W. Judy. Multielectrode microprobes for deep-brain stimulation fabricated with a customizable 3-d electroplating process. *IEEE Transactions on Biomedical Engineering*, 52(5):923–933, 2005.

[400] Patrick T. McCarthy, Kevin J. Otto, and Masaru P. Rao. Robust penetrating microelectrodes for neural interfaces realized by titanium micromachining. *Biomedical Microdevices*, 13(3):503–515, 2011.

[401] David Zhou and Elias Greenbaum, editors. *Implantable Neural Prostheses 2*. Springer, New York NY, 2010.

[402] Jason J. Burmeister, Karen Moxon, and Greg A. Gerhardt. Ceramic-based multisite microelectrodes for electrochemical recordings. *Analytical Chemistry*, 72(1):187–192, 2000.

[403] N. N. Donaldson and P. E. K. Donaldson. Speeding-up the cure of one-part silicone rubber, when encapsulating neurological prostheses: the permeable mould. *Medical Engineering & Physics*, 22(4):301–306, 2000.

[404] M. Schuettler, A Vanhoestenberghe, N. Saeidi, X. Liu, J. Evans, Cindy Colinge, A Demosthenous, and N. Donaldson. Realization of an active book for multichannel intrathecal root stimulation in spinal cord injury #x2014; preliminary results. In *Annual International Conference of the IEEE Engineering in Medicine and Biology Society*, pages 2965–2968, 2011.

[405] M. F. Ashby and David R. H. Jones. *Engineering materials 1: an introduction to poperties, applications and design.* Elsevier Butterworth-Heinemann, Oxford, [U.K.]; Burlington, Mass., 3 edition, 2005.

[406] MatWeb LLC. AISI type 316l stainless steel, annealed bar. `http://www.matweb.com/search/datasheet.aspx?MatGUID=a2d0107bf958442e9f8db6dc9933fe31`. Accessed: 2014-08-15.

[407] MatWeb LLC. 99.5% alumina, thin film substrate. `http://www.matweb.com/search/datasheet.aspx?MatGUID=cf62e273c8c1403387b6e124814f3403`, 2014. Accessed: 2014-08-19.

[408] R.S. Clement, A Singh, B. Olson, K. Lee, and J. He. Neural recordings from a benzocyclobutene (BCB) based intra-cortical neural implant in an acute animal model. In *Annual International Conference of the IEEE Engineering in Medicine and Biology Society*, volume 3, pages 2176–2179 Vol.3, 2003.

[409] MatWeb LLC. Gold, au. `http://www.matweb.com/search/DataSheet.aspx?MatGUID=d2a2119a08904a0fa706e9408cddb88e&ckck=1`, 2014. Accessed: 2014-08-27.

[410] The PGM Database. Iridium. `http://www.pgmdatabase.com/jmpgm/index.jsp?record=1064`. Accessed: 2014-08-15.

[411] Tufts.edu. Parylene conformal coating specifications & properties. http://engineering.tufts.edu/microfab/documents/Parylene.pdf, 2014. Accessed: 2014-08-19.

[412] MatWeb LLC. Platinum, pt, CP grade, annealed. http://www.matweb.com/search/DataSheet.aspx?MatGUID=4e81bfe98eef4c368363c9c67426850b. Accessed: 2014-08-15.

[413] The PGM Database. Platinum - 10.00% iridium. http://www.pgmdatabase.com/jmpgm/index.jsp?record=1064. Accessed: 2014-08-15.

[414] Udo Lang and Jürg Dual. Mechanical properties of the intrinsically conductive polymer poly(3,4-ethylenedioxythiophene) poly(styrenesulfonate) (PEDOT/PSS). *Key Engineering Materials*, 345-346:1189–1192, 2007.

[415] H. Valentova and J. Stejskal. Mechanical properties of polyaniline. *Synthetic Metals*, 160(7-8):832–834, 2010.

[416] FujiFilm. Durimide 7000 US12. http://www.fujifilmusa.com/shared/bin/Durimide%207000_US12.pdf, May 2012. Accessed: 2014-08-19.

[417] HD MicroSystems. PI-2600 process guide. http://hdmicrosystems.com/HDMicroSystems/en_US/pdf/PI-2600_ProcessGuide.pdf, September 2009. Accessed: 2014-08-19.

[418] P. Murray, G. M. Spinks, G. G. Wallace, and R. P. Burford. In-situ mechanical properties of tosylate doped (pts) polypyrrole. *Synthetic Metals*, 84(1–3):847–848, 1997.

[419] MatWeb LLC. Silicon, si. http://www.matweb.com/search/DataSheet.aspx?MatGUID=7d1b56e9e0c54ac5bb9cd433a0991e27. Accessed: 2014-08-15.

[420] I. D. Johnston, D. K. McCluskey, C. K. L. Tan, and M. C. Tracey. Mechanical characterization of bulk sylgard 184 for microfluidics and microengineering. *Journal of Micromechanics and Microengineering*, 24(3):035017, March 2014.

[421] M. Schuettler, D. Pfau, J.S. Ordonez, C. Henle, P. Woias, and T. Stieglitz. Stretchable tracks for laser-machined neural electrode arrays. In *Annual International Conference of the IEEE Engineering in Medicine and Biology Society*, pages 1612–1615, 2009.

[422] Jiali Gao, Le Guan, and Jinkui Chu. Determining the young's modulus of SU-8 negative photoresist through tensile testing for MEMS applications. In *Proceedings of the Sixth International Symposium on Precision Engineering Measurements and Instrumentation*, volume 7544, pages 754464–754464–7, 2010.

[423] Soonwan Chung and Seungbae Park. Effects of temperature on mechanical properties of SU-8 photoresist material. *Journal of Mechanical Science and Technology*, 27(9):2701–2707, 2013.

[424] MatWeb LLC. Tungsten, w, (drawn wire). `http://www.matweb.com/search/DataSheet.aspx?MatGUID=37fde7152eb94e3dbcbde8e2edc0a497`. Accessed: 2014-08-15.

[425] Liang Guo, Mingming Ma, Ning Zhang, Robert Langer, and Daniel G. Anderson. Stretchable polymeric multielectrode array for conformal neural interfacing. *Advanced Materials*, 26(9):1427–1433, 2014.

[426] Catalina Vallejo-Giraldo, Adriona Kelly, and Manus J. P. Biggs. Biofunctionalisation of electrically conducting polymers. *Drug Discovery Today*, 19(1):88–94, 2014.

[427] Juan Ordonez, Martin Schuettler, Christian Boehler, Tim Boretius, and Thomas Stieglitz. Thin films and microelectrode arrays for neuroprosthetics. *MRS Bulletin*, 37(06):590–598, 2012.

[428] A. Benvenuto, S. Raspopovic, K.P. Hoffmann, J. Carpaneto, G. Cavallo, G. Di Pino, E. Guglielmelli, L. Rossini, P.M. Rossini, M. Tombini, and S. Micera. Intrafascicular thin-film multichannel electrodes for sensory feedback: Evidences on a human amputee. In *Annual International Conference of the IEEE Engineering in Medicine and Biology Society*, pages 1800–1803, 2010.

[429] AA Fomani, R.R. Mansour, C.M. Florez-Quenguan, and P.L. Carlen. Development and characterization of multisite three-dimensional microprobes for deep brain stimulation and recording. *Journal of Microelectromechanical Systems*, 20(5):1109–1118, 2011.

[430] AA Fomani and R.R. Mansour. Flexible neural microelectrode arrays reinforced with embedded metallic micro-needles. In *2010 IEEE Sensors*, pages 1601–1604, 2010.

[431] Shoji Takeuchi, Takafumi Suzuki, Kunihiko Mabuchi, and Hiroyuki Fujita. 3d flexible multichannel neural probe array. *Journal of Micromechanics and Microengineering*, 14(1):104, 2004.

[432] Shoji Takeuchi, D. Ziegler, Y. Yoshida, K. Mabuchi, and T. Suzuki. Parylene flexible neural probes integrated with microfluidic channels. *Lab on a Chip*, 5(5):519–523, 2005.

[433] S.R. Kane, S.F. Cogan, J. Ehrlich, T.D. Plante, D.B. McCreery, and P.R. Troyk. Electrical performance of penetrating microelectrodes chronically implanted in cat cortex. *IEEE Transactions on Biomedical Engineering*, 60:2153–2160, 2013.

[434] Wen Li, Damien Rodger, Parvathy Menon, and Yu-Chong Tai. Corrosion behavior of parylene-metal-parylene thin films in saline. *ECS Transactions*, 11(18):1–6, 2008.

[435] Kee-Keun Lee, Jiping He, A Singh, and Bruce Kim. Benzocyclobutene (BCB) based intracortical neural implant. In *International Conference on MEMS, NANO and Smart Systems*, pages 418–422, 2003.

[436] K. Lee, J. He, and L. Wang. Benzocyclobutene (BCB) based neural implants with microfluidic channel. *Annual International Conference of the IEEE Engineering in Medicine and Biology Society.*, 6:4326–4329, 2004.

[437] Keekeun Lee, Jiping He, Ryan Clement, Stephen Massia, and Bruce Kim. Biocompatible benzocyclobutene (BCB)-based neural implants with micro-fluidic channel. *Biosensors and Bioelectronics*, 20(2):404–407, 2004.

[438] Amarjit Singh, Haixin Zhu, and Jiping He. Improving mechanical stiffness of coated benzocyclobutene (BCB) based neural implant. *Annual International Conference of the IEEE Engineering in Medicine and Biology Society.*, 6:4298–4301, 2004.

[439] Ane Altuna, Liset Menendez de la Prida, Elisa Bellistri, Gemma Gabriel, Anton Guimera, Javier Berganzo, Rosa Villa, and Luis J. Fernández. SU-8 based microprobes with integrated planar electrodes for enhanced neural depth recording. *Biosensors and Bioelectronics*, 37(1):1–5, 2012.

[440] Krishnamurthy V. Nemani, Karen L. Moodie, Jeoffry B. Brennick, Alison Su, and Barjor Gimi. In vitro and in vivo evaluation of SU-8 biocompatibility. *Materials Science and Engineering: C*, 33(7):4453–4459, 2013.

[441] C. Veraart, W.M. Grill, and J.T. Mortimer. Selective control of muscle activation with a multipolar nerve cuff electrode. *IEEE Transactions on Biomedical Engineering*, 40(7):640–653, 1993.

[442] M. Schuetter, S Stiess, B V King, and G J Suaning. Fabricating microelectrode arrays by laser-cutting of platinum foil an d silicone rubber. In *Proceedings of the 9th Annual Conference of the IFESS*, Bournemouth, UK, 2004. IFESS.

[443] M Schuettler, S Stiess, B V King, and G J Suaning. Fabrication of implantable microelectrode arrays by laser cutting of silicone rubber and platinum foil. *Journal of neural engineering*, 2(1):S121–128, 2005.

[444] G.G. Naples, J.T. Mortimer, A Scheiner, and J.D. Sweeney. A spiral nerve cuff electrode for peripheral nerve stimulation. *IEEE Transactions on Biomedical Engineering*, 35(11):905–916, 1988.

[445] JT Mortimer. Electrodes for functional electrical stimulation. Final Report 4, NIH-NINDS, 2000.

[446] G.J. Suaning, M. Schuettler, J.S. Ordonez, and N.H. Lovell. Fabrication of multi-layer, high-density micro-electrode arrays for neural stimulation and bio-signal recording. In *3rd International IEEE/EMBS Conference on Neural Engineering.*, pages 5–8, 2007.

[447] V. Carrington, L. Zhou, and Professor N. Donaldson. Noise from implantable cooper cable. *Medical and Biological Engineering and Computing*, 43(5):618–621, 2005.

[448] Stephanie Perichon Lacour, S. Wagner, Zhenyu Huang, and Z. Suo. Stretchable gold conductors on elastomeric substrates. *Applied Physics Letters*, 82(15):2404–2406, 2003.

[449] Stéphanie P. Lacour, Samia Benmerah, Edward Tarte, James FitzGerald, Jordi Serra, Stephen McMahon, James Fawcett, Oliver Graudejus, Zhe Yu, and Barclay Morrison. Flexible and stretchable micro-electrodes for in vitro and in vivo neural interfaces. *Medical & Biological Engineering & Computing*, 48(10):945–954, 2010.

[450] Oliver Graudejus, Barclay Morrison, Cezar Goletiani, Zhe Yu, and Sigurd Wagner. Encapsulating elastically stretchable neural interfaces: Yield, resolution, and recording/stimulation of neural activity. *Advanced Functional Materials*, 22(3):640–651, 2012.

[451] John A. Rogers, Takao Someya, and Yonggang Huang. Materials and mechanics for stretchable electronics. *Science*, 327(5973):1603–1607, 2010.

[452] Woo Hyeun Kang, Wenzhe Cao, Sigurd Wagner, and Barclay Morrison. Stretchable neural interfaces. In Takao Someya, editor, *Stretchable Electronics*, pages 379–399. Wiley-VCH Verlag GmbH & Co. KGaA, 2012.

[453] Paolo M. Rossini, Silvestro Micera, Antonella Benvenuto, Jacopo Carpaneto, Giuseppe Cavallo, Luca Citi, Christian Cipriani, Luca Denaro, Vincenzo Denaro, Giovanni Di Pino, Florinda Ferreri, Eugenio Guglielmelli, Klaus-Peter Hoffmann, Stanisa Raspopovic, Jacopo Rigosa, Luca Rossini, Mario Tombini, and Paolo Dario. Double nerve intraneural interface implant on a human amputee for robotic hand control. *Clinical Neurophysiology*, 121(5):777–783, 2010.

[454] N. Donaldson, R. Rieger, M. Schuettler, and J. Taylor. Noise and selectivity of velocity-selective multi-electrode nerve cuffs. *Medical & Biological Engineering & Computing*, 46(10):1005–1018, 2008.

[455] Soo Hyun Lee, Jung Hwan Jung, Youn Mee Chae, Jun-Kyo Francis Suh, and Ji Yoon Kang. Fabrication and characterization of implantable and flexible nerve cuff electrodes with pt, ir and IrOx films deposited by RF sputtering. *Journal of Micromechanics and Microengineering*, 20(3):035015, 2010.

[456] K H Polasek, M A Schiefer, G C J Pinault, R J Triolo, and D J Tyler. Intraoperative evaluation of the spiral nerve cuff electrode on the femoral nerve trunk. *Journal of neural engineering*, 6(6):066005, 2009.

[457] M. Schuettler, S. Schroeer, J.S. Ordonez, and T. Stieglitz. Laser-fabrication of peripheral nerve cuff electrodes with integrated microfluidic channels. In *5th International IEEE/EMBS Conference on Neural Engineering*, pages 245–248, 2011.

[458] Katherine Musick, David Khatami, and Bruce C. Wheeler. Three-dimensional micro-electrode array for recording dissociated neuronal cultures. *Lab on a Chip*, 9(14):2036–2042, 2009.

[459] H Lancashire, C Pendegrass, A Vanhoestenberghe, and G Blunn. Towards a 3-dimensional model of neural tissue with integrated recording sites. In *26th Annual Conference, European Society for Biomaterials*, page P534, Liverpool, UK, 2014.

[460] Hong-Bo Zhou, Gang Li, Xiao-Na Sun, Zhuang-Hui Zhu, Qing-Hui Jin, Jian-Long Zhao, and Qiu-Shi Ren. Integration of au nanorods with flexible thin-film microelectrode arrays for improved neural interfaces. *Journal of Microelectromechanical Systems*, 18(1):88–96, 2009.

[461] Gregory Panaitov, Simon Thiery, Boris Hofmann, and Andreas Offenhäusser. Fabrication of gold micro-spine structures for improvement of cell/device adhesion. *Microelectronic Engineering*, 88(8):1840–1844, 2011.

[462] Richárd Fiath, Laszlo Grand, Balint Kerekes, Anita Pongracz, Eva Vazsonyi, Gergely Marton, Gabor Battistig, and Istvan Ulbert. A novel multisite silicon probe for laminar neural recordings. *Procedia Computer Science*, 7:310–311, 2011.

[463] S.R.I Gabran, M.T. Salam, J. Dian, Y. El-Hayek, J.L. Perez Velazquez, R. Genov, P.L. Carlen, M.M.A Salama, and R.R. Mansour. 3-d flexible nano-textured high-density microelectrode arrays for high-performance neuro-monitoring and neuro-stimulation. *IEEE Transactions on Neural Systems and Rehabilitation Engineering*, 22(5):1072–1082, 2014.

[464] J.S. Ordonez, C. Boehler, M. Schuettler, and T. Stieglitz. Improved polyimide thin-film electrodes for neural implants. In *Annual International Conference of the IEEE Engineering in Medicine and Biology Society*, pages 5134–5137, 2012.

[465] F.S. Hamdi, M. Woytasik, M. Couty, O. Francais, B. Le Pioufle, and E. Dufour-Gergam. Low temperature irreversible poly(DiMethyl) siloxane packaging of silanized SU8 microchannels: Characterization and lab-on-chip application. *Journal of Microelectromechanical Systems*, 23(5):1015–1024, 2014.

[466] Li Yao, Kristen L. Billiar, Anthony J. Windebank, and Abhay Pandit. Multichanneled collagen conduits for peripheral nerve regeneration: Design, fabrication, and characterization. *Tissue Engineering Part C: Methods*, 16(6):1585–1596, 2010.

[467] Thomas Stieglitz, Hansjoerg Beutel, and J.-Uwe Meyer. "Microflex"—A New Assembling Technique for Interconnects. *Journal of Intelligent Material Systems and Structures*, 11(6):417–425, 2000.

[468] Martin Schuettler, Christian Henle, Juan S. Ordonez, Wolfgang Meier, Thomas Guenther, and Thomas Stieglitz. Interconnection technologies for laser-patterned electrode arrays. *Annual International Conference of the IEEE Engineering in Medicine and Biology Society*, 2008:3212–3215, 2008.

[469] J.-U. Meyer, T. Stieglitz, O. Scholz, W. Haberer, and H. Beutel. High density interconnects and flexible hybrid assemblies for active biomedical implants. *IEEE Transactions on Advanced Packaging*, 24:366–374, 2001.

[470] Irina I. Stoyanova, Richard J. A. van Wezel, and Wim L. C. Rutten. In vivo testing of a 3d bifurcating microchannel scaffold inducing separation of regenerating axon bundles in peripheral nerves. *Journal of Neural Engineering*, 10(6):066018, 2013.

[471] H. Schmid and B. Michel. Siloxane polymers for high-resolution, high-accuracy soft lithography. *Macromolecules*, 33(8):3042–3049, 2000.

[472] C. Henle, W. Meier, M. Schuettler, T. Boretius, and T. Stieglitz. Electrical characterization of platinum, stainless steel and platinum/iridium as electrode materials for a new neural interface. In Olaf Dössel and Wolfgang C. Schlegel, editors, *World Congress on Medical Physics and Biomedical Engineering, September 7 - 12, 2009, Munich, Germany*, number 25/9 in IFMBE Proceedings, pages 100–103. Springer Berlin Heidelberg, 2009.

[473] Leigh R. Hochberg, Mijail D. Serruya, Gerhard M. Friehs, Jon A. Mukand, Maryam Saleh, Abraham H. Caplan, Almut Branner, David Chen, Richard D. Penn, and John P. Donoghue. Neuronal ensemble control of prosthetic devices by a human with tetraplegia. *Nature*, 442(7099):164–171, 2006.

[474] Eduardo Fernández, Bradley Greger, Paul A. House, Ignacio Aranda, Carlos Botella, Julio Albisua, Cristina Soto-Sánchez, Arantxa Alfaro, and Richard A. Normann. Acute human brain responses to intracortical microelectrode arrays: challenges and future prospects. *Frontiers in Neuroengineering*, 7:24, 2014.

[475] Jitte Groothuis, Nick F. Ramsey, Geert M. J. Ramakers, and Geoffrey van der Plasse. Physiological challenges for intracortical electrodes. *Brain Stimulation*, 7(1):1–6, 2014.

[476] B. Wodlinger, J. E. Downey, E. C. Tyler-Kabara, A. B. Schwartz, M. L. Boninger, and J. L. Collinger. Ten-dimensional anthropomorphic arm control in a human brain-machine interface: difficulties, solutions, and limitations. *Journal of Neural Engineering*, 12(1):016011, 2015.

[477] Thomas Sinkjaer, Morten Haugland, Andreas Inmann, Morten Hansen, and Kim D Nielsen. Biopotentials as command and feedback signals in functional electrical stimulation systems. *Medical Engineering & Physics*, 25(1):29–40, 2003.

[478] K.H. Polasek, H.A. Hoyen, M.W. Keith, R.F. Kirsch, and D.J. Tyler. Stimulation Stability and Selectivity of Chronically Implanted Multicontact Nerve Cuff Electrodes in the Human Upper Extremity. *IEEE Transactions on Neural Systems and Rehabilitation Engineering*, 17(5):428–437, 2009.

[479] L E Fisher, D J Tyler, J S Anderson, and R J Triolo. Chronic stability and selectivity of four-contact spiral nerve-cuff electrodes in stimulating the human femoral nerve. *Journal of neural engineering*, 6(4):046010, 2009.

[480] K. Warwick, M. Gasson, B. Hutt, I. Goodhew, P. Kyberd, H. Schulzrinne, and X. Wu. Thought communication and control: a first step using radiotelegraphy. *IEEE Proceedings - Communications*, 151(3):185–189, 2004.

[481] Gurpreet S Dhillon, Stephen M Lawrence, Douglas T Hutchinson, and Kenneth W Horch. Residual function in peripheral nerve stumps of amputees: implications for neural control of artificial limbs. *The Journal of Hand Surgery*, 29(4):605–615, 2004.

[482] S. Micera, M.C. Carrozza, L. Beccai, F. Vecchi, and P. Dario. Hybrid Bionic Systems for the Replacement of Hand Function. *Proceedings of the IEEE*, 94(9):1752–1762, 2006.

[483] S. Micera, L. Citi, J. Rigosa, J. Carpaneto, S. Raspopovic, G. Di Pino, L. Rossini, K. Yoshida, L. Denaro, P. Dario, and P.M. Rossini. Decoding Information From Neural Signals Recorded Using Intraneural Electrodes: Toward the Development of a Neurocontrolled Hand Prosthesis. *Proceedings of the IEEE*, 98(3):407–417, 2010.

[484] S. Micera, X. Navarro, J. Carpaneto, L. Citi, O. Tonet, P.M. Rossini, M.C. Carrozza, K.P. Hoffmann, M. Vivo, K. Yoshida, and P. Dario. On the Use of Longitudinal Intrafascicular Peripheral Interfaces for the Control of Cybernetic Hand Prostheses in Amputees. *IEEE Transactions on Neural Systems and Rehabilitation Engineering*, 16(5):453–472, 2008.

[485] T. Boretius, K. Yoshida, J. Badia, K. Harreby, A. Kundu, X. Navarro, W. Jensen, and T. Stieglitz. A transverse intrafascicular multichannel electrode (TIME) to treat phantom limb pain #x2014; Towards human clinical trials. In *4th IEEE RAS EMBS International Conference on Biomedical Robotics and Biomechatronics*, pages 282–287, 2012.

[486] Xiaofeng Jia, Matthew A. Koenig, Xiaowen Zhang, Jian Zhang, Tongyi Chen, and Zhongwei Chen. Residual motor signal in long-term human severed peripheral nerves and feasibility of neural signal-controlled artificial limb. *The Journal of Hand Surgery*, 32(5):657–666, 2007.

[487] Xiao-wen Zhang, Yu-pu Yang, Xiao-ming Xu, Tian-pei Hu, Zhong-hua Gao, Jian Zhang, Tongyi Chen, and Zhong-wei Chen. Clinical detection and movement recognition of neuro signals. *Journal of Zhejiang University. Science. B*, 6(4):272–279, 2005.

[488] G. Di Pino, E. Guglielmelli, and P. M. Rossini. Neuroplasticity in amputees: main implications on bidirectional interfacing of cybernetic hand prostheses. *Progress in Neurobiology*, 88(2):114–126, 2009.

[489] G. S. Dhillon, T. B. Krüger, J. S. Sandhu, and K. W. Horch. Effects of short-term training on sensory and motor function in severed nerves of long-term human amputees. *Journal of Neurophysiology*, 93(5):2625–2633, 2005.

[490] M.D. Tarler and J.T. Mortimer. Selective and independent activation of four motor fascicles using a four contact nerve-cuff electrode. *IEEE Transactions on Neural Systems and Rehabilitation Engineering*, 12(2):251–257, 2004.

[491] Xavier Navarro, Elena Valderrama, Thomas Stieglitz, and Martin Schüttler. Selective fascicular stimulation of the rat sciatic nerve with multipolar polyimide cuff electrodes. *Restorative Neurology and Neuroscience*, 18(1):9–21, 2001.

[492] P. J. Rousche and R. A. Normann. A method for pneumatically inserting an array of penetrating electrodes into cortical tissue. *Annals of Biomedical Engineering*, 20(4):413–422, 1992.

[493] Almut Branner, Richard B Stein, and Richard A Normann. Selective Stimulation of Cat Sciatic Nerve Using an Array of Varying-Length Microelectrodes. *Journal of Neurophysiology*, 85(4):1585–1594, 2001.

[494] X. Navarro, N. Lago, M. Vivo, K. Yoshida, K.P. Koch, W. Poppendieck, and S. Micera. Neurobiological evaluation of thin-film longitudinal intrafascicular electrodes as a peripheral nerve interface. In *IEEE 10th International Conference on Rehabilitation Robotics*, pages 643–649, 2007.

[495] James J. FitzGerald, Stephanie P. Lacour, and James W. Fawcett. Recording with microchannel electrodes in a noisy environment. *Annual International Conference of the IEEE Engineering in Medicine and Biology Society.*, 2008:34–37, 2008.

[496] Diana Angius, Huan Wang, Robert J. Spinner, Yearim Gutierrez-Cotto, Michael J. Yaszemski, and Anthony J. Windebank. A systematic review of animal models used to study nerve regeneration in tissue-engineered scaffolds. *Biomaterials*, 33(32):8034–8039, 2012.

[497] Luis E. Savastano, Sergio R. Laurito, Marcos R. Fitt, Jorge A. Rasmussen, Virginia Gonzalez Polo, and Sean I. Patterson. Sciatic nerve injury: A simple and subtle model for investigating many aspects of nervous system damage and recovery. *Journal of Neuroscience Methods*, 227:166–180, 2014.

[498] Ahmet Höke. Mechanisms of Disease: what factors limit the success of peripheral nerve regeneration in humans? *Nature Clinical Practice Neurology*, 2(8):448–454, 2006.

[499] M M Carr, T J Best, S E Mackinnon, and P J Evans. Strain differences in autotomy in rats undergoing sciatic nerve transection or repair. *Annals of plastic surgery*, 28(6):538–544, 1992.

[500] Doreen Berman and Barbara E. Rodin. The influence of housing condition on autotomy following dorsal rhizotomy in rats. *PAIN*, 13(3):307–311, 1982.

[501] Stefania Raimondo, Michele Fornaro, Federica Di Scipio, Giulia Ronchi, Maria G. Giacobini-Robecchi, and Stefano Geuna. Methods and Protocols in Peripheral Nerve Regeneration Experimental Research: Part II—Morphological Techniques. In Stefano Geuna; Pierluigi Tos and Bruno Battiston, editor, *International Review of Neurobiology*, volume 87, pages 81–103. Academic Press, 2009.

[502] John D. Bancroft and Alan Stevens, editors. *Theory and practice of histological techniques*. Churchill Livingstone, Edinburgh ; New York, 3rd ed edition, 1990.

[503] Thomas M. Brushart. *Nerve Repair*. Oxford University Press, 2011.

[504] Federica Di Scipio, Stefania Raimondo, Pierluigi Tos, and Stefano Geuna. A simple protocol for paraffin-embedded myelin sheath staining with osmium tetroxide for light microscope observation. *Microscopy Research and Technique*, 71(7):497–502, 2008.

[505] Luis de Medinaceli, William J. Freed, and Richard Jed Wyatt. An index of the functional condition of rat sciatic nerve based on measurements made from walking tracks. *Experimental Neurology*, 77(3):634–643, 1982.

[506] J.B. Bain, S. E. Mackinnon, and R.T Hunter. Functional evaluation of complete sciatic, peroneal, and posterior tibial nerve lesions in the rat. *Plastic and Reconstructive Surgery*, 83(1):129–136, 1989.

[507] C. J. Brown, S. E. Mackinnon, P. J. Evans, J. R. Bain, A. P. Makino, O. A. Hunter, and G. M. T. Hare. Self-evaluation of walking-track measurement using a sciatic function index. *Microsurgery*, 10(3):226–235, 1989.

[508] Vanessa Vilela Monte-Raso, Cláudio Henrique Barbieri, Nilton Mazzer, Alexandre Calura Yamasita, and Giuliano Barbieri. Is the sciatic functional index always reliable and reproducible? *Journal of Neuroscience Methods*, 170:255–261, 2008.

[509] The Mammal Society. National hedgehog survey - volunteer pack, 2012.

[510] F Kanaya, J C Firrell, and W C Breidenbach. Sciatic function index, nerve conduction tests, muscle contraction, and axon morphometry as indicators of regeneration. *Plastic and reconstructive surgery*, 98(7):1264–1271, discussion 1272–1274, 1996.

[511] Theofano Eftaxiopoulou, Warren Macdonald, David Britzman, and Anthony M. J. Bull. Gait compensations in rats after a temporary nerve palsy quantified using temporo-spatial and kinematic parameters. *Journal of Neuroscience Methods*, 232:16–23, 2014.

[512] Frank Werdin, Hannes Grüssinger, Patrick Jaminet, Armin Kraus, Theodora Manoli, Timm Danker, Elke Guenther, Max Haerlec, Hans-Eberhard Schaller, and Nektarios Sinis. An improved electrophysiological method to study peripheral nerve regeneration in rats. *Journal of Neuroscience Methods*, 182(1):71–77, 2009.

[513] Roberto Sergio Martins, Mario Gilberto Siqueira, Ciro Ferreira da Silva, Benedito Ortiz de Godoy, and José Píndaro Pereira Plese. Electrophysiologic assessment of regeneration in rat sciatic nerve repair using suture, fibrin glue or a combination of both techniques. *Arquivos de Neuro-Psiquiatria*, 63(3A):601–604, 2005.

[514] Roberto S. Martins, Mario G. Siqueira, Ciro F. Da Silva, and José P. P. Plese. Overall assessment of regeneration in peripheral nerve lesion repair using fibrin glue, suture, or a combination of the 2 techniques in a rat model. Which is the ideal choice? *Surgical Neurology*, 64, Supplement 1:S10–S16, 2005.

[515] Lawrence R. Williams, Nils Danielsen, Harald Müller, and Silvio Varon. Exogenous matrix precursors promote functional nerve regeneration across a 15-mm gap within a silicone chamber in the rat. *The Journal of Comparative Neurology*, 264(2):284–290, 1987.

[516] Marie Jubran and Johan Widenfalk. Repair of peripheral nerve transections with fibrin sealant containing neurotrophic factors. *Experimental Neurology*, 181(2):204–212, 2003.

[517] Byung-Ho Choi, Sang-Gyun Han, Sung-Hoon Kim, Shi-Jiang Zhu, Jin-Young Huh, Jae-Hyung Jung, Seoung-Ho Lee, and Byung-Yong Kim. Autologous fibrin glue in peripheral nerve regeneration in vivo. *Microsurgery*, 25(6):495–499, 2005.

[518] W F den Dunnen and M F Meek. Sensory nerve function and auto-mutilation after reconstruction of various gap lengths with nerve guides and autologous nerve grafts. *Biomaterials*, 22(10):1171–1176, 2001. PMID: 11352096.

[519] Ian M. R. Lowdon, Anthony V. Seaber, and James R. Urbaniak. An improved method of recording rat tracks for measurement of the sciatic functional index of de medinaceli. *Journal of Neuroscience Methods*, 24(3):279–281, 1988.

[520] M. Sakurai. Use of bromphenol blue printing method for detecting sweat on the palm. *The Journal of Hand Surgery: British & European Volume*, 11(1):125–130, 1986.

[521] Masayoshi Ikeda and Yoshinori Oka. The relationship between nerve conduction velocity and fiber morphology during peripheral nerve regeneration. *Brain and Behavior*, 2(4):382–390, 2012.

[522] Shoshana L. Woo, Melanie G. Urbanchek, Paul S. Cederna, and Nicholas B. Langhals. Revisiting Nonvascularized Partial Muscle Grafts: A Novel Use for Prosthetic Control. *Plastic and Reconstructive Surgery*, 134(2):344e–346e, 2014.

[523] ISO/TC 61/SC 11. *ISO 9142:2003, Adhesives - Guide to the selection of standard laboratory ageing conditions for testing bonded joints*. American National Standards Institute, 2007.

[524] A. S. Maxwell, W R Broughton, G. Dean, and G. S. Sims. *Review of Accelerated Ageing Methods and Lifetime Prediction Techniques for Polymeric Materials*. National Physical Laboratory, Teddington, UK, 2005.

[525] V. Giagka, N. Saeidi, A. Demosthenous, and N. Donaldson. Controlled silicon IC thinning on individual die level for active implant integration using a purely mechanical process. In *64th IEEE Electronic Components and Technology Conference*, pages 2213–2219, May 2014.

[526] Pallav Sengupta. The Laboratory Rat: Relating Its Age With Human's. *International Journal of Preventive Medicine*, 4(6):624–630, 2013.

[527] H Abdi. Bonferroni and Šidák corrections for multiple comparisons. In N.J. Salkind, editor, *Encyclopedia of Measurement and Statistics.* Sage, Thousand Oaks, CA., 2007.